

TIME-RESOLVED, OPTICAL STUDIES OF  
LASER-PRODUCED PLASMAS

by

John Murdoch

Imperial College  
London

Thesis submitted for the degree of Doctor of Philosophy of  
the University of London and for the Diploma of Membership  
of the Imperial College of Science and Technology.

November, 1979

TIME-RESOLVED, OPTICAL STUDIES OF  
LASER-PRODUCED PLASMAS

Abstract

Two important aspects of laser fusion research are (i) the efficiency with which laser energy is coupled to the target and (ii) the transport of deposited energy to the imploding compression front. Results of a number of experiments relevant to (i) and (ii) are presented. Mainly optical diagnostics are used giving measurements of plasma expansion, emission and opacity.

The two principal experiments are:

- (a) thin foil burn through experiment in which the behaviour of polystyrene foils irradiated with 100 ps neodymium laser pulses is studied.
- (b) Brillouin backscatter experiment in which back-reflected light from microballoon targets irradiated by 1.6 ns pulses is spectrally and temporally resolved.

Comparison of the results of (a) with various models indicates that foils remain highly absorbing when underdense. Also, lateral thermal conduction is inhibited. It is proposed that ion turbulence is responsible for both of these observations.

In (b), time resolved spectra of backscattered light at near the laser frequency, display both red and blue shifts. Spectra are interpreted in terms of Doppler and Brillouin effects; coronal electron temperatures and density scale lengths are derived.

## CONTENTS

### 1 INTRODUCTION

1.1	General introduction	1
1.2	Brief review of some absorption and transport processes	3
1.3	Neodymium laser; description and focussing	17
1.4	Target details	21

### 2 RUBY LASER

2.1	General description	23
2.2	Fast switching circuit	27
2.3	Back-lighting optics	31
2.4	Bremsstrahlung emission	35

### 3 DIAGNOSTICS

3.1	Calorimetry	39
3.2	Prepulse monitor	41
3.3	Lens plane pictures	43
3.4	Scattered light photodiodes	45
3.5	Focal plane pictures	49
3.6	Streak photography	55
3.7	Ion emission measurements	69
3.8	X-ray diodes	71
3.9	Magnetic field probes	71
3.10	Spectroscopy	73

### 4 THIN FOIL BURNTROUGH EXPERIMENT

4.1	Review of thin foil experiments	77
4.2	Description of the experiment	85
4.3	Observations	87
4.4	Second harmonic emission from thick foil targets	115
4.5	Time and space resolved $3/2 \omega_0$ emission	119

5	<u>DISCUSSION OF THIN FOIL DATA</u>	
5.1	Comparison between S1 and S20 data	123
5.2	Fractional energy transmission	125
5.3	Energy balance	129
5.4	Damage threshold	133
5.5	Spreading of opaque region	135
5.6	Self-similar model of foil expansion	140
5.7	One-dimensional computer model of foil expansion	148
5.8	Two-dimensional computer model	161
5.9	Ion turbulence	165
5.10	Features after burnthrough	172
6	<u>BRILLOUIN EXPERIMENT</u>	
6.1	Review of theory	174
6.2	Review of experimental work	186
6.3	Experimental arrangement	194
6.4	Results	198
6.5	Discussion	200
6.6	Conclusion	207
7	<u>FURTHER EXPERIMENTS WITH SPHERICAL TARGETS</u>	
7.1	Second harmonic generation	208
7.2	Second harmonic emission from microballoons	210
7.3	Back-lighting of microballoons	215
8	<u>CONCLUSION</u>	218
	<u>REFERENCES</u>	221

## LIST OF TABLES

4.1	Effect of prepulse level on time-integrated transmission and absorption	84
4.2	List of shots with time-integrated energy measurements	86
4.3	List of shots with S1 data available	95
4.4	Variation of opacity and burnthrough times with incident intensity	96
4.5	Variation of the duration of the opaque period with prepulse level	103
4.6	Summary of observations	107
4.7	List of shots with S20 data available	108
4.8	Ion probe data	112
4.9	Shots with $3/2 \omega_0$ emission	120
5.1	Energy balance for Shot 11/210778	128
5.2	Energy balance for Shot 16/200778	128
5.3	Energy balance from data of Ref N2 (NRL)	128
6.1	List of data shots for the Brillouin experiment	199
7.1	List of data shots for the second harmonic emission from microballoon experiment	213

### Acknowledgements

I would like to thank Dr. J.D. Kilkenny for supervising the work presented below and for reading the preliminary draft of the thesis. I am also indebted to Professor M.G. Haines, to W.T. Toner for help with the streak photography and many late nights, to Dr. R.G. Evans for assistance with the Brillouin experiment and Medusa simulations, to J. Westlake for help with the ruby laser and avalanche circuit and to Dr. D.R. Gray for much assistance with the thin foil experiment, especially the photodiodes. Thanks are also due to T.G. Goldsack, S. Veats, S.M.L. Sim, A.J. Cole, Dr. P.T. Rumsby (ion emission measurements and target fabrications), Dr. M.S. White (photodiodes) and to members of the Rutherford Laboratory staff. I would also like to thank Sue MacDonald for the typing.

## CHAPTER 1

### INTRODUCTION

This chapter comprises an introduction, a review of some physical processes referred to in later Chapters, and a description of the laser pulses and targets used in the experiments.

#### 1.1 General Introduction

With the development of lasers from 1960, it was quickly realised that a technique for compressing matter to high densities had become available. Sufficient irradiance can be generated on a target surface to cause rapid ablation leading to an inward propagating compression front. In a spherical target irradiated with two or more beams, dense plasma is formed where the compression fronts converge. The conditions required for fusion can be reached in this manner (N3,A5).

The presence of fusion reactions in a laser-produced plasma of suitable material was first demonstrated in 1968 (B5) and the subsequent neutron emission is now a standard diagnostic. The success or failure of laser driven fusion as an energy source for the future depends on the efficiency of a number of processes, both in the generation of laser pulses and in the details of energy deposition and pellet implosion.

The study of laser-produced plasmas and of energy deposition and transport presents some severe experimental problems. The small length and timescales involved generally result in highly integrated measurements. However, the development of fast streak cameras (B1) has enabled time-resolved measurements to be made with resolution better than 10 psec. Spatial resolution down to 1  $\mu\text{m}$  can be achieved with standard optics.

Two important aspects of pellet implosion are (i) the efficiency of energy deposition in the outer regions of the target and (ii) the efficiency of energy transport from the deposition region to the imploding compression front.

With regard to (i), absorption processes so far identified are inverse bremsstrahlung (or collisional absorption), resonance absorption (active in the presence of a density gradient at the critical surface) and absorption by parametric decay instabilities, which allows laser energy to be coupled to particular plasma resonances. Electromagnetic radiation may also be absorbed in plasma turbulence.

With regard to (ii), behaviour of the thermal conductivity in large temperature gradients is not clear; some experiments imply a reduced heat flux. Generation of suprathermal (or fast) electrons during resonance absorption poses further problems; the long mean free path of energetic electrons can result in heating of the pellet core before the arrival of the compression fronts. This degrades the implosion and results in a departure from the ideal isentropic case.

The present work consists of a series of experiments, using mainly optical diagnostics, relevant to both (i) and (ii) above. The two principal experiments are (a) a thin foil burn through experiment (Chs. 4 and 5) and (b) a Brillouin backscatter experiment (Ch. 6).

In (a), thin, polystyrene foils are irradiated with 100 ps FWHM, 1.06  $\mu\text{m}$  laser pulses and their subsequent expansion is measured. Comparison with simulations (Ch. 5) indicates that lateral thermal conduction is inhibited. Time-resolved measurements of transmitted light show that foils remain highly absorbing even after the density becomes sub-critical. This is consistent with high integrated absorption measurements. It is proposed that short wavelength ion turbulence is responsible for both anomalous absorption and reduced thermal conductivity.

In (b), spherical targets are irradiated with 1.6 ns FWHM pulses and backscattered light at near the laser frequency is temporally and spectrally resolved. Blue and red wavelength shifts are observed and are interpreted in terms of Doppler and Brillouin effects respectively.

The thin foil experiment made use of a probe beam from a ruby



laser. The diagnostic ruby laser is described in Ch. 2 together with a fast driver circuit for a Pockels cell in the ruby cavity. The Pockels cell driver was especially developed for this application.

Diagnostics used in the experiments are discussed in Ch. 3. Further applications are described in Ch. 7.

We begin with a brief review of some of the processes that participate in laser light absorption and thermal transport (1.2).

Time-resolved measurements of the transparency of thin foils (Ch. 4) have not been made hitherto and the new diagnostic techniques have yielded unexpected results. The Brillouin experiment (Ch. 6) provides measurements of backscattered light under new conditions. Spectral and temporal resolutions are such as to allow the detection of previously unobserved features. Measurements of the coronal expansion of microballoon targets (Ch. 7) confirm the results of other laboratories. Again, time-resolved observations of back-illuminated targets (7.3) have not been made before.

The author has contributed principally to the experimental realization, the data analysis and the modelling of the work presented in this thesis.

## 1.2 Review of Absorption and Thermal Transport Processes

### (a) Classical inverse bremsstrahlung

Electrons accelerated in the applied laser field undergo collisions with nearly stationary ions and absorption of the incident energy results. Dielectric properties of the plasma are contained in the complex permittivity  $\tilde{\epsilon} = \epsilon + \frac{4\pi i\sigma}{\omega}$  where  $\epsilon$  and  $\sigma$  are the real, frequency independent permittivity and conductivity respectively. A simple, classical model (e.g. G5) can yield an expression for  $\tilde{\epsilon}$  as a function of  $\nu_{ei}$ , the effective electron-ion collision frequency. The intensity attenuation coefficient,  $K$ , for electromagnetic radiation is given by  $K = \frac{2\omega}{c} \text{Im} \sqrt{\tilde{\epsilon}}$ .

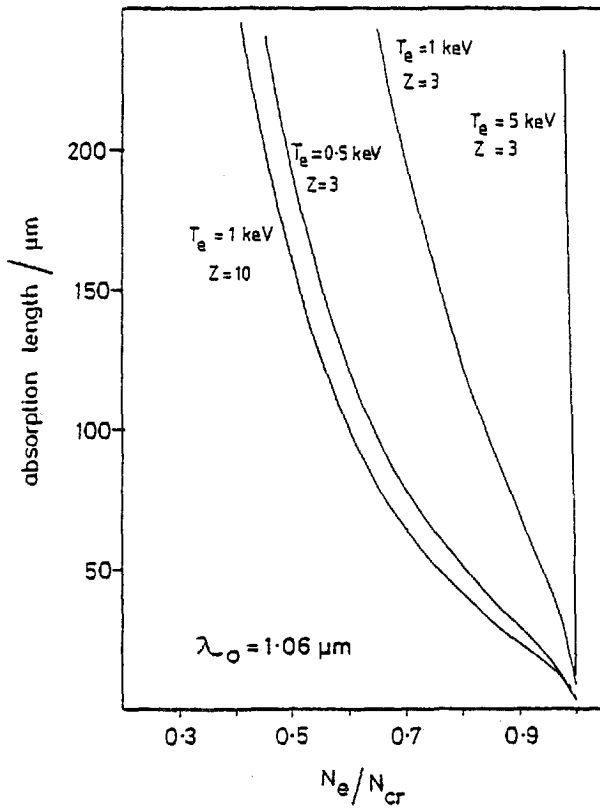
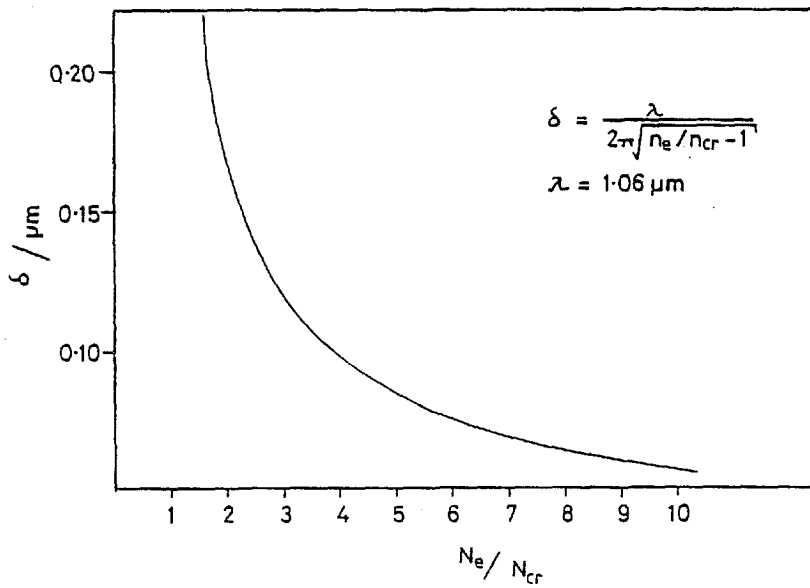


Fig 1.1 Absorption length due to inverse bremsstrahlung

Fig 1.2 Skin depth as a function of density



Substitution for  $v_{ei}$  (from B2 for example) together with the approximations  $\text{Re } \tilde{\epsilon} \gg \text{Im } \tilde{\epsilon}$  and  $\omega^2 \gg v_{ei}^2$  yields the standard expression for  $K$  (J1);

$$K = \frac{16\pi e^6 n_e^2 Z \ell n \Lambda}{3c v_{ei}^2 (2\pi m_e k T_e)^{3/2}} \frac{1}{(1 - v_p^2/v^2)^{1/2}}$$

The singularity at the critical surface ( $v = v_p$ ) is a result of the approximation  $\text{Re } \tilde{\epsilon} \gg \text{Im } \tilde{\epsilon}$  and does not exist in the full solution. Numerically, the Johnston and Dawson (J1) formula reduced to

$$K = 7.824 \cdot 10^{-9} \text{ cm}^{-1} \frac{Z^2 (n_e n_i \text{ cm}^6) \ell n \Lambda}{(v \text{ sec})^2 \left(\frac{T_e}{\text{eV}}\right)^{3/2} \left(1 - \frac{v_p^2}{v^2}\right)^{1/2}}$$

where the Coulomb logarithm is given by

$$\begin{aligned} \ell n \Lambda &= \frac{\lambda_{De}^m v_e}{\hbar} \\ &= 23.993 + \ell n \left[ \left(\frac{T_e}{\text{eV}}\right) \left(\frac{\text{cm}^{-3}}{(1+Z)n_e}\right)^{1/2} \right] \end{aligned}$$

Examples of the full solution are given in Fig. 1.1. The absorption length  $K^{-1}$  due to inverse bremsstrahlung becomes short near the critical density. For a  $T_e = 1 \text{ keV}$ ,  $Z = 3$  plasma,  $K^{-1} \sim 4 \mu\text{m}$  at the critical surface but increases to  $200 \mu\text{m}$  at  $0.7 n_{cr}$ . In addition, it is seen that absorption becomes less effective as the temperature rises.

(b) Resonance absorption

Laser radiation ( $v_o, \lambda_o$ ) cannot propagate in densities higher than the critical density;

$$\begin{aligned} n_{cr} &= \frac{m_e v_o^2 \pi}{e^2} \quad (\text{esu}) \\ &= 1.115 \cdot 10^{21} \left(\frac{\mu\text{m}}{\lambda_o}\right)^2 \text{ cm}^{-3} \end{aligned}$$

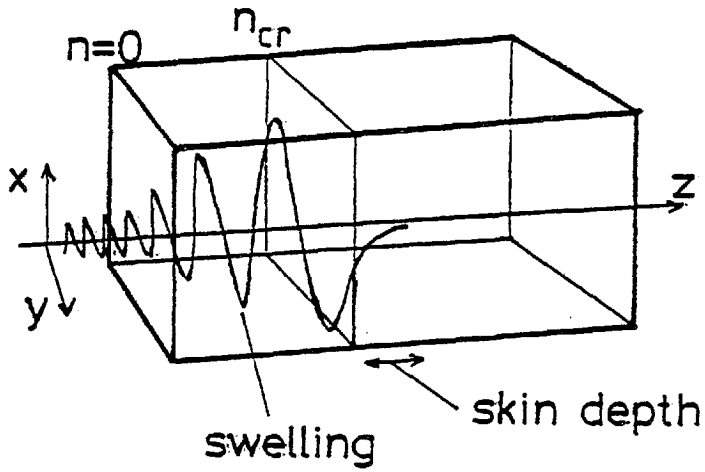


Fig 1.3 Radiation incident normally on a plasma with a density gradient along  $z$

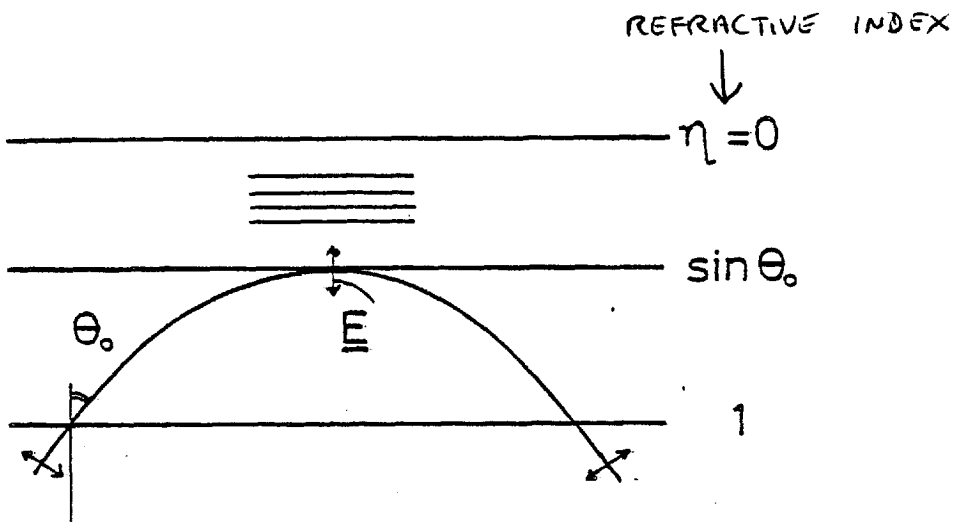


Fig 1.4 Resonance absorption of obliquely incident radiation

At higher densities, light decays as an evanescent wave over a distance characterised by the collisionless skin depth;

$$\delta = \frac{\lambda_0}{2\pi\sqrt{n_e/n_{cr} - 1}}$$

This is plotted in Fig. 1.2.

Therefore, laser light can only be absorbed in the region  $n_e < n_{cr}$ . Resonance absorption occurs when a p-polarised wave (E vector in plane of incidence) is incident obliquely on an inhomogeneous plasma.

Maxwell's equations lead to the equation

$$\nabla^2 \underline{E} - \nabla(\nabla \cdot \underline{E}) + \frac{\omega^2}{c^2} \underline{\epsilon} \underline{E} = 0$$

for the electric field of a wave, frequency  $\omega_0$ , propagating in a plasma. For normal incidence along the z axis (Fig. 1.3) with slab symmetry, the solution under the approximation of geometrical optics is (Ref. G5)

$$E_x(z) = E_y(z) = \frac{c_{\pm}}{(\underline{\epsilon}(z))^{1/4}} \exp - \left[ \frac{i\omega}{c} \int_{z=0}^z \sqrt{\underline{\epsilon}(z)} dz \right]$$

$c_{\pm}$  is a constant.

Ignoring collisional absorption,

$$v_{ei} = 0 \quad \rightarrow \quad \underline{\epsilon}(z) = 1 - \frac{\omega_p^2}{\omega^2}$$

so that at the critical surface,  $\omega_p \rightarrow \omega$  and  $|E| \rightarrow \infty$ . Thus if a wave is incident on a linear density ramp, the E vector grows and has a maximum at the critical surface. This behaviour is retained for (speed) oblique incidence although, in this case, the wave penetrates only to  $n = \sin \theta_0$ , where  $\theta_0$  is the angle of incidence and n the refractive index.

A p-polarised wave, incident obliquely on a density gradient, results in the E vector being parallel with the density gradient at the turning point (Fig. 1.4). This large field can drive longitudinal

out of plasma waves which propagate ~~to~~ the plasma. The energy of the plasma waves is eventually thermalised mainly by Landau damping (C4, Ch. 7) and the incident laser energy is thus absorbed.

Electrons moving at near the phase velocity of the plasma waves may experience an accelerating potential. They are decoupled from the thermal electron distribution and can propagate over large distances (1.2(h)).

The rôle of resonance absorption is now well established experimentally (F7,E3,F8). Closely associated with resonance absorption is the process of second harmonic ( $2\omega_0$ ) generation, (7.1.)

(c) Parametric processes

At high incident irradiance, a number of non-linear processes can contribute to laser light absorption. These include the parametric decay instability, the two plasmon instability and stimulated Raman and Brillouin scattering. The first two processes can be traced to the  $\underline{E} \cdot \underline{\nabla E}$  term in the ponderomotive force (C5);

$$\begin{aligned} \underline{F}_p &= - \frac{\omega_p^2}{\omega_0^2} \underline{\nabla} \left( \frac{\langle \underline{E}^2 \rangle}{16\pi} \right) \\ &= - \frac{\omega_p^2}{\omega_0^2} \frac{1}{8\pi} \left\langle \left[ \underline{E} \cdot \underline{\nabla E} + \underline{E} \times (\underline{\nabla} \times \underline{E}) \right] \right\rangle \end{aligned}$$

where angular brackets indicate time averaging over one cycle of the laser field  $\underline{E}$ . Scattering processes are identified with the  $\underline{E} \times (\underline{\nabla} \times \underline{E})$  term. These processes generally require that matching conditions be satisfied;

$$\omega_0 = \omega_1 + \omega_2$$

$$\underline{k}_0 = \underline{k}_1 + \underline{k}_2$$

which may be interpreted as conservation of energy and momentum respectively. However, density gradient steepening (A6) also associated

with the ponderomotive force, reduces the volume of plasma in which a given matching condition can be satisfied. This results in absorption by parametric processes being less important than resonance absorption in high temperature plasmas.

The scattering instabilities represent a severe problem because laser light can be scattered out of the plasma before significant absorption has taken place. Brillouin backscattering is potentially the most serious energy loss mechanism and for this reason has been studied extensively (Ch. 6).

(d) Absorption in ion turbulence

Inverse bremsstrahlung absorption becomes inefficient at high temperatures and density profile modification limits absorption by parametric decay instabilities near the critical surface. However, experimentally observed absorption fractions (30-60%) indicate that processes are present which ~~accept~~ a significant proportion of the incident laser energy; a further absorption mechanism is required (M11). One process that has been proposed (M6, M10) is absorption in short wavelength ion turbulence. Sources of ion turbulence are various streaming instabilities and Brillouin scattering. The presence of fast electrons usually results in cold electron return currents which are unstable to the ion-acoustic instability.

Absorption by ion turbulence is effective in a fairly wide density range  $n_{cr} > n_e > 0.1 n_{cr}$  and so is not affected by steepening at the critical density surface. Ion trapping (1.2(g)) sets a limit of  $\sim 10\%$  on the density fluctuations, depending on  $T_e/T_i$ . This limits the absorption by ion turbulence to  $\sim 20\%$ . The heated electron distribution does not contain hard components.

A simple model (F6) with applied laser field  $\underline{E}_0 \cos \omega_0 t$  and density

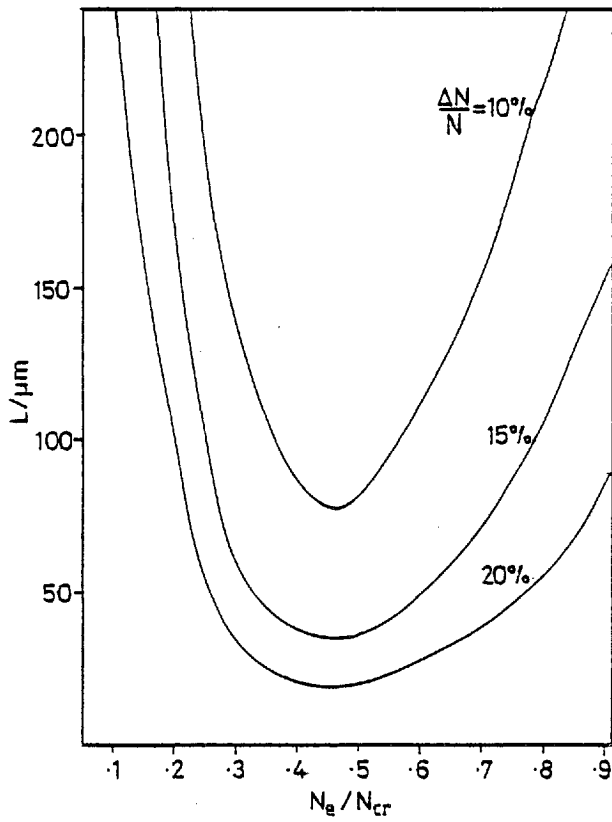


Fig 1.5 Absorption length in ion turbulence

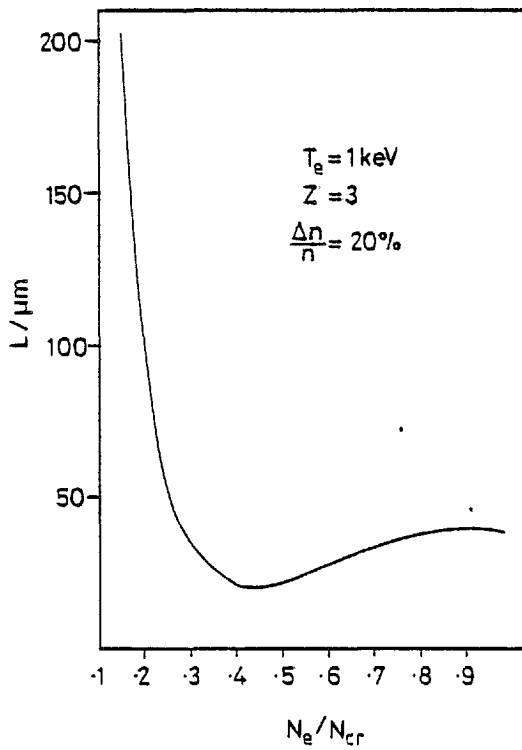


Fig 1.6 Absorption length due to both inverse bremsstrahlung and ion turbulence



$$n = n_p + \sum_{k_i} \delta n_{k_i} \cos(\underline{k}_i \cdot \underline{x})$$

gives the effective damping rate  $v^*$  for em waves;

$$v^* = \frac{\omega_0}{2} \sum_{k_i} \left( \frac{\delta n_{k_i}}{n_{cr}} \right)^2 \text{Im} \left( \frac{1}{\epsilon_L} \right) \cos^2 \theta_i$$

where  $\theta_i$  is the angle between  $\underline{k}_i$  and  $\underline{E}_0$ . Averaging over turbulence broad in angle and with a spectrum of  $\underline{k}_i$  gives;

$$v^* = \frac{\omega_0}{4} \left( \frac{\Delta n}{n_{cr}} \right)^2 \langle \text{Im} \left( \frac{1}{\epsilon_L} \right) \rangle$$

where  $(\Delta n)^2$  is the mean square density fluctuation and the angular brackets indicate an average over  $k_i$ . The dielectric function term is given in Ref. F6 as a function of  $k_0$ .

The phase velocity of the em wave is

$$v_p = \frac{c}{\sqrt{1 - \omega_p^2/\omega_0^2}}$$

and so the absorption length due to ion turbulence is

$$K_i^{-1} = \frac{v_p}{v^*} = \frac{c}{v^*} [1 - \omega_p^2/\omega_0^2]^{-\frac{1}{2}}$$

This is plotted in Fig. 1.5 as a function of density. The total absorption length due to ion turbulence and inverse bremsstrahlung ( $K_T = K + K_i$ ) is given in Fig. 1.6.

(e) Thermal conductivity

Thermal energy is carried principally by the electrons because of their greater mobility. The classical thermal conductivity  $K_{cl}$  is given by Spitzer (S3);

$$K_{cl} = 20 \left(\frac{2}{\pi}\right)^{3/2} \frac{T_e^{5/2} k_B}{m_e^{1/2} e^4 Z \ln \Lambda} \quad (\text{esu})$$

where  $T_e$  is in energy units. This is strictly for a Lorentz gas; for a real gas  $K = \epsilon \delta_T K_{cl}$  where  $\epsilon$  is due to thermoelectric effects and  $\delta_T$  is due to the departure from the Lorentz case. Values of  $\epsilon$  and  $\delta_T$  as functions of  $Z$  may be found in Ref. S3. Numerically,

$$K_{cl} = 74.13 \left(\frac{T_e}{\text{eV}}\right)^{5/2} \frac{W}{\text{cm eV}}$$

The 2.5 dependence on temperature can be simply demonstrated using a model in which electrons are assumed to travel one mean free path  $\lambda_d$  and then dump all their energy. The net flux between two points with a temperature difference  $\delta T_e$  is

$$K_{cl} \frac{\delta T_e}{\lambda_d} = \frac{9}{4} n_e \left(\frac{3k_B T_e}{m_e}\right)^{1/2} k_B \delta T_e$$

The mean free path  $\lambda_d \sim T_e^{1/2} \tau_{ei}$  where  $\tau_{ei}$  is the electron-ion energy transfer time and scales  $\tau_{ei} \sim T_e^{3/2}$ . The 2.5 dependence of  $K_{cl}$  on  $T_e$  follows.

Classical Fourier theory breaks down when the temperature gradient becomes so steep that all available electrons are participating in thermal transport. This situation represents an upper limit on the heat flux, the free streaming limit;

$$\begin{aligned} Q_{FS} &= \frac{3}{2} n_e T_e v_e \\ &= 1.746 \cdot 10^{-11} \left(\frac{n_e}{\text{cm}^{-3}}\right) \left(\frac{T_e}{\text{eV}}\right)^{3/2} \text{ W.cm}^{-2} \end{aligned}$$

A number of experimental results have been interpreted as implying a reduction in the free streaming limit (e.g. M4). A heuristic flux limit,  $f$ , is generally used ( $Q_{\max} = f Q_{FS}$ ) with typical

value of 1-10%. The ion-acoustic instability (B3), turbulence (M7), magnetic fields (M8) and suprathermal electron currents (M9) can all lead to a reduced conductivity.

(f) Flux inhibition by self-generated magnetic fields

A number of sources of magnetic fields are present in a laser-produced plasma. Non-colinear temperature and density gradients give rise to the growth of a d.c. field;

$$\frac{\partial B}{\partial t} = - \frac{c}{en_e} \nabla n_e \times \nabla T_e + \dots$$

In a laser plasma,  $\nabla T_e$  is generally radial and  $\nabla n_e$  axial. Magnetic fields are then azimuthal around the laser axis (Fig. 1.7).

Small scale inhomogeneities in the plasma density and temperature due to hot spots, discontinuities of ionization state etc. can also give rise to fields. There are magnetic fields associated with resonance absorption (B4), with ripples at the critical density surface (E4), and with suprathermal electron fluxes if the currents are not completely neutralised due to resistivity. There is also a magnetic instability (T2) which allows growth of magnetic fields with parallel zero order temperature and density gradients. All these processes, with their respective saturation mechanisms, can be shown to give rise to fields of the order of mega-Gauss. A review of these processes is given in Ref. M8.

Laser-produced plasmas generally have high  $\beta$  values, where  $\beta = 8\pi n_e T_e / B^2$ , so that self-generated fields do not affect the hydrodynamic behaviour. However, they do affect the electron thermal conduction. In a collisionless plasma, electrons are tied to the field lines thereby stopping any cross-field conduction. However, collisions with ions allow a flux

$$\underline{Q} = - \frac{K_{cl}}{1 + \Omega_e^2 \tau_{ei}^2} \underline{\nabla} T_e$$

where  $\Omega_e$  is the electron Larmor frequency

$$\Omega_e = \frac{eB}{m_e c} = 1.76 \cdot 10^7 \left( \frac{B}{\text{Gauss}} \right) \text{sec}^{-1}$$

There are a number of other mechanisms which allow electrons to propagate perpendicular to  $\underline{B}$  if fluctuations  $\delta \underline{B}$  are present. These include resonant scattering, field line wandering and neoclassical diffusion (M8).

Most of these mechanisms allow thermal fluxes up to a few percent of  $Q_{FS}$ . For example, with typical parameters ( $n_e = 10^{21} \text{ cm}^{-3}$ ,  $T_e = 1 \text{ keV}$ ,  $Z = 3$ ),

$$\tau_{ei} = 0.36 \text{ ps}$$

$$\text{and } \Omega_e \tau_{ei} = 6.3 \left( \frac{B}{\text{MG}} \right)$$

With fields of 1 MG, the  $\underline{\nabla} n \times \underline{\nabla} T$  source term reduces the thermal conductivity by

$$\frac{1}{1 + \Omega_e^2 \tau_{ei}^2} = 0.025$$

consistent with flux limits of a few percent.

(g) Flux inhibition by ion turbulence

Ion turbulence, with a density fluctuation level  $\delta n/n$ , has associated with it fluctuations in potential  $\phi$  given by

$$\frac{e\phi}{T_e} = \frac{\delta n}{n}$$

This turbulence can modify the electron flux responsible for thermal

conduction. A quasi-linear model (M7) gives an approximate expression for the anomalous thermal conductivity  $K_{an}$ . If the ion turbulence gives rise to potential fluctuations of the form

$$\phi(\underline{r}, t) = \int_k \phi(k) \cos(\underline{k} \cdot \underline{r} - \omega t)$$

then

$$K_{an} = \frac{2\sqrt{2\pi}}{\pi k} v_e \left( \frac{e\phi(k)}{T_e} \right)^{-2}$$

where the heat flux is then given by

$$\underline{Q} = -K_{an} n_e \underline{\nabla} T_e$$

Putting  $Q = -n_e T_e v_e f$ , where  $f$  is the flux limit parameter defined above, yields

$$f = \frac{2\sqrt{2\pi}}{\pi k} \left( \frac{e\phi(k)}{T_e} \right)^{-2} \frac{1}{L}$$

where  $L$  is the temperature gradient scale length; with  $k = 1/2\lambda_D$ ,  $\delta n/n = 10\%$ ,  $L = 10 \mu m$  and typical parameters,  $f \sim 5\%$ .

Ion trapping arguments give a maximum for the turbulence level of (F6, K2)

$$\frac{\delta n}{n} \sim \frac{1}{2} \left[ \left( 1 + \frac{T_i}{T_e} \right)^{\frac{1}{2}} - \left( \frac{3T_i}{T_e} \right)^{\frac{1}{2}} \right]^2$$

This is plotted in Fig. 1.8, and may be derived by considering the motion of an ion in the rest frame of an ion wave. The ion can be trapped in the wave potential  $\phi$  if

$$e\phi \gtrsim m_i \left[ \left( \frac{T_i}{m_i} \right)^{\frac{1}{2}} - c_s \right]^2$$

where  $c_s$  is the sound speed (6.1). The result follows.

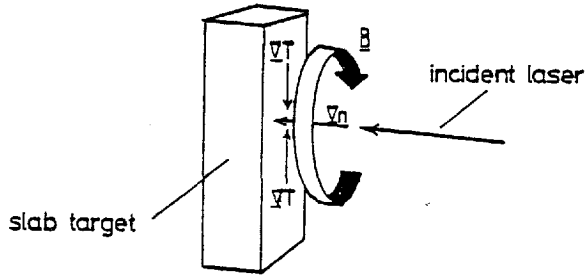


Fig 1.7 Generation of azimuthal magnetic fields on plane targets

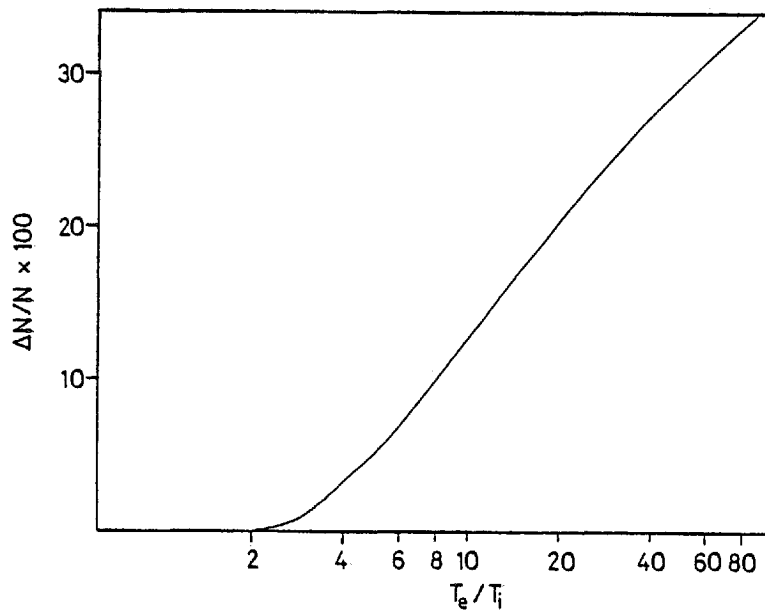


Fig 1.8 Maximum fluctuation level of ion turbulence, limited by ion trapping, as a function of  $T_e/T_i$

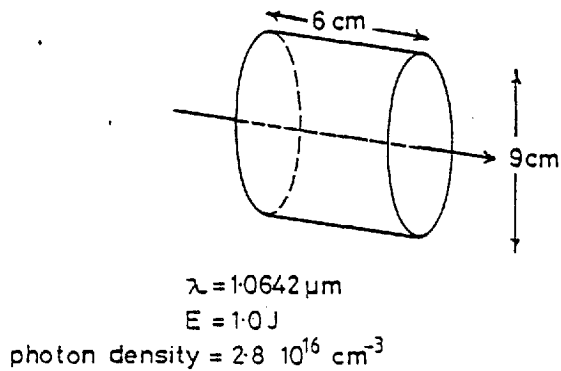


Fig 1.9 Schematic picture of the incident, mode-locked laser pulse

(h) Suprathermal electrons

Resonance absorption gives rise to non-Maxwellian electron velocity distributions. Typically, hot electron tails are generated which show up as two component X-ray continuum spectra. The mean free path for electrons is

$$\lambda_d = \frac{1}{8 \ln \Lambda} \lambda_{\text{Coul}}$$

where

$$\lambda_{\text{Coul}} = \frac{1}{n_i \pi} \left( \frac{3T_e}{Ze^2} \right)^2$$

Clearly, as the temperature increases,  $\lambda_d$  increases and hot electrons are essentially decoupled from the thermal plasma (F9).

1.3 Description of Neodymium Laser System and Focussing

(a) Laser system

The main laser pulses ( $\lambda_0 = 1.064 \mu\text{m}$ ) for these experiments were provided by the Quantel neodymium (YAG) laser at the Rutherford Laboratory (R9). The system is described in Refs. R4, R6. The thin foil experiment (Ch. 4) required short pulses. A passively mode-locked oscillator generates a chain of  $\sim 10$  pulses with separation 7 ns and width 100 ps FWHM. One pulse of energy  $\sim 1$  mJ is switched out by a Pockels cell gate and is passed through a series of rod and disc amplifiers. Energy delivered to the target is 1-5 J in the thin foil experiment. Apodizers and spatial filters are used in the amplifier chain to improve beam quality and to fill the aperture of the amplifiers. Faraday rotators protect the laser from reflection from the target and a saturable dye cell is used to reduce the amount of energy incident on the target prior to the arrival of the main pulse.

Beam diagnostics include calorimetry, prepulse monitor (3.2), far and near field monitors (3.5) and, for most data shots, streak

photography to give incident power as a function of time.

The longer pulses (1.6 ns FWHM) used in the Brillouin backscatter experiment were generated by actively Q-switching the neodymium laser cavity and by chopping out some of the pulse with a second Pockels cell driven by a laser-triggered spark gap.

The 9 cm diameter beam (Fig. 1.9) is nearly diffraction limited;

$$\text{divergence} = \frac{2.44 \lambda_0}{d} = 30 \mu\text{rad}.$$

The beam is focussed on target with an aspheric f/1 lens of focal length 10 cm. Far field measurements (3.5) give a focal spot diameter of  $\sim 30 \mu\text{m}$ . Equivalent plane monitoring of the far field is also available giving information on the angular distribution of the incident pulse. Average irradiance on target is  $10^{14}$ - $10^{16} \text{ W.cm}^{-2}$  for the experiments to be described in Chapters 4, 6 and 7.

Amplified, spontaneous emission results in  $\sim 100 \mu\text{J}$  deposited on target. Because this is delivered over a long time, no damage results.

Prepulse levels are typically  $\sim 10^{-5} E_{\text{INC}}$  (50 dB), where  $E_{\text{INC}}$  is the energy in the main, incident pulse. Target behaviour is found to be sensitive to prepulses in excess of  $\sim 20 \mu\text{J}$  or about  $3 \text{ J cm}^{-2}$ . Mead et al. (M1) find a damage threshold of  $\sim 4.5 \text{ J cm}^{-2}$ . The prepulse monitor and precisely what is meant by 'prepulse' are discussed in 3.2.

Thermal lensing effects can result in a variation of the beam divergence ( $\sim 500 \mu\text{rad}$ ) during the incident pulse. This is caused by radial, refractive index gradients in the rod amplifiers due to temperature variations. It is found that the focus shifts away from the focussing lens by  $\sim 40 \mu\text{m}$ .

The plane of polarisation of the neodymium pulse depended on the number of passes made through the disc amplifiers:

By pass discs                      horizontally polarised



Single pass                      45° polarisation  
 Double pass                      vertically polarised.

The coherence length of the neodymium pulse, being mode-locked, was of the same order as its length ( $\sim 3$  cm) for the thin foil experiments. The Brillouin backscatter experiment used Q-switched pulses (1 ns FWHM). Streak pictures give  $\Delta\lambda = 1-2 \text{ \AA}$ . The coherence length is, then,

$$L = \frac{c}{\Delta\nu} = \frac{\lambda^2}{\Delta\lambda} \sim 1 \text{ cm}$$

A number of modes must be present.

If the neodymium beam is focussed down to an irradiance of  $I_0$ , the electric field of the light wave is (r.m.s.)

$$\frac{E_0}{V \text{ cm}^{-1}} = 19.41 \left( \frac{\mu_r}{\epsilon_r} \right)^{\frac{1}{4}} \left( \frac{I_0}{W \text{ cm}^{-2}} \right)^{\frac{1}{2}} = [\sqrt{\mu/\epsilon} I_0]^{\frac{1}{2}}$$

The peak field is  $\sqrt{2}$  times this.

The quiver velocity of electrons in the field is given by

$$v_0 = \frac{eE_0}{m_e \omega_0}$$

So, putting  $\mu_r = \epsilon_r = 1$ ,

$$v_0 = 25.61 \left( \frac{I_0}{W \text{ cm}^{-2}} \right)^{\frac{1}{2}} \left( \frac{\lambda_0}{\mu\text{m}} \right) \text{ cm sec}^{-1}$$

The wave frequency,  $\omega_0$ , is

$$\omega_0 = \frac{c2\pi\text{rad}}{\lambda_0} = 1.885 \cdot 10^{15} \left( \frac{\mu\text{m}}{\lambda_0} \right) \text{ rad sec}^{-1}$$

The energy of a photon, wavelength  $\lambda_0$ , is

$$E_0 = \frac{hc}{\lambda_0} = \frac{12.4155}{\lambda/\text{\AA}} \text{ keV}$$

So the flux of photons,  $f_0$ , in the focal volume is

$$f_0 = \frac{I_0}{E_0} = 5.031 \cdot 10^{18} \left( \frac{I_0}{\text{W cm}^{-2}} \right) \left( \frac{\lambda_0}{\mu\text{m}} \right) \text{ cm}^{-2} \text{ sec}^{-1}$$

The momentum carried by each photon is

$$p = \hbar k_0 = 6.63 \cdot 10^{-28} \left( \frac{\mu\text{m}}{\lambda_0} \right) \text{ N sec}$$

and so the light pressure is

$$P = pf_0 = 3.3 \cdot 10^5 \left( \frac{I_0}{10^{15} \text{ W cm}^{-2}} \right) \text{ atm}$$

(1 atm =  $1.013 \cdot 10^6 \text{ dyn cm}^{-2}$ ).

(b) Target focussing and alignment

The target position is fixed approximately by the centre of the target chamber and the tip of a conical surrogate target is used as the reference position. The main beam axis is fixed by the line passing through the target and replaceable cross hairs mounted on the chamber windows. The main 1.06  $\mu\text{m}$  beam is made colinear with this line by means of a He-Ne alignment beam. The main focussing lenses are installed and made normal to the beam axis by using multiple reflections. They are centred on the beam axis by restoring the direction of the alignment beam. Centering and angling the lenses is to a certain extent an iterative procedure.

Targets are positioned at the lens focus by making use of the back-reflection of a CW YAG laser beam coincident with the main beam.

Compensation may be made to take account of thermal lensing.

#### 1.4 Target Details

##### (a) Plane foil targets

The thin foil burn through experiment was conducted using polystyrene ((CH)<sub>n</sub>) foils of thickness 0.05-0.34 μm fabricated as follows. A microscope slide is coated with a release agent (soap) and immersed in a solution of polystyrene in amyl acetate. The solution is drained off slowly, leaving a film of plastic on the slide. Longer immersion gives thicker films. The slide is placed in water and the plastic film floats to the surface. A brass mounting plate is then brought up under the film which adheres to it. The film thickness is measured using an interference microscope. Target fabrication is conducted under clean conditions (Class 100) to avoid dust being trapped in the film.

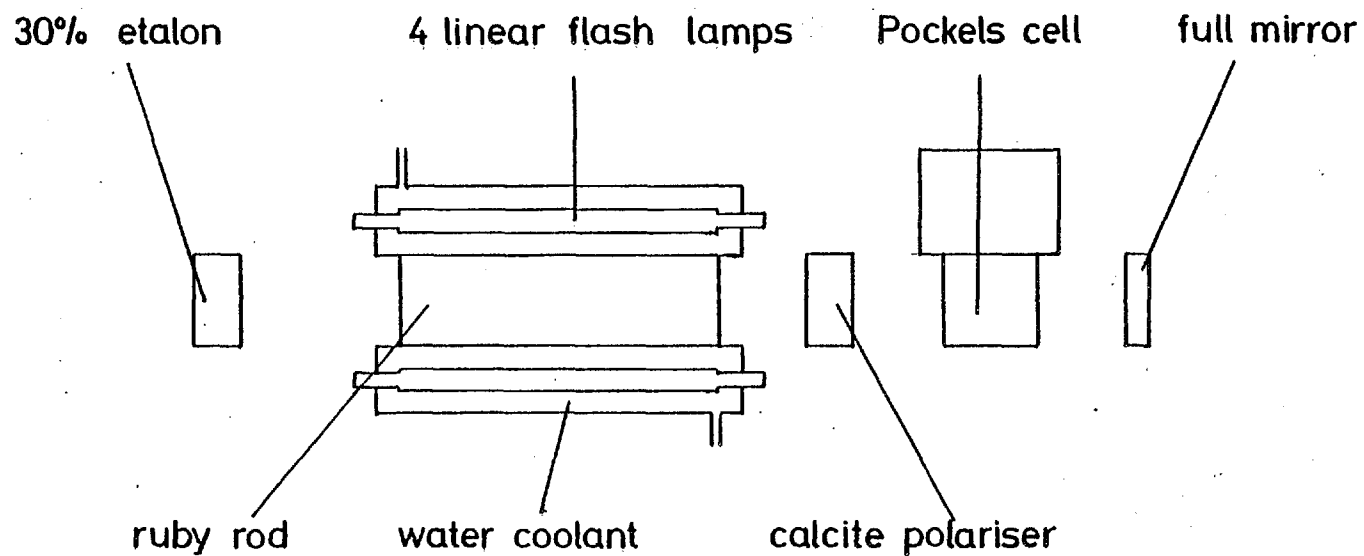
Early trials were conducted using carbon films but these were found to be too fragile.

##### (b) Spherical targets

Second harmonic emission and Brillouin backscatter studies (Chs. 6, 7) were conducted using microballoon targets. Glass microspheres are purchased in bulk and subjected to several sorting procedures. Typical dimensions are 80 μm diameter, 0.5 μm wall thickness mounted on a 0.5 μm diameter glass stalk. Spheres can be filled with various gases (light gases are easier) by diffusion. Coating with aluminium makes alignment and focussing quicker.

Targets are irradiated in an evacuated target chamber to avoid air breakdown. Typical pressures are 10<sup>-5</sup>-10<sup>-4</sup> torr. No special precautions were taken to avoid contamination of the target surface.

Fig 2.1 Arrangement of components within the ruby laser cavity



CHAPTER 2

RUBY LASER

Both thin foil (Ch. 4) and spherical targets (Ch. 7) have been observed while back-illuminated by a ruby probe beam. In this chapter, the ruby laser and related optics are described. A fast Pockels cell driver circuit, especially developed for this application, is given in 2.2.

2.1 General Description

The ruby laser bed is made of Dural and rests on a kinematic mount so that thermal expansion does not lead to misalignment of the cavity. Mirror and rod assemblies are bolted to the bed; the arrangement of components is shown in Fig. 2.1. The 10 cm long ruby rod is water cooled and pumped by four linear flash tubes in a reflective cylindrical housing. The flash tubes carry a 1 msec discharge from a bank of  $32 \times 40 \mu\text{F}$  capacitors. The capacitors are charged to 2.5 kV and then store 4 kJ (3.2 c). The laser efficiency is  $\sim 0.03\%$  with 1 J of energy in the output pulse. The rise-time of the discharge current is controlled by induction coils and by the length of cable from the capacitor bank to the lamps. The rise-time of the current was reduced from 350  $\mu\text{sec}$  to 200  $\mu\text{s}$  when the number of turns on each of the two induction coils was reduced from 47 to 28. This rise-time may be monitored using a test coil ( $\sim 40$  turns, 1 cm diam.) and integrator ( $RC = 10$  msec) placed near the inductances.

The ruby rod is orientated azimuthally so that horizontally polarised light is preferentially amplified. The calcite polariser (Fig. 2.1) is orientated to pass the same polarisation. The Pockels cell is  $\frac{1}{4}$ -wave switched because this puts less stringent requirements on

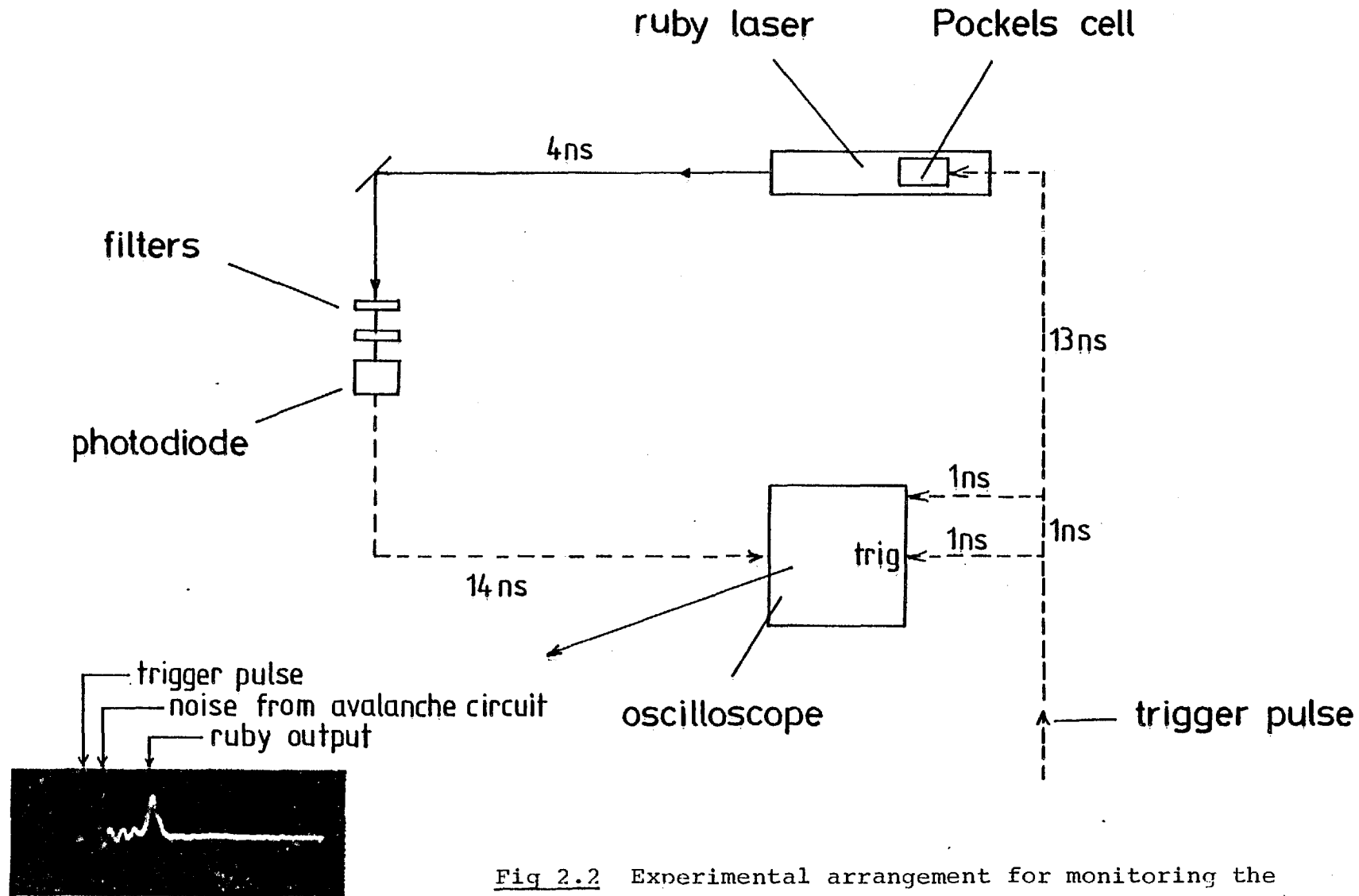


Fig 2.2 Experimental arrangement for monitoring the output of the ruby laser

the driver unit than  $\frac{1}{2}$ -wave switching (see 2.2). The Q-switching of the cavity works as follows; A constant HT of  $\sim 2$  kV is applied to the Pockels cell making it act like a  $\frac{1}{4}$ -wave plate. A plane polarised pulse from the calcite polariser passes through the Pockels cell, becomes circularly polarised and is reflected at the back mirror. The sense of the circular polarisation is reversed on reflection, so after passing through the Pockels cell, the reflected pulse becomes plane polarised normal to the incident pulse. It is, therefore, blocked by the calcite polariser and no lasing can take place. The flash lamps are fired and population inversion is generated in the chromium ions of the ruby rod. The driver unit then delivers a fast rise-time ( $< 10$  ns) pulse that removes the HT from the Pockels cell. Lasing can then occur and a 20 ns Q-switched pulse of energy  $\sim 1$  J is emitted at the output etalon.

The ruby rod is aligned azimuthally in one of two ways. A straight edge in the vertical direction appears doubled when the rod is correctly aligned because of double refraction in the material. Alternatively, the rod may be placed between crossed polarisers with transmission axes horizontal and vertical. The rod is orientated correctly when an axial He-Ne beam is extinguished. The remaining optical components are aligned parallel with the faces of the ruby rod by using an auto-collimator.

The output of the laser is monitored by a standard p-i-n diode arrangement (Fig. 2.2) and has the following properties;

Wavelength	6943 Å
Energy	1 J
Length of pulse	20 ns
Average power	50 MW
Beam diameter	1 cm at output
Divergence	$\sim 3$ mrad

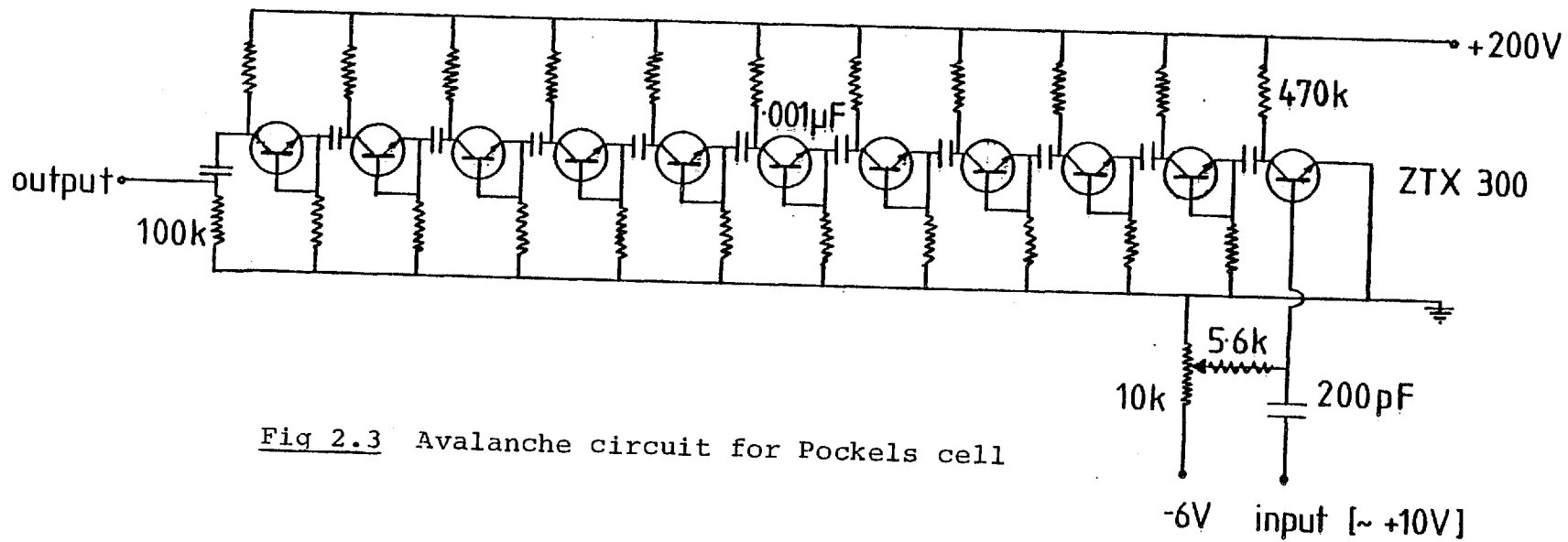


Fig 2.3 Avalanche circuit for Pockels cell



Jitter	A few ns when stable
Polarisation	Horizontal
Mode beating	100 ps period and 2 ns period
Build-up time	100 - 130 ns

The longer timescale mode beating was removed when a pin-hole was inserted in the cavity. However, the 100 ps beating remained and was presumably due to beating between longitudinal modes.

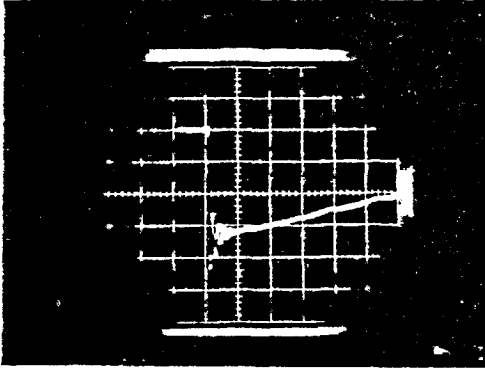
The Pockels cell must be switched about 750  $\mu$ s after the flash tubes for optimal gain. When synchronisation with the main neodymium laser is required, the Pockels cell must be triggered from a photodiode sensitive to the switched out Nd pulse, early in the amplifier chain.

An example of the ruby output pulse is included in Fig. 2.2.

## 2.2 Fast Switching Driver Circuit for Pockels Cell

The thin foil experiment made use of mode-locked pulses from the neodymium laser. This resulted in the necessity of triggering the diagnostic ruby laser from the switched-out 1.06  $\mu$ m pulse. The path length from the Nd laser oscillator to the target fixed the time available for generating and delivering a backlighting beam. After subtracting path lengths, approximately 100 ns was available for generating the ruby pulse; this was equal to the build-up time in the ruby cavity. Therefore, the driver circuit for the Pockels cell was required to deliver fast rising 2 kV pulses with near zero delay and jitter. Usual techniques for generating such pulses make use of Krytron valves (L3). However, these were found to introduce  $\sim$ 20 ns delay and considerable jitter ( $\sim$ ns). An all-transistor avalanche circuit was designed (Fig. 2.3) that generated the required pulses with near zero delay and jitter; Fig. 2.4 gives the output pulse of the circuit. Careful screening ensured that the circuit was not triggered by noise;

voltage; 1 kV/div



time; 100 ns/div  
probe; P6105

Fig 2.4 Output pulse of avalanche circuit

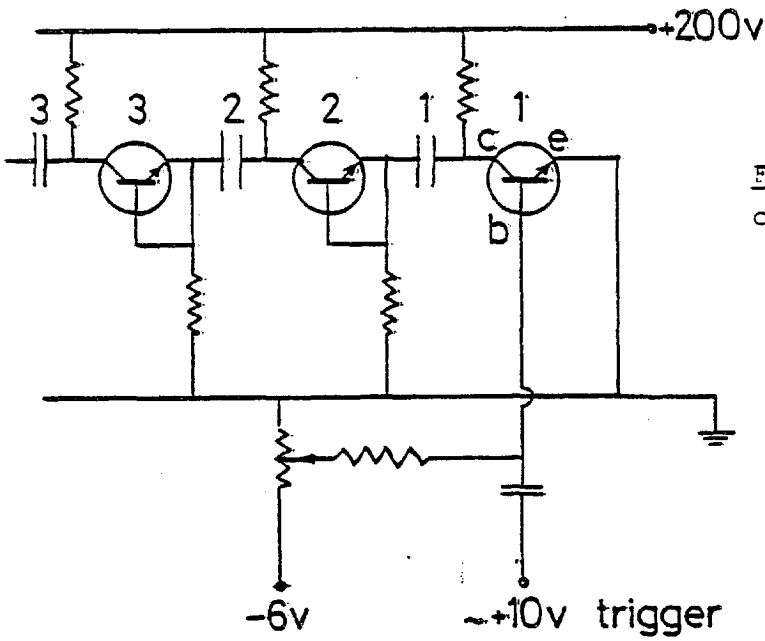


Fig 2.5 Operation of avalanche circuit

power supplies were dry cell batteries mounted in a screened box. The screened trigger circuit was mounted directly above the Pockels cell to preserve the fast rise-time of the output pulse. Positive 10 volt pulses were required to trigger the unit, and these were provided by a p-i-n diode sensitive to the switched out neodymium beam.

There follows an explanation of the operation of the circuit. Just prior to the arrival of a trigger pulse, the first ZTX 300 transistor (transistor 1 in Fig. 2.5) is reverse biased. When a small current flows from the base to the emitter, the transistor switches and changes from an open to a closed circuit across C-E. This happens when a trigger pulse arrives. The capacitors 1, 2, 3..... are connected in parallel across earth and + 200 volt lines. The switching of transistor 1, earths the right hand side of capacitor 1, and because capacitors initially retain their charge, the left hand plate is dragged down to - 200 V. Transistor 2 then has + 200 V on the collector and - 200 V on the base and emitter. The C-B junction, although reverse-biased, breaks down, or avalanches, becoming an effective short circuit. Then the right hand side of capacitor 2 is at - 200 V, dragging the left hand plate down to - 400 V. The process continues down the chain, each transistor-capacitor pair contributing  $\sim 200$  volts to the output pulse. The capacitors are charged in parallel and discharged in series as in a traditional Marx circuit.

In practice, later stages contribute less to the output pulse than earlier stages in the chain. The components were mounted in a circle to minimise inductive effects, with eleven transistors in the chain. Two chains were used to  $\frac{1}{4}$ -wave switch the Pockels cell. Self-triggering can become serious for long chains of transistors; this is due to noise in the transistors themselves. Selection of low-noise transistors helps to reduce self-triggering. The input impedance of the avalanche circuit was measured to be  $220 \Omega$ .

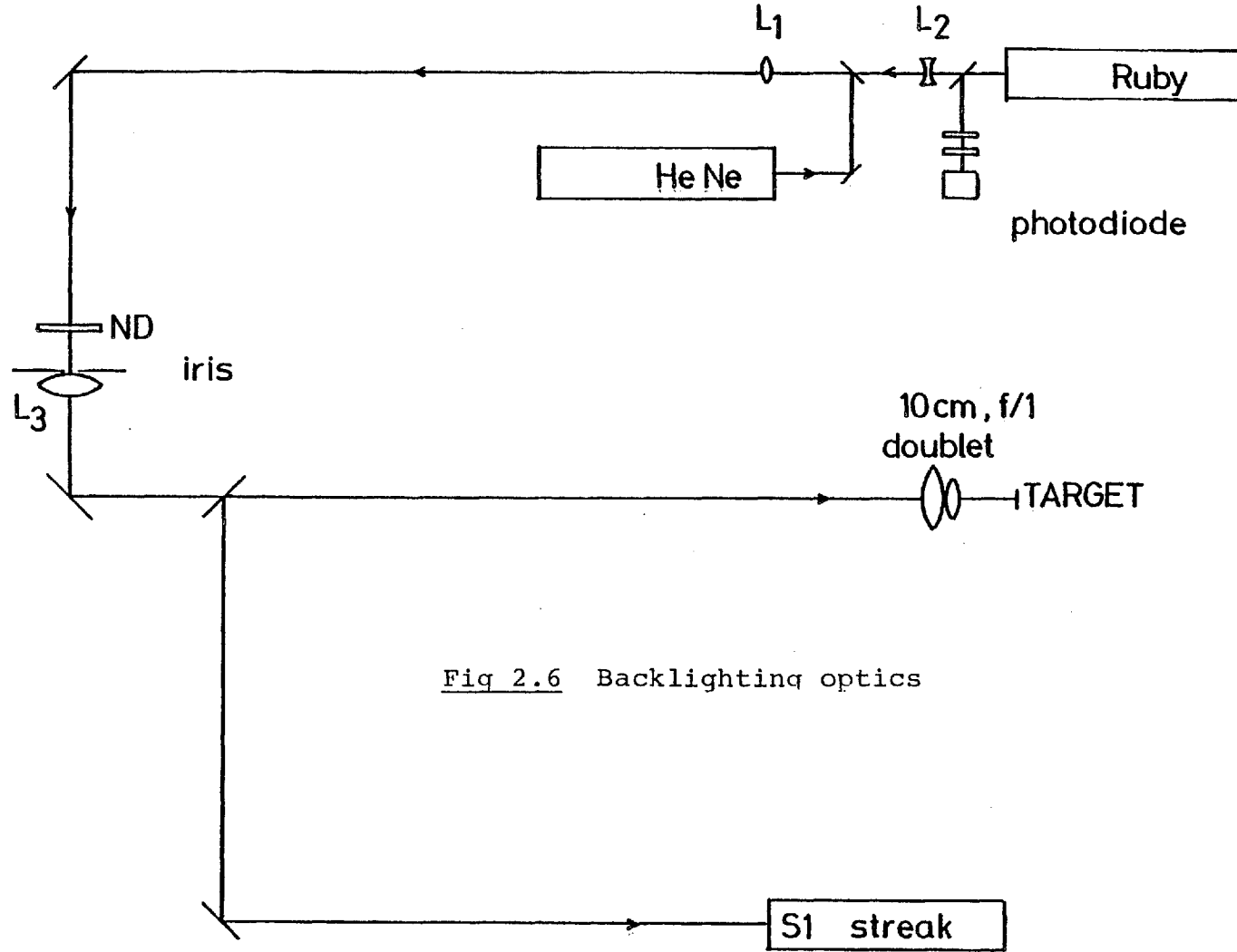


Fig 2.6 Backlighting optics

An alternative to  $\frac{1}{4}$ -wave switching, described in 2.1, is to  $\frac{1}{2}$ -wave switch the cavity. The Pockels cell is then made to operate as a half wave plate; that is, an incident wave plane polarised at angle  $\theta$  to the optic axis emerges with the plane of polarisation rotated by  $2\theta$ . However, in half-wave switching, twice the voltage must be applied across the Pockels cell. Quarter-wave switching was preferred because of the less stringent requirements placed on the driver circuit.

### 2.3 Backlighting Optics

The principal application of the ruby probe beam was to backlight thin foils during irradiation by neodymium laser pulses. The associated optics are described in this section. Backlighting at  $90^\circ$  to the main laser axis is described in Ch. 7 for the spherical target experiments.

The arrangement for axial backlighting is shown in Fig. 2.6. The main focussing lenses were f/1 ICOS doublets with focal length of  $\approx 10$  cm. Identical lenses were positioned in front of and behind the target, and are labelled East and West respectively. The precise focal length of the lenses is;

f/mm	$\lambda/\mu\text{m}$
97.65	0.6328
98.04	0.6943
99.44	1.0640
93.61	0.5233

The target-West lens separation was fixed by imaging the target in  $1.06 \mu\text{m}$  light at the S1 streak camera, the entrance slit of which was at an image distance of 3.12 m. The target was then imaged by the west lens in ruby light at the iris plane of Fig. 2.6. The magnification from the iris to the target was 0.032. The lens  $L_1$  imaged the output

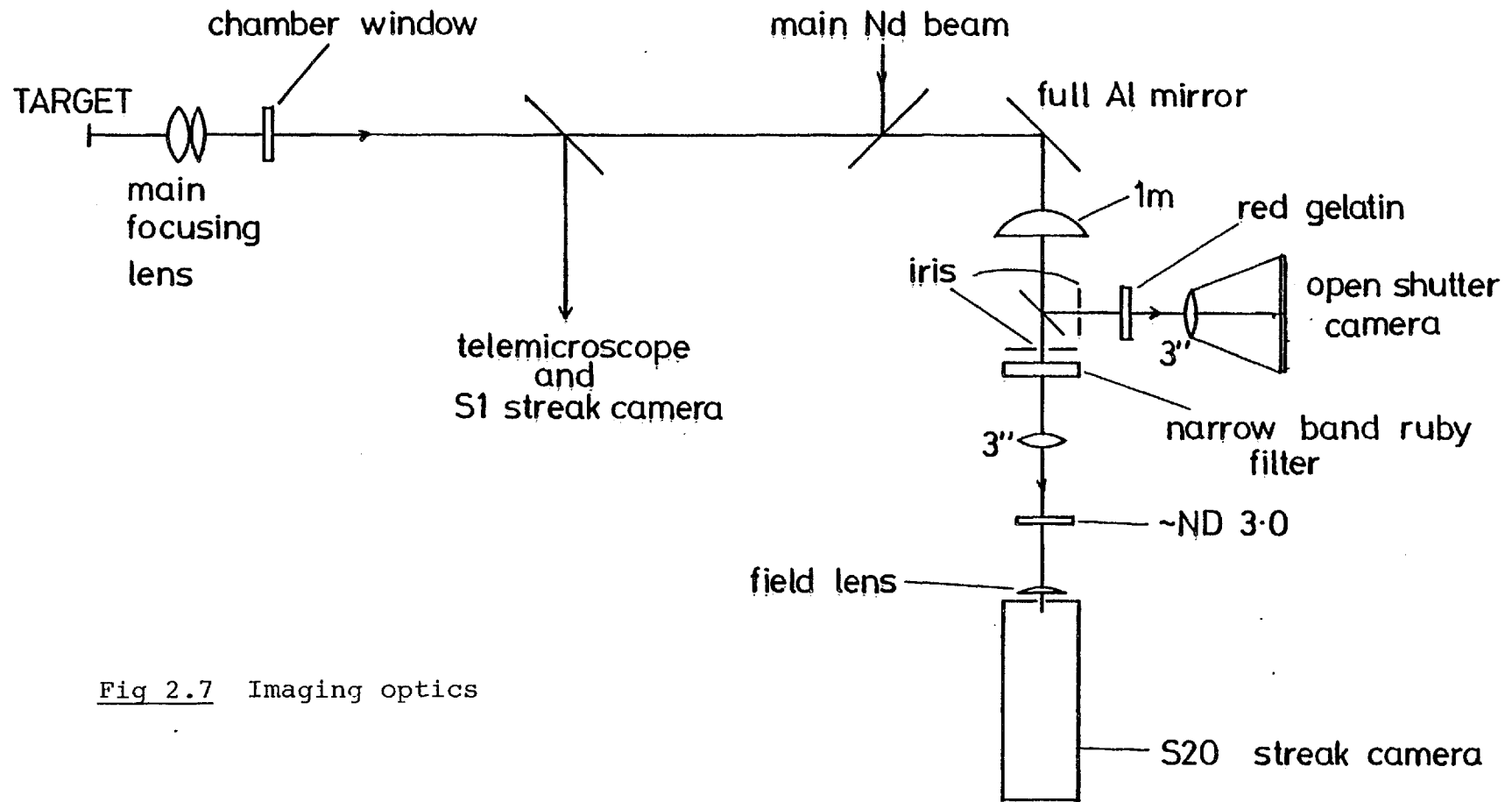


Fig 2.7 Imaging optics

face of the ruby rod at the iris with a magnification of 4.94. The negative lens  $L_2$  reduced the irradiance level of the beam in the neighbourhood of the turning prisms. Lens  $L_3$  was used as a field lens to ensure that all the ruby light entered the west lens.

During the experiment, the ruby laser was operated with a pin-hole in the cavity in order to reduce the number of transverse modes. The diameter of the output beam was then 2 mm at the ruby output,  $\sim 10$  mm at the iris and  $\sim 300$   $\mu\text{m}$  at the target. Calorimeter measurements of the ruby pulse energy at the iris gave  $20 \pm 2$  mJ. Taking estimates for the attenuation in each optical component results in  $\sim 13$  mJ on target. This is near the damage threshold for foil targets. However, irradiation of even the thinnest foils (0.05  $\mu\text{m}$  thick) resulted in no observable damage.

The imaging of the target in ruby light at the S20 streak camera is shown in Fig. 2.7. Further discussion of the streak camera may be found in 4.2. The target-east lens separation was fixed by the requirement that the main Nd beam was focussed onto the target. This resulted in the target image being positioned at a distance of 7 m from the east lens, with a magnification of 70. A 1 m lens brought the image to a more convenient place. A copy lens ( $f = 2''$ ) relayed the image to the entrance slit of the S20 camera. A beam splitter provided a second channel for imaging the target onto an open shutter camera, in order to monitor the ruby beam alignment. Fig. 2.8 shows a picture from the open shutter camera with a 70  $\mu\text{m}$  diameter microballoon in the target position. The ruby beam diameter is  $\sim 4$  balloon diameters, consistent with the figure given above.

Aluminium coating on microballoons was removed after a few ruby shots. Fig. 2.9 shows the open shutter pictures for two consecutive shots together with the respective S20 streaks.

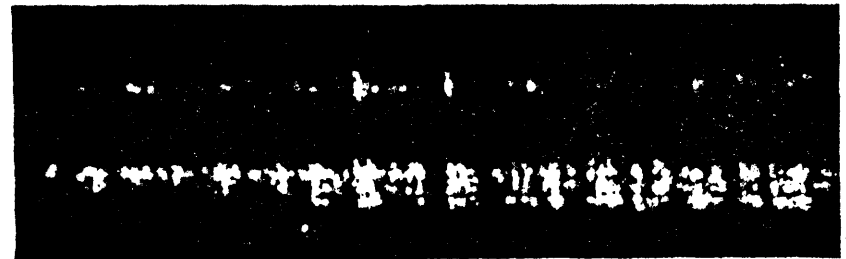
# Al coated microballoon backlit with ruby beam

Open shutter monitor

S20 streak picture

time →

SHOT 1



SHOT 2

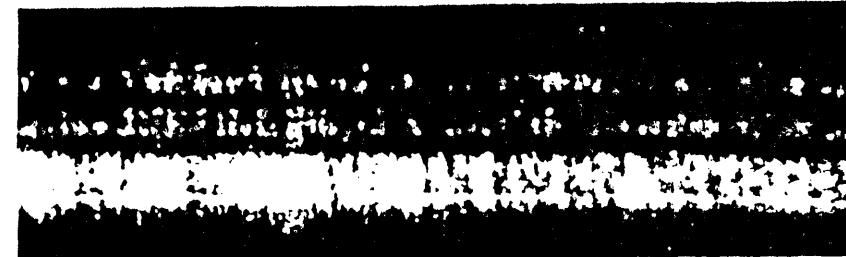


Fig 2.9



## 2.4 Plasma Emission

In order to perform a shadowgraphy experiment, the backlighting source must be more intense than the plasma emission itself. In the configuration of the thin foil experiment, the ruby irradiance on target was  $10^8 - 10^9 \text{ W cm}^{-2}$ . The two dominant emission processes are bremsstrahlung and harmonic emission. These are now discussed in turn.

The radiated power due to bremsstrahlung per unit volume per unit frequency range is (B6)

$$\frac{dP}{d\omega} = \frac{16n_i n_e e^2}{3c^3} \left( \frac{Ze^2}{m_e} \right)^2 \left( \frac{m_e}{2\pi T_e} \right)^{\frac{1}{2}} \ln \left( \frac{2T_e}{m_e \omega^2 b_{\min}^2} \right)$$

where  $b_{\min}$  is an impact parameter which we shall take as Debye length.

Putting  $Zn_i = n_e$  this reduces to (for  $Z = 1$ );

$$\frac{dP}{d\omega} = 2.737 \cdot 10^{-6} \left( \frac{n_e}{n_{cr}} \right)^2 \left( \frac{eV}{T_e} \right)^{\frac{1}{2}} \ln \left[ 1.273 \cdot 10^{31} \left( \frac{\text{sec}^{-1}}{\omega} \right)^2 \right] \text{ W cm}^{-3} \cdot \text{Hz}^{-1}$$

where  $n_{cr}$  is the critical density for  $1.06 \mu\text{m}$  light. For ruby light,  $\omega = 2.73 \cdot 10^{15} \text{ sec}^{-1}$  and taking  $n_e = n_{cr}$  and  $T_e = 1 \text{ keV}$  we obtain;

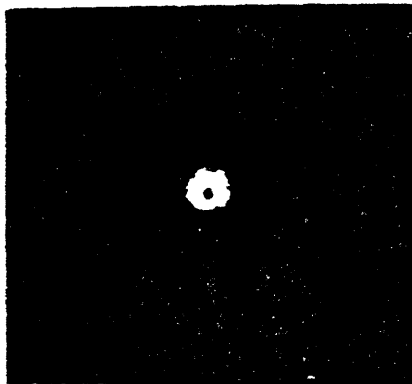
$$\frac{dP}{d\omega} = 4.6 \cdot 10^{-8} \text{ W cm}^{-3} \text{ Hz}^{-1}$$

Most of the observations were made through interference filters with bandwidth  $\approx 20 \text{ \AA}$  (or  $\Delta\omega = 1.26 \cdot 10^{12} \text{ Hz}$ ). Taking  $100 \mu\text{m}$  depth of plasma the irradiated power is

$$I_{Br} = 5.8 \cdot 10^2 \text{ W cm}^{-2}$$

which is several orders of magnitude below the backlighting level, as required for shadowgraphy.

In addition to bremsstrahlung emission, the plasma also emits at



70 μm diameter microballoon

Fig 2.8 Open shutter picture of microballoon

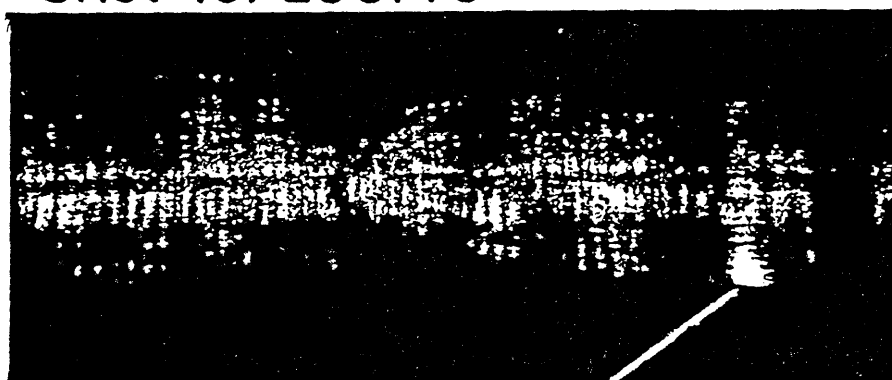
Shot 2/020278



reference

$3/2\omega_0$

Shot 10/200778



reference

Fig 2.10 S20 streak pictures with and without  $3/2\omega_0$  emission

$1.5 \omega_0$  due to two plasmon decay at the quarter critical density surface (B7). The finite bandwidth of the harmonic line at  $0.71 \mu\text{m}$  results in some emission around the  $0.69 \mu\text{m}$  ruby line (R6). In the first run of the thin foil experiment (Ch. 4),  $\frac{3}{2} \omega_0$  emission was observed at the peak of the incident pulse. This was checked by firing a main laser shot with the ruby output blocked. Discussion of the  $\frac{3}{2} \omega_0$  emission is postponed to 4.5.

The emission made interpretation of the S20 streak pictures difficult. A second run was performed with a narrow band pass filter and more intense backlighting. The plasma emission was then suppressed, as shown in Fig. 2.10. The structure of these streak pictures is explained in 4.2.

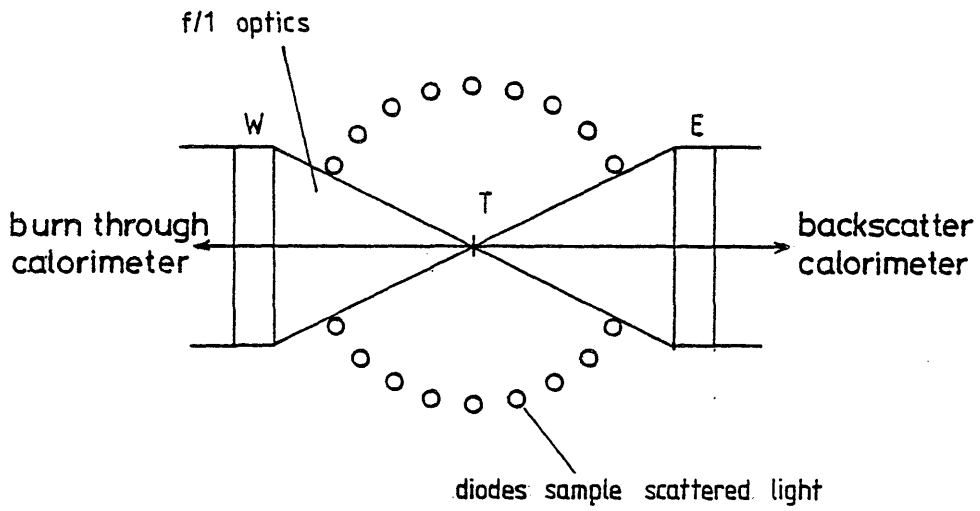


Fig 3.1 Schematic summary of energy measurements for the thin foil burnthrough experiment

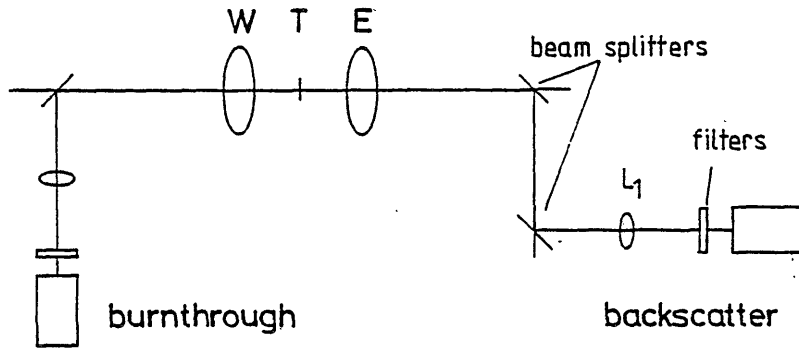


Fig 3.2 Experimental arrangement for calorimetry

CHAPTER 3

DIAGNOSTICS

In this chapter, the diagnostics used in the experiments are described together with the associated data analysis.

3.1 Calorimetry

The energy incident on the target ( $E_{INC}$ ) constitutes approximately 70% of the main laser beam energy  $E_{LAS}$ , because of absorption at mirror, window and lens surfaces. A fraction of  $E_{INC}$  is absorbed in the target and eventually reappears as kinetic energy of the ablating ions. The unabsorbed energy is scattered out of the target plasma in various ways. In the single beam irradiation of thin foils, it is convenient to treat the scattered  $\omega_0$  radiation in three parts;

- (i) energy transmitted into the rear f/1 lens,  $E_{BT}$
- (ii) energy backscattered and reflected into the (front) main focussing lens,  $E_{BS}$
- (iii) energy scattered out of the lens cones, that is, into the solid angle defined by  $27^\circ < \theta < \pi - 27^\circ$ ,  $0 < \phi \leq 2\pi$ . ( $\theta$  and  $\phi$  are defined in Fig. 3.9),  $E_{SC}$

In addition, small quantities of energy are taken up by bremsstrahlung, recombination and harmonic emissions. Fig. 3.1 summarises the energy measurements made during the thin foil experiments (5.3). Light at the laser frequency ( $\omega_0$ ) collected by the front and rear lenses was measured by absorbing glass calorimeters (Fig. 3.2). The transmission calorimeter was calibrated by firing a laser pulse of independently measured energy  $E_0$  in the absence of a target. Suppose the transmission calorimeter measures an energy  $\epsilon_0$ . Then the percentage transmission on a target shot with respective measurements  $E_{INC}$  and

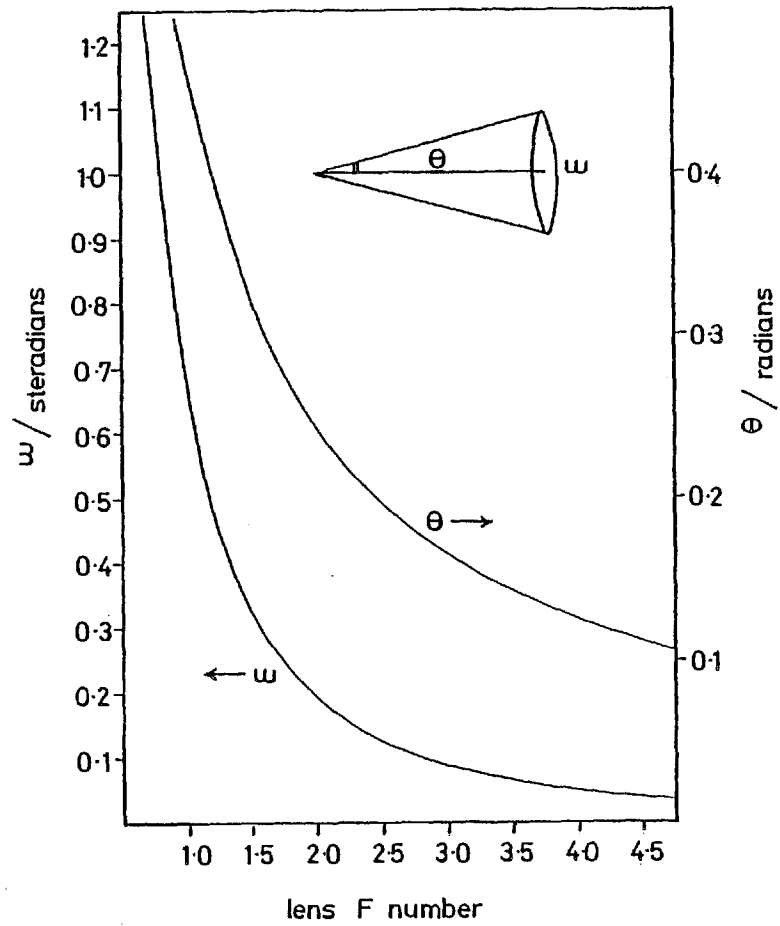


Fig 3.3 Plane and solid angles subtended at the target by a lens of given f number

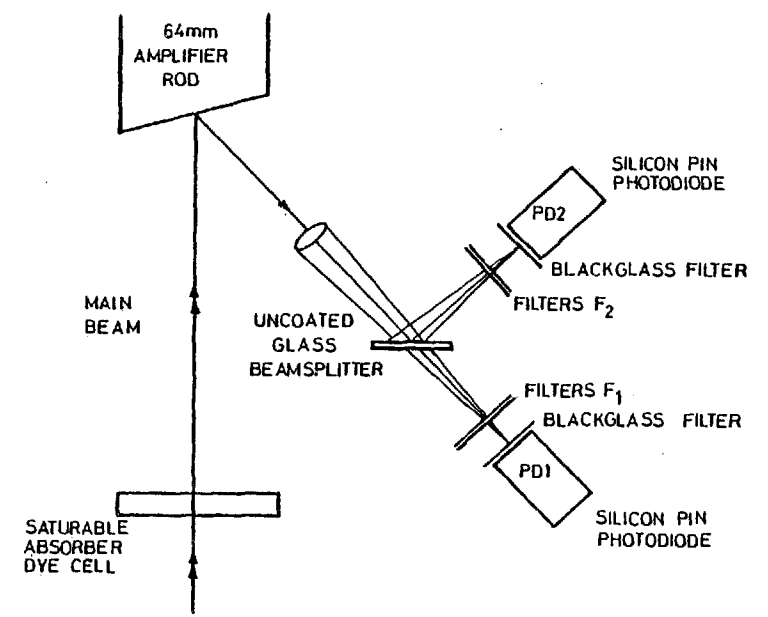


Fig 3.4 Experimental arrangement of prepulse monitor

$\epsilon$  is

$$t = \frac{\epsilon}{\epsilon_0} \frac{E_0}{E_{INC}} \quad 100\%$$

In a single beam experiment, the backscatter calorimeter is more difficult to calibrate. A target of known reflectivity  $R$  must be used with low energy laser pulses. Suppose a calibration shot of laser energy  $E_0$  gives a reading  $\epsilon_0$  on the backscatter calorimeter. Then  $\epsilon_0 = E_0 R a$  where  $a$  is the absorption in a single transit from the target to the calorimeter. If a target shot with main laser energy  $E_{INC}$  gives a reading  $\epsilon$  on the calorimeter, the target reflectivity is

$$r = \frac{\epsilon}{aE_{INC}} = \frac{\epsilon}{\epsilon_0} \frac{E_0}{E_{INC}} R \quad 100\%$$

Comparison of reflection and transmission data from different laboratories (4.1) must take into account the  $f$  number of the collection optics (Fig. 3.3).

Light scattered outside the lens cones was sampled by an array of 15 calibrated photodiodes. This is discussed in 3.4. Measurement of the energy in the expanding ion distribution is discussed in 3.7.

### 3.2 Prepulse Monitor

Energy delivered to the target prior to the main pulse can severely modify target behaviour. It is therefore important to measure this 'prepulse' energy. The prepulse monitor is shown in Fig. 3.4 and operates as follows. The filters  $F_1$  and  $F_2$  are arranged so that the photodiode PD2 does not saturate with the arrival of the main laser pulse while diode PD1 saturates at  $\sim 10^{-4} E_{LAS}$ . The outputs from the diodes are displayed on an oscilloscope; the signal from PD2 is used as a time-marker and the signal from PD1 displays prepulse energy in the range  $10^{-6} - 10^{-5} E_{LAS}$  (Fig. 3.5).

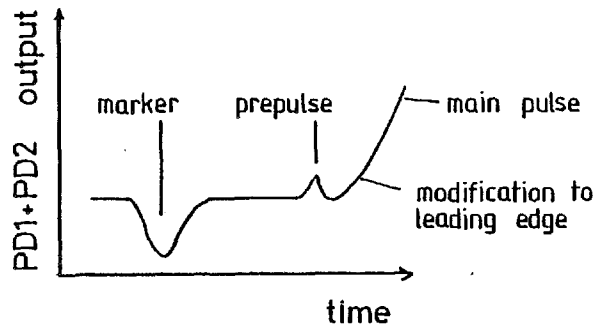
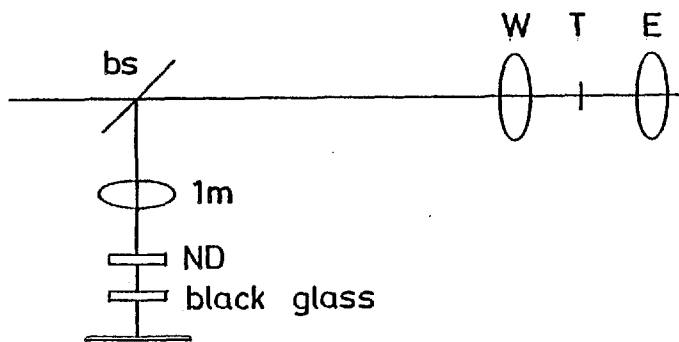


Fig 3.5 Schematic example of diode outputs



Kodak 4143 or 1Z

Fig 3.6 Experimental arrangement for imaging the transmission lens plane

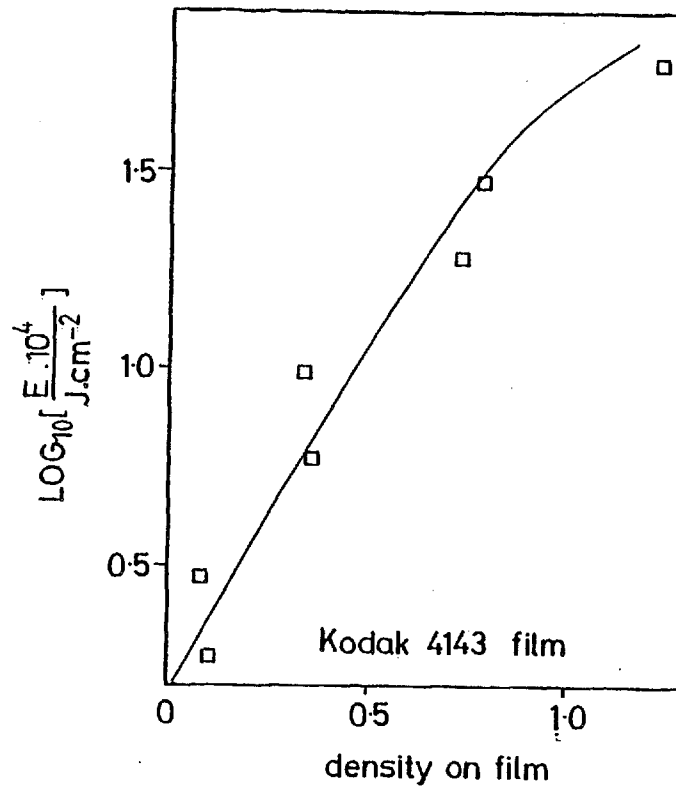


Fig 3.7 Calibration curve for Kodak 4143 film



Prepulse energy may be due to (i) poor switch out from the mode-locked chain of neodymium pulses; (ii) interpulse noise; (iii) modification to the leading edge of the main pulse. The effect of prepulse energy on the behaviour of thin foils is discussed in Ch. 4.

Amplified spontaneous emission (ASE) also gives rise to finite energy deposited onto the target before the arrival of the main pulse. A saturable dye cell is included in the main beam with 10% small signal and 70% large signal transmission in an effort to reduce ASE. Estimates of the energy associated with ASE are of the order of 100  $\mu\text{J}$  (R6). However, no target damage was observed when the amplifiers were fired in the absence of an oscillator pulse.

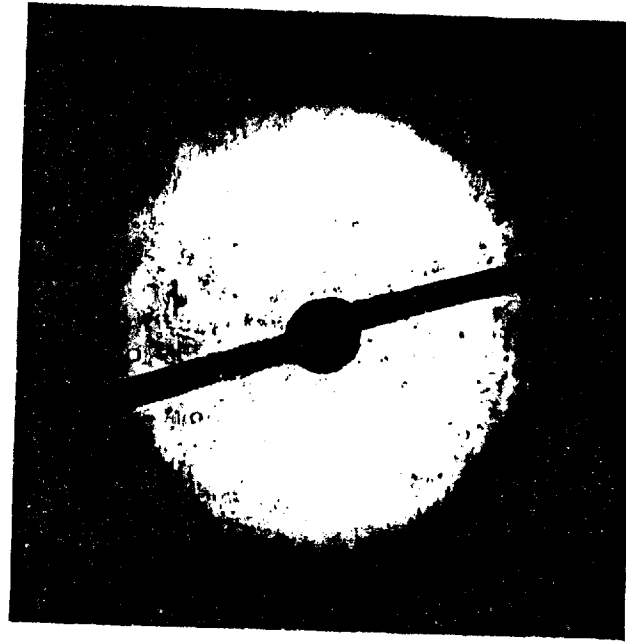
### 3.3 Lens Plane Pictures

The angular distribution of  $\omega_0$  radiations scattered into the lens cones may be measured by imaging the lens planes onto photographic film. A typical experimental arrangement is shown in Fig. 3.6. Infra-red sensitive film (Kodak 4143) was used, having been calibrated against a calorimeter by irradiation with pulses from the neodymium laser oscillator. The  $\gamma$  curve for 4143 film is shown in Fig. 3.7. Images of the rear (transmission) lens plane in the absence of a target and in the presence of a foil target are shown in Fig. 3.8. The horizontal bars are supports for ion probes situated in axial holes in the lenses.

A densitometer trace is made along a diameter of the lens plane picture. With the film calibration, and after normalisation to the calorimeter measurement, this gives the energy density  $E$  ( $\text{J cm}^{-2}$ ) in the lens plane as a function of radius. However, to facilitate comparison with the photodiode data (3.4), the measurements are converted to the form of energy per unit solid angle  $E$  ( $\text{J sr}^{-1}$ ) as a function of polar angle  $\theta$ .

Azimuthal symmetry is assumed in this conversion as is most

no foil



foil target present



Fig. 3.8 Examples of lens plane pictures

frequently observed within the lens cones. Simple geometry then shows that

$$E(\theta) = \frac{(r^2 + f^2 \cos^2 \theta_0)^{3/2}}{f \cos \theta_0} E(r)$$

where  $r$ ,  $f$  and  $\theta_0$  are defined in Fig. 3.10. Integration of  $E(\theta)$  over the solid angle of the lens cone gives the total (calorimeter) energy  $E_{TOT}$ ;

$$\begin{aligned} E_{TOT} &= \int_{\theta=0}^{\theta_0} 2\pi E(\theta) d(\cos \theta) \text{ rad}^2 \\ &= \int_1^{\cos \theta_0} 2\pi E(\cos \theta) d(\cos \theta) \text{ sr} \end{aligned}$$

Therefore if  $E(\cos \theta)$  is plotted as a function of  $\cos \theta$ , the area under the curve is equal to  $E_{TOT}/2\pi \text{sr}$ . This removes the necessity of having to normalise  $E(r)$  at the beginning of the calculation. As an example, Fig. 3.11 shows  $E(\cos \theta)$  for a constant  $E(r) = \xi \text{ J cm}^{-2}$ .

### 3.4 Scattered Light Measurements

Incident laser light scattered outside the lens collection cones was monitored by an array of 15 silicon photodiodes. The signals from the diodes (an example is shown in Fig. 3.12) are proportional to the energies incident upon them. Each diode was calibrated against a calorimeter using the neodymium oscillator output.

Diodes were mounted on the inner wall of the target chamber in an assembly which included an iris, neutral density filters and black glass filters (blocks visible but transmits  $1.06 \mu\text{m}$  radiation with attenuation of ND 0.4). The iris defined a collection angle of  $1.8 \cdot 10^{-4} \text{ sr}$ . Signals were recorded for shots with no target present,

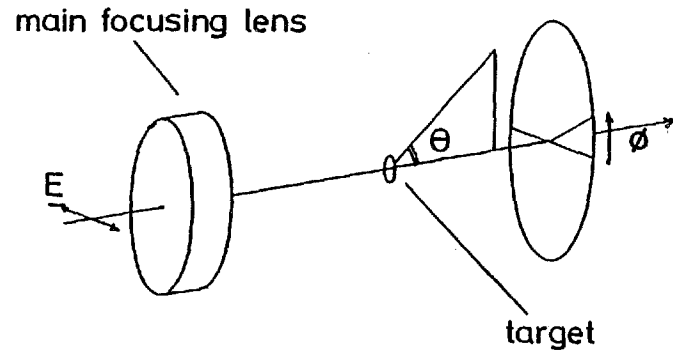


Fig 3.9 Definitions of azimuthal and polar angles

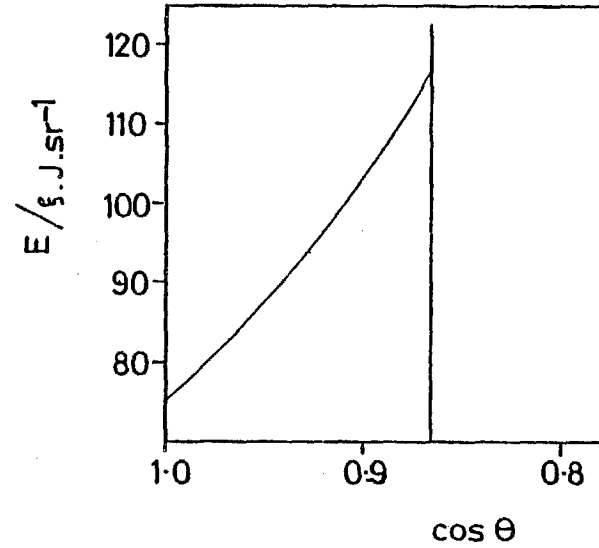


Fig 3.11  $\xi(\theta)$  for a constant  $E(r)$

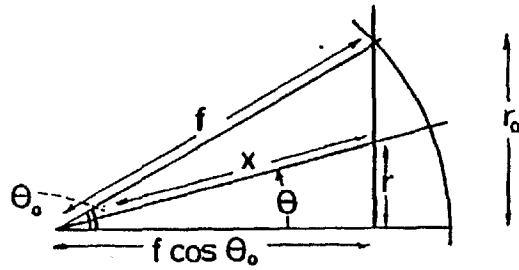


Fig 3.10 Definitions of symbols

indicating the presence of background scatter. These signals were subtracted from the data shots.

The diode measurements give, after reduction, the scattered energy per unit solid angle  $E(\theta, \phi)$ , the scattered light distribution is not, in general, azimuthally symmetric. In order to obtain the absorption for each shot, the scattered light must be integrated over  $\theta_0 < \theta < \pi - \theta_0$  and  $0 \leq \phi < 2\pi$ , where  $\theta_0$  is the half plane angle subtended at the target by the main focussing lenses. Data points are plotted on a  $\theta - \phi$  graph and a fitting routine is used on a computer to interpolate between the points. The "volume" under the plot is then calculated, giving the total scattered energy. Fig. 3.13 shows an example of treated data.

The scattered light distribution is found to have lobes in planes normal to the plane of polarisation of the incident laser beam. We follow Ref. S2 and fit the  $\phi$  dependence with a sine function;

$$E(\theta, \phi) = a(\theta) + b(\theta) |\sin \phi|$$

The total scattered energy is then

$$\begin{aligned} E_{SC} &= \int E(\theta, \phi) d\omega \\ &= \int_{\cos \theta_0}^{\cos(\pi - \theta_0)} d(\cos \theta) [2\pi a(\theta) + 4b(\theta)] \text{ sr} \end{aligned}$$

Therefore if  $2\pi a(\theta) + 4b(\theta)$  is plotted as a function of  $\cos \theta$ , the area under the graph is equal to the total scattered energy. This procedure gives similar results to the numerical analysis.

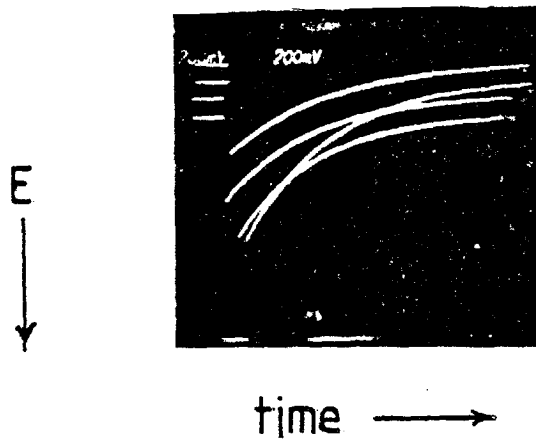
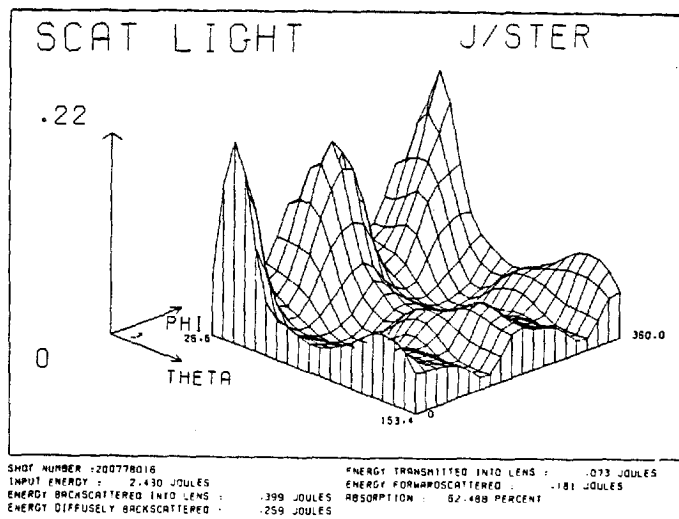


Fig 3.12 Example of the outputs from four photodiodes

Fig 3.13 Example of treated data



### 3.5 Focal Plane Pictures

The distribution of incident laser light in the focal plane of the main focussing lens gives the irradiance on target. The far-field distribution was measured in two ways. Firstly, the focus formed by the east lens was imaged by the west lens onto photographic film. Secondly, the 'equivalent planes' of a third, long focal length lens were monitored. These measurements are discussed in turn.

#### (a) Imaging of planes near the focus

Eight planes around the focal plane of the east focussing lens were imaged by the west lens onto Kodak 4143 film (Fig. 3.14). The images were generated from the reflections off four beam splitters. The separation and magnification of the pairs of imaged planes are shown schematically in Fig. 3.15 and the resulting exposures are shown in Fig. 3.16. Exposures were made for a main shot in the absence of a target and also with a continuous YAG beam, coincident with the main beam. It was arranged that the CW focus coincided with one of the imaged planes. Comparison between the CW focus and the main shot focal position then allowed an estimate to be made of thermal lensing effects.

The images of the near-focal planes were traced on a microdensitometer along a diameter. Use of the 4143 film calibration (Fig. 3.7) then gave the energy density  $E(r)$  in arbitrary units. Normalisation of the energy distribution to the incident laser energy yielded  $E(r)$  in  $J\text{ cm}^{-2}$ . This data analysis is summarised in Fig. 3.17.

For a circular distribution, normalisation is achieved using

$$E_{\text{INC}} = \int_0^{\infty} 2\pi r E(r) dr$$

For an elliptical distribution (as was found to be approximately the case), densitometer traces must be made along both the major and minor axes, so that  $\epsilon = a/b$  may be measured. Then if  $E(r)$  is derived from

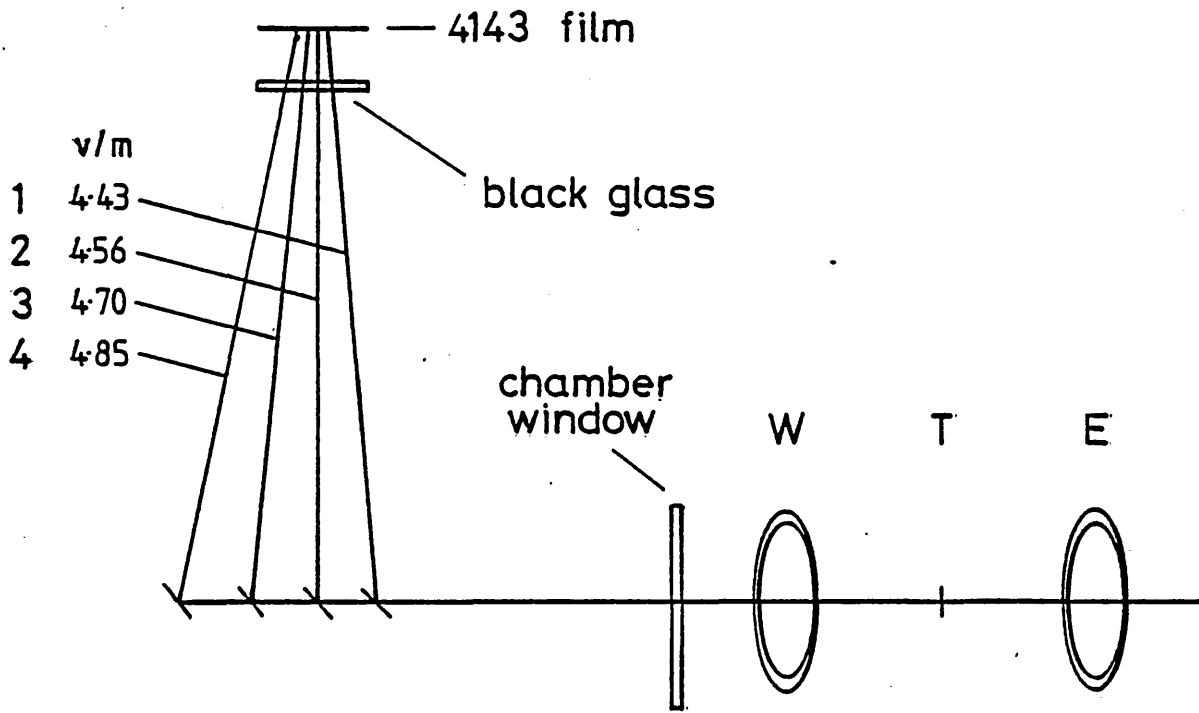


Fig 3.14 Experimental arrangement for imaging four planes near the focus of the main (E) focussing lens

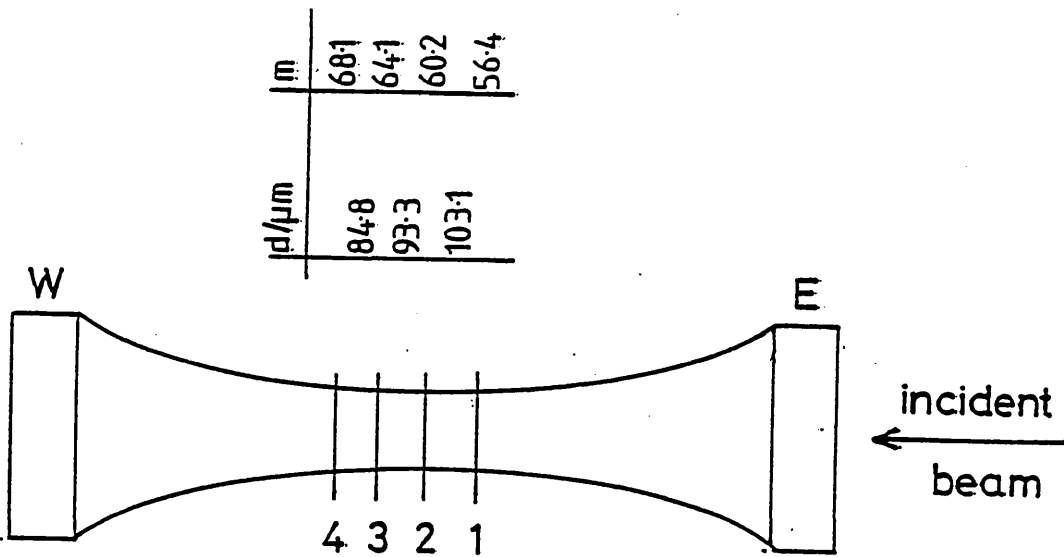


Fig 3.15 Separation and magnification of the planes imaged by the arrangement of Fig 3.14



the major axis trace,

$$E_{\text{INC}} = \int_0^{\infty} \frac{1}{\epsilon} 2\pi r E(r) dr.$$

Results for the irradiance distribution on a main shot in that plane which contains the smallest CW YAG focus are;

	2a   $\mu\text{m}$	2b   $\mu\text{m}$	
I/2	22	12	
I/10	66	35	
E/2	30	16	$\pm 2 \mu\text{m}$
E/10	61	32	

There was found to be a modulation factor of  $\sim 2$  in the irradiance level, with a  $5 \mu\text{m}$  scale length. Thermal lensing shifted the main beam focus by  $\sim 50 \mu\text{m}$ . A focal spot diameter of  $25\text{--}30 \mu\text{m}$  with the assumption of circular symmetry gives reasonable estimates of the irradiance on target.

(b) Equivalent plane pictures

A portion of the main laser beam is split off and focussed by a long focal length lens L (Fig. 3.18). The far-field distribution at the focus of L can be monitored on target shots with photographic film. This provides information on the angular variations of the main beam, but, unlike (a), aberrations caused by the main focussing lens are not included in the measurement.

The plane situated a distance  $\Delta$  from the focal plane of L (Fig. 3.18) corresponds to a plane at distance  $\delta$  from the focal plane of E, where

$$\delta = \frac{f_1^2 \Delta}{f_2^2 + (\ell_1 - \ell_2) \Delta + (f_2 - f_1) \Delta}$$

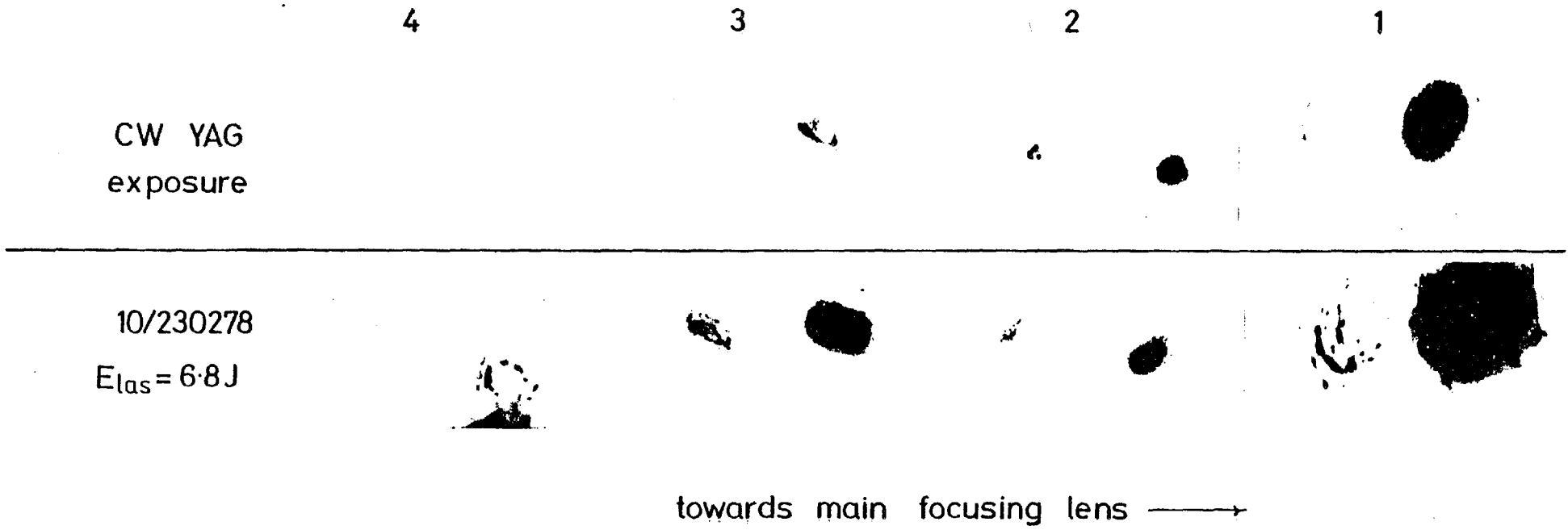


Fig 3.16 Examples of focal plane pictures

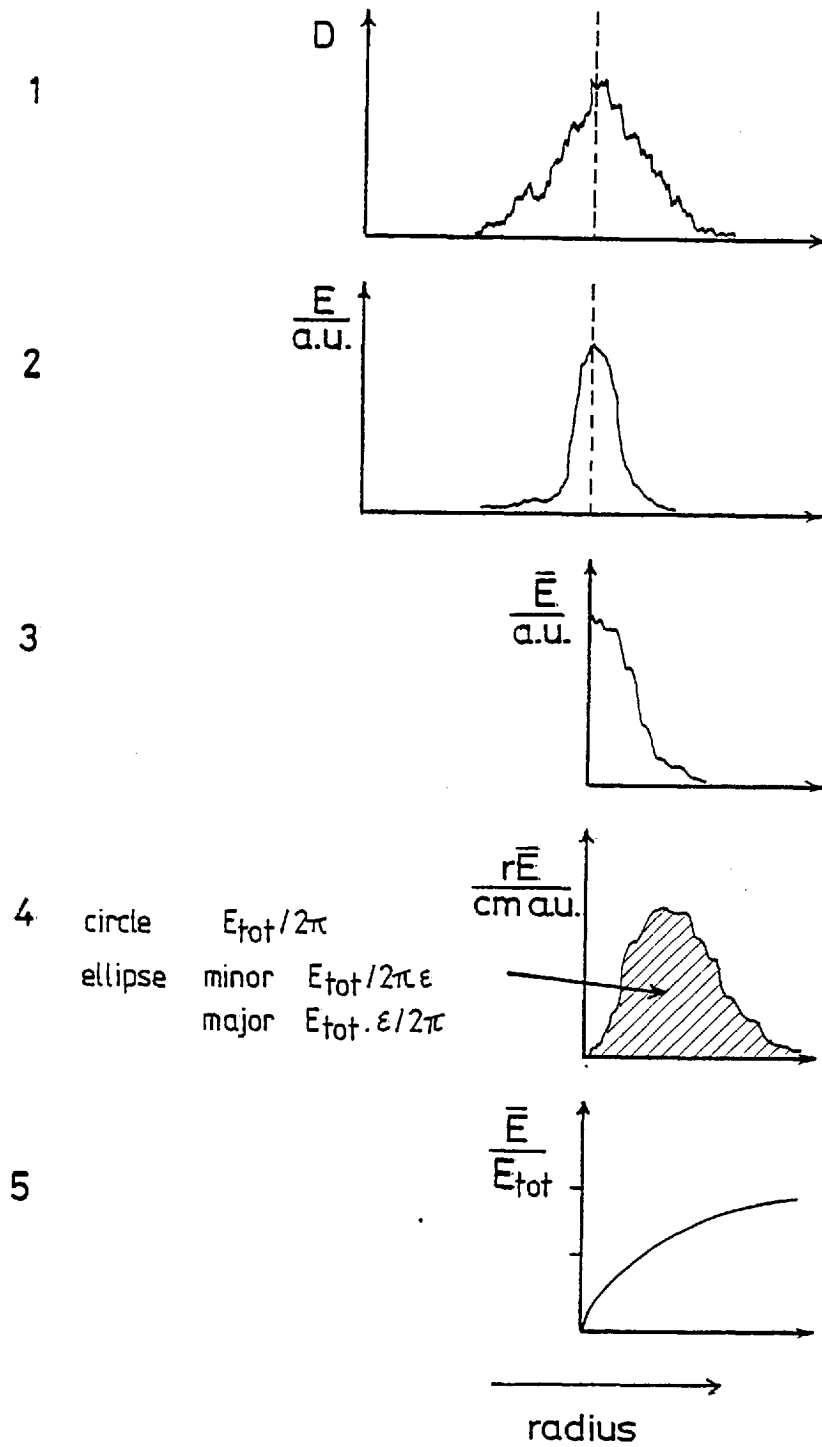
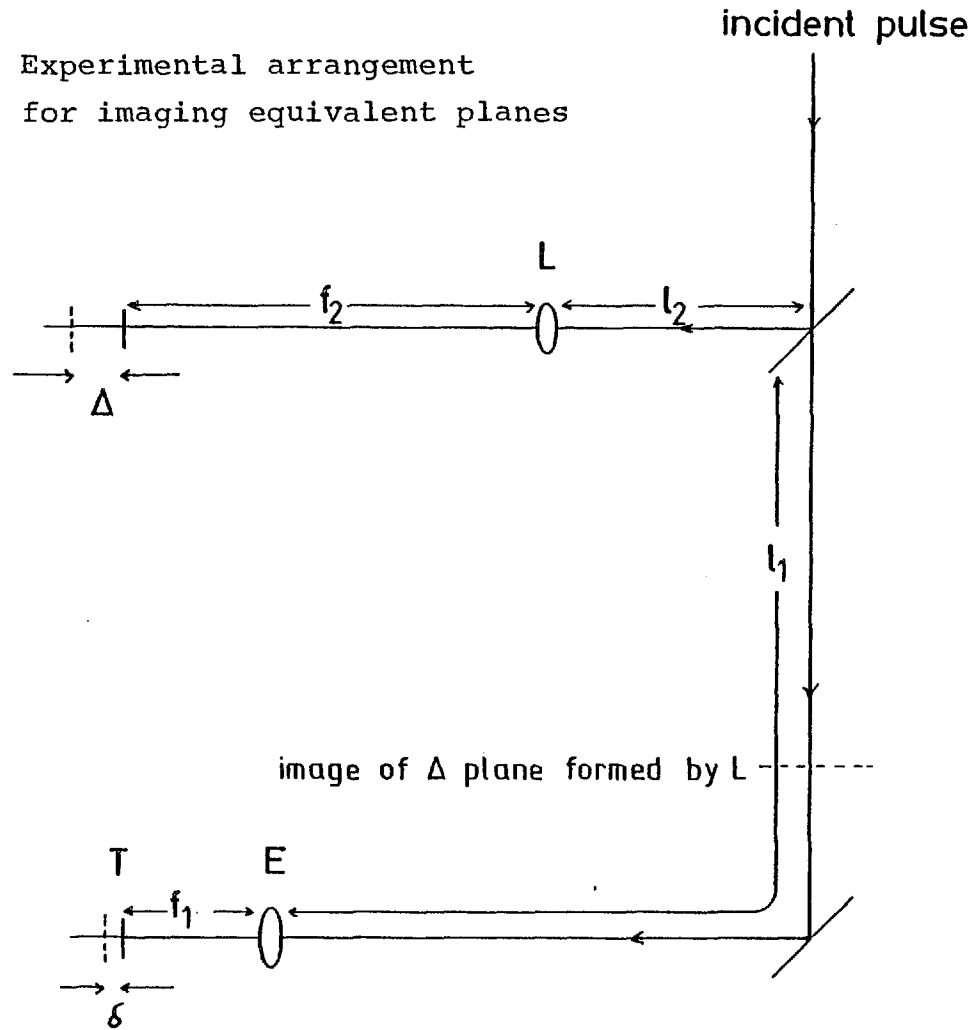


Fig 3.17 Summary of the data analysis of the far field measurements

Fig 3.18 Experimental arrangement  
for imaging equivalent planes



where  $\ell_1 > \ell_2$  and  $f_2 > f_1$ . Both  $\Delta$  and  $\delta$  are positive if outside the focus and negative if inside. The magnification factor is

$$M = \frac{f_1 \Delta}{f_2 \delta} \approx \frac{f_2}{f_1}$$

Examples of the equivalent plane pictures are shown in Fig. 3.19. A series of beam splitters allowed the monitoring of eight equivalent planes. The focal spots are smaller than those generated in (a) and are more circular.

### 3.6 Streak Photography

The diagnostics reviewed in 3.1-3.5 give time-integrated data. In this section, the principal time resolving diagnostic, streak photography, is described. The discussion is divided into three parts; (a) a description of the streak cameras used together with some experimental notes, (b) calibration and (c) data analysis.

#### (a) Description of streak cameras

Two streak cameras were used in the present work; an EPL camera with an S1 photocathode and a magnetic coil image intensifier (Fig. 3.20) and an Imacon camera with an S20 photocathode, channel plate intensifier and Photochron II streak tube (Fig. 3.21). The spectral response of S1 and S20 cathodes is shown in Fig. 3.22; further details may be found in R9. Photographic film (Kodak 2485) was used to record the streak pictures.

An image of the target is formed at the entrance slit of the streak camera. The camera generates an image of the slit which is swept in time along a line perpendicular to the slit. In this way, a space-time plot is produced; Fig. 4.2 shows an example from the thin foil experiment. The streak rate is the time scanned per unit distance on the

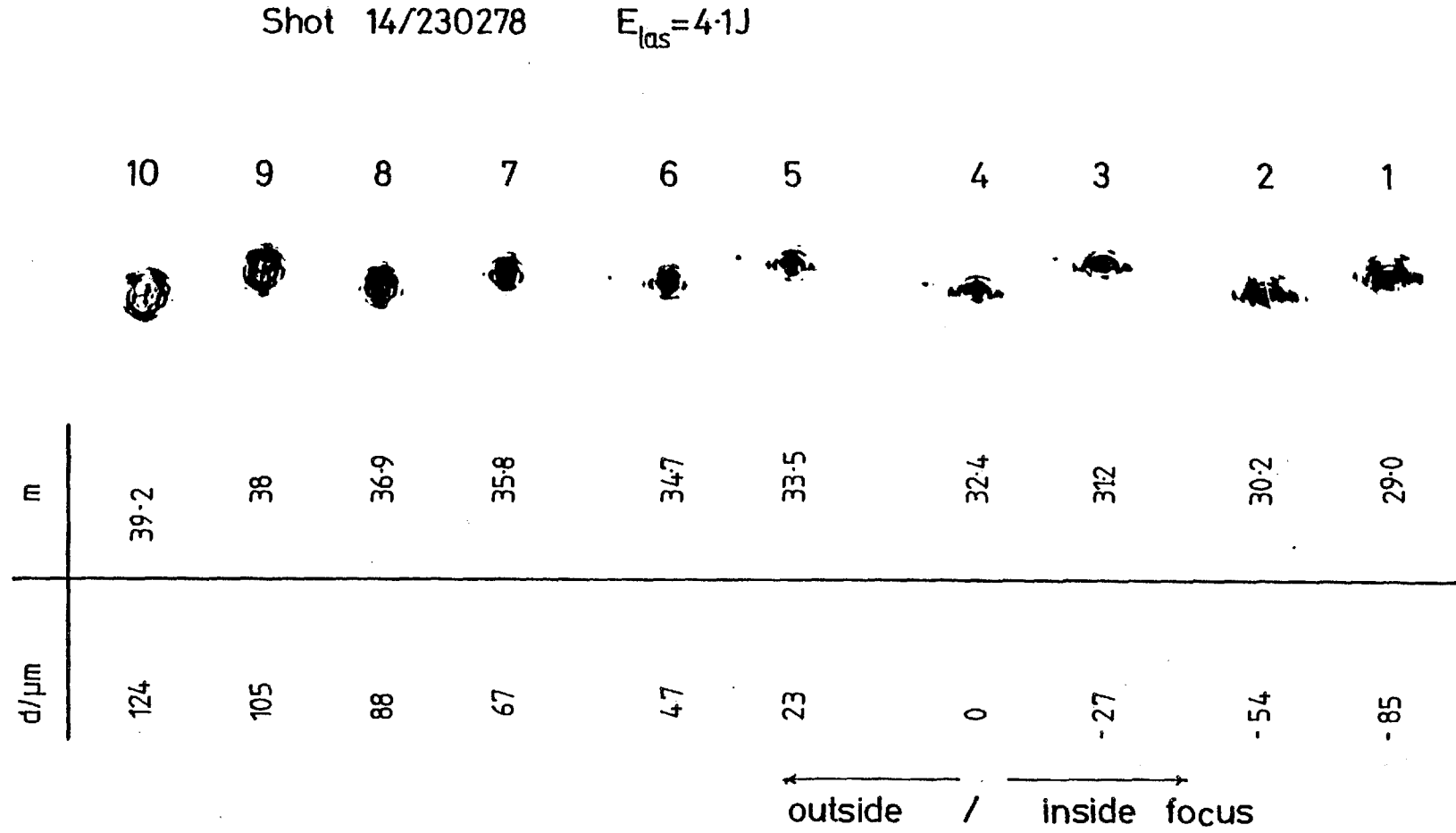


Fig 3.19 Examples of equivalent plane pictures

recording film. Streak rates of 500 ps/cm were used on the S1 camera, and up to 300 ps/cm on the S20 camera. The optimum temporal resolution is equal to the product of slit width  $\delta$  and streak rate  $r$

$$\Delta t \geq \delta r$$

For  $\delta = 200 \mu\text{m}$  and  $r = 500 \text{ ps/cm}$ ,  $\Delta t = 10 \text{ ps}$ . However, there are other effects which may degrade the temporal resolution. The spatial resolution at the entrance slit when in the streak mode is  $\sim 100\text{-}400 \mu\text{m}$ . (A figure of 10 line pairs per mm or  $50 \mu\text{m}$  is quoted in B1.) If the target is imaged at the slit with a magnification of 50, the spatial resolution in the target plane is better than  $10 \mu\text{m}$ . Fig. 3.23 shows a static mode image of a microballoon on the S20 camera.

The streak length on film is 4 cm and this defines the time window. For the fastest streaks, the window is  $\sim 1.2 \text{ ns}$  and so careful synchronisation is required. The streak cameras are triggered from silicon photodiodes sensitive to the main laser pulse early in the amplifier chain. Cable delay is adjusted until the streak duration and target event are synchronised. Fig. 3.24 illustrates the procedure for synchronising a streak camera with target events and with a reference pulse. The reference pulse is a small fraction of the main laser beam and, in addition to giving  $I_{\text{INC}}(t)$ , also provides a time origin on the streak pictures.

The use of streak cameras in particular experiments is described in Chs. 4, 6 and 7.

#### (b) Calibration

Three calibrations may be identified; the streak rate as a function of position along the centre line of the streak track, the shape of the constant space and time contours and lastly the intensity response of the camera and film. All these calibrations may be performed simultaneously

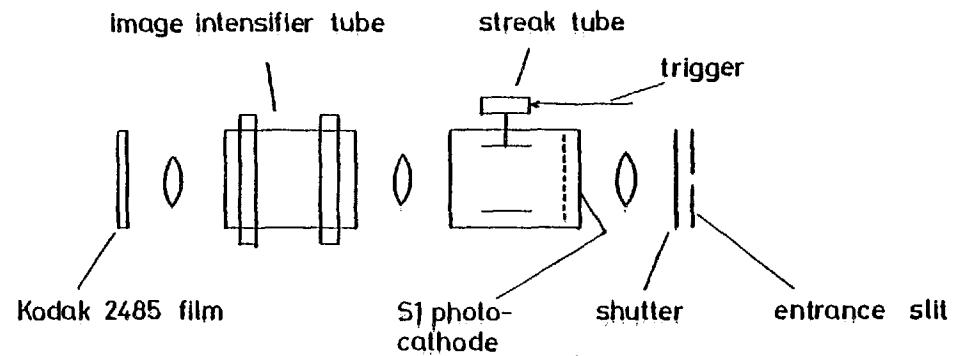


Fig 3.20 Schematic diagram of the S1 streak camera

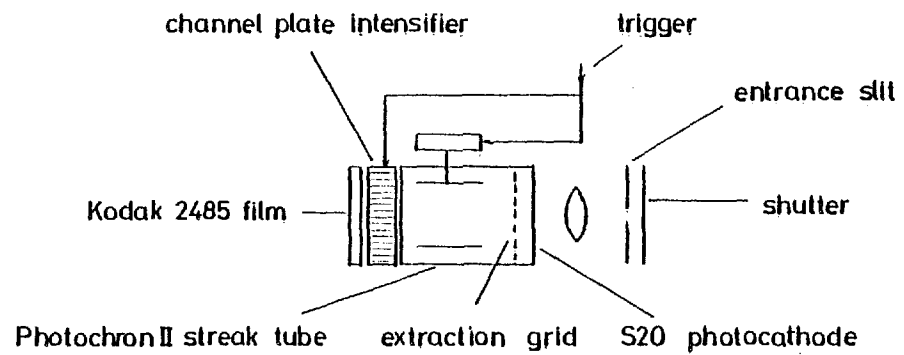


Fig 3.21 Schematic diagram of the S20 streak camera



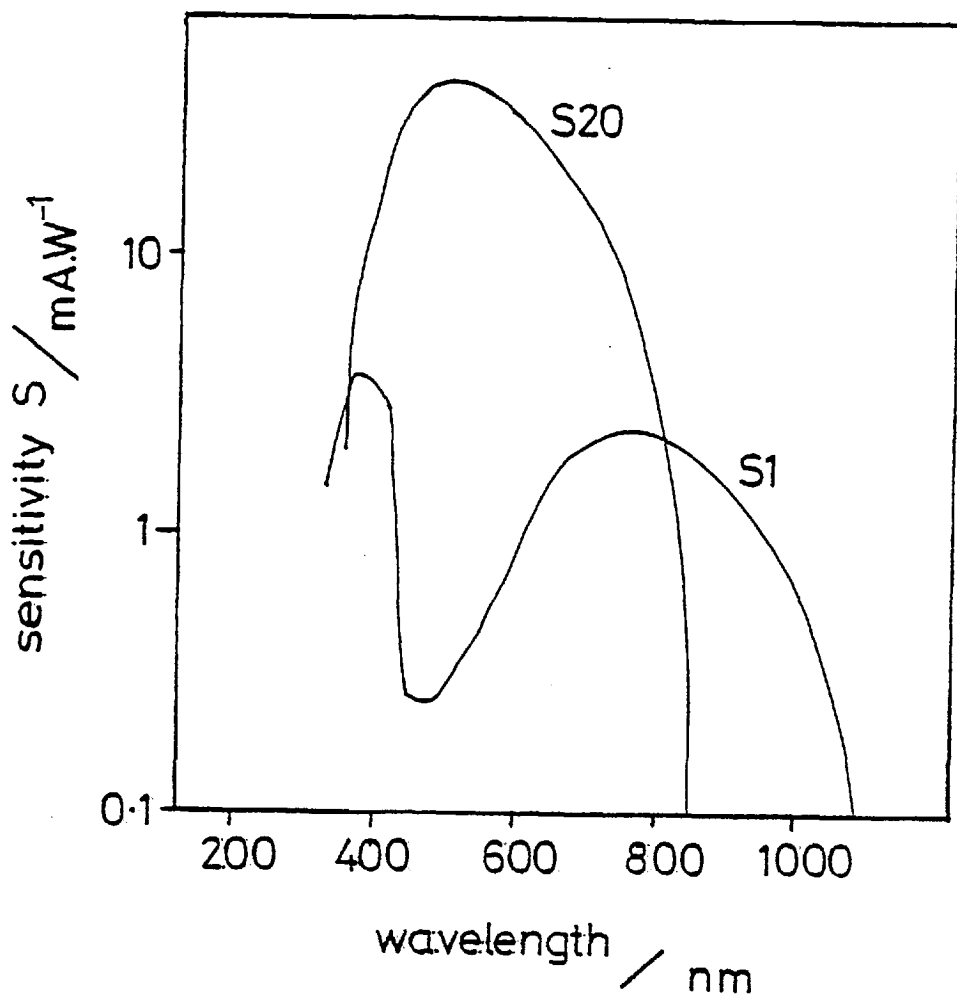
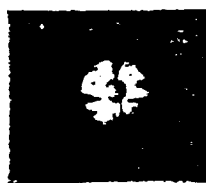


Fig 3.22 Response curves of S1 and S20 photocathodes

S20; focus mode



77 $\mu\text{m}$  diameter microballoon

Fig 3.23 Static mode picture of a microballoon on the s20 streak camera

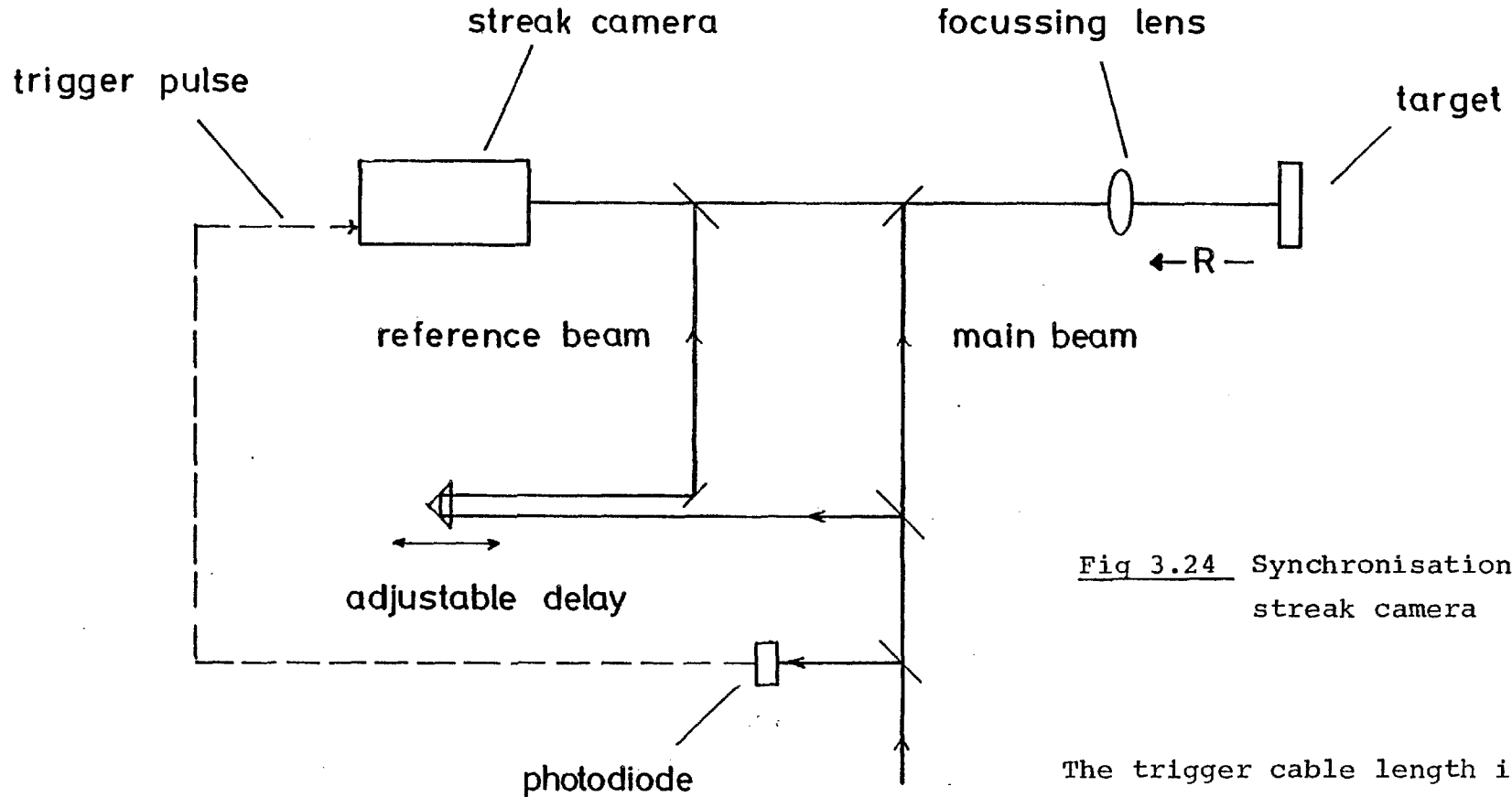


Fig 3.24 Synchronisation of a streak camera

The reference beam path length is adjusted until the reference pulse arrives at the streak camera at approximately the same time as R.

The trigger cable length is adjusted until the reflection R from a surrogate target appears on the streak picture.

by streaking the output of a mode-locked dye laser, as described below.

The dye laser produces a chain of pulses with a duration of  $\mu\text{secs}$  and of wavelength 5700-6100 Å. The pulse separation is  $\sim 4$  ns and the pulse width is  $\sim 10$  ps, depending on the condition of the mode-locking dye. The lasing medium is Rhodamine 6G and the mode-locking dye is DODCI. The separation between the pulses is too long to be useful for streak rate calibration on the faster sweep speeds. The dye laser output is therefore passed through an etalon of known reflectivities and mirror separation before being steered onto the streak camera entrance slit. A Pockels cell may be used to switch out one mode locked pulse; this avoids exposing the photocathode to a long chain of pulses. The etalon generates a series of pulses (Fig. 3.25) of decreasing amplitude and fixed separation (the mirror separation can be measured to 1 mm or 7 ps). The experimental arrangement is summarised in Fig. 3.26 and a streak picture from the S1 camera is shown in Fig. 3.27.

The fixed separation between the series of pulses from the etalon allows the streak rate to be measured. Examples of the resulting calibration are shown in Fig. 3.28 for the S1 camera and in Fig. 3.29 for the S20 camera. Most of the non-linearity in Fig. 3.29 is due to the channel-plate intensifier.

By illuminating the entire length of the entrance slit, constant space contours may be mapped out on the streak track. As can be seen from Fig. 3.27, the S1 camera has very little distortion; the slit images are parallel and normal to the time axis, However, the S20 camera generates considerable pin-cushion distortion, again due to the intensifier. Constant space contours, mapped out by the above technique are shown in Fig. 3.30.

The fixed ratio of intensity between one pulse and the next from the etalon output, allows a measurement of the linearity of the streak cameras' intensity response. In practice, the density on the photo-

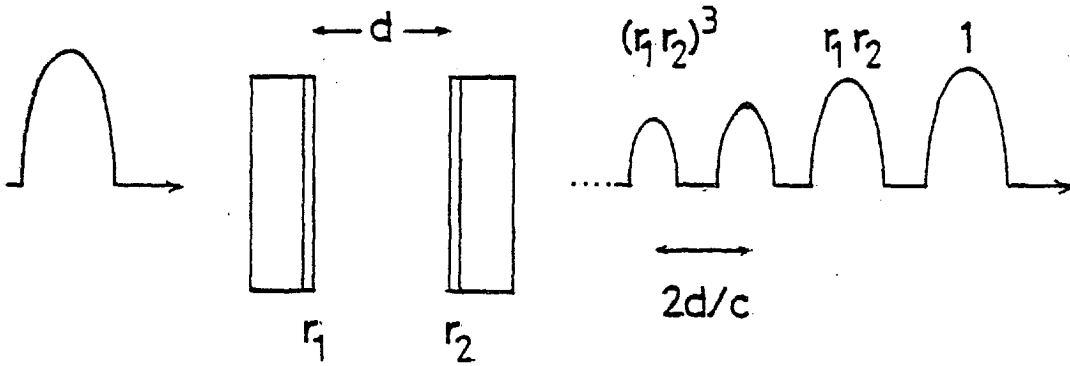


Fig 3.25 Etalon used in the dye laser calibration of the streak cameras

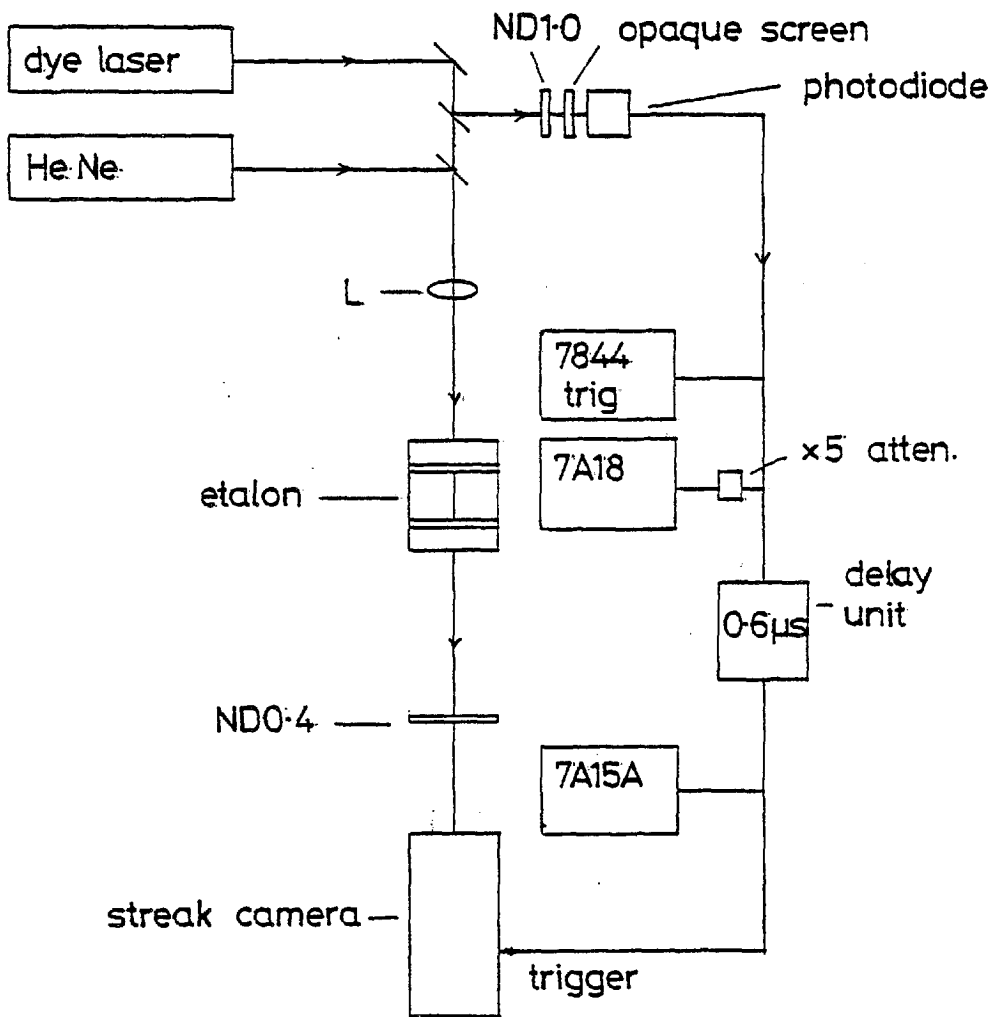
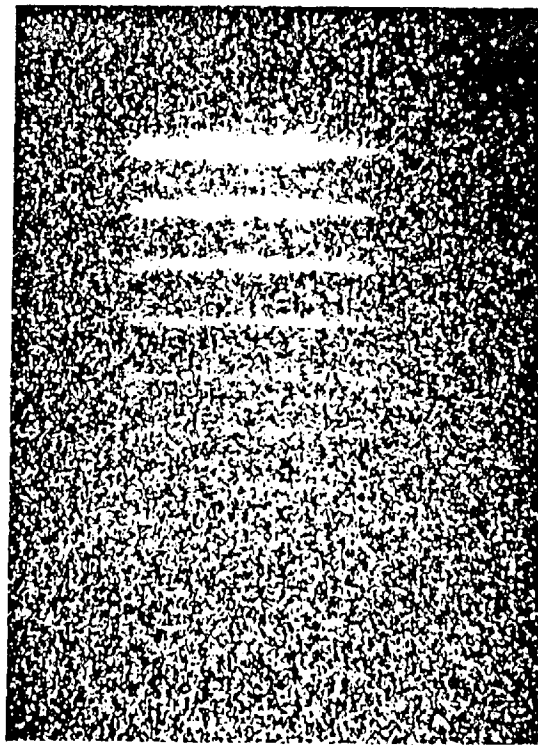


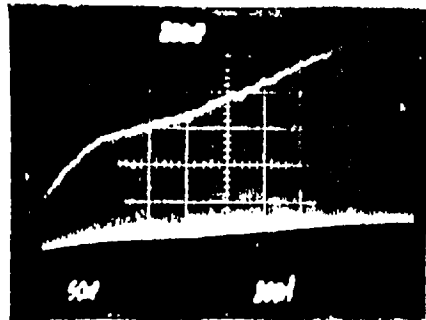
Fig 3.26 Experimental arrangement for dye laser calibration of streak cameras



DYE LASER  
CALIBRATION SHOT 4  
(20 10 77)

500ps  
↓

Fig 3.27 Example of a streak picture of the dye laser output



DYE LASER  
OUTPUT  
100 ns/div

[R/IC]

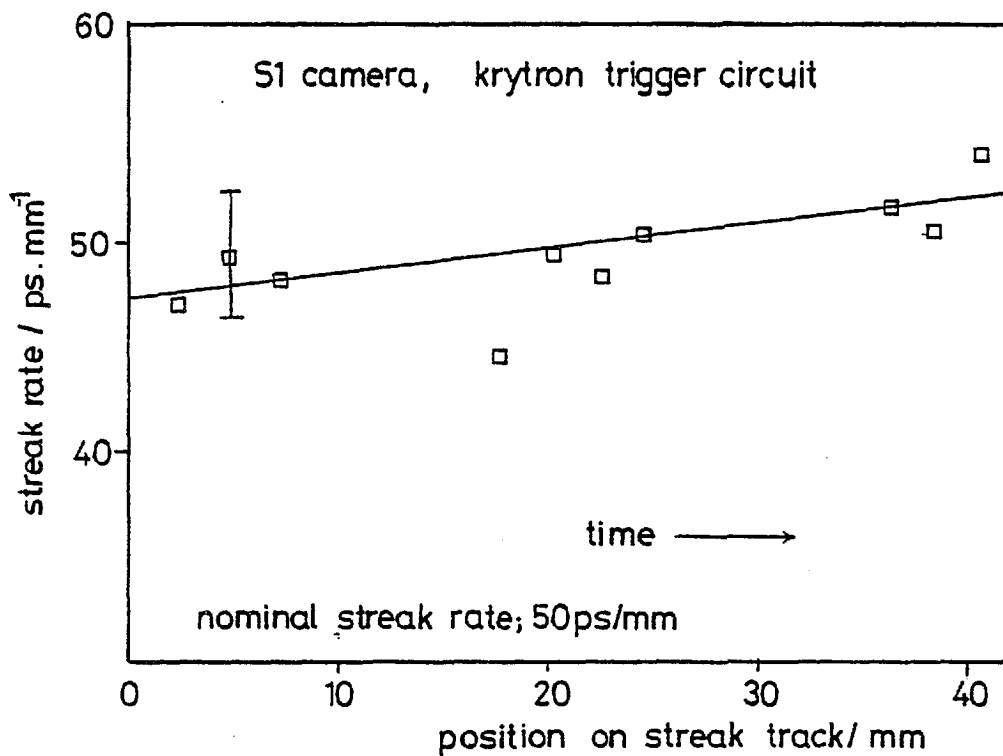


Fig 3.28 Streak rate calibration curve for the S1 streak camera

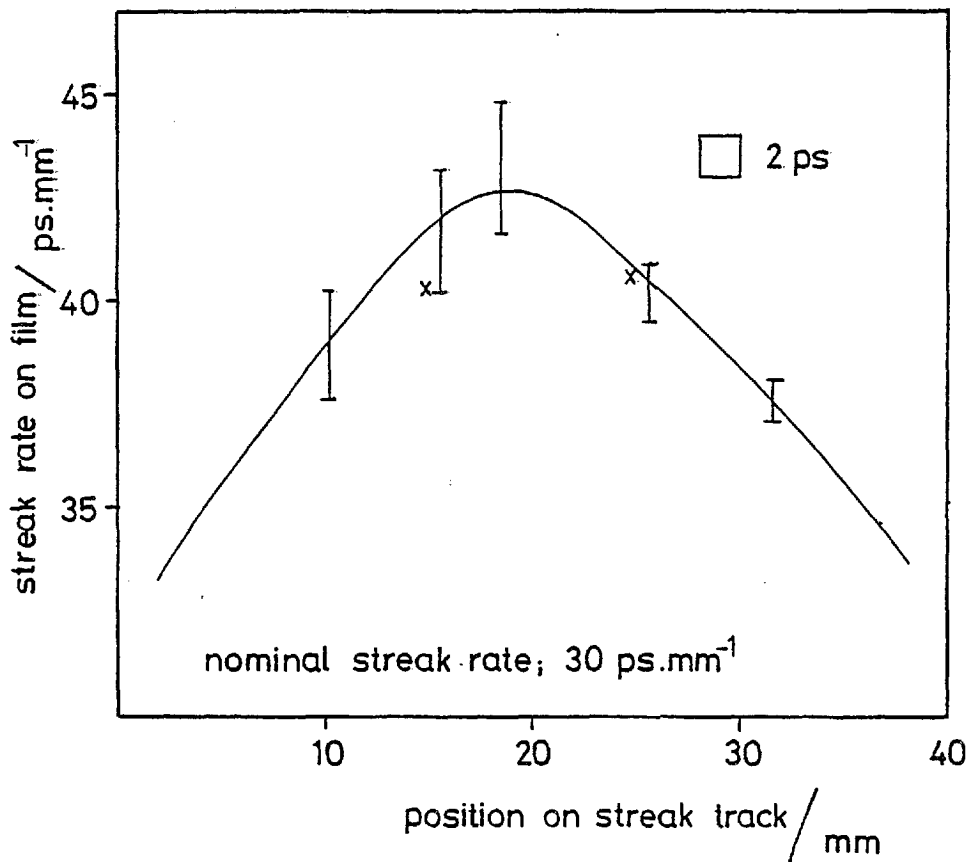


Fig 3.29 Streak rate calibration curve for the S20 camera

graphic film is measured on a microdensitometer giving a relative calibration of the film and camera together. Fig. 3.31 shows the calibration for the S1 camera and Fig. 3.32 for the S20 camera. These relative calibrations are sufficient because data streaks are normalised to calorimeter measurements in the experiments.

Finally, the dye laser calibration also gives information on pulse broadening due to over-exposure of the photocathode. Fig. 3.33 shows the pulse width as a function of peak density on film.

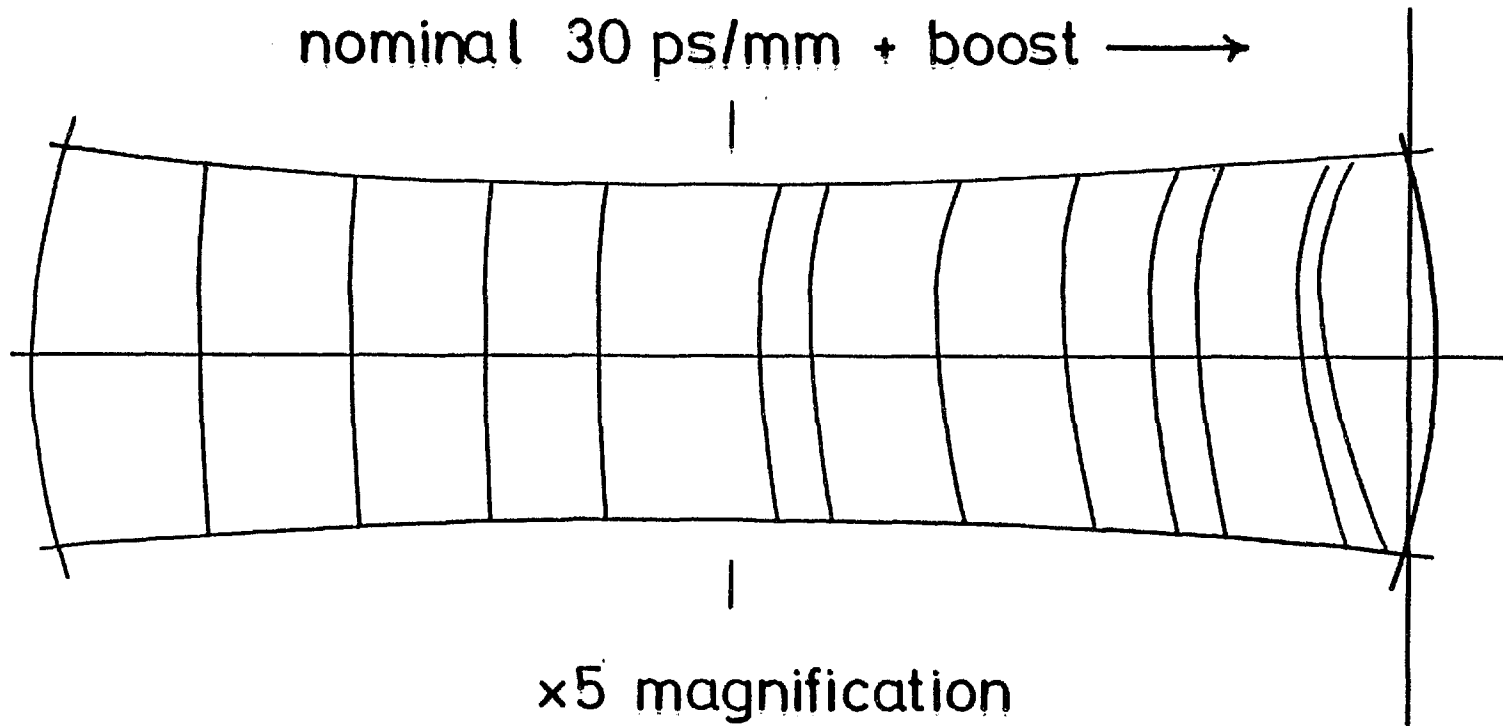
Data with maximum density above ND have poor time resolution.

(c) Data analysis

The principal application of streak photography is in the thin foil experiment. Some aspects of the reduction of the thin foil data are discussed in this section.

The S1 streak camera was used to measure the incident, transmitted and reflected  $\omega_0$  radiation as a function of time (Fig. 3.34). No spatial information is contained in the streaks. The data reduction begins with a microdensitometer scan along the time axis of each pulse. Using the camera and film calibration curve, the density scan is converted to power in arbitrary units as a function of time. The area under this curve is equated to the associated calorimeter measurement. The power scale is then fixed. The incident, transmitted and reflected pulses are synchronised by such techniques as indicated in Fig. 3.24 and the peak of the incident pulse is defined as  $t = 0$ . After synchronisation, the transmitted and reflected powers may be divided by the incident power to give the fractional transmission and reflection as functions of time. Sources of error include; error in calorimeter measurements (few percent), densitometry (5%) and uncertainties in the calibration curves. Power curves are accurate to  $\sim 10\%$  (Fig. 3.35) and fractional transmission and reflection curves to  $\sim 20\%$ , depending on the magnitude of the incident pulse at the particular instant (Fig. 3.36).

Fig 3.30 Constant space contours for the S20 streak pictures





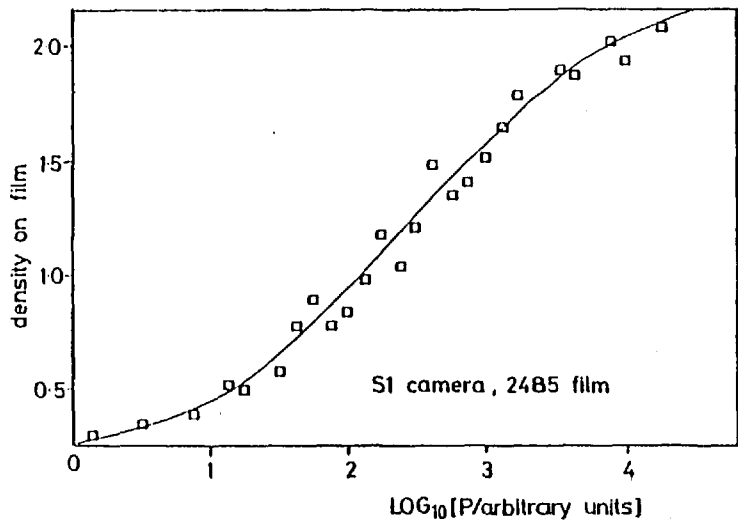


Fig. 3.31 Intensity calibration curve for the S1 camera

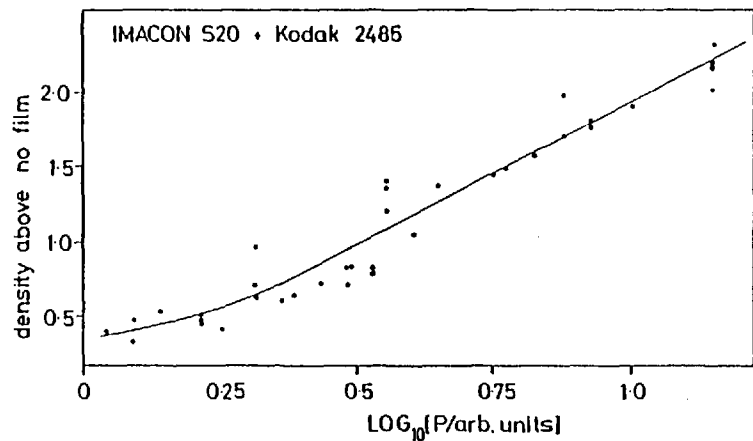


Fig. 3.32 Intensity calibration curve for the S20 camera

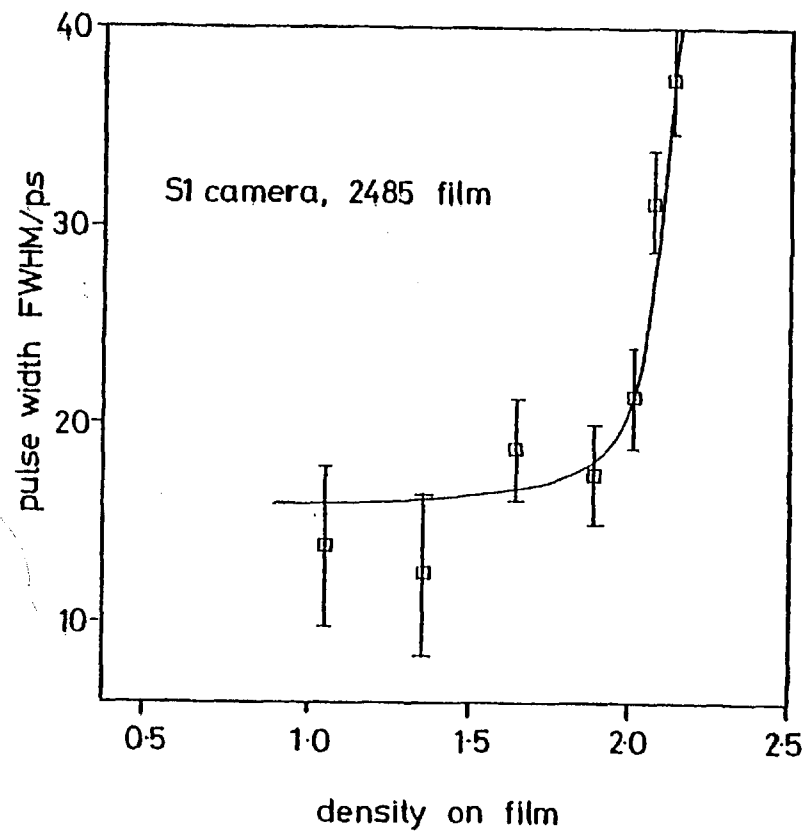


Fig 3.33 Pulse broadening due to overexposure on the S1 camera

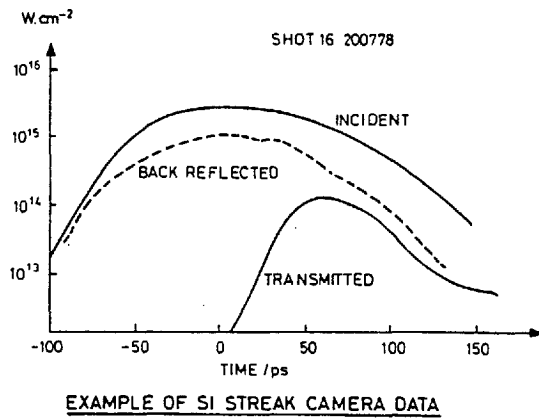
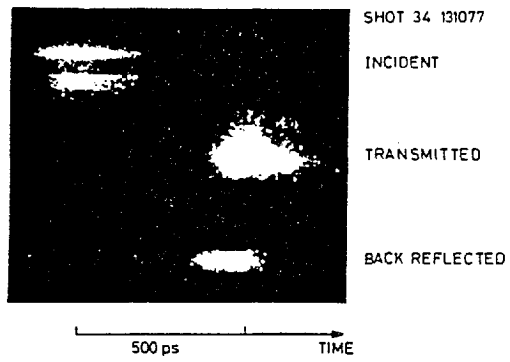


Fig 3.34 Example of SI streak pictures during the thin foil experiment

There are some other effects which can introduce errors into the streak data. It seems that a given pulse will have different streak lengths depending on the exposure level. This may be due to fogging associated with development of the photographic film. The point is illustrated in Fig. 3.37. This effect becomes serious only for very faint (under-exposed) streaks. Fig. 3.38 shows a comparison between a power curve generated by the photographic recording followed by the above data reduction and a curve generated by a one-dimensional optical multi-channel analyzer in place of the film; agreement is good.

Finally, a note is included on the procedure adopted to remove the distortion in the S20 streak pictures. The constant space contour grid (Fig. 3.30) was used to trace back an interval  $\Delta$  off the centre line AB back to an interval  $\Delta'$  on the centre line. The streak rate calibration curve could then be used to find the implied time interval. It was arranged that spatial information fell in the region of the streak track where distortion was small (see Fig. 4.11 for example).

### 3.7 Ion Collectors

Faraday cup collectors were used to sample the ion blow-off. They were positioned on the inner wall of the target chamber and in axial holes in the front and rear lenses. Further details and results are given in 4.3.

Charge collectors deliver a current,  $i$ , equal to the rate of arrival of charge in the collection aperture. If  $s$  is the area of the aperture,

$$i = sn_i Z e v_i$$

where  $n_i$ ,  $v_i$  and  $Ze$  are the number density, velocity and charge of the ions, respectively. The rate of arrival of mass is

$$\frac{dm}{dt} = sn_i M m_p v_i$$

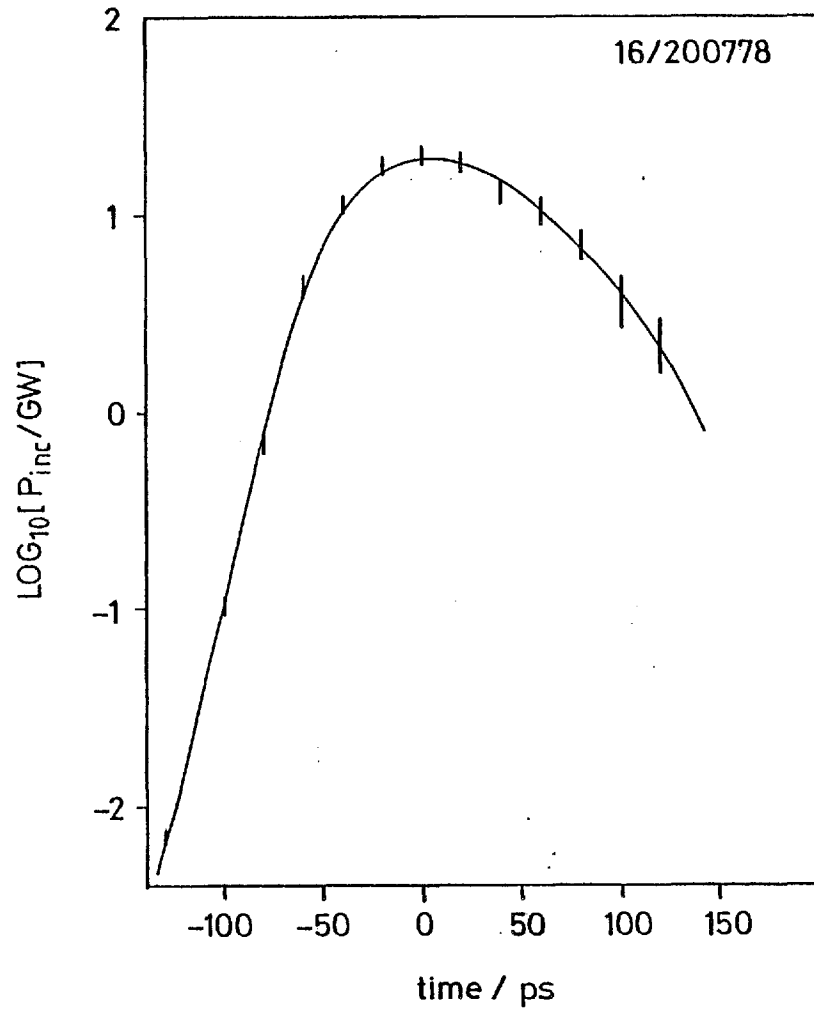


Fig 3.35 Typical error bars on the S1 power curves

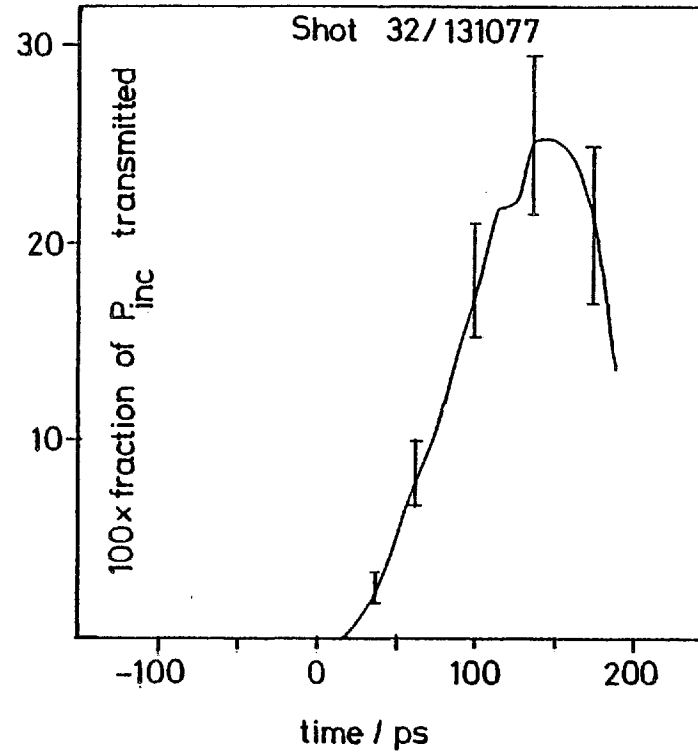


Fig 3.36 Typical error bars for the S1 fractional transmission and backscatter curves

where  $Mm_p$  is the ion mass. So

$$\frac{dm}{dt} = \left( \frac{m_p}{e} \right) \left( \frac{M}{Z} \right) i$$

Similarly, the rate of arrival of energy is

$$\begin{aligned} \frac{de}{dt} &= sn_i v_i \left( \frac{1}{2} Mm_p v_i^2 \right) \\ &= \frac{dm}{dt} \frac{d^2}{2} \frac{1}{t^2} \end{aligned}$$

where  $d$  is the target-collector separation and  $t$  the time. Therefore a knowledge of  $M/Z$  is required to calculate  $dm/dt$  and  $de/dt$ . In the present work,  $M/Z$  was assumed to be 13/7 for the polystyrene  $((CH)_n)$  foils.

The sampled ion distribution may be integrated over solid angle to obtain the total recovered mass and energy.

### 3.8 X-ray Diodes

Measurements of the soft X-ray continuum were available from sets of filtered diodes. A number of filter cut-off energies allowed measurement of the background "thermal" electron temperature. Further details and results are given in 4.3 for the thin foil experiment.

### 3.9 Magnetic Probes

During the early development of these experiments, coils were used to detect magnetic fields a large distance ( $\sim 1$  cm) from the plasma.

A coil provides a signal proportional to  $dB/dt$  which may be integrated to give  $B$ .

Rotation of the coil through  $180^\circ$  results in a change in sign of the signal due to fields. Components of the signal which do not change

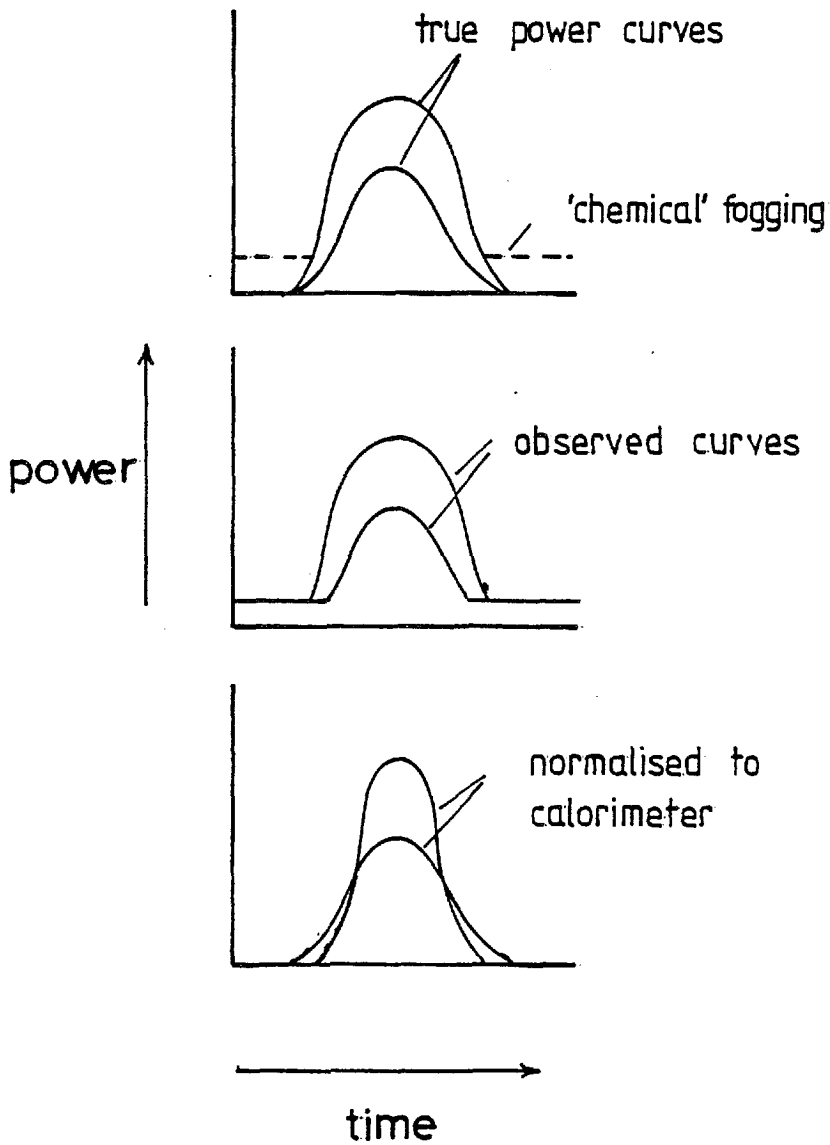


Fig 3.37 Different pulse lengths caused by fogging

sign are associated with noise. An example of a signal is given in Fig. 3.39 and displays a 'fast' and 'slow' component. The 'slow' component is in a direction consistent with the  $\nabla T \times \nabla n$  source term.

For the thin foil experiments, fields were found to be predominantly azimuthal and to reverse direction each side of the foil. Typical magnitudes were  $\sim 1$  Gauss at 10 mm from the target. This is consistent with a field of 1 MG in a plasma of volume  $(100 \mu\text{m})^3$ , assuming conservation of B/p.

### 3.10 Time-Resolved Spectroscopy

Harmonics of the laser frequency emitted by the plasma are sufficiently bright to allow spectroscopic study. Grating spectrometers are used with typical dispersions of  $4 \text{ \AA mm}^{-1}$  in the film plane. In the Brillouin backscatter experiment to be discussed in Ch. 6, back-reflected light at approximately the laser frequency is passed through a reflection grating spectrometer and then relayed to a streak camera. In this way spectral and temporal dispersion is achieved.

The topic to be discussed in this section is the loss in time resolution suffered by a pulse in passing through the spectrometer. The theoretical resolving power of a spectrometer is

$$R_{\text{th}} = \frac{\lambda}{\Delta\lambda} = \frac{\text{maximum path difference}}{\lambda}$$

But the maximum path difference through the spectrometer also sets the error  $\Delta t$  in the timing;

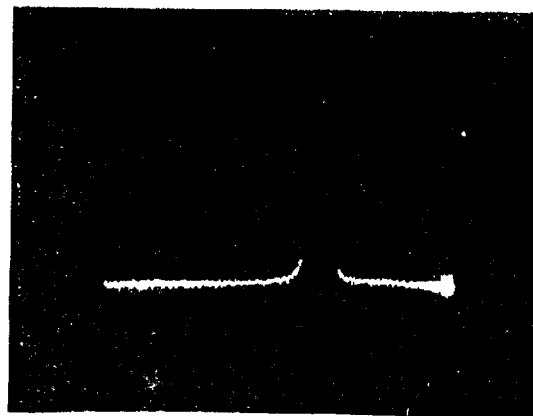
$$\Delta t = \frac{\text{maximum path difference}}{c}$$

so

$$\Delta t = \frac{\lambda^2}{c\Delta\lambda}$$

that is, there is a trade-off between spectral and temporal resolution.

OMA

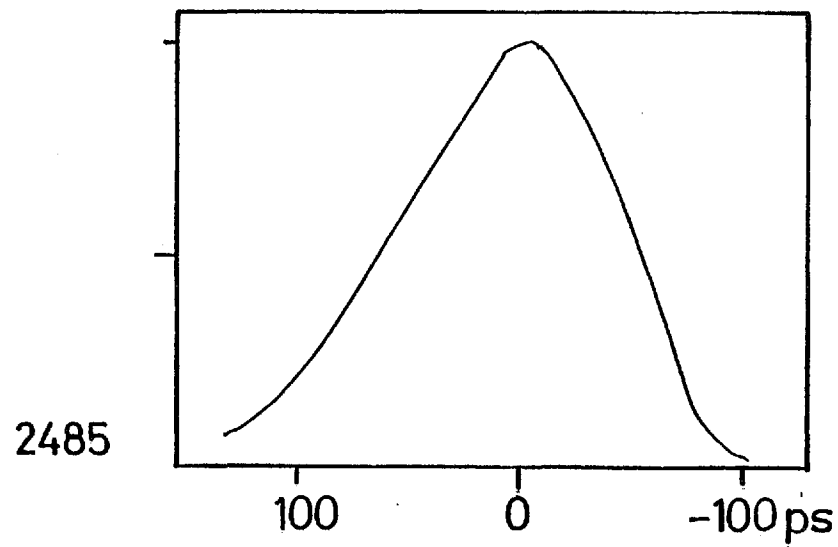


175/120178

17/4 ps per channel

117 ps FWHM

← time



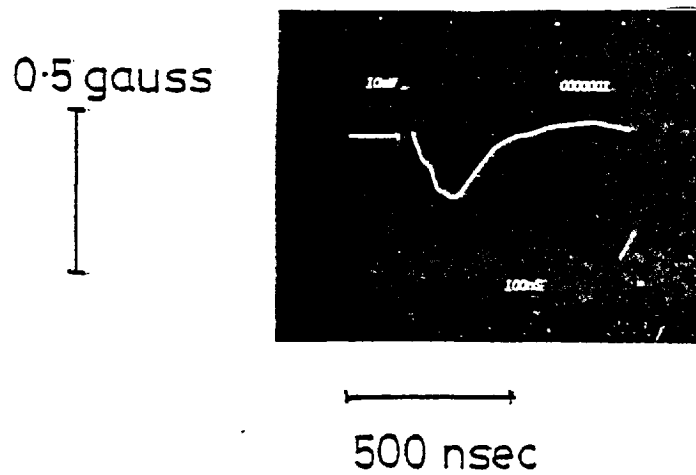
6/200778

Fig 3.38 OMA and film comparison



For example, if a wavelength resolution of  $0.5 \text{ \AA}$  is acceptable at  $1.06 \text{ \mu m}$ , then  $\Delta t = 75 \text{ ps}$ . For this reason, long (1.6 ns FWHM) were preferred over short pulses for the Brillouin backscatter experiment (Ch. 6).

magnetic field  
SHOT 34 (23-3)  
0.09  $\mu\text{m}$  foil



[R/I.C.]

probe - target separation: 13mm

Fig 3.39 Example of magnetic fields

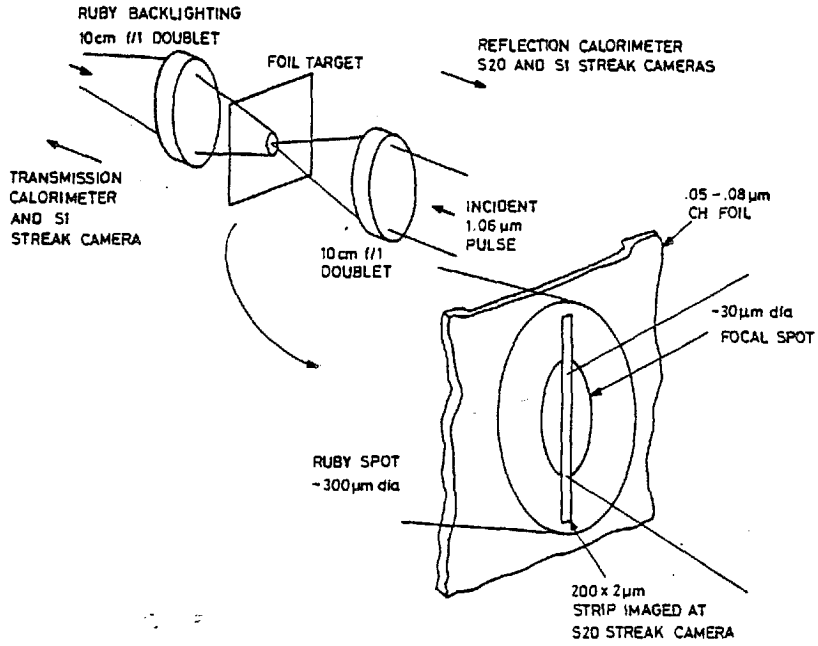


Fig 4.1 Schematic diagram of the thin foil experiment

## CHAPTER 4

### THIN FOIL BURN THROUGH EXPERIMENT

The results of an experiment involving the irradiation of thin, plastic foils by high power laser pulses are presented (4.3). Previous work is reviewed in 4.1 and the experiment is described in 4.2. A discussion of the results is postponed to Ch. 5.

In 4.4, results from a related but separate experiment are presented. Back-reflected light at twice the laser frequency was observed.

In 4.5, observations of  $\frac{3}{2} \omega_0$  emission from thin foil targets are presented.

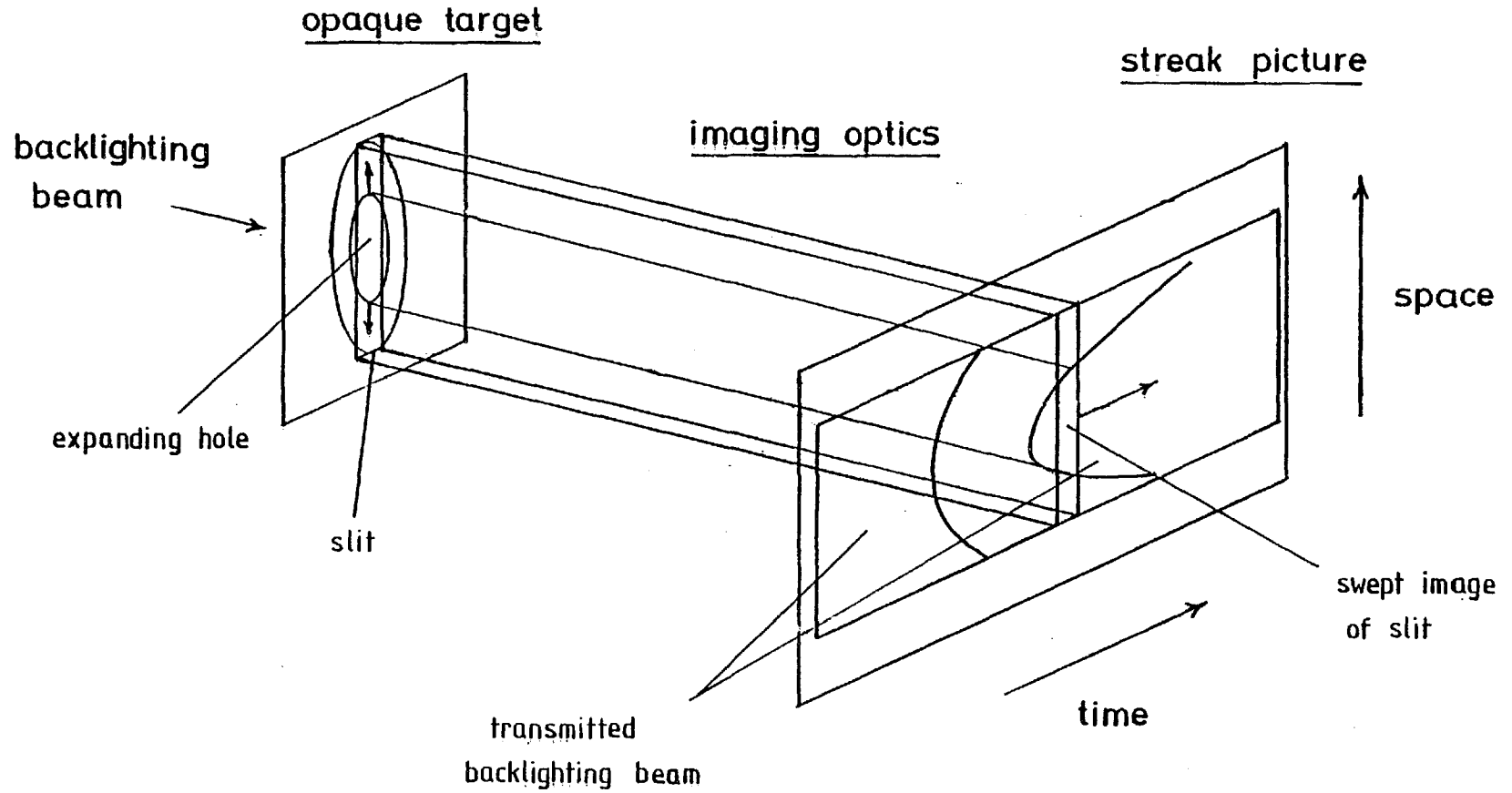
#### 4.1 Review of Thin Foil Experiments

The behaviour of thin film targets under irradiation by high power laser pulses has been studied by a number of researchers in an effort to understand laser-plasma transport processes.

Early work (M4) indicated that electron thermal conduction was reduced from classical values. The fraction of incident laser energy which was transmitted by plastic (CH) foils was measured as a function of foil thickness. Approximately 50% of the incident energy (delivered in a 25 ps FWHM pulse with  $I_{\max} = 5 \cdot 10^{15} \text{ W cm}^{-2}$ ) was transmitted by 0.04  $\mu\text{m}$  thick foils. Comparison with a 1 D, Lagrangian code with an adjustable flux limit  $f$ , required  $f \sim 1\%$  to match the data. The simulation did not include fast electron transport, ponderomotive force or absorption after the target becomes underdense.

The same data have been reinterpreted after comparison with a more sophisticated code (G4). It has been found that the experimental results can be fitted without adjusting the thermal conduction coefficient or flux limit. In this simulation, fast electrons and ponderomotive

Fig 4.2 Schematic diagram showing the generation of the S20 streak pictures



force effects have been included, but 100% transmission is still assumed after the foil has become underdense.

Measurements of the ion blow-off (P2) were also originally thought to imply a reduction in the flux limit. The thermal ion fluxes from the front and rear of a 0.11  $\mu\text{m}$  polystyrene foil were compared while varying the incident laser intensity. When the irradiance exceeded  $10^{14} \text{ W cm}^{-2}$  (50 ps FWHM pulse), the ions at the front (laser side) of the target became hotter as would be expected, but those at the rear became cooler. Also the fraction of transmitted energy was found to drop from 4% to 0.5% at the same irradiance. The transmission figures should be treated with caution because of the small solid angle used to collect the light.

More recent results (P3) show a dependence of the ion fluxes on the incident pulse polarization. The ions at the rear of the target are heated more relative to the front ions by an S-polarised pulse. This has been interpreted as evidence for reduced conductivity caused by fields associated with resonance absorption.

High Z targets have been found to transmit more than low Z (M5). A 4  $\mu\text{m}$  polyethylene film irradiated at  $3 \cdot 10^{14} \text{ W cm}^{-2}$  (160 ps FWHM) transmitted  $\sim 1\%$  of the incident energy into 0.4 sr (f/1.33). This rose to 10% with a 1  $\mu\text{m}$  coating of nickel on the front surface. On the basis of these observations, it has been proposed that X-ray radiation is participating in energy transport in high Z targets. However, as discussed below, prepulse energy plays an important part in the burn through of thin foils and could have affected the results of Ref. M5.

The fractional transmission and reflection from thin, polystyrene foils has been measured at the Ecole Polytechnique (A3, A4) over a range of foil thicknesses. Approximately 70% transmission is observed through 0.05  $\mu\text{m}$  foils, dropping to 2.6% for 0.18  $\mu\text{m}$ , with  $I \sim 2 \cdot 10^{14} \text{ W cm}^{-2}$

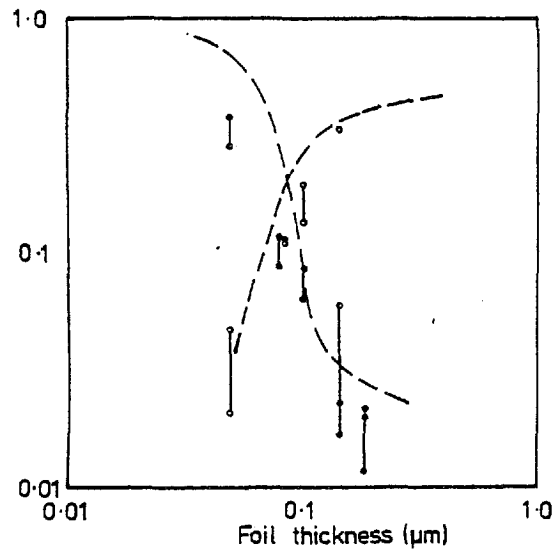


Fig 4.3 Fractional transmission (●) and reflection as a function of foil thickness

The dashed line summarises the results of ref A3 at an irradiance of  $2 \times 10^{14} \text{ W cm}^{-2}$

(100 ps FWHM, 1.06  $\mu\text{m}$ ). In Ref. A4, the burn depth has been inferred from three separate diagnostics namely, transmission of thin foils, ion blow-off measurements and X-ray emission spectra. Two laser wavelengths (1.06  $\mu\text{m}$  and 0.53  $\mu\text{m}$ ) were used. Comparison with a 1 D, Lagrangian code shows that, even with a flux limit of 0.05, the observed burn depths are smaller than calculated. However, scaling with laser wavelength is correctly predicted with a 5% flux limit and without including fast electrons. The main conclusions of the Ecole Polytechnique work are (i) greater heat front penetration is achieved by shorter wavelength light, (ii) a flux limit is required to explain observations, (comparable at the two wavelengths), (iii) fast electrons do not significantly contribute to transport. This last conclusion rests on a comparison between ion and X-ray emission at the two laser wavelengths

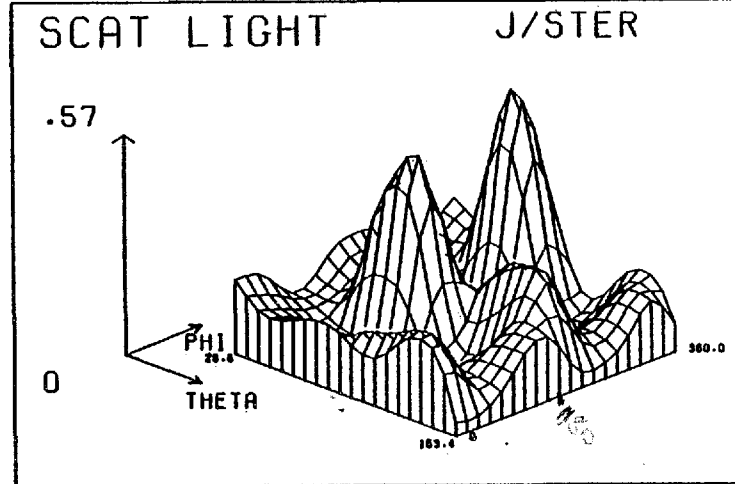
The work presented below provides data on the transmission and reflection from thin, polystyrene foils (1.4) with carefully monitored prepulse (3.2). The transmitted and reflected light has been time-resolved (3.6) to give a measure of the time-dependent absorption. In addition, a back-lighting technique has been used to observe the transparency of the target as a function of radius and time. Measurements of the time-integrated absorption have also been made (3.4).

The principal observations are (i) the transmission and absorption are affected by a prepulse level of  $\sim 10^{-5} E_{\text{INC}}$ , (ii) burn through occurs at a time dependent upon foil thickness, (iii) transmitted light after burn through suffers absorption in the underdense plasma, (iv) finite back-reflection is generated even after burn through and (v) the transmission region in the target spreads radially at a rate that can be compared with simulations.

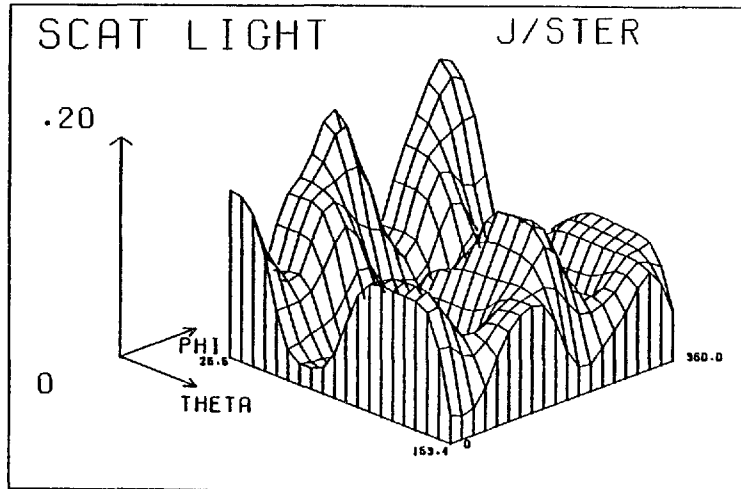
The conclusions that are drawn from these observations are summarised in 5.11.

# Scattered light data

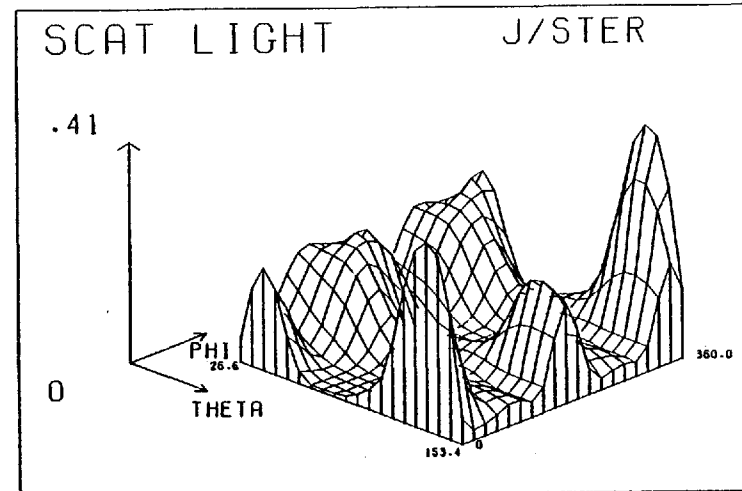
Fig 4.4 Examples of scattered light measurements



SHOT NUMBER = 210770013 ENERGY TRANSMITTED INTO LENS = 2.856 JOULES  
 INPUT ENERGY = 8.400 JOULES ENERGY FORWARDSCATTERED = .698 JOULES  
 ENERGY BACKSCATTERED INTO LENS = 0 JOULES ABSORPTION = 47.451 PERCENT  
 ENERGY DIFFUSELY BACKSCATTERED = .062 JOULES

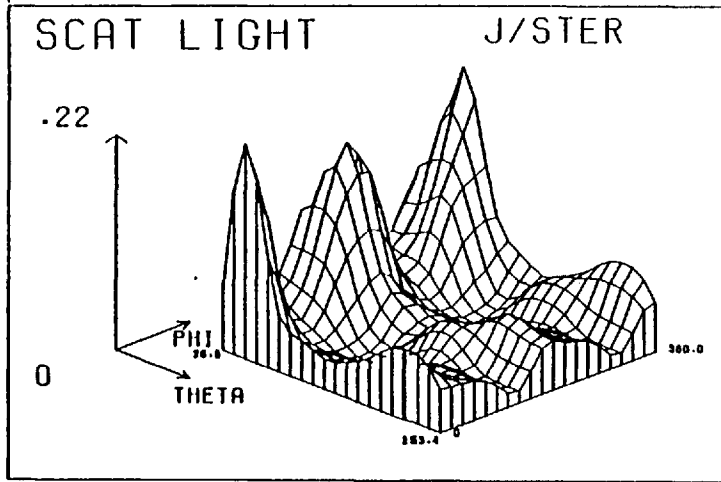


SHOT NUMBER = 210770017 ENERGY TRANSMITTED INTO LENS = .283 JOULES  
 INPUT ENERGY = 2.400 JOULES ENERGY FORWARDSCATTERED = .437 JOULES  
 ENERGY BACKSCATTERED INTO LENS = .207 JOULES ABSORPTION = 45.223 PERCENT  
 ENERGY DIFFUSELY BACKSCATTERED = .308 JOULES

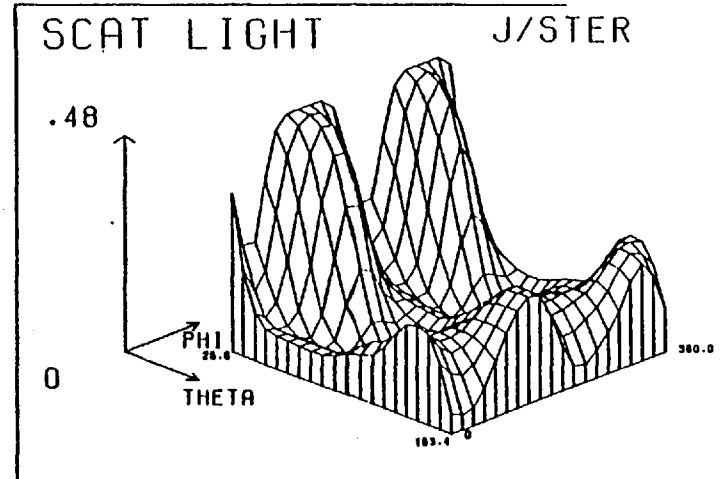


SHOT NUMBER = 200770012 ENERGY TRANSMITTED INTO LENS = .146 JOULES  
 INPUT ENERGY = 2.240 JOULES ENERGY FORWARDSCATTERED = .399 JOULES  
 ENERGY BACKSCATTERED INTO LENS = .011 JOULES ABSORPTION = 24.113 PERCENT  
 ENERGY DIFFUSELY BACKSCATTERED = .344 JOULES

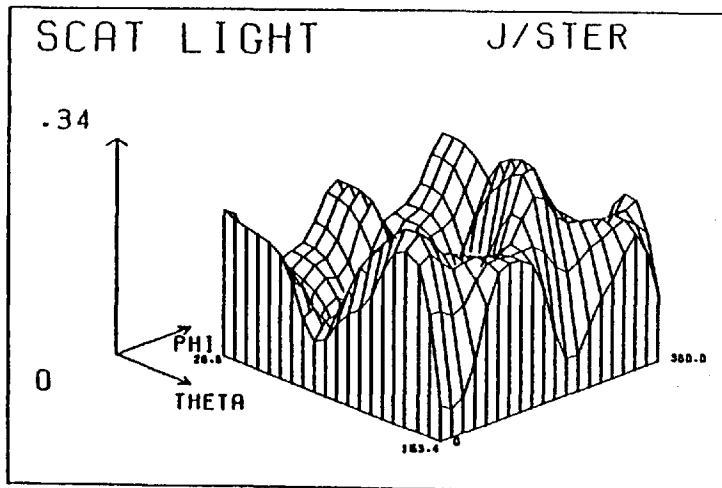




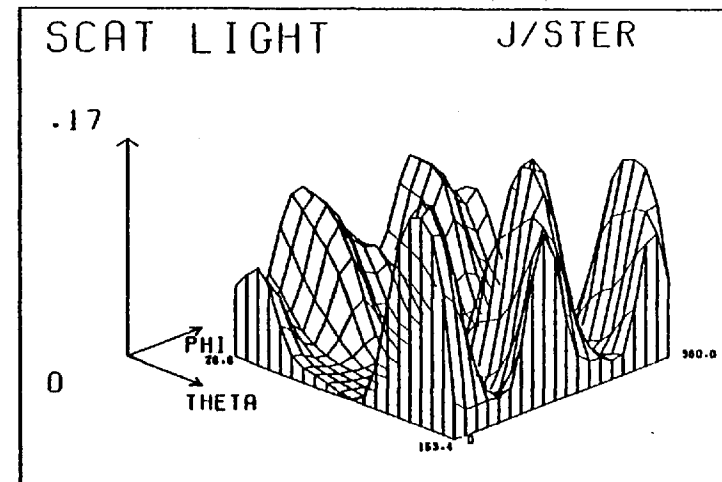
SHOT NUMBER = 21877018  
 INPUT ENERGY = 2.430 JOULES  
 ENERGY TRANSMITTED INTO LENS = .075 JOULES  
 ENERGY BACKSCATTERED INTO LENS = .300 JOULES  
 ENERGY DIFFUSELY BACKSCATTERED = .058 JOULES  
 ENERGY FORWARDSCATTERED = .101 JOULES  
 ABSORPTION = 82.408 PERCENT



SHOT NUMBER = 21877018  
 INPUT ENERGY = 2.480 JOULES  
 ENERGY TRANSMITTED INTO LENS = .220 JOULES  
 ENERGY BACKSCATTERED INTO LENS = .202 JOULES  
 ENERGY DIFFUSELY BACKSCATTERED = .074 JOULES  
 ENERGY FORWARDSCATTERED = .050 JOULES  
 ABSORPTION = 84.075 PERCENT



SHOT NUMBER = 21877022  
 INPUT ENERGY = 3.000 JOULES  
 ENERGY TRANSMITTED INTO LENS = .530 JOULES  
 ENERGY BACKSCATTERED INTO LENS = .170 JOULES  
 ENERGY DIFFUSELY BACKSCATTERED = .400 JOULES  
 ENERGY FORWARDSCATTERED = .030 JOULES  
 ABSORPTION = 28.014 PERCENT



SHOT NUMBER = 21877008  
 INPUT ENERGY = 2.420 JOULES  
 ENERGY TRANSMITTED INTO LENS = .760 JOULES  
 ENERGY BACKSCATTERED INTO LENS = .114 JOULES  
 ENERGY DIFFUSELY BACKSCATTERED = .148 JOULES  
 ENERGY FORWARDSCATTERED = .041 JOULES  
 ABSORPTION = 48.826 PERCENT

Shot Number	Foil Thickness / $\mu\text{m}$	$I_{\text{max}} / \text{W cm}^{-2}$	Prepulse energy / $E_{\text{inc}}$	Prepulse energy / $\mu\text{J}$	$\frac{E_{\text{bt}}}{E_{\text{inc}}}$	$\frac{E_{\text{bs}}}{E_{\text{inc}}}$	$\frac{E_{\text{abs}}}{E_{\text{inc}}}$
17/210778	0.08	$3 \cdot 10^{15}$	$2 \cdot 10^{-6}$	5	12	12	45
20/210778	0.08	$4 \cdot 10^{15}$	$3 \cdot 10^{-5}$	81	12	11	42
22/210778	0.08	$4 \cdot 10^{15}$	$1 \cdot 10^{-4}$	290	19	6	39
21/210778	0.08	$3 \cdot 10^{15}$	$1.2 \cdot 10^{-4}$	276	50	0	27

Table 4.1 Variation of transmission, reflection and absorption on prepulse level  
Energies are expressed as percentages of the incident energy

#### 4.2 Description of the Experiment

Polystyrene (CH) foils were irradiated at normal incidence by 100 ps FWHM neodymium laser pulses of energy 2-12 J (Fig. 4.1). The beam was focussed to a 30  $\mu\text{m}$  diameter spot by a 10 cm focal length, f/1 doublet to give power densities up to  $10^{16}$ - $10^{17}$  W  $\text{cm}^{-2}$ . Prepulse energies (3.2) were typically  $2 \cdot 10^{-6} E_{\text{INC}}$ .

An EPL S1 streak camera (3.6) measured the incident, transmitted and back-reflected power as a function of time, collecting over 0.66 sr (f/1), with temporal resolution of  $\sim 15$  ps (Fig. 3.1). In order to measure the onset of opacity and the radial extent of the underdense plasma, the foil was backlit with a ruby laser pulse (2.3). The plane of the foil was imaged at the entrance slit of an Imacon S20 streak camera (3.6) with a magnification of 46. Time-resolved measurements of the transmission of the ruby light were made in the  $200 \times 2 \mu\text{m}$  field of view at the target with temporal and spatial resolutions of 5-20 ps and  $\sim 10 \mu\text{m}$  respectively.

Calorimeters provided integrated measurements of the incident energy and of the energy transmitted and back-reflected into the f/1 collection cones (3.1). Fifteen time-integrating diodes sampled the distribution of 1.06  $\mu\text{m}$  light scattered outside the lenses (3.4). Faraday cup detectors (3.7) sampled the ion blow-off and a measurement of the soft X-ray continuum emission allowed a determination of  $T_e$  (3.8). In addition, the transmitted energy distribution in the plane of the rear f/1 doublet was measured in order to determine its angular dependence for matching with the diode data (3.3).

Before the detailed presentation of results in the next section, a short qualitative description of the foil behaviour will now be given.

In the early stages of the incident pulse, the foil is heated and eventually becomes ionized. The foil is initially transparent, so that absorption of the laser light is low. It is not clear precisely

Table 4.2 List of shots with time integrated data

SHOT NUMBER	$E_{\text{las}}/\text{J}$	FOIL/ $\mu\text{m}$	PREPULSE/ $10^{-6}$	% TRANSMISSION	% REFLECTION	% ABSORPTION
8/200778	2.3	0.14	2	6		44
9/200778	0.7	0.14	2.5	5		55
10/200778	10.5	0.14	2.5	8.8	5.3	57
12/200778	2.24	0.10	3	6.5	13.8	24
14/200778	2.2	0.10	4	8.6		60
15/200778	1.9	0.10		2.8	17.5	66
16/200778	2.4	0.10		3.0	16.5	61
17/200778	11.4	0.10		9.4	6.7	60
9/210778	2.7	0.05	3	29	4.8	47
11/210778	2.6	0.05	4	39	2.1	40
12/210778	1.5	0.05		39	0.1	33
13/210778	8.4	0.05	6	34		47
16/210778	2.5	0.08	1.7	9	11.1	25
17/210778	2.4	0.08	2	12	11.5	45
19/210778	2.5	0.08		10	10.2	44
20/210778	2.7	0.08	30	12	10.5	42
21/210778	2.3	0.08	120	50		39
22/210778	2.9	0.08	100	19	6.0	27

what mechanism leads to the onset of ionization; dielectric breakdown and multi-photon ionization are possible processes. However, once initiated, the ionization must proceed rapidly. Very quickly, the electron density will exceed the critical density defined by the laser wavelength. Then, provided there is a sufficient thickness of over-dense plasma, the transmission of laser light will cease. At this time, resonance absorption and other processes associated with the presence of a critical surface may operate.

The plasma, being hot, expands and to a first approximation the expansion is one-dimensional along the laser axis. At some time the density will, therefore, drop below the critical value and the laser pulse, if it is still present, will be transmitted again. This is loosely called 'burn through'.

The back-lighting pulse is present throughout these changes and the S20 streak data therefore provides information on the time and radius at which 'opacity' begins and ends. The target must become opaque and transmit again at first in the focal spot region. Fig. 4.2 shows the expected S20 streak picture (c.f. Fig. 4.9).

#### 4.3 Observations

The experimental observations are presented in the order; (a) time-integrated data, (b) time-resolved transmission and reflection (S1 data), (c) time-resolved back-lighting measurements (S20 data), (d) other diagnostic measurements.

##### (a) Time-integrated data

The fraction of the incident energy transmitted and reflected into the lens cones is shown in Fig. 4.3 as a function of foil thickness. Shots with  $I_{INC} \sim 2 \cdot 10^{15} \text{ W cm}^{-2}$  and with low prepulse ( $\lesssim 5 \cdot 10^{-6}$ ) have been selected for the graph. With increasing foil thickness, ( $> 0.15 \mu\text{m}$ ),

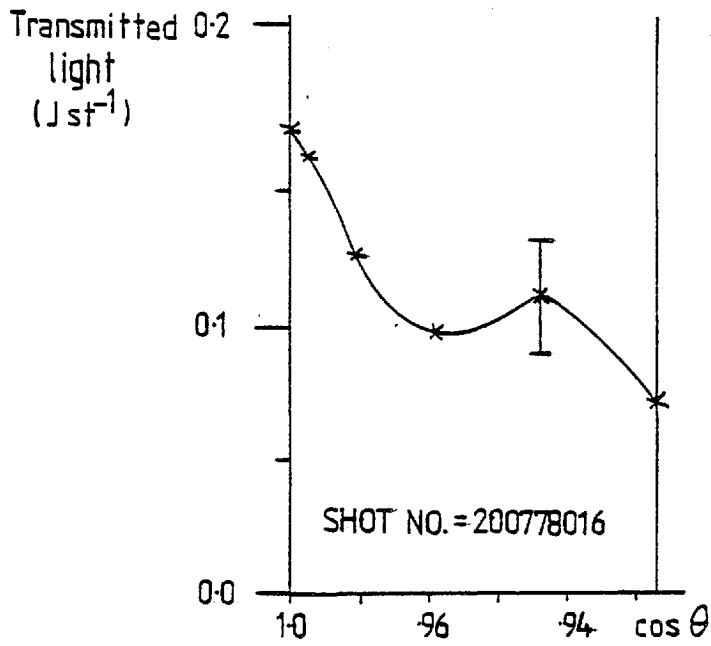


Fig 4.5 Example of distribution of light in the rear lens

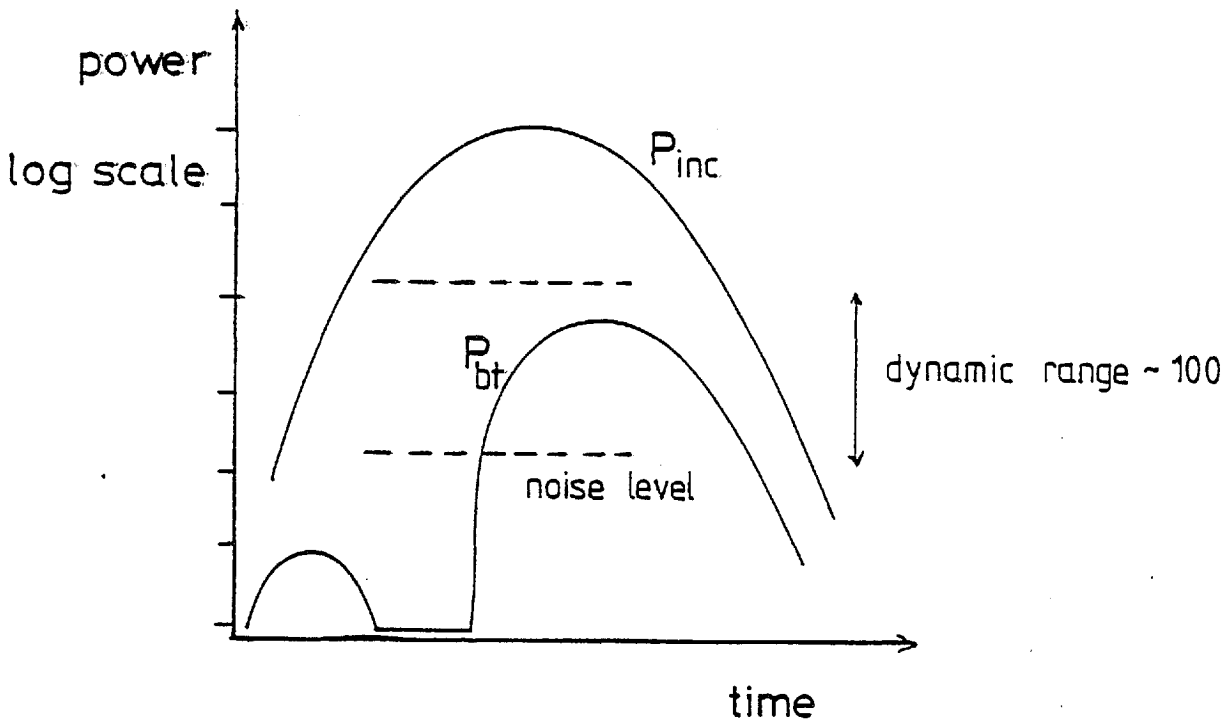


Fig 4.6 Schematic diagram showing how the early transmission is below noise level on the S1 camera

the transmitted energy levels off at 0.1 - 1.0% and the backscattered energy at ~30%. These measurements are compared with the data from other laboratories in 5.2.

Increasing the prepulse level results in higher fractional transmission as indicated in Table 4.1. The meaning of 'prepulse' is discussed in 4.3(d).

Fifteen silicon photodiodes sampled 1.06  $\mu\text{m}$  radiation scattered  <sup>$\epsilon$</sup>  outside the lens cones. Integration of the signals over all solid angles gives an estimate of the scattered energy. The absorption of laser light in the target is then  $(E_{\text{INC}} - E_{\text{BT}} - E_{\text{BS}} - E_{\text{SC}}) \div E_{\text{INC}}^*$ . These values, accurate to ~10% (5.3) are listed in Table 4.2. There is a shot-to-shot variation in the measured absorption which does not correlate with the shot parameters. This is probably due to small scale irregularities in the scattered light distribution which are not resolved by the diodes. Examples of the scattered light distribution are shown in Fig. 4.4. The typical (M1) azimuthal dependence is observed, with peaks in the plane perpendicular to the plane of polarization of the incident pulse. This is generally attributed to resonance absorption (M1) and Brillouin backscatter (P1).

The distribution of transmitted light within the lens cone for the shot of Fig. 3.13 is shown in Fig. 4.5 and matches the diode data quite well. No azimuthal dependence is seen in the lens solid angle in contrast to the forward scattered light. This is discussed in 5.2.

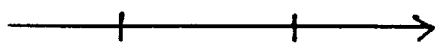
The fractional absorption is seen to fall with increase in prepulse level and to slightly rise as the incident irradiance is increased from 3 to 10  $10^{15} \text{ W cm}^{-2}$ . However, the absorption figures are generally quite high (~60% for thicker foils).

A complete list of shots with time-integrated measurements is given in Table 4.2.

\* defined on p. 39

S1 streak pictures

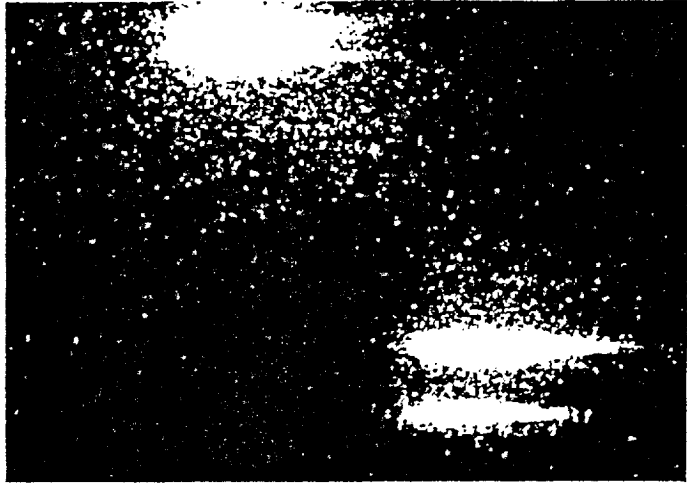
200 ps

time 

16/280777

$E_{\text{las}} = 4.6 \text{ J}$

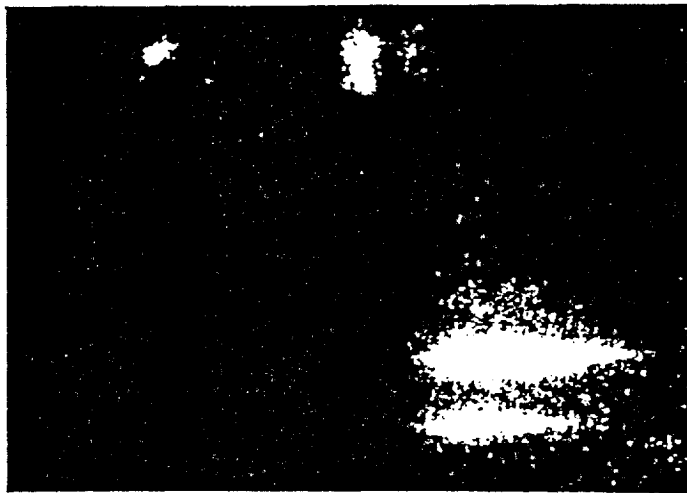
no foil



17/280777

$E_{\text{las}} = 5.2 \text{ J}$

0.34  $\mu\text{m}$  foil



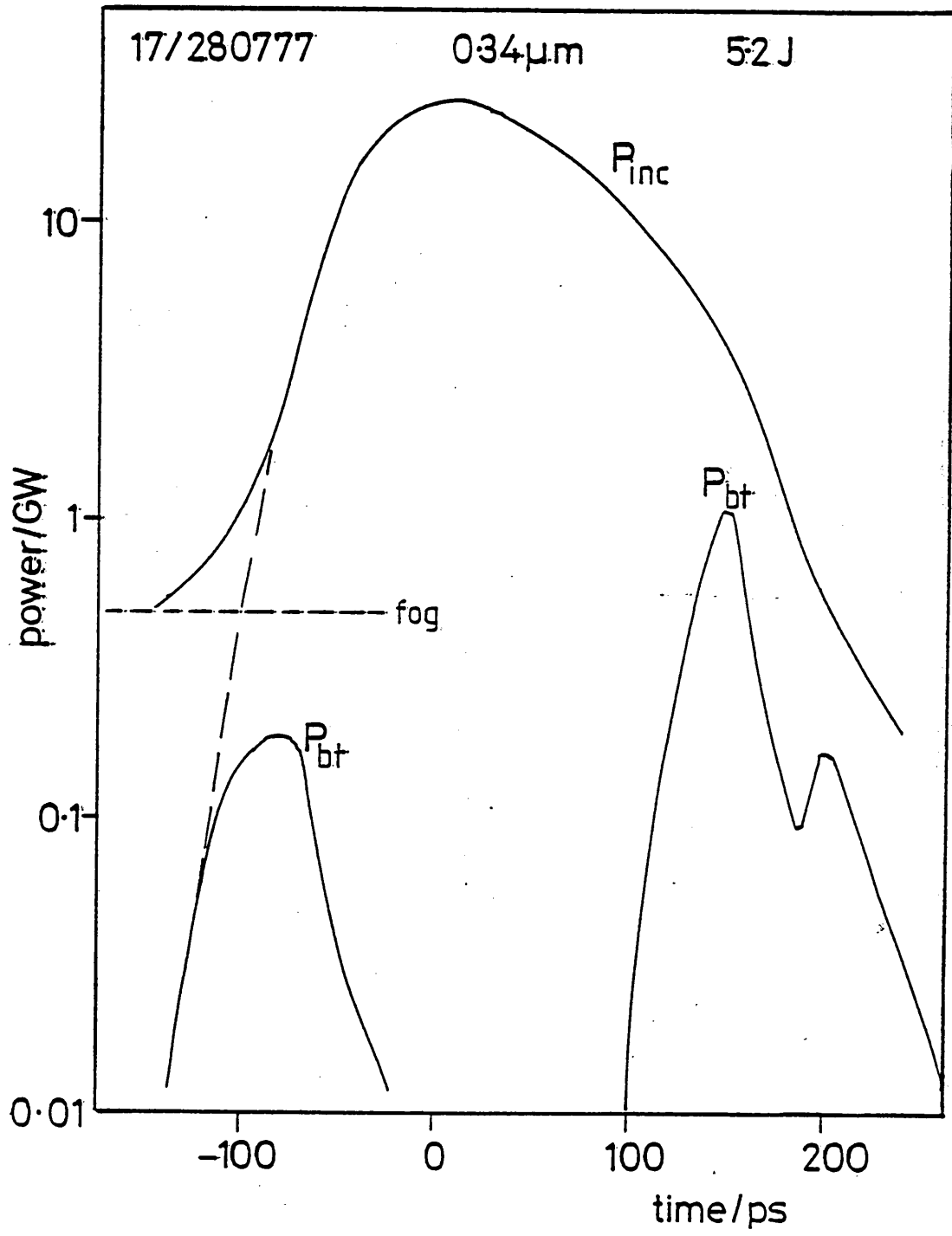
transmitted pulse

incident pulse

Fig 4.7 S1 streak picture for a 0.34 $\mu\text{m}$  foil showing transmission early in the pulse



Fig 4.7 continued; transmission curve



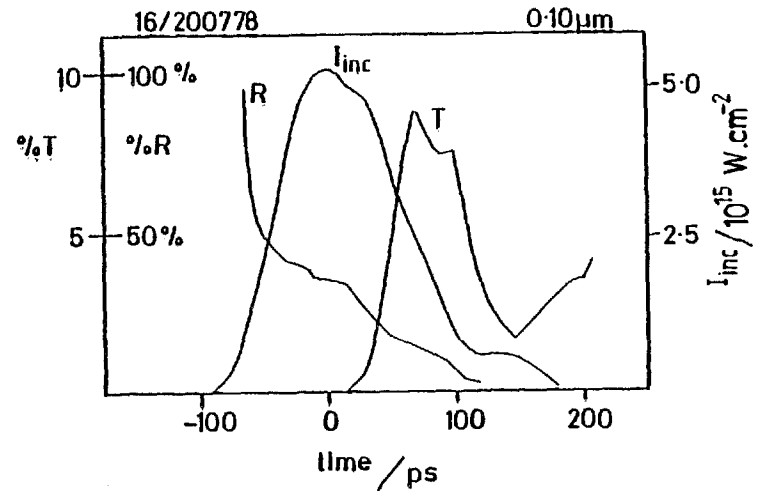
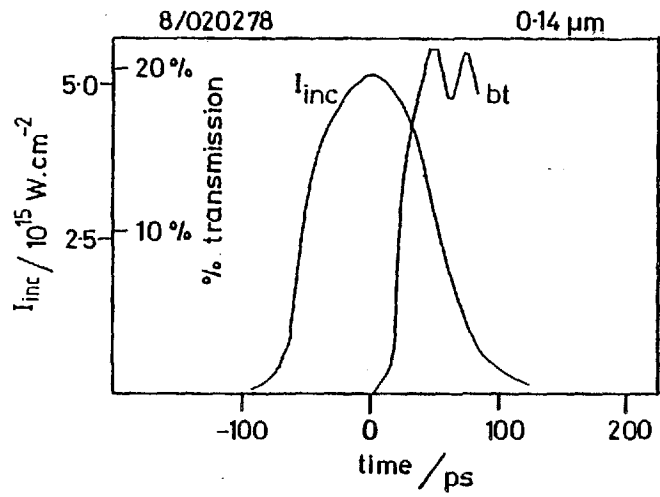
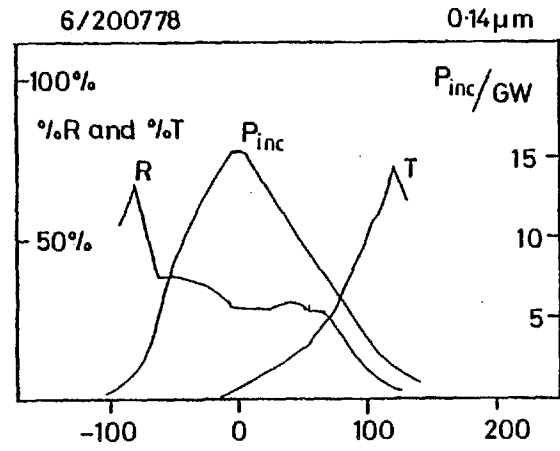
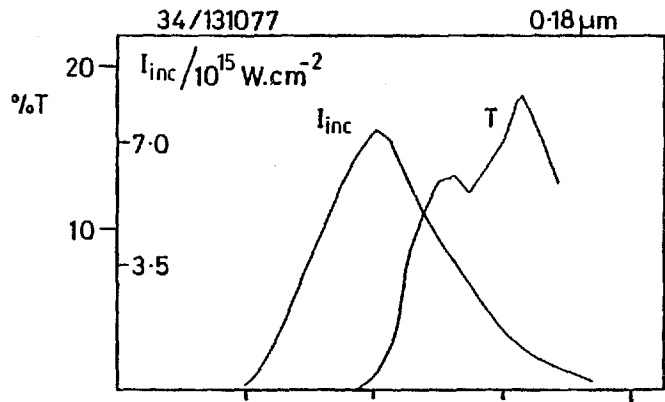


Fig 4.8 Examples of S1 data

(b) Time-resolved transmission and reflection

The 1.06  $\mu\text{m}$  light transmitted and reflected into the f/1 lenses was time-resolved by the S1 streak camera along with a fraction of the incident pulse.

An example of the data is shown in Fig. 3.34 with the transmission and reflection curves deduced from the densitometer scans of a number of streaks in Fig. 4.8. The data reduction procedure has been described in 3.6(c).

The transmission of 1.06  $\mu\text{m}$  light is observed to conform to the discussion of 4.2. Initially, the foil is transparent to the main laser pulse. However, this early transmission is usually not observable on the streak camera because of the limited dynamic range. The input beam to the streak camera must be filtered to give a correct exposure when the transmission is resumed near the peak of the pulse. The early transmission is then below the noise level (Fig. 4.6). This is not true when the foil is sufficiently thick ( $\lambda \approx 0.3 \mu\text{m}$ ) that burn through occurs late in the pulse. An example is shown in Fig. 4.7.

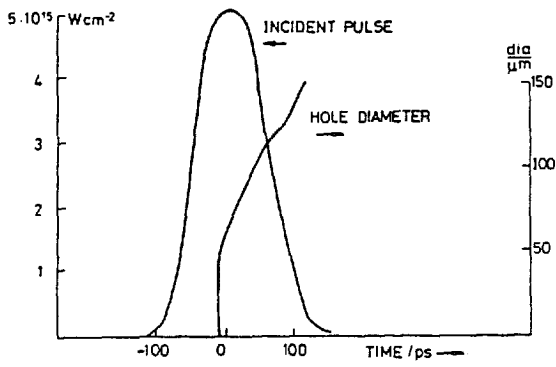
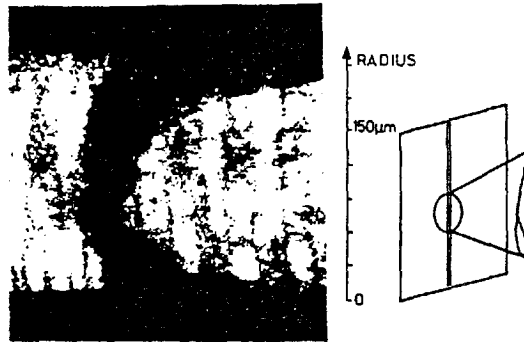
The main feature of the transmission characteristic is the onset in transmission associated with the plasma expansion and the concomitant reduction in density.

The backscattered  $\omega_0$  light peaks at  $\sim 90\%$  early in the laser pulse after the foil has become overdense, but is still present even after transmission has been resumed;  $\sim 10 - 20\%$  of the incident power is backscattered at this time. In 5.9, this anomalous reflection is identified as Brillouin backscatter.

Thin foils ( $0.05 - 0.08 \mu\text{m}$ ) begin to transmit at around the peak of the incident pulse ( $I_{\text{INC}} \sim 10^{15} - 10^{16} \text{ W cm}^{-2}$ ). Thicker foils begin to transmit later. Table 4.3 lists a number of shots with the time of transmission, defined by  $P_{\text{BT}} = 0.1 P_{\text{INC}}$ .

The 0.34  $\mu\text{m}$  foil shot (Fig. 4.7) became opaque at 100 ps before

SHOT 16 210778 0.08  $\mu\text{m}$  FOIL



EXAMPLE OF S20 STREAK CAMERA DATA

Fig 4.9

Table 4.3

Selection of 1.06 $\mu$ m burnthrough times defined by  $P(t_{bt})=0.1P_{inc}(t_{bt})$ 

SHOT	$E_{inc}$	Foil thickness	$t_{bt}$ / ps	Prepulse energy / $E_{inc}$
17/280777	5.2 J	0.34 $\mu$ m	+ 150	$10^{-5}$
32/131077	3.6	0.18	+ 15	$10^{-5}$
34/131077	3.4	0.18	+ 35	$10^{-5}$
7/020278	2.9	0.14	- 20	$10^{-4}$
8/020278	2.1	0.14	+ 20	$10^{-6}$
6/200778	1.8	0.14	+ 30	$3 \cdot 10^{-6}$
11/200778	1.8	0.10	+ 40	$3 \cdot 10^{-6}$
16/200778	2.4	0.10	+ 75	$2 \cdot 10^{-6}$
6/210778	1.0 approx	0.05	- 70	$3 \cdot 10^{-6}$

Shot number	Foil thickness / $\mu\text{m}$	$I_{\text{max}} / \text{W cm}^{-2}$	Prepulse energy / $E_{\text{inc}}$	$t_{\text{op}}$	$t_{\text{bt}}$	$t_{\text{bt}} - t_{\text{op}}$
8/20o778	0.14	$3 \cdot 10^{15}$	$2 \cdot 10^{-6}$	-116	82	198
10/200778	0.14	$1 \cdot 10^{16}$	$3 \cdot 10^{-6}$	-140	-8	132
8/210778	0.05	$3.4 \cdot 10^{15}$	$9 \cdot 10^{-6}$	-90	-24	66
11/210778	0.05	$3.5 \cdot 10^{15}$	$4 \cdot 10^{-6}$	-91	-40	51
13/210778	0.05	$1 \cdot 10^{16}$	$6 \cdot 10^{-6}$	-151	189	62

Table 4.4 Variation of opacity and burnthrough times on  $I_{\text{inc}}$   
Times  $t_{\text{op}}$  and  $t_{\text{bt}}$  are measured from the incident pulse peak in picoseconds

the peak of the 140 ps FWHM pulse. The irradiance on target was then  $1.3 \cdot 10^{13} \text{ W cm}^{-2}$ .

Increasing the irradiance results in earlier burn through whereas larger prepulses ( $> 10^{-5} E_{\text{INC}}$ ) delay burn through.

Further examples of transmission and reflection data are given in Fig. 4.8.

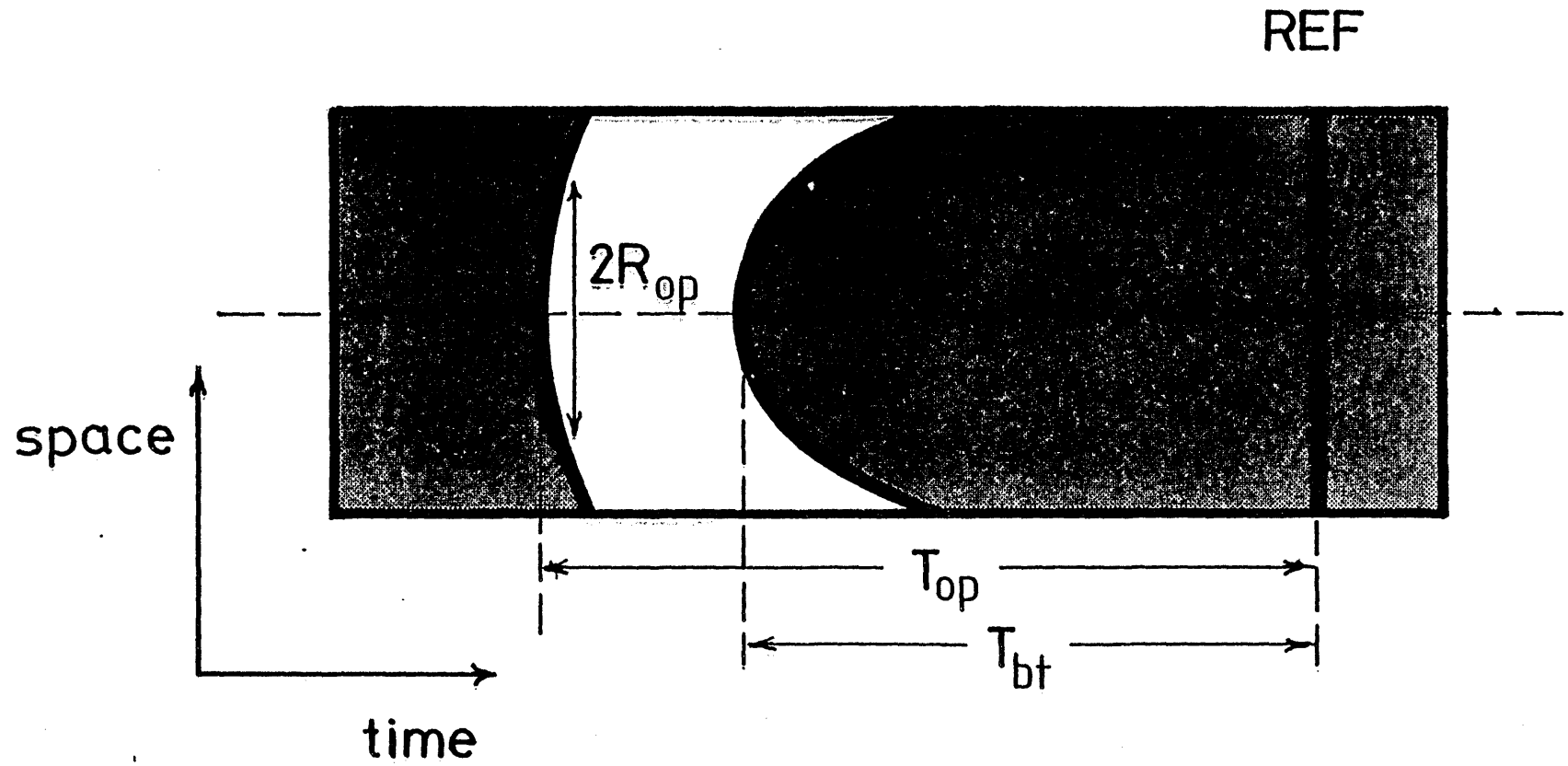
The principal observations are;

- (i) The transmission into the rear lens is only 10 - 20% immediately after burn through and often remains at this level throughout the remainder of the pulse. This may be due to scattering out of the lens cone or to absorption (5.2).
  - (ii) There is finite backscatter after the critical surface has dispersed.
  - (iii) The times with respect to the incident pulse at which opacity and transmission occur are dependent upon irradiance, prepulse level and foil thickness. Comparison can be made with the S20 data (5.1).
- (c) Time-resolved back-lighting measurements

The back-lighting diagnostic provided time and space resolved information on the transparency of the target to ruby light during irradiation by the  $1.06 \mu\text{m}$  pulse. An example of the data is shown in Fig. 4.9, with the accompanying measurements of the burn through hole diameter as a function of time. The general shape of the picture is seen to conform to the discussion of 4.2.

The foil is initially transparent and only the mode beating in the ruby pulse can be seen. Approximately one pulse width before the arrival of the neodymium pulse, the foil becomes opaque on the laser axis. This happens at  $t = -90 \text{ ps}$  for shot 16/210778 where all times are measured from the peak of the incident pulse. Opacity, as measured by the S20 streak camera, corresponds to an attenuation of 0.2 - 0.05 for the back-lighting, depending on the irradiance of the ruby light at

Fig 4.10 Principal observables on the S20 streaks.





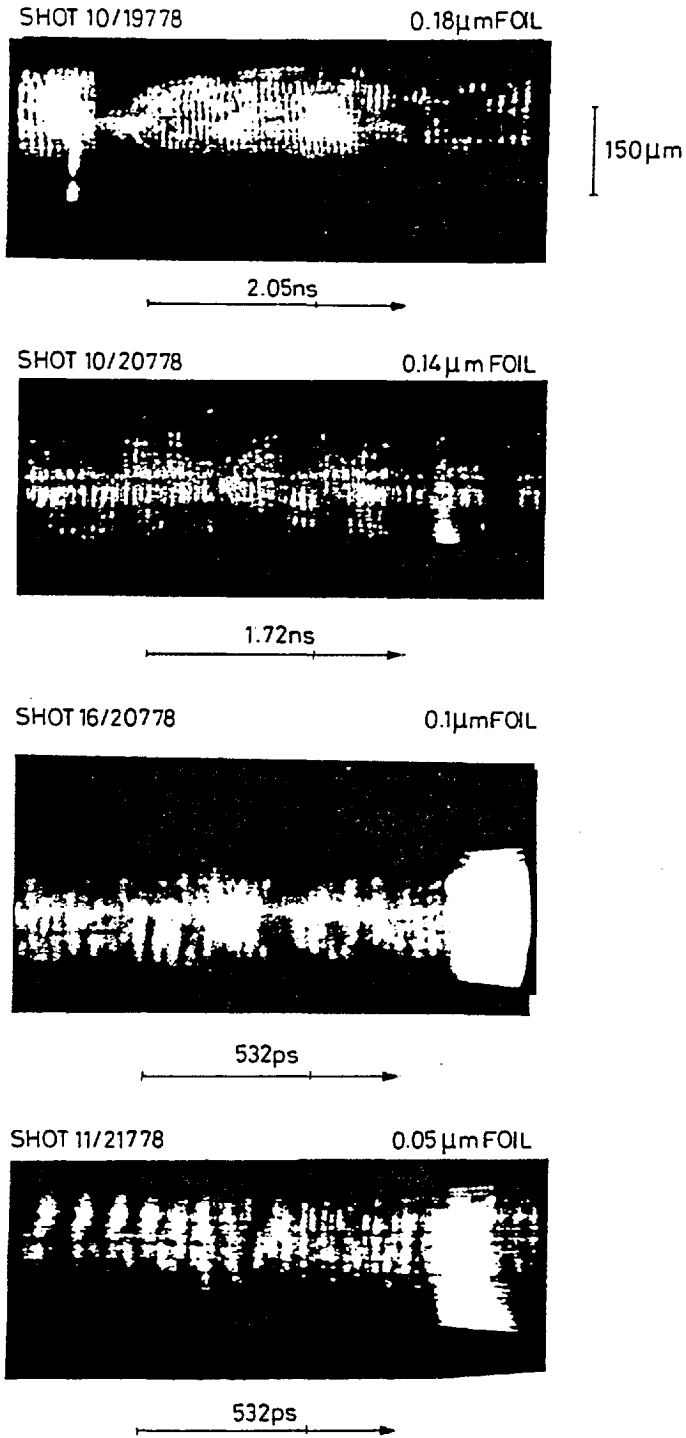


Fig 4.11 Examples of S20 streak pictures, showing variation with foil thickness

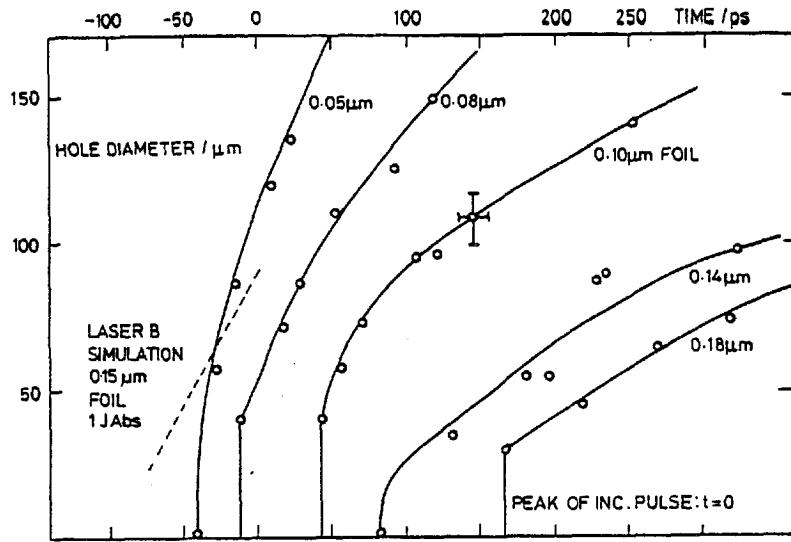


Fig 4.13 DIAMETER OF HOLES BURNT IN THIN POLYSTYRENE FOILS AS A FUNCTION OF TIME. -30 μm DIAMETER FOCAL SPOT,  $I = 2 \cdot 10^{15} \text{ W cm}^{-2}$ .

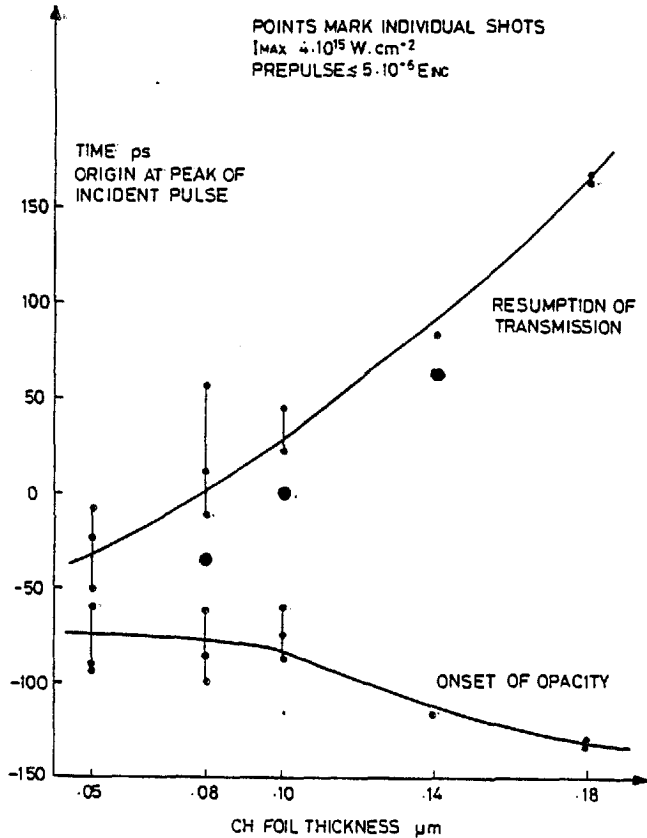


Fig 4.12 DURATION OF HIGH OPACITY TO RUBY BACK LIGHTING AS A FUNCTION OF FOIL THICKNESS

MEDUSA predictions (●) ; see 5.7

the target and the signal level at the streak camera. For the example shown (Fig. 4.9) the ruby beam must be attenuated by  $\sim 0.06$  for zero signal on the streak picture.

At  $t = -90$  ps, the incident  $1.06 \mu\text{m}$  irradiance is  $6 \cdot 10^{13} \text{ W cm}^{-2}$  and approximately  $10^{-3} E_{\text{INC}}$  has been delivered to the target (not necessarily all absorbed). These figures are derived from the S1 data (Fig. 4.8).

At a later time ( $t = +40$  ps), the streak picture shows the foil beginning to transmit on axis. The diameter of the transmission region is measured as a function of time; the data reduction procedure has been discussed in 3.6. At the onset of transmission, the hole diameter is  $40 \pm 10 \mu\text{m}$ , corresponding to the focal spot size. By  $+250$  ps, the diameter is  $140 \pm 10 \mu\text{m}$ .

The principal observables were (Fig. 4.10);

- (i) the times of onset of opacity and transmission on axis, relative to the incident pulse,
- (ii) spreading of opaque region (radius as a function of time),
- (iii) spreading of transmission region (radius as a function of time).

The main variable parameters were the incident pulse energy, foil thickness and prepulse level.

In principle, the fractional transmission of the ruby light is measurable after burn through. However, this was not possible in practice because of the rapid variations in the back-lighting level, due to mode beating. The back illumination level was fixed by the requirement that the streak camera photocathode was not to be over-exposed; a d.c. light source can generate unacceptable noise in the streak tube and intensifier. This resulted in only a factor of  $\sim 5$  between maximum signal and noise. These difficulties do not interfere with the data if the streak pictures are considered as on/off measurements of transmission. Therefore, in general, the S20 data is used only to give the

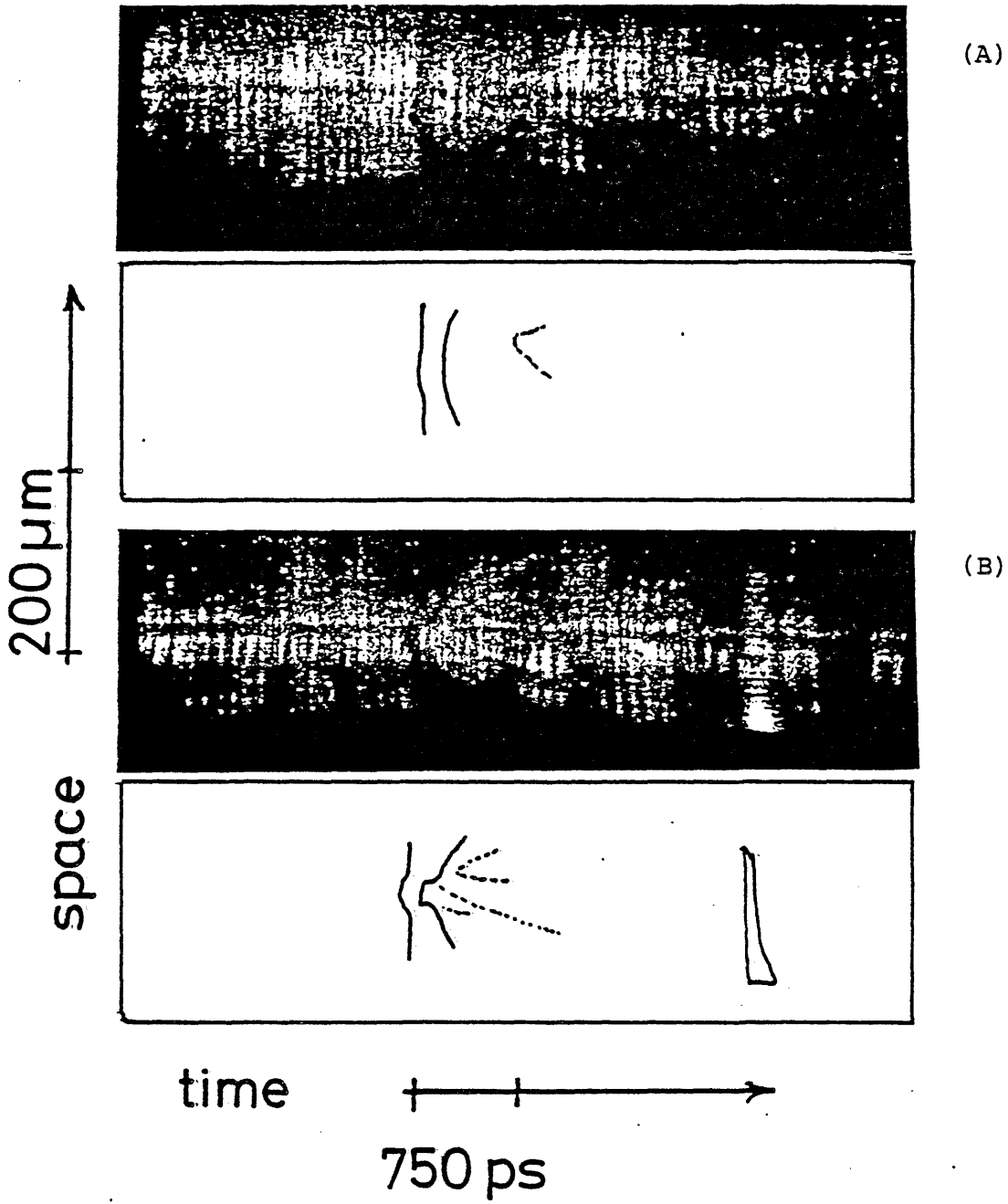


Fig 4.14 S20 streak pictures for a low and a high irradiance shot

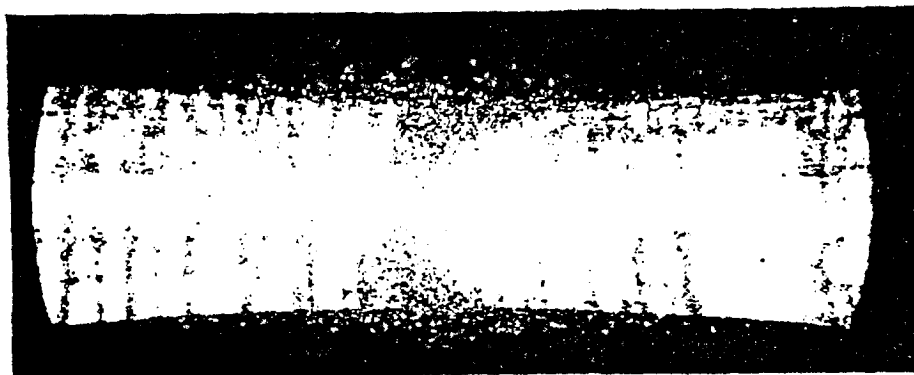
Shot A 9/200778 0.7J

Shot B 10/200778 10.5J

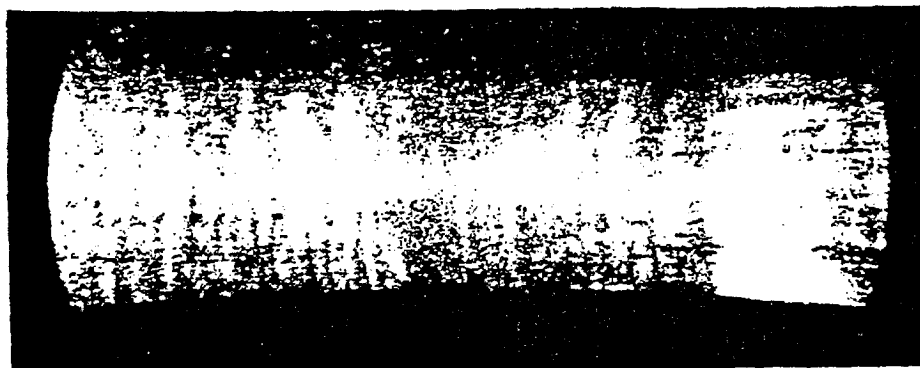
Shot number	Foil thickness / $\mu\text{m}$	$I_{\text{max}} / \text{W cm}^{-2}$	Prepulse energy / $E_{\text{inc}}$	$t_{\text{op}}$	$t_{\text{bt}}$	$t_{\text{bt}} - t_{\text{op}}$
17/210778	0.08	$3 \cdot 10^{15}$	$2 \cdot 10^{-6}$	-76	12	88
20/210778	0.08	$4 \cdot 10^{15}$	$3 \cdot 10^{-5}$	-73	44	117
22/210778	0.08	$4 \cdot 10^{15}$	$1 \cdot 10^{-4}$	-66	60	126
21/210778	0.08	$3 \cdot 10^{15}$	$1.2 \cdot 10^{-4}$	no opacity		

Table 4.5 Variation of opacity and burnthrough times on prepulse level

Times  $t_{\text{op}}$  and  $t_{\text{bt}}$  are measured from the incident pulse peak in picoseconds



(A)



(B)



(C)

Fig 4.15 S20 streak pictures for shots with different prepulses;

A	Shot 17	prepulse energy = $2 \cdot 10^{-6}$	$E_{inc}$
B	20	$3 \cdot 10^{-5}$	
C	22	$1 \cdot 10^{-4}$	

All shots taken on 210778

contours of onset of opacity and transmission. Further information on fractional transmission can be derived in certain cases.

The S1 data provides fractional transmission measurements for the neodymium pulse. Reference pulses allow the S1 and S20 sets of data to be synchronised to  $\pm 20$  ps. A more accurate synchronisation is possible by considering certain data shots with plausible assumptions about the target behaviour (5.1).

Further examples of the S20 streak pictures are given in Fig. 4.11. As can be seen from the streaks themselves, the times for which foils are opaque are dependent upon foil thickness; this is shown in Fig. 4.12. Variation of the incident power also affects times of opacity and transmission as indicated in Table 4.4. However, for thinner foils ( $0.05 - 0.08 \mu\text{m}$ ), increasing the incident power does not change the duration of the opaque period.

The spreading of the opaque region early in the incident pulse is independent of foil thickness but is modified by an increase in the power on target. Fig. 4.14 shows two streaks for shots with  $E_{\text{INC}}$  differing by a factor of 15. The high energy shot causes the foil to become opaque early on axis but the opaque region remains localised in the focus region for  $\sim 75$  ps. This does not happen in the low energy shot.

Increasing the prepulse energy affects the duration of opacity as illustrated in Table 4.5 for  $0.08 \mu\text{m}$  foils. The duration of opacity increases with a rise in prepulse energy up to  $\sim 300 \mu\text{J}$  ( $10^{-4} E_{\text{INC}}$ ). For higher prepulse levels, the foil ceases to attenuate the backlighting beam (by more than 0.5) at any time; that is, ruby light is not interrupted on the S20 streak picture. This is presumably because the prepulse destroys the foil without forming a critical density surface. The onset of transmission contours become blurred in the presence of

/200778 20mJ 0.1 $\mu$ m

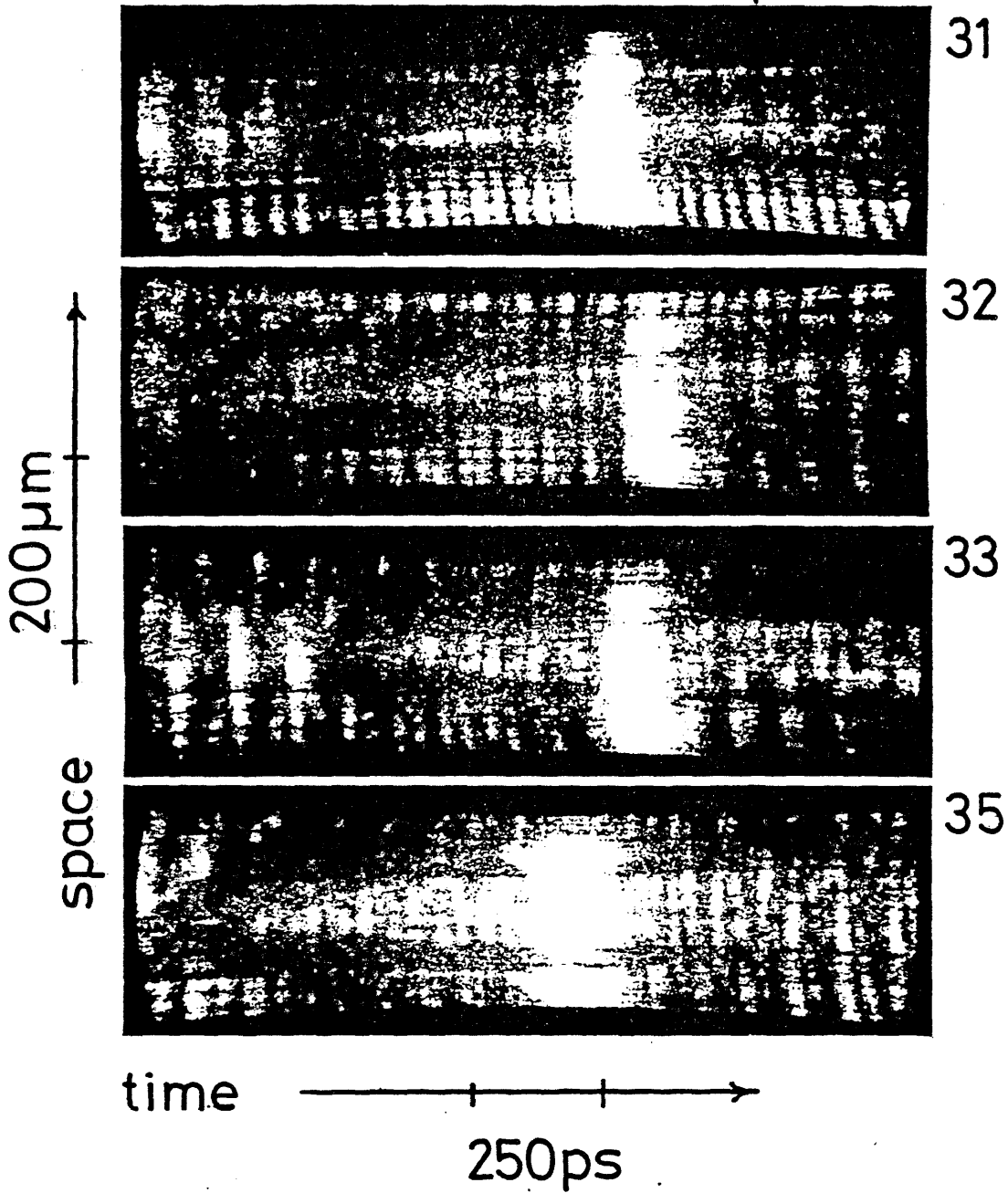


Fig 4.16 S20 streak pictures for low irradiance shots



<u>OBSERVABLE</u>	<u>DEPENDENCE ON</u>		
	<u>FOIL THICKNESS</u>	<u>INCIDENT POWER</u>	<u>PREPULSE</u>
Times of opacity and transmission	Yes	Yes	Yes
Duration of opacity	Yes	No, for thin foils	Yes
Spreading of opaque region	No	Yes	Yes
Spreading of transmission region	Yes	No	Yes

Table 4.6 Summary of Section 4.3(c)

Table 4.7 List of shots with S20 data available

SHOT NUMBER	$E_{\text{las}}/\text{J}$	FOIL/ $\mu\text{m}$	PREPULSE/ $10^{-6}$	$t_{\text{op}}$	$t_{\text{bt}}$	$(t_{\text{bt}} - t_{\text{op}}) / \text{ps}$
9/190778	3.7	0.18	4	-130	166	296
10/190778	3.8	0.18	2.8	-131	163	294
8/200778	2.3	0.14	2	-116	82	198
10/200778	10.5	0.14	2.5	-140	-8	132
15/200778	1.9	0.10		-60	22	82
16/200778	2.4	0.10		-87	44	131
17/200778	11.4	0.10		-73	19	92
33/200778	0.02	0.10		-50	146	196
8/210778	2.4	0.05	9	-90	-24	66
11/210778	2.6	0.05	4	-91	-40	51
12/210778	1.5	0.05		-59	-7	52
13/210778	8.4	0.05	6	-151	-89	62
16/210778	2.5	0.08	1.7	-99	-11	88
17/210778	2.4	0.08	2	-76	12	88
19/210778	2.5	0.08		-52	56	108
20/210778	2.7	0.08	30	-73	44	117
21/210778	2.3	0.08	120	no opacity		
22/210778	2.9	0.08	100	-66	60	126

larger prepulses. This is illustrated in Fig. 4.15.

The observations of the preceding paragraphs are qualitatively summarised in Table 4.6. The statistical significance of the observations can be gauged from the complete list of S20 data shots given in Table 4.7.

(d) Subsidiary diagnostic measurements

Measurements of the electron temperature were made using a filtered diode array sensitive to the X-ray continuum emission from the target. Two diodes were fitted with absorber foils of fairly low cut-off energies (3.5 keV and 5.1 keV) so that the temperature associated with the thermal distribution was measured. The ratio of the transmitted intensities gave a temperature of 2 keV for shots with  $I_{\text{INC}} \sim 10^{15} \text{ W cm}^{-2}$  and 5 keV with  $I_{\text{INC}} \sim 10^{16} \text{ W cm}^{-2}$ . These measurements are accurate to  $\sim 20\%$ .

The prepulse monitor detected partial switch-out of a preceding mode-locked pulse (these shots were discarded), inter-pulse noise and modification to the leading edge of the main pulse (3.2). The larger of the final two sources is called the prepulse energy in this work.

Comparison between S1 and S20 data indicates that the foils become opaque at a time when the incident irradiance is  $\sim 10^{13} \text{ W cm}^{-2}$  (Fig. 5.5). In order to check this, foils were irradiated with low energy ( $\sim 20 \text{ mJ}$ ) shots and with ruby back-lighting. These shots (31-35/200778 in Table 4.7) gave peak irradiances  $\sim 10^{13} \text{ W cm}^{-2}$ . The foils became opaque over a small radius ( $\lesssim 100 \mu\text{m}$ ) with a longer duration of opacity on axis than observed at higher irradiances, presumably because expansion velocities were lower due to lower temperatures. Fig. 4.16 gives examples of the S20 streak pictures for these low irradiance shots.

Foils were irradiated also with  $10 \mu\text{J}$  pulses from the neodymium laser oscillator with all subsequent amplifiers unpumped. Occasional damage was sustained by foils under repeated irradiation. Damage and

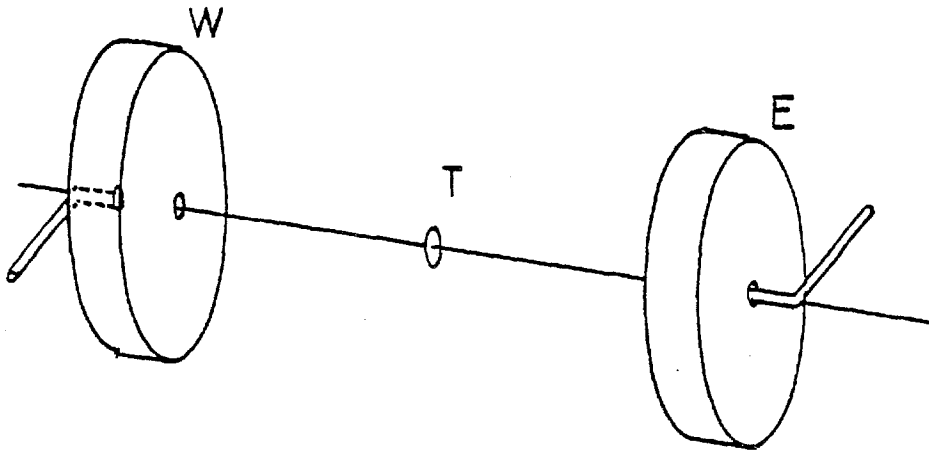


Fig 4.17 Ion probe supports

Back ion probe signal  
SHOT 020278/8:04 $\mu$  foil

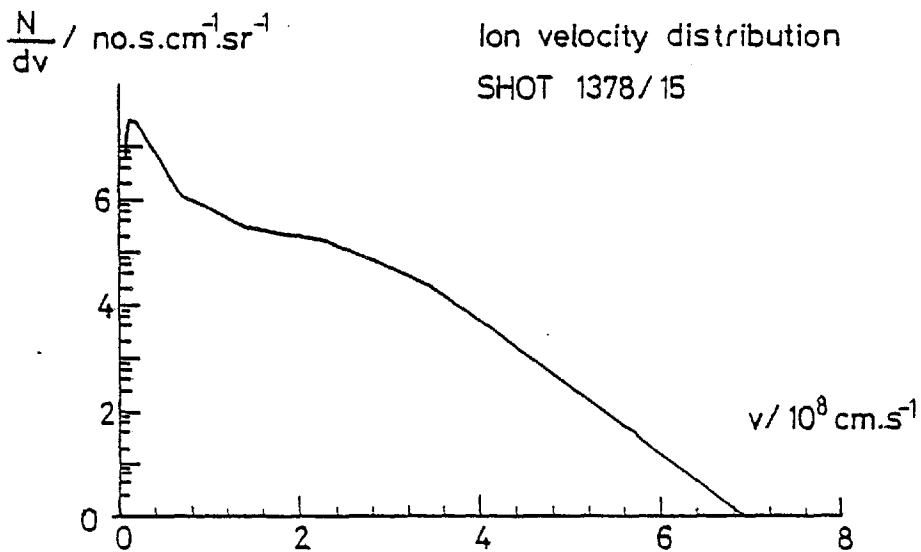
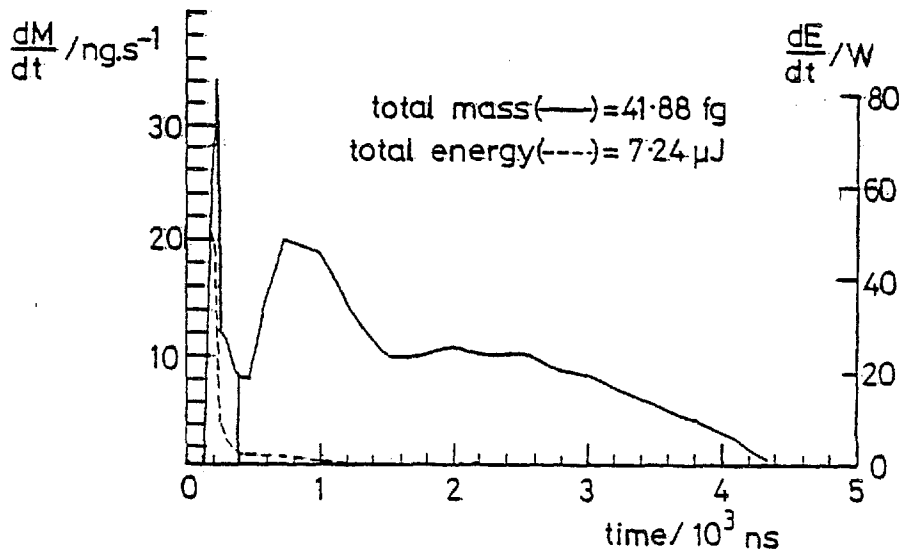


Fig 4.18 Examples of treated ion probe data

opacity thresholds are discussed further in 5.4.

Pictures of the rear (transmission) lens plane are shown in Fig. 3.8. The horizontal lines are the mounting supports for miniature ion probes positioned in axial holes in the (SORO) lenses (Fig. 4.17). Two observations are; (i) the spreading of the transmission beam compared with the beam in the absence of a foil target. This can be matched with the scattered light diode measurements as in Figs. 3.13 and 4.5, (ii) the loss of information about the first (front) probe support after passage through the target. This is presumably due to spatial filtering in the target plane effected by the localised transmission region.

The ion probes gave typical (P2) double peaked signals indicating the presence of both slow ( $v_i < 10^8$  cm/s) and fast ( $> 10^8$  cm/s) components in the ion blow-off. Table 4.8 lists the total mass and energy recovered by probes situated on the laser axis and observing the target through holes in the main focussing lenses. Each charge collector was positioned 38 cm from the target and subtended an angle of  $\sim 2 \cdot 10^{-5}$  sr. The measurements are fairly reproducible with integrated total recovered energies in the range 10 - 15%  $E_{LAS}$ . These absorption estimates are based on the assumption that the half maximum full width angles of the ion plumes are  $20^\circ$ . The presence of a prepulse softens the ion velocity distribution and results in a lower absorption ( $\sim 5\%$ ).

The angular distribution of the ion blow-off was measured on an earlier run with an array of off-axis collectors. The figure of  $20^\circ$  was deduced from the data, but is accurate to only about  $\pm 10^\circ$  because ion probes were not placed within the lens cones except on axis.

For shots 15 and 23/131077 (0.13  $\mu\text{m}$  foils), the total mass recovered as fast ions corresponds to a foil area of 42  $\mu\text{m}$  diameter. The total mass of fast and slow ions corresponds to 170  $\mu\text{m}$  diameter. These figures are based on an assumed M/Z of 1.75. Examples of ion traces are shown in Fig. 4.18.

SHOT	$E_{\text{las}}$ / J	Front or back	$m_{\text{T}}$ / fg	$E_{\text{T}}$ / $\mu\text{J}$	$m_{\text{F}}$ / $m_{\text{T}}$	$E_{\text{F}}$ / $E_{\text{T}}$
7/170278	4.4	F	61.8	4.1	6.3 %	68.6 %
0.14 $\mu\text{m}$ foil		B	38.1	5.2	4.3	45.4
8/170278	3.1	F	41.9	7.2	11.5	79.7
0.14 $\mu\text{m}$ foil		B	44.6	5.0	3.7	72.5
9/200278	2.7	F	55.3	3.2	1.1	31
0.14 $\mu\text{m}$ foil		B	19.7	1.4	2.6	18.3
3/220278	6.4	F	66.7	6.7	10.3	79
0.14 $\mu\text{m}$ foil		B	63.5	16.6	11.3	80
4/230278	5.6	F	72.7	7.6	8.8	79.1
		B	62.9	21.1	13.7	85
5/240278		F	61.7	2.71	1.1	25
		B	51.5	11.9	12.6	78.2

Table 4.8

Ion Probe Data

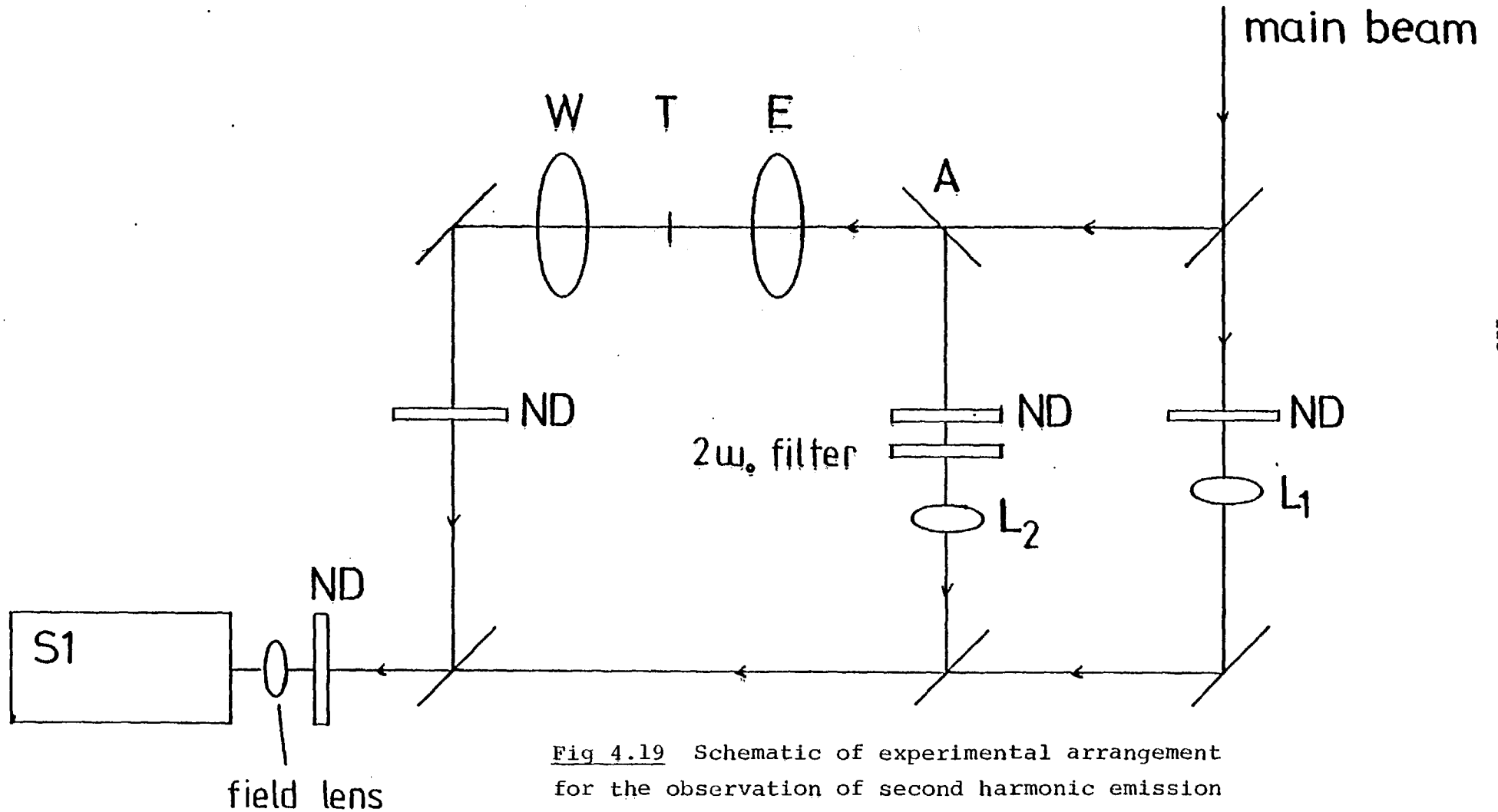


Fig 4.19 Schematic of experimental arrangement for the observation of second harmonic emission from thick foil targets

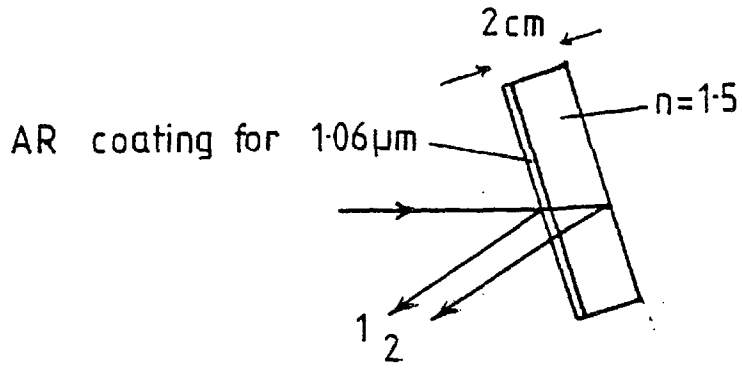


Fig 4.20 Coated beam splitter marked A in Fig 4.19

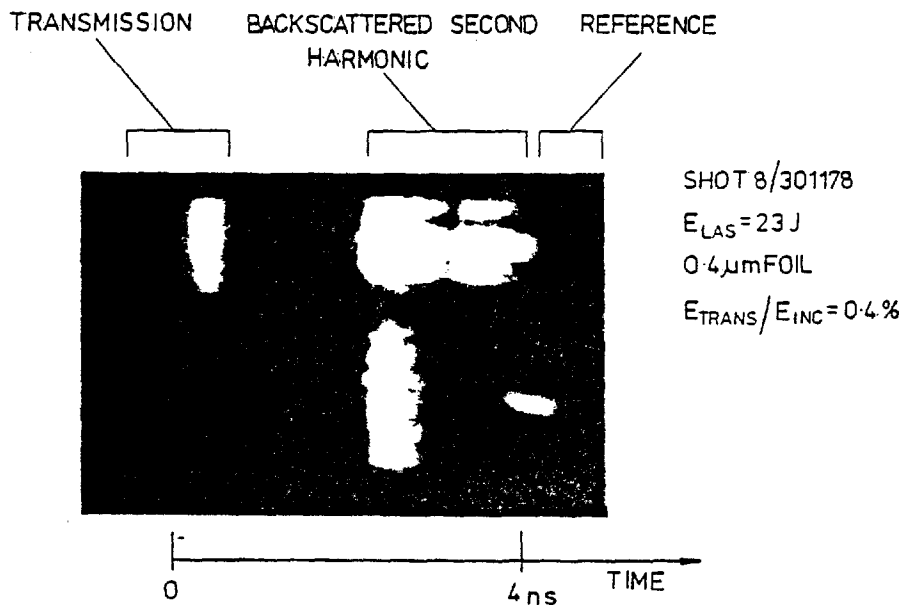


Fig 4.21 Example of S1 streak picture



#### 4.4 Second Harmonic Generation from Thick Foil Targets

As part of a separate harmonic spectroscopy experiment, polystyrene foils of thickness 0.08 - 0.7  $\mu\text{m}$  were irradiated by 100 ps FWHM neodymium laser pulses of irradiance  $\sim 3 \times 10^{16} \text{ W cm}^{-2}$ . The EPL S1 streak camera (3.6) was used to temporally resolve the incident and transmitted 1.06  $\mu\text{m}$  light. In addition, backscattered light at 0.53  $\mu\text{m}$  was relayed to the S1 camera. The experimental arrangement is shown schematically in Fig. 4.19.

Although HA3 and interference filters may be used to separate the green backscattered light from the dominant 1.06  $\mu\text{m}$ , it is useful to have an independent check on whether the required discrimination is being achieved. In the configuration of Fig. 4.19 this could be done by using the relative reflectivities of the surface of the coated beam splitter marked A. The thickness, refractive index and angle of incidence of every beam splitter in the arrangement is known and so the time separation between the reflections at front and rear surfaces may be calculated. This allows the correct identification of the sources of double pulses on the streak pictures (Fig. 4.21); in particular, the double pulses from beam splitter A can be isolated. If this beam splitter is anti-reflection coated for 1.06  $\mu\text{m}$  on one face, the relative intensities of the front and rear reflections will switch when changing from 1.06 to 0.53  $\mu\text{m}$  (Fig. 4.20). In this way it can be verified that predominantly green light is reaching the streak camera.

The idea of the experiment is as follows. If the second harmonic light is generated at the critical surface (E2,C1), then when the incident pulse burns through the foil, the green backscattered light should switch off.

An example of the S1 streak data is shown in Fig. 4.21 with the corresponding power curves in Fig. 4.22. The data reduction follows the procedure outlined in 3.6(c).

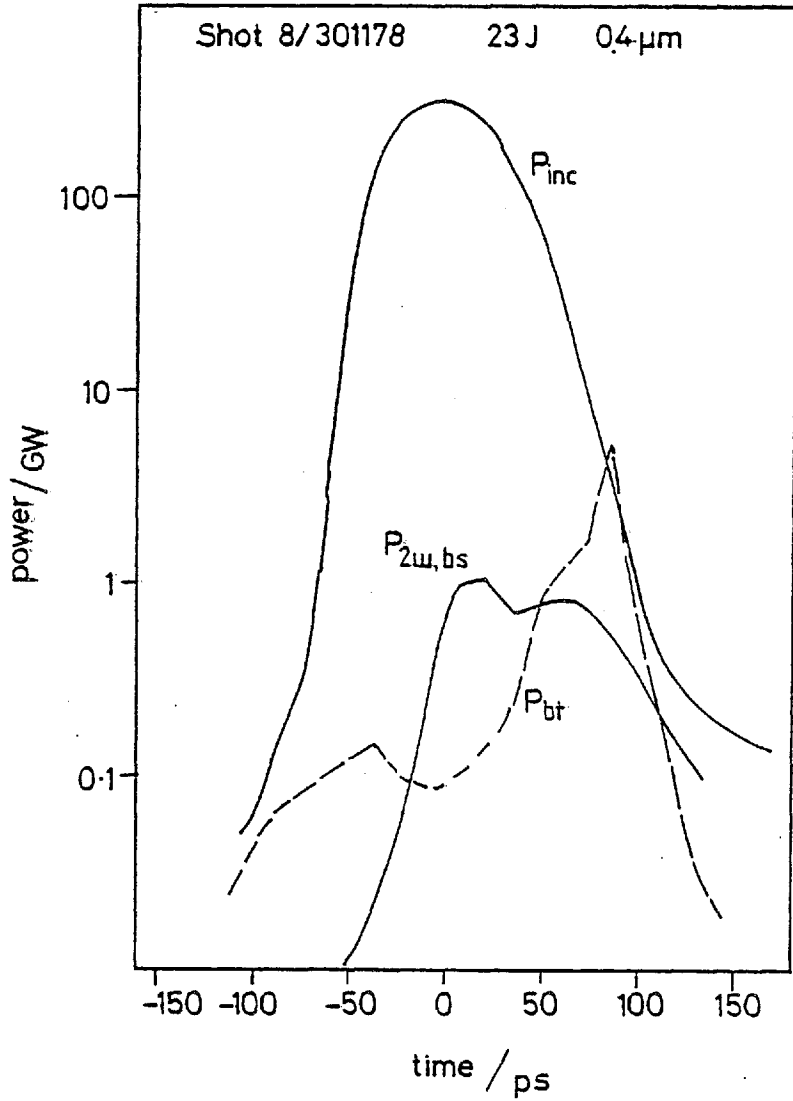


Fig 4.22 Power curves for the shot of Fig 4.21

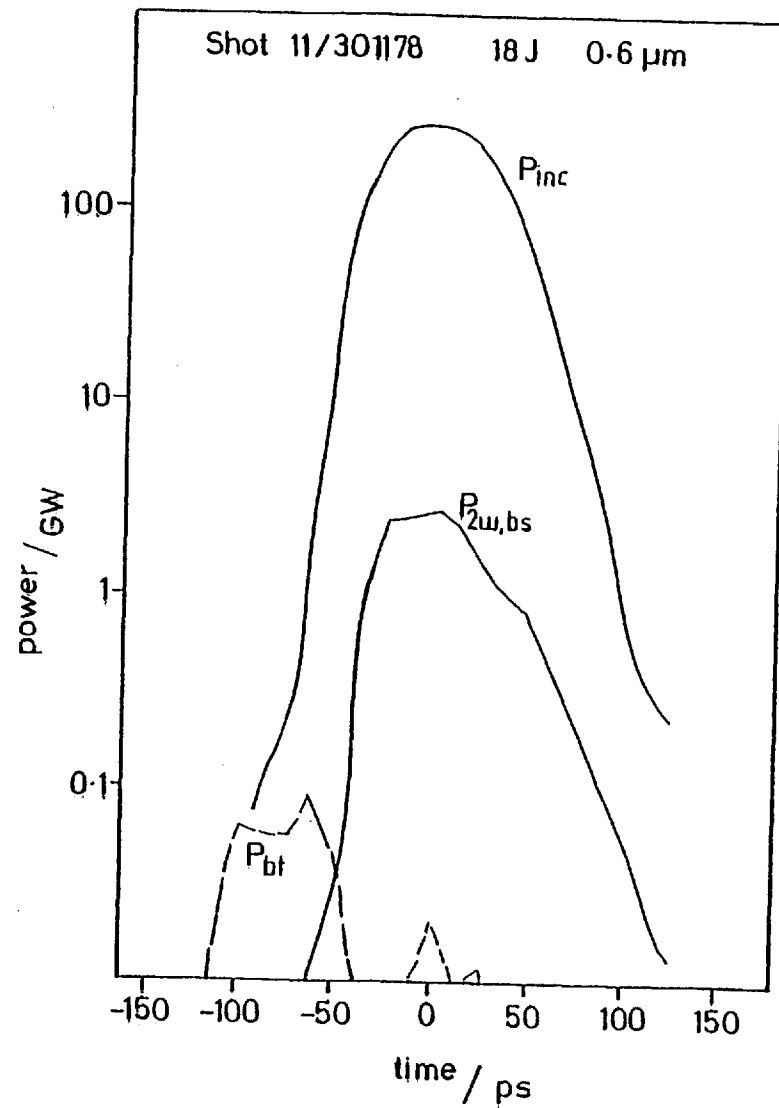
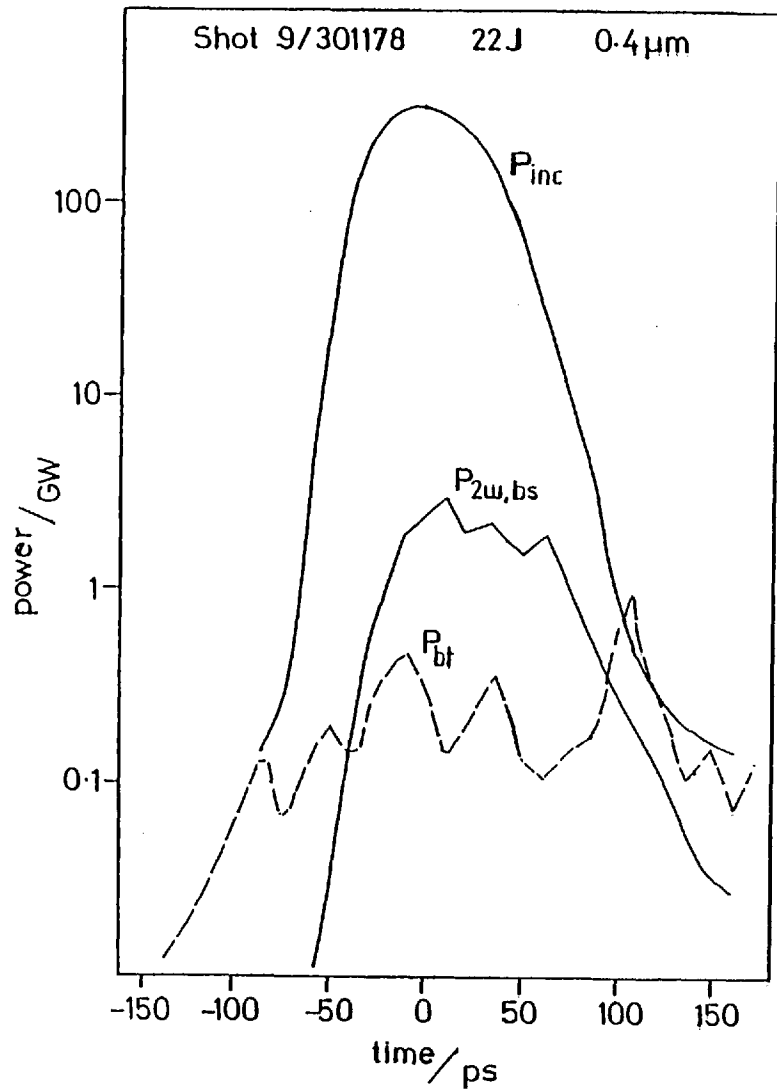


Fig 4.23 Further power curves from the second harmonic thick foil experiment

50  $\mu\text{m}$

space  $\longrightarrow$

13 / 020278

16

19

27

time  $\uparrow$   
250 ps

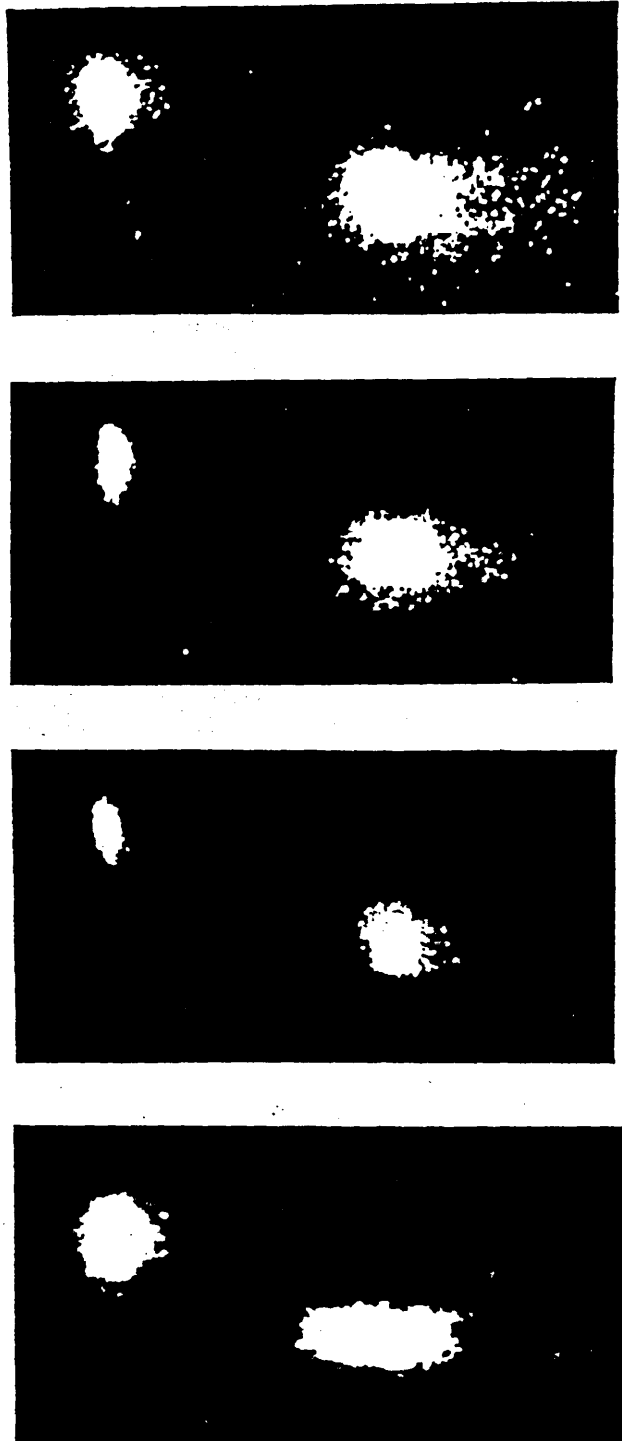


Fig 4.24

Examples of  $3/2 \omega_0$   
emission data

incident pulse  $\uparrow$

$3/2 \omega_0$  emission  $\uparrow$

Because the foils are thick (a choice governed by the requirements of an experiment running simultaneously), there is no clear onset of transmission until late in the tail of the incident pulse. The second harmonic reflected light switches on only after the transmission is attenuated consistent with the expected behaviour. However, there is seen to be small but finite transmission throughout the incident pulse. It is not clear if this is due to the higher irradiance levels leading to anomalous transmission (R7,S1) or if prepulse effects are playing a part. Unfortunately, prepulse data is not available for these shots; a level of  $\sim 10^{-6} E_{\text{INC}}$  is required to be sure that the target is intact for the main pulse. This condition corresponds to the same prepulse energy as indicated in 4.3 where a threshold of  $10^{-5} E_{\text{INC}}$  was inferred from the data; the main pulses were an order of magnitude smaller than in the green backscatter experiment.

Further curves are shown in Fig. 4.23 and display the same behaviour.

#### 4.5 Time and Space Resolved $\frac{3}{2} \omega_0$ Emission

A spin-off from an early thin foil run was the observation of plasma emission at  $\frac{3}{2} \omega_0$  (Fig. 2.10).

A 10 Å band pass filter centred on the ruby wavelength 6943 Å was used to observe light backscattered from the foil targets. Part of the blue wing of the  $\frac{3}{2} \omega_0$  emission at 0.71 μm was observed through this filter on the EPL S20 streak camera. This was expected on the basis of time-integrated spectra at  $\frac{3}{2} \omega_0$  (R6, Fig. 309). The streak camera provided space and time resolved measurements with resolution  $\sim 10$  μm and 20 ps respectively. A reference pulse was used to find the time of emission in the incident pulse.

Typical streak pictures are shown in Fig. 4.24. with shot details in Table 4.9. A densitometer trace along the time axis for a typical shot is shown in Fig. 4.25 and along the space axis in Fig. 4.26.

SHOT NUMBER	$E_{1as}/J$	FOIL THICKNESS/ $\mu m$	FILTER
13/020278	6.2	0.18	ruby ( 20A)
16/020278	4.2	0.18	ruby
19/020278	3.9	0.18	ruby
27/020278	6.3	0.10	$3/2\omega_0$ (50A)

Table 4.9 Shot details for data of Fig 4.24

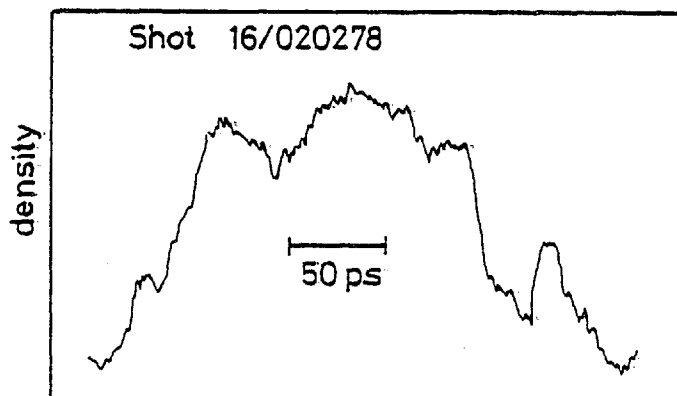


Fig 4.25 Microdensitometer scan along the time axis

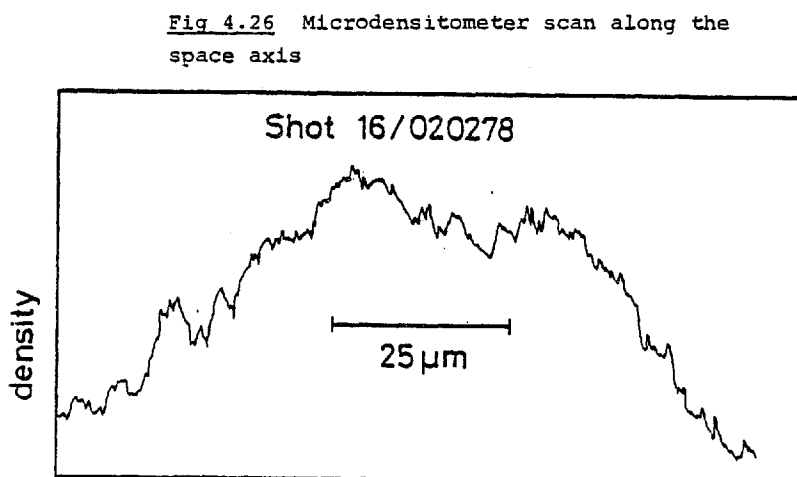


Fig 4.26 Microdensitometer scan along the space axis

The principal observations are

- (i) emission localised in the focal spot region
- (ii) emission occurs around the peak of the incident pulse
- (iii) there is small scale structure in the emission near the resolution limit of the detector.

Fig 5.1 Example of the synchronisation of the S1 and S20 data

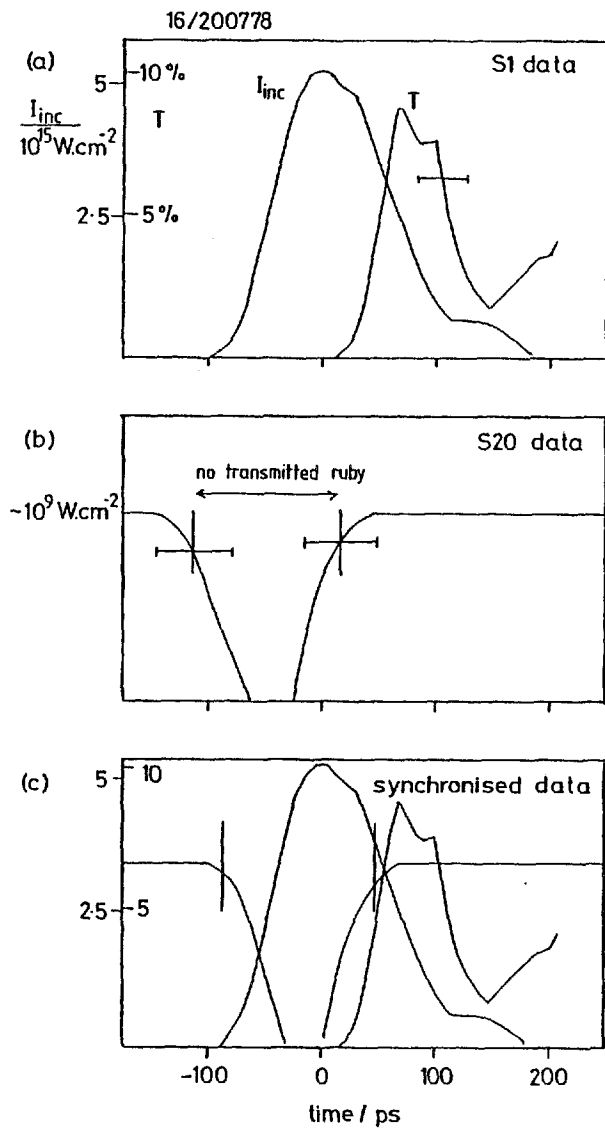
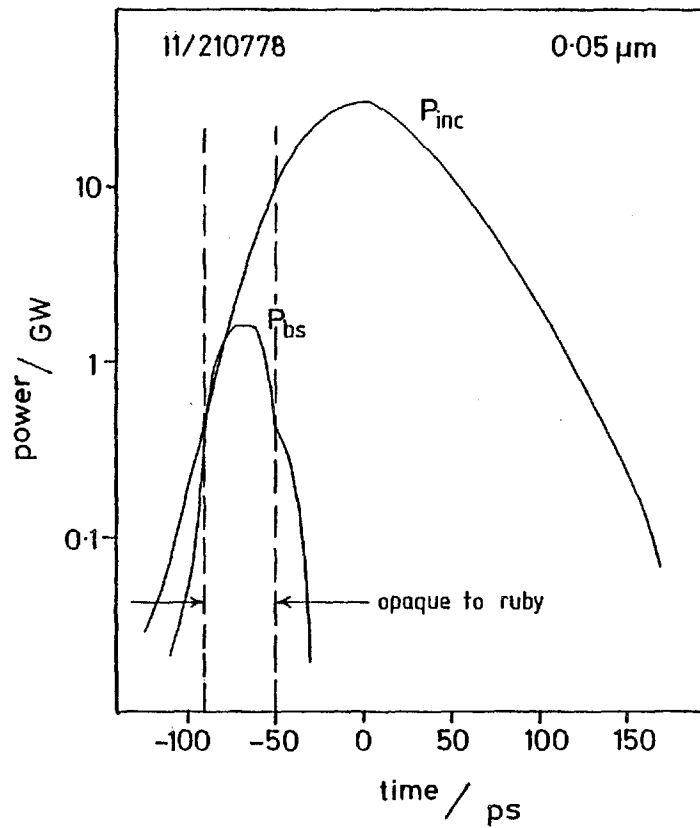


Fig 5.2 Shot with backscattered neodymium light and opacity to ruby backlighting





CHAPTER 5

DISCUSSION OF THIN FOIL DATA

A number of points are discussed arising from the observations presented in Ch. 4. A conclusion may be found in 5.11.

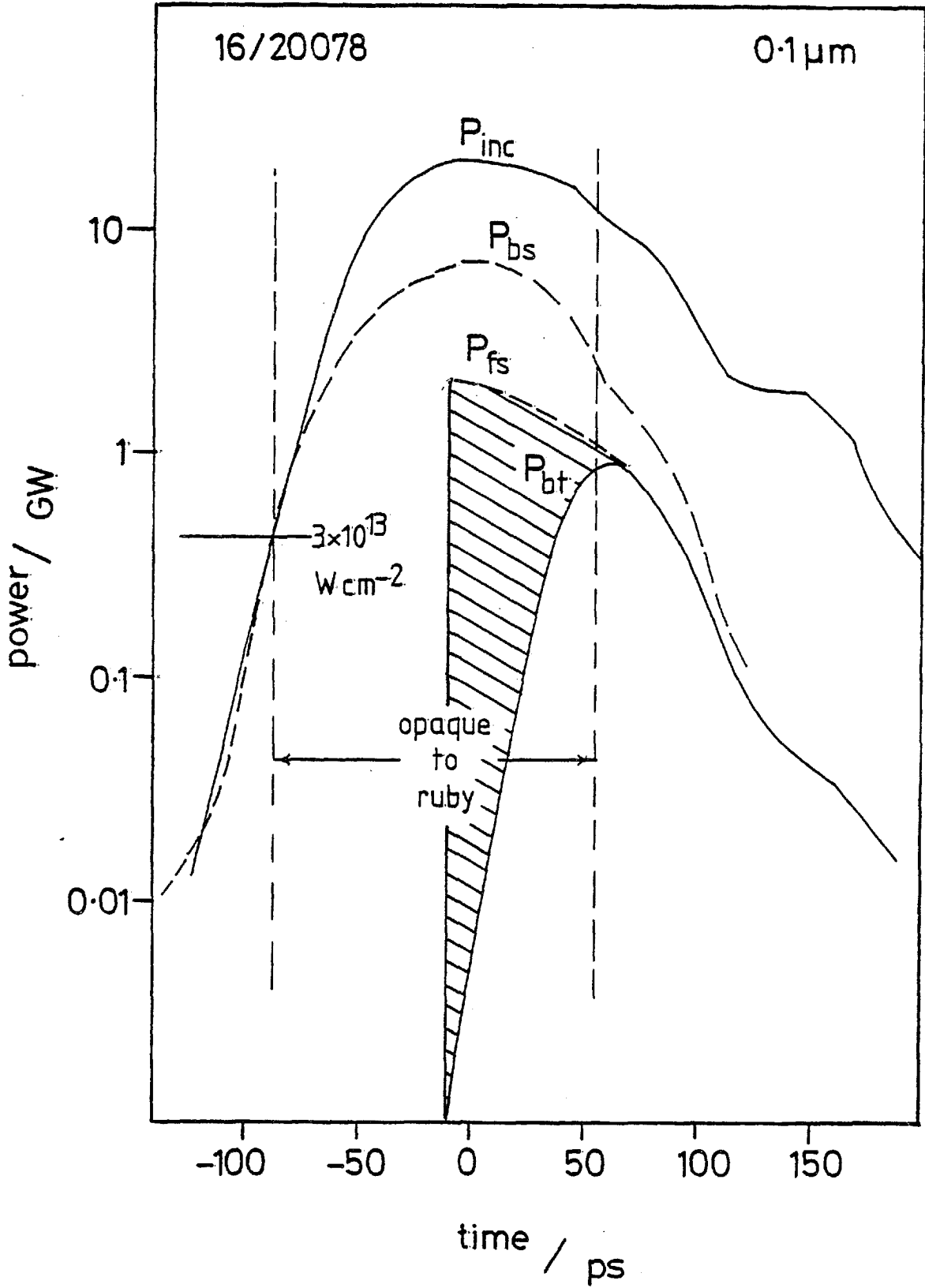
5.1 Comparison Between the S1 and S20 Data

The data provided by the S1 streak camera are presented in 4.3(b) and give the time at which the incident neodymium beam burns through the foil targets. The ruby back-lighting measurements, recorded on the S20 camera, are described in 4.3(c) and give the same burn through time for ruby light. In this section, the two measurements of the burn through time are compared.

Both sets of data are available on shot 16/200778 and the uncertainties in the reference pulse timing are shown in Fig. 5.1(a) and (b). It is seen that the error bar on the S20 timing has been shown larger than the S1 error. The larger uncertainty for the S20 data is due to the reference pulse being superimposed on the ruby back-lighting. The modulation in the back-lighting interferes with the identification of the reference pulse shape.

The net uncertainty in the synchronisation between the two measurements is  $\sim 50$  ps which is too long to allow meaningful comparisons to be made. However, on the basis of one assumption concerning the back-reflected light, an improved synchronisation can be obtained. Fig. 5.2 shows the S1 and S20 data for shot 11/210778. The back-reflected  $1.06 \mu\text{m}$  light is found to have approximately the same duration as the opaque period measured from the ruby back-lighting streak. In addition, the reflected light occurs approximately when the foil is opaque. The two sets of data may be shifted in time with respect to each other and

Fig 5.3 Proposed fraction of forward scattered radiation



within the error bar so as to centre the reflected light on the opaque period. Then, on the assumption that the back-reflected light occurs predominantly when the foil is opaque, the synchronisation can be improved to within  $\pm 15$  ps.

The data for shot 16/200778 have been synchronised on the basis of the above argument and the result is shown in Fig. 5.1(c). It is found that the implied time at which foils become opaque to ruby light is approximately equal to the time that  $1.06 \mu\text{m}$  light is severely attenuated by thick foil targets (Fig. 4.7). This increases our confidence in the synchronisation procedure; the ionization process is very rapid and wavelength differences may be neglected.

The time of onset of transmission is less clear cut, although the two beams appear to be transmitted at approximately the same time despite the differences in wavelength and irradiance level.

## 5.2 Fractional Energy and Power Transmission

Time-integrated transmission measurements are presented in 4.3(a). In this section the measurements are compared with data from other laboratories. This is followed by a discussion of the fractional power transmission with an examination of the amount of light scattered outside the rear collection lens.

Transmitted energy measurements for low prepulse shots (Fig. 4.3) are consistently lower than the Ecole Polytechnique data, reproduced from Ref. A3 in Fig. 4.3. In addition, increase in the prepulse level has been observed to give rise to increased transmission (Table 4.1). We attribute the different transmission figures of Ref. A3 to a larger prepulse level; similar laser pulses and collection optics ( $f/1$ ) were used in the two experiments.

Backscattered energy measurements (Fig. 4.3) are also slightly lower than reported in Ref. A3. The presence of a larger prepulse would

tend to increase Brillouin backscatter because of the generation of longer scale length coronas.

In Ref. P2, 0.11  $\mu\text{m}$  thick foils were irradiated with 50 ps pulses. Transmission is observed to be 4% at  $I_{\text{INC}} = 10^{13} \text{ W cm}^{-2}$  and 0.5% at  $I_{\text{INC}} = 10^{14} \text{ W cm}^{-2}$ . However, Fig. 4.3 shows that the transmission is a few percent up to  $2 \cdot 10^{15} \text{ W cm}^{-2}$  for 100 ps pulses. The Pearlman and Anthes measurements may be affected by the small collection solid angle for the transmitted light.

Malone, McCrory and Morse (M4) observed  $\sim 50\%$  transmission through 0.04  $\mu\text{m}$  foils with pulses of only 25 ps FWHM. On the basis of the measurements of Fig. 4.3, the data of M4 seem high, but no direct comparison can be made.

The time dependence of transmitted light was monitored by the S1 streak camera, as described in 4.3(b). Perhaps the most unexpected result of these measurements is that, after burn through, the power transmitted into the rear lens is generally only a fraction ( $\sim 20\%$ ) of the incident power. This is true out to the tail of the incident pulse when the transmission region has large diameter ( $>100 \mu\text{m}$ ). There are two possible explanations for this;

- (i) the transmitted beam suffers scattering so that most of the light is scattered outside the f/1 collection cone,
- (ii) the incident laser light suffers considerable absorption while traversing the underdense plasma.

The discussion which follows is aimed at deciding which explanation is correct.

The light scattered outside the lens was measured by the diode array and integration of the distribution gives the total forward scattered energy. Taking shot 16/200778 as an example, the analysis gives,

Energy scattered into rear lens	3.0%
Forward scattered energy	7.4%
Total	<u>10.4%</u>

If the foil begins to transmit abruptly at 100%, then the 10.4% transmission implies a burn through time of +75 ps. This figure is obtained by integrating under the  $P_{INC}$  curve (Fig. 5.3) generated by the S1 reference pulse. The fact that transmitted 1.06  $\mu\text{m}$  light is observed as early as -10 ps, means that the experimental data does not support an abrupt and sharp onset of transmission (as assumed in the analysis of Ref. G4 for example). The direct implication is that transmitted light suffers absorption in the underdense plasma.

A complete diagnosis of the transmitted light requires a time-resolved measurement of the light scattered outside the rear lens in addition to the measurements described in Ch. 4. Unfortunately, only time-integrated measurements of the scattered light are available. However we may proceed with a simple model which is suggested by an observation noted in 4.3(d). The forward scattered light is polarization dependent, whereas the light transmitted into the lens is not. This suggests that the forward scattered light is transmitted when the burn through hole is small. This is because at this time, the presence of a critical surface gives rise to resonance absorption which is polarization dependent and radial density gradients lead to strong refraction. The light transmitted into the lens occurs mostly when the burn through hole is large, and so no polarization dependence is observed. It is proposed, therefore, that the forward scattered light occurs in a wide angle burst just at the onset of transmission. Subsequent incident radiation is transmitted mainly into the lens. Absorption takes place for both the scattered and transmitted light.

It can be checked whether or not the available experimental data

Table 5.1

ENERGY BALANCE FOR SHOT 11/210778

Foil thickness = 0.05 $\mu$ m  
 $I_{inc} = 3.5 \cdot 10^{15} \text{ W cm}^{-2}$   
 Prepulse =  $4 \cdot 10^{-6}$

Transmitted into rear f/l lens	37 - 41 %
Reflected and backscattered into front f/l lens	2 - 3 %
Scattered outside lens cones	15 - 24 %
Absorbed	32 - 46 %
	86 - 114 %

Table 5.2

ENERGY BALANCE FOR SHOT 16/200778

Foil thickness = 0.10 $\mu$ m  
 $I_{inc} = 3.4 \cdot 10^{15} \text{ W cm}^{-2}$   
 Prepulse =  $5 \cdot 10^{-6}$

Transmitted into rear f/l lens	2 - 4 %
Reflected and backscattered into front f/l lens	15 - 18 %
Scattered outside lens cones	15 - 25 %
Absorbed	54 - 67 %
	86 - 114 %

Table 5.3

ENERGY BALANCE OF NRL DATA (Ref N2)

	$I_{inc} / \text{W cm}^{-2}$		
	$3 \cdot 10^{12}$	$10^{13}$	$7 \cdot 10^{14}$
$E_{bs} + E_{bt} + E_{sc}$	14 - 4	15 - 25	34 - 54 %
Ions, UV and X rays	80 - 100	68 - 88	42 - 62 %
Absorption	90	80	55 %

support the above picture. Taking shot 16/200778 as an example, the simplest assumption that can be made is that transmission ( $P_{BT} + P_{FS}$ ) switches on abruptly at  $t = -20$  ps when light is first detected by the S1 camera. Transmission is taken as 11% for all  $t > -20$  ps. The slow rise of  $P_{BT}$  is then due to forward scattering and integration shows that the implied forward scattered energy is 130 mJ (Fig. 5.3). The measured value is  $E_{FS} = 180$  mJ. We conclude that the experimental measurements do not contradict the picture outlined above.

Whether or not the above model is entirely accurate does not affect the conclusion that incident laser light is significantly absorbed in the underdense plasma.

### 5.3 Energy Balance

This section contains a discussion of the time-integrated energy measurements described in 4.3(a). Taking shot 11/210778 as an example, the distribution of the incident energy is repeated from Table 4.2;

$$\begin{aligned}
 E_{INC} &= 2.6 \text{ J} \\
 E_{BT} &= 39\% \\
 E_{BS} &= 2\% \\
 E_{SC} &= 19\% \\
 E_{ABS} &= 40\%
 \end{aligned}$$

These figures will now be examined in more detail in order to find the error associated with the absorption estimate. The energy measurements together with their respective approximate uncertainties are;

$E_{INC}$	$2.6 \text{ J} \pm 100 \text{ mJ}$	
$E_{BT}$	$1.01 \text{ J} \pm 10 \text{ mJ}$	41 - 37%
$E_{BS}$	$54 \text{ mJ} \pm 10 \text{ mJ}$	2.5 - 1.6%
$E_{SC}$	$500 \text{ mJ} \pm 100 \text{ mJ}$	24 - 15%

The errors arise mainly from the calibrations. In the case of the scattered energy ( $E_{SC}$ ) integration over  $4\pi$  sr from 15 data points gives rise to the  $\pm 20\%$  uncertainty. The burn through energy measurement ( $E_{BT}$ ) is accurate ( $\pm 1\%$ ) because the calibration is straight forward; a laser shot is fired in the absence of a target. The back-reflected energy ( $E_{BS}$ ) requires a less direct calibration and gives rise to larger errors ( $\pm 18\%$ ).

The absorbed energy therefore lies in the range 810 - 1250 mJ corresponding to a fractional absorption of 32 - 46%. These figures are summarised in Table 5.1.

The discussion which follows is aimed at accounting for the absorbed energy. Bremsstrahlung, recombination and laser harmonic emissions are neglected because only a small amount of energy is associated with them. The energy taken to heat and ionize the foil is also small. If all electrons in a 30  $\mu\text{m}$  diameter area of the target are assigned 1keV, the total energy is only  $\sim 2$  mJ. It is clear that the ions must receive most of the absorbed energy. A rough calculation follows to see if  $\sim 1$  J can be accepted by the ions.

The ion probe data (4.3(d)) indicate that fast ions ( $v_i > 10^8$  cm/s) have a mass equivalent to a  $\sim 40$   $\mu\text{m}$  diameter area of the foil target. If a velocity of  $2 \cdot 10^8$  cm/s is assigned to all ions in this area, an energy of 270 mJ results. The remaining 730 mJ (out of the absorbed energy) must be taken up by the main thermal ion distribution. If 500 eV ( $v_i = 9 \cdot 10^6$  cm/s) is assigned to every ion within a ring of outer radius 770  $\mu\text{m}$  and inner radius 20  $\mu\text{m}$ , the required energy is obtained. Although this calculation is over-simplified, it does indicate that the absorbed energy can reasonably be accepted by the ions.

The ion probe data have been integrated over time and angle to give the total amount of energy and mass carried by the ion emission. Approximately 15% of the incident energy is recovered in the ion flux



which is in disagreement with the absorbed energy (40-60%). Roughly 80% of the ion energy is carried by the fast ions but they constitute only 10% of the total recovered mass. Both fast and slow ions are emitted in plumes centred on the target normal (4.3(d)) with half maximum full angles of  $20^\circ$ . About twice as much mass is recovered at the front of the foil than at the back for both fast and slow components.

These figures are derived from an integration of the ion flux over  $4\pi$  sr. However, the flux is sampled only at a finite number of angles and so considerable interpolation is required. In particular, the ion flux cannot be measured within the lens cones ( $\theta < 29^\circ$ ) except on the laser axis. This puts a considerable uncertainty on the cone angle figure of  $20^\circ$ .

The recovered energy of 15%  $E_{\text{INC}}$  derived from the ion data is in disagreement with the 32-46% absorption derived from scattered light measurements. However, if the cone angle of the ion plumes is taken to be  $30^\circ$  instead of  $20^\circ$ , the ion data then implies an absorption of 33%, assuming uniform emission within the solid angles of the cones. This is in better agreement with the scattered light result. Experiments at NRL (N2) have shown that half of the blow-off ion mass is contained in a cone of half angle  $35^\circ$ .

The ion data also shows a decrease in absorption in the presence of a prepulse. Absorption falls to 7% ( $20^\circ$  angle) or 15% ( $30^\circ$  angle). This is the same trend as displayed by the scattered light measurements in Table 4.1.

The energy balance is summarised for a low prepulse shot in Table 5.1 and for a low prepulse shot in Table 5.2 for a foil of twice the thickness.

Energy balance calculations have been performed on thin foil experiments at NRL (N2). Polystyrene foils, 10-15  $\mu\text{m}$  thick, were irradiated

Fig 5.4 Opacity and damage thresholds

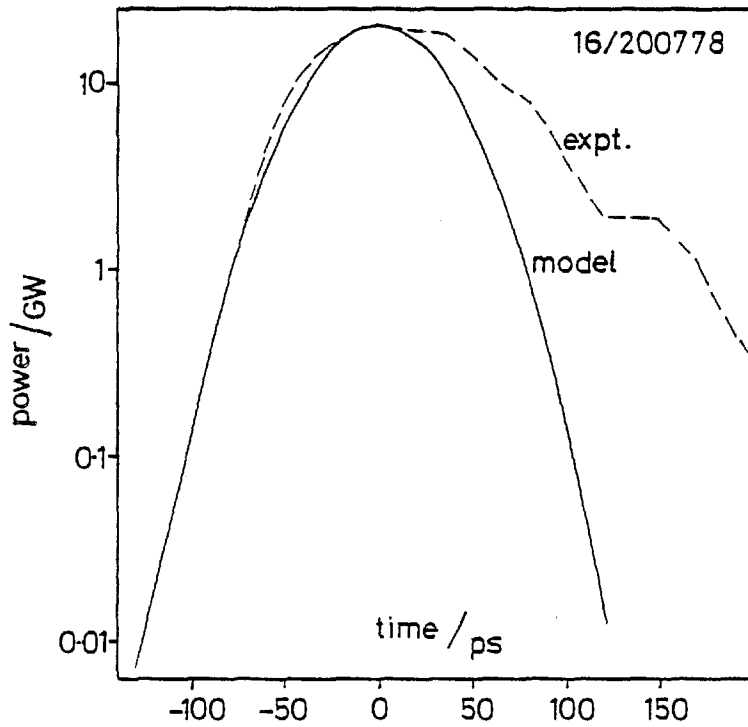
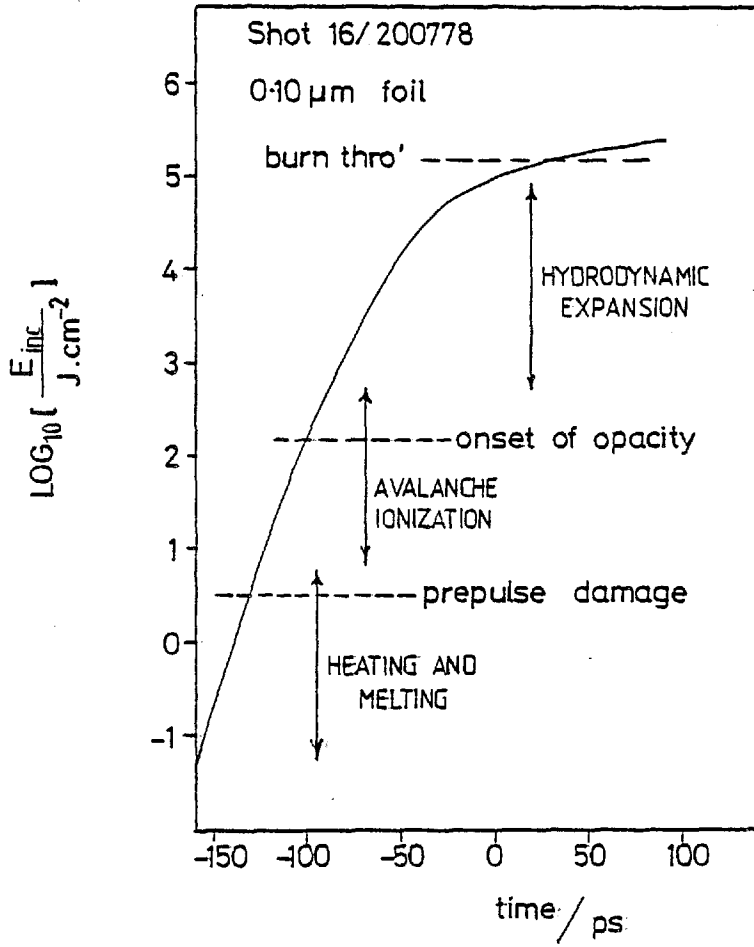


Fig 5.5 Gaussian fit to  $P_{\text{inc}}$  used to generate the curve of Fig 5.4

with 3ns FWHM laser pulses with  $I \sim 10^{12}-10^{14} \text{ W cm}^{-2}$ . Their measurements are given in Table 5.3, and closely match our data for foils of thickness  $\geq 0.10 \mu\text{m}$  for which the burn through energy is small (a few percent). Thinner foils give rise to substantial transmission and the absorption is consequently lower.

The similarity of the NRL data and the measurements reported here is surprising in view of the very different pulse lengths employed. However, both experiments were conducted in a burn through or near burn through regime.

In contrast, a series of experiments at Livermore (S2) were conducted with an effective slab target with no burn through. Discs of Parylene and Tungsten glass, 5 - 10  $\mu\text{m}$  thick, were irradiated by 200 ps FWHM pulses. They report 30 - 40% absorption at  $I_{\text{INC}} = 10^{14} \text{ W cm}^{-2}$  and 20 - 30% at  $6 \cdot 10^{14} \text{ W cm}^{-2}$ , with no difference in the absorption between the two target materials. Clearly, these figures are lower than reported by NRL or indicated by our own measurements. Naively, this implies that the net absorption in the presence of a critical surface (slab target) is lower than if the critical surface is absent (burn through). This does not extend to very thin foils in which burn through occurs early in the incident pulse. This is not as implausible as it may sound in view of the attenuation of the transmitted light observed in underdense plasma (4.3(b)) and in view of the loss mechanisms associated with the critical surface (reflection, for example). However, direct comparison between the measurements from different laboratories is difficult because of the many parameters involved (e.g. modulation in laser focus, prepulse level etc.).

#### 5.4 Damage Threshold and Onset of Opacity

Four separate observations of damage and opacity thresholds have been described:

- (i) The S20 streak data (4.3(c)) fixes the time at which foils become opaque to ruby light. This happens at  $\sim 100$  ps before the incident pulse peak, earlier for higher energy shots and later for lower energy shots. For the peak irradiance in the range  $10^{13} - 10^{16} \text{ W cm}^{-2}$  foils become opaque at a time when the irradiance is  $4 \cdot 10^{12} - 3 \cdot 10^{13} \text{ W cm}^{-2}$ . This corresponds to approximately  $150 \text{ J cm}^{-2}$  having been delivered by the laser pulse for all shots in this irradiance range. Not all the delivered energy is absorbed by the foil, of course.
- (ii) Foils have been irradiated with shots of peak irradiance  $\sim 10^{13} \text{ W cm}^{-2}$  (Fig. 4.16). Back-lighting streaks show that the opaque region of the target remains small during irradiation. The foil behaviour is generally consistent with the opacity thresholds derived from (i).
- (iii) In 4.3(a) it was concluded that the fractional transmission data is seriously modified by prepulse in excess of  $\sim 25 \mu\text{J}$  energy. This corresponds to  $3.5 \text{ J cm}^{-2}$ , in close agreement with the figure of  $4.5 \text{ J cm}^{-2}$  quoted by Mead et al. (M1).
- (iv) In 4.3(a) it was noted that foils sustained occasional damage when repeatedly irradiated with  $10 \mu\text{J}$  oscillator pulses. This appears to corroborate the conclusion of (iii).

The discussion of this section is summarised in Fig. 5.4 which shows the energy deposited on target as a function of time for shot 16/200778 ( $30 \mu\text{m}$  diameter focus). The curve shown was generated by fitting the Gaussian

$$P(t) = 20.15 \text{ GW} \exp \left( - \frac{t^2}{2013.8 \text{ ps}^2} \right)$$

to the experimentally observed pulse. Fig. 5.5 shows the Gaussian fit to the curve derived from the S1 reference streak.

### 5.5 Spreading of Opaque Region

The S20 streak data shows foils becoming opaque in the focus region at first and then later at larger radii. The spreading of the opaque region is rapid; some examples are given in Fig. 5.6. This behaviour is governed by two factors;

- (i) the distribution of energy in the laser focus,
- (ii) the thermal flux in the target plane.

The distribution of deposited energy in the focal spot has been measured only out to a radius of  $\sim 20 \mu\text{m}$ . Fig. 5.7 shows the micro-densitometer scan of a far-field picture. A functional dependence on the radius of  $E(r) \sim \exp(-r/r_1)$ , where  $r_1$  is a constant, fits the data well in the range of observation as illustrated in Fig. 5.8. However, any discussion of the deposited energy at radii larger than  $20 \mu\text{m}$  requires considerable extrapolation from the data. It is possible that the focal intensity distribution has wings out to large radii which would invalidate a logarithmic extrapolation.

The question of lateral heat conduction arises if the far-field intensity distribution falls logarithmically or faster with radius. For in this case, the laser deposits insufficient energy at large radii to account for the observed opacity. This statement rests on the opacity threshold of  $150 \text{ J cm}^{-2}$  discussed in 5.4.

It follows that energy transport within the target must be responsible for the required energy deposition. (Hydrodynamic flow is too slow to be responsible for the spreading of the opaque region which occurs on a timescale of 50 ps.) Classical thermal conduction is described by the diffusion equation

$$\frac{dT_e}{dt} = \frac{K}{n_e} \nabla^2 T_e$$

where  $K$  is the classical conductivity (S3) given in 1.2(e). If  $L_T$  is

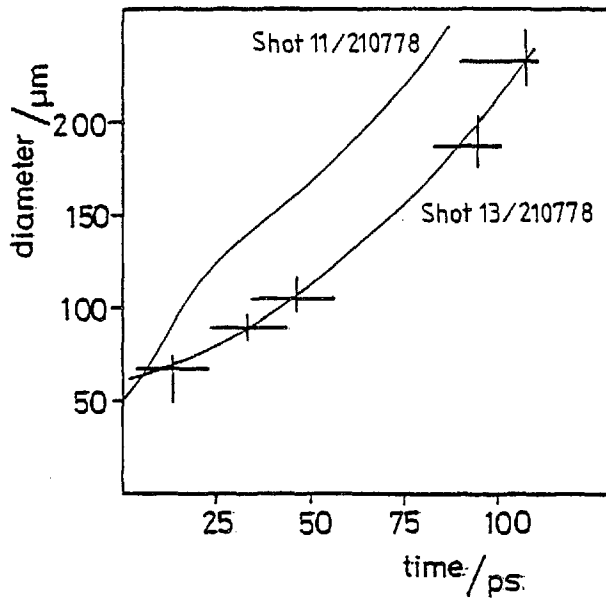


Fig 5.6 Spreading of the opaque region on the S20 streak pictures

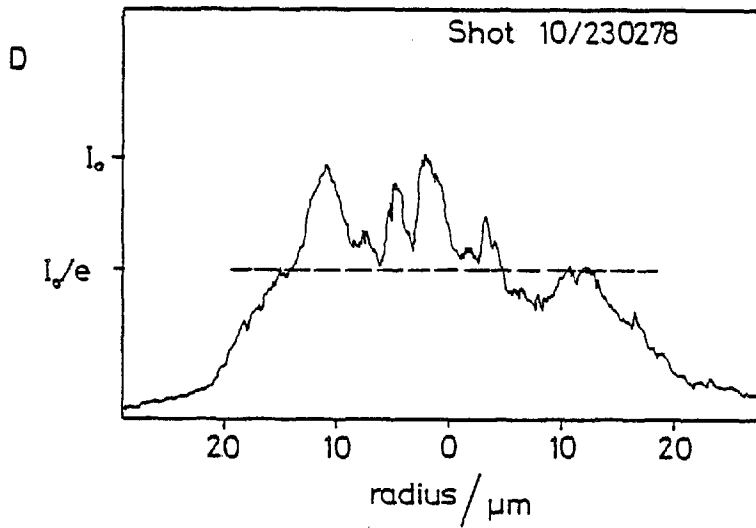


Fig 5.7 Microdensitometer scan of the far field distribution (see Fig 3.16, Image 2)

the scalelength of the temperature gradient, a timescale for classical thermal conduction follows;

$$\tau \sim \frac{L_T^2 n_e}{K}$$

or, numerically,

$$\tau \sim 6.269 \cdot 10^{-8} \text{ sec} \left( \frac{n_e}{n_{cr}} \right) \left( \frac{L_T}{\mu\text{m}} \right)^2 \left( \frac{\text{eV}}{T_e} \right)^{\frac{5}{2}}$$

where we have taken  $Z = 4$  and the Spitzer coefficients  $\epsilon$  and  $\delta_T$  have been included in the conductivity. Taking  $n_e = n_{cr}$ ,  $L_T = 10 \mu\text{m} = \text{focal spot dimension}$  and  $T_e \geq 200 \text{ eV}$  we obtain;

$$\tau \leq 11 \text{ ps}$$

This corresponds to the timescale for the spreading of the overdense region and indicates that classical conduction is likely to be responsible.

An alternative model to describe this part of the S20 streaks, is to postulate inhibited radial conduction together with fast electron transport. On axis, where the foil is overdense, fast electrons may be generated at the critical surface (1.2(h)). They move predominantly parallel to the laser axis and deposit a very small amount of energy in the foil during one transit. This is a result of the long mean free path of energetic electrons given in 1.2(h). Numerically,

$$\left( \frac{\lambda}{\mu\text{m}} \right) \approx \left( \frac{n_{cr}}{Z n_i} \right) \frac{1}{Z} 1.72 \cdot 10^{-5} \left( \frac{T_e}{\text{eV}} \right)$$

This shows that thermal electrons (1 keV) have a mean free path of a few microns, whereas suprathermal electrons (8 keV) travel  $\sim 300 \mu\text{m}$ .

However, the fast electrons do not leave the target but, because of space charge effects, reflex back and forth (Fig. 5.9) through the foil. During this motion they lose energy to fast ions at the reflec-

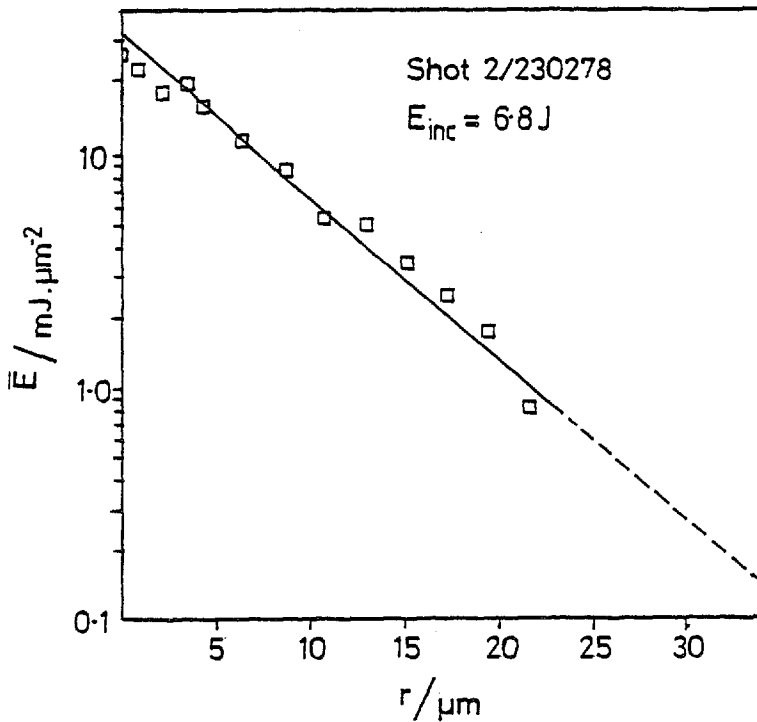


Fig 5.8 Logarithmic fit to the far field distribution of Fig 5.7

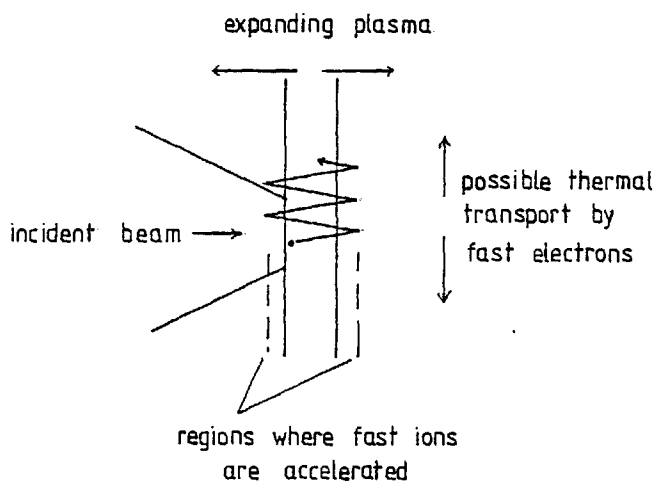


Fig 5.9 Supposed trajectory of fast electrons

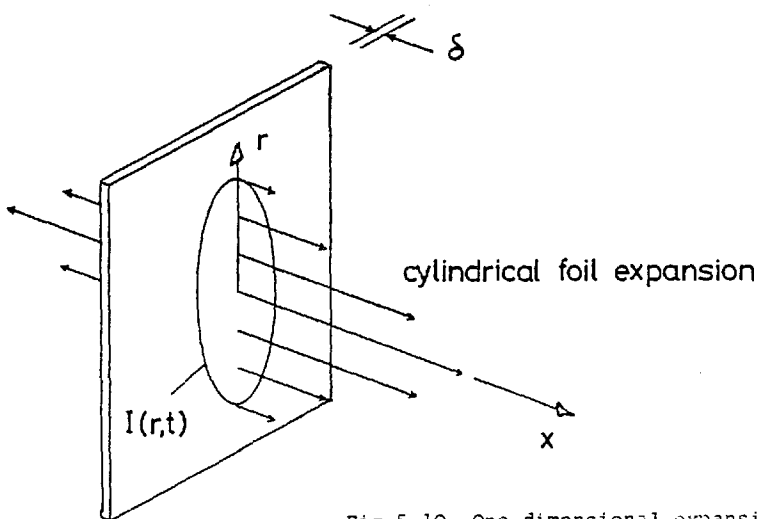


Fig 5.10 One dimensional expansion model



tion regions and undergo a few collisions within the target plasma. Any such collisions will tend to increase the radial velocity component of the fast electrons and lead to radial energy transport.

Fast electron transport (or some other mechanism) is required if the thermal conduction is reduced from its classical value. For example, if the conductivity is  $0.1 K_{c1}$ , the timescale for conduction is increased to 111 ps which is too slow to explain the spread of opacity.

The classical heat flux is given by

$$Q = K_{c1} \frac{T_e}{L_T} = 25.52 \cdot 10^4 \left( \frac{\mu\text{m}}{L_T} \right) \left( \frac{T_e}{\text{eV}} \right)^{\frac{7}{2}} \text{ W cm}^{-2}$$

or, expressed as a fraction of the free streaming flux  $Q_{FS}$  (1.2(e));

$$\frac{Q}{Q_{FS}} = 1.462 \cdot 10^{-5} \left( \frac{n_{cr}}{n_e} \right) \left( \frac{\mu\text{m}}{L_T} \right) \left( \frac{T_e}{\text{eV}} \right)^2$$

With the parameters used above,  $Q/Q_{FS} = 6\%$  which is just equal to the maximum flux proposed by other workers (M4,P2). Therefore the probable plasma conditions at the onset of opacity make it unlikely that the thermal flux is sufficiently large for the magnitude of the flux limit to affect the observations under discussion.

The spreading of the opaque region can be satisfactorily explained by classical thermal conduction and, in the absence of any other evidence, this model must be preferred over the more complicated one involving fast electron transport. However, the foil behaviour at burn through strongly suggests that thermal conduction is inhibited at later times (5.8). The role of fast electrons must then be considered.

## 5.6 Self-Similar Solution for Foil Expansion

### (a) Introduction

The main feature of the S20 backlighting streaks (Fig. 4.11) is the cusp shape formed by the expanding transmission region. The implied spreading of the burn through hole is shown in Fig. 4.13. In this section, a one-dimensional analytic model is constructed to give a qualitative understanding of the hydrodynamic expansion of the foil targets. Points of interest are;

- (i) the time taken for the targets to transmit the incident and backlighting beams on axis,
- (ii) the radial spreading of the transmission region with time.

### (b) Model and assumptions

The cylindrical expansion (Fig. 5.10) of foils thickness  $\delta$ , areal mass density  $\mu$ , is modelled using a self-similar solution to the hydrodynamic equations. The focal spot intensity is taken to be

$$I(r,t) = I(t) R(r)$$

where  $R(r)$  is dimensionless and has a maximum value of unity. Ultimately,  $I(t)$  is fitted to the S1 reference streak and  $R(r)$  to the observed far-field distribution. A fraction  $\xi I(r,t)$  is absorbed by the target and is converted into internal energy  $e(r,t)$ . The time-integrated absorption fraction obtained from energy balance considerations (5.3) is used for  $\xi$ ; this is an approximation because the absorption must in reality be a function of time. The absorbed energy is assumed to be deposited uniformly throughout the volume of the foil. This is in contrast with the experimental situation, where the laser energy is deposited on one surface. The applicability of the self-similar solution depends on the heat transport into the foil. If fast electrons are present, their long mean free path (5.5) results in effective volume deposition of energy. Similarly, the model is applicable if heat conduction is

classical. However, if thermal conduction is inhibited and fast electrons do not dominate energy transport, the self-similar solution is a poor model and the computer models must be used (5.7, 5.8).

The absorbed energy causes the target plasma to expand and, because of the finite mass present, the density falls. One-dimensional expansion is assumed so that, if  $\rho(x,t)$  is the density,

$$\int_{-\infty}^{\infty} \rho(x,t) dx = \mu$$

is constant, for all  $r$ .

The fluid equations describing the expansion allow a self-similar solution given in 5.6(c). The plasma is treated as an ideal gas and a number of further assumptions are made. The initial internal energy of the foil is neglected and no axial thermal transport is admitted. This last assumption is justified a posteriori by the isothermal nature of the solution.

The time dependent part of  $I(r,t)$  is fitted with a function

$$I(t) = \beta(1 + \alpha) t^\alpha$$

where  $(\beta) = W \text{ sec}^{-\alpha} \text{ cm}^{-2}$ . The maximum density at time  $t$  is then given by the self-similar solution (5.6(c));

$$\rho_m(r,t) = \mu \left( \frac{a(r)}{\pi t^{3+\alpha}} \right)^{\frac{1}{2}}$$

where  $a(r) \sim 1/R(r)$ . By putting  $\rho_m = \rho_{cr}$ , the critical density, the model generates contours of constant (critical) density in  $r$ - $t$  space. These may be compared with the S20 data (5.4(d)).

The model neglects ponderomotive force effects (F4) which would lengthen the time for burn through. In addition, it is assumed that the foil is not ionized further after  $t_{op}$ , the time of onset of opacity. A constant charge number of  $Z = 4$  is used during the expansion. This

is an approximation since in reality the foil must be ionised further after  $t_{op}$ , which increases  $n_e$  and lengthens the time for which the plasma is overdense. It is expected, therefore, that the model underestimates the duration of opacity ( $t_{BT} - t_{op}$ ), the error being greater for thicker foils.

As noted in 5.5, the focal spot distribution is well modelled with a function of the form

$$R(r) = e^{-r/r_1}$$

The parameter  $r_1$  is varied until the model prediction curves fit the S20 data. Then a comparison between  $r_1$  and the measured focal radius will give information on lateral thermal transport.

(c) Self-similar solution

The foil is described by the mass density  $\rho$ , velocity  $v$ , pressure  $p$  and specific internal energy  $\epsilon$ . The hydrodynamic evolution of the foil in one dimension is governed by the equations of continuity, momentum, energy and state (ideal gas,  $\gamma = \frac{5}{3}$ ) given by Farnsworth et al. (F5). By choosing a source term  $\epsilon(1 + \alpha)t^\alpha$  in the energy equation, the well-known (L2) adiabatic expansion may be obtained by setting  $\alpha = -1$ . The solution for adiabatic expansion (zero deposited energy) is

$$v = \frac{x}{t}, \quad e = 0, \quad \rho = \frac{\mu}{(4\pi\epsilon t^2)^{\frac{1}{2}}} \exp\left\{-\frac{x^2}{4\epsilon t^2}\right\}$$

where here  $\epsilon$  is the internal energy per unit mass at  $t = 0$ .

Farnsworth et al. have found the self-similar solution for the case of finite deposited energy;

$$v = \left(\frac{3 + \alpha}{2}\right) \frac{x}{t} \quad e = \frac{2(1 + \alpha)\epsilon t^{1+\alpha}}{(3 + \alpha)\gamma + \alpha - 1}$$

$$\rho = \mu \left(\frac{a}{\pi t^{3+\alpha}}\right)^{\frac{1}{2}} \exp\left\{-\frac{ax^2}{t^{3+\alpha}}\right\}$$

where

$$a = \frac{(3 + \alpha)[(3 + \alpha)\gamma + \alpha - 1]}{16(\gamma - 1)\epsilon} = \frac{\eta}{\epsilon}$$

which defines the constant  $\eta$ . The absorbed power per unit area has been modelled with the function

$$\begin{aligned} \xi I(r,t) &= \xi I(t)R(r) \\ &= \xi R(r)\beta(1+\alpha)t^\alpha \\ &= \mu^\epsilon(1+\alpha)t^\alpha \end{aligned}$$

so  $\epsilon = \frac{1}{\mu} \xi R(r)\beta$ ,  $[\epsilon] = W \text{ sec}^{-\alpha} \text{ gm}^{-1}$

so  $a = \frac{\eta\mu}{\xi R(r)\beta}$

The maximum of the electron density profile is then

$$\begin{aligned} n_{e,m} &= \frac{Z}{M} \frac{\rho_m}{m_p} \\ &= \frac{Z}{M} \frac{\mu}{m_p} \left( \frac{\eta\mu}{\xi R(r)\beta\pi t^{3+\alpha}} \right)^{\frac{1}{2}} \end{aligned}$$

Setting  $n_{e,m} = n_{cr}$ , we obtain;

$$[R(r)]^{\frac{1}{2}} = \frac{Z}{M} \frac{\mu}{m_p} \frac{1}{n_{cr}} \left( \frac{\eta\mu}{\xi\beta\pi t^{3+\alpha}} \right)^{\frac{1}{2}}$$

These contours may be compared with the S20 data, once the critical density  $n_{cr}$  has been chosen. For ruby backlighting, the critical density is  $2.313 \cdot 10^{21} \text{ cm}^{-3}$ . However, the threshold of transmission may occur at densities lower than this ( $0.3 - 0.1 n_{cr,r}$ ) in the presence of ion turbulence (5.9).

(d) Comparison with observations

Thin ( $0.05 \mu\text{m}$ ) foils burn through before the peak of the incident pulse, so the leading edge of the pulse can be usefully modelled with

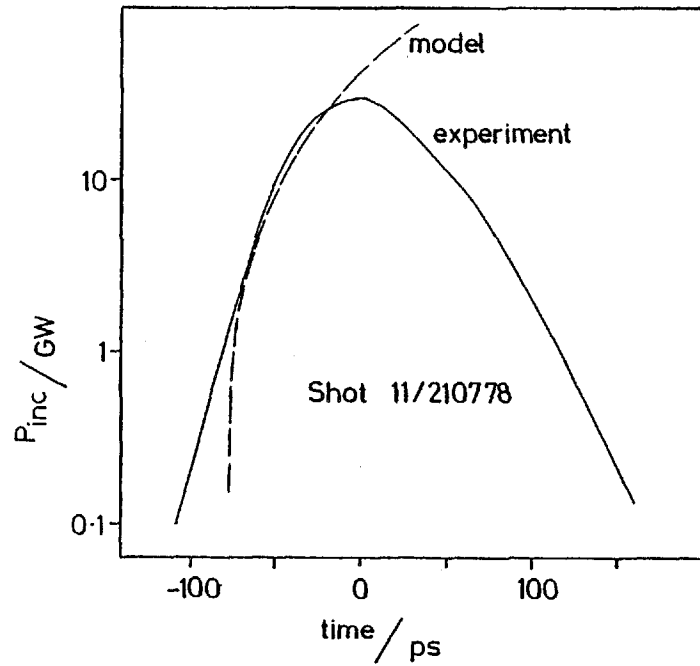


Fig 5.11 Fit to the incident power curve for a self similar solution to the foil expansion

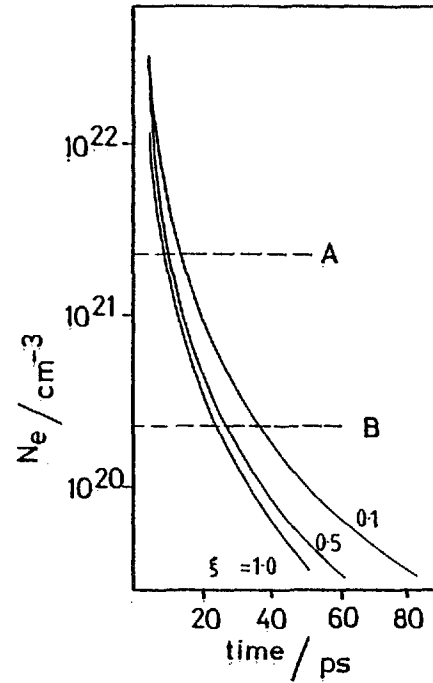


Fig 5.12 Decay of the density as a function of time according to the self similar solution

A;  $n_{crit}(ruby)$   
 B;  $n_{crit}(ruby)/10$

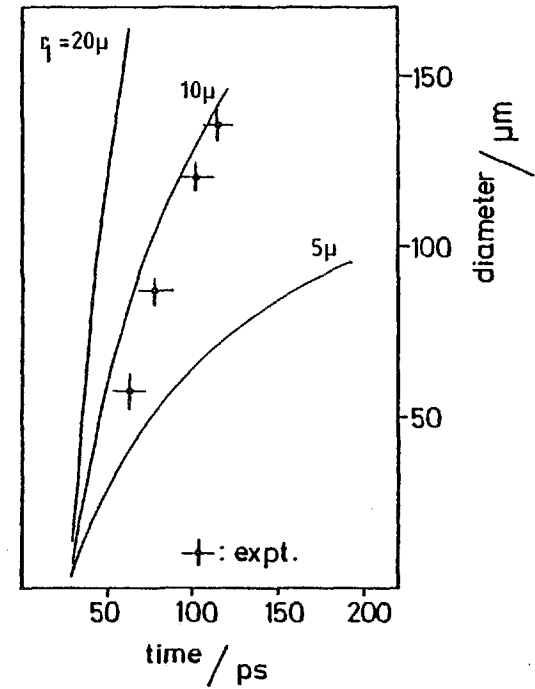


Fig 5.13 Diameter of transmission region as a function of time, according to the self similar solution

a power law function of time;

$$I(t) \sim t^\alpha \quad \alpha > 0$$

Thicker foils burn through late so a top hat incident pulse ( $\alpha = 0$ ) is then a better model.

Shot 11/210778 ( $\delta = 0.05 \mu\text{m}$ ) is taken as an example, and the early part of the incident pulse is modelled by;

$$I(t) = 2.66 \cdot 10^{11} [1 + 1.985] \left(\frac{t}{\text{ps}}\right)^{1.985} \text{ W cm}^{-2}$$

Fig. 5.11 shows this curve superimposed on the experimentally observed  $I_{\text{INC}}$  derived from the S1 reference streak.

Taking  $\gamma = 1.667$ ,  $\rho = 1.06 \text{ gm cm}^{-3}$  and  $Z/M = 0.62$ , we obtain for the maximum density at  $r = 0$ ;

$$n_{e,m} = 5.942 \cdot 10^{23} \xi^{-\frac{1}{2}} \left(\frac{t}{\text{ps}}\right)^{-2.493} \text{ cm}^{-3}$$

This is plotted in Fig. 5.12 with different values of  $\xi$ , the absorption fraction.

The experimental results are  $\xi = 0.4$  and  $t_{\text{BT}} - t_{\text{op}} = 50 \text{ ps}$ . The model underestimates the burn through time giving (for  $\xi = 0.4$ ) a time of  $\sim 15 \text{ ps}$  for the density to drop to  $n_{\text{cr}}$  (ruby) and  $\sim 30 \text{ ps}$  to  $0.1 n_{\text{cr}}$  (ruby).

With  $\xi = 0.4$ , the contours of 0.1 ruby critical density are;

$$r = 2r_1 \ln[2.46 \cdot 10^{-4} \left(\frac{t}{\text{ps}}\right)^{2.493}]$$

which are plotted in Fig. 5.13 with different values of  $r_1$  and with the S20 data for this shot. A value of  $r_1 \sim 10 \mu\text{m}$  fits the data reasonably well.

The measured focal spot distribution is shown in Fig. 5.7 as a densitometer scan. Using the Kodak 4143 film calibration (3.3) the  $e^{-1}$

diameter of the focal spot is  $27 \pm 5 \mu\text{m}$ . This is in close agreement with  $2r_1 = 20 \mu\text{m}$  and indicates that the focal spot scalelength determines the burn through hole characteristics. Attention is drawn to the discussion at the beginning of 5.5. The focal spot distribution is measured out to a radius of  $\sim 20 \mu\text{m}$  whereas the first S20 data point is at  $r \approx 30 \mu\text{m}$ . Therefore this discussion rests on a logarithmic extrapolation of the far-field distribution.

Nevertheless the result is unexpected. The burn through hole diameter must be determined by the scalelength for radial thermal conduction. Taking  $T_e = 2 \text{ keV}$  (from the X-ray diode measurements 4.3(d)),  $n_e = 2n_{cr}$  and  $L_T = 30 \mu\text{m}$  the thermal flux ratio (5.3) is

$$\frac{Q}{Q_{FS}} = 0.97$$

Therefore the thermal flux is taken to be equal to its maximum value, namely  $Q_{FS}$ . Under these conditions, the timescale for conduction is simply

$$\tau = \frac{L_T}{v_e}$$

or, numerically

$$\tau = 2.384 \left( \frac{L_T}{\mu\text{m}} \right) \left( \frac{T_e}{\text{eV}} \right)^{-\frac{1}{2}} \left( \frac{1}{f} \right) \text{ ps}$$

where the flux limit parameter,  $f$ , has been included. With the above values and with  $f = 1$ , we have

$$\tau = 1.6 \text{ ps}$$

This is a short time compared with the time available during expansion for radial conduction to occur. On this basis, the burn through hole diameter is expected to be large compared with the focal spot. However, if the maximum heat flux is limited to a few percent of the free streaming limit, then the timescale for conduction is increased to



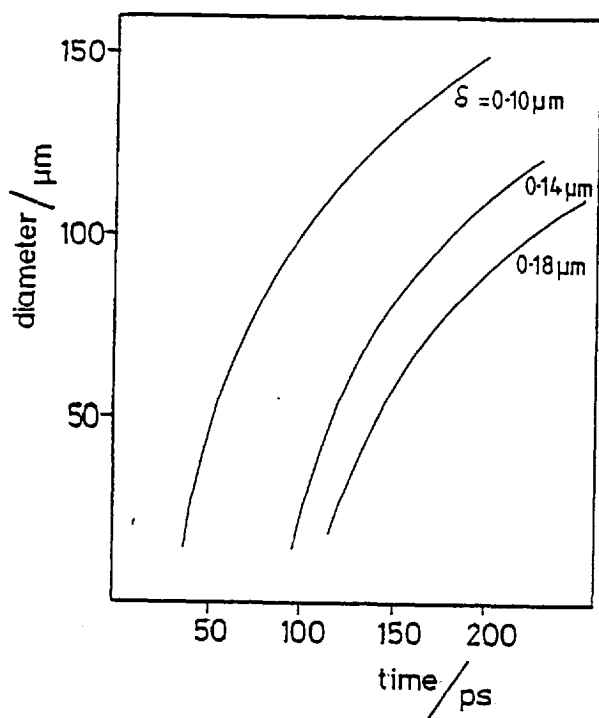
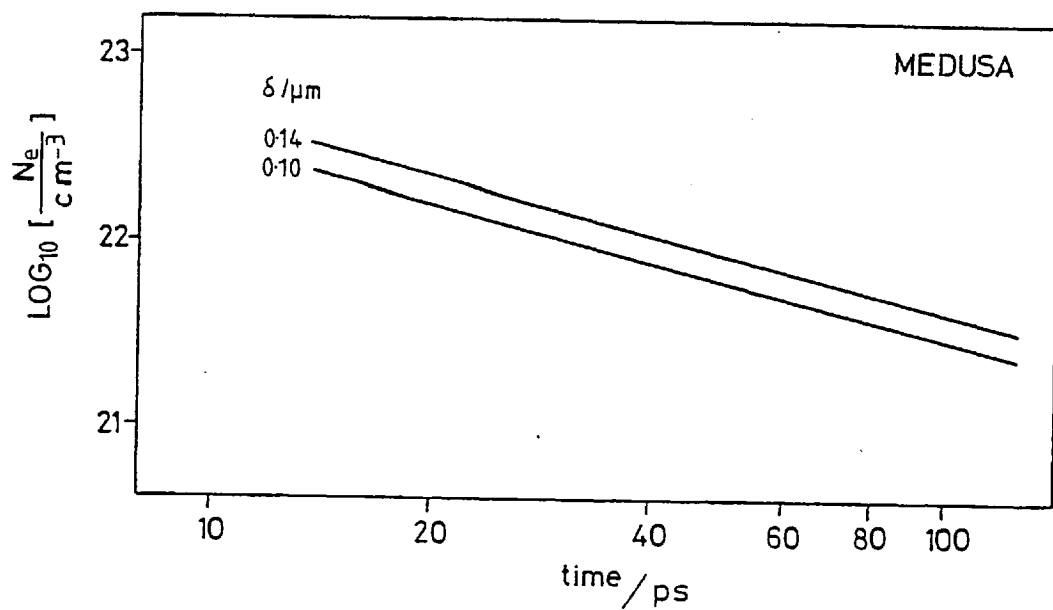


Fig 5.14 Spreading of the transmission region for thicker foils, according to the self similar solution

Fig 5.15 MEDUSA simulation of the adiabatic expansion of thin foils



$\tau \sim 53$  ps

( $f = 3\%$ )

In this case, the burn through hole diameter is expected to be determined by the intensity distribution in the focal spot.

The fact that the data can be modelled reasonably well assuming an expansion governed by the focal irradiance distribution, suggests that the radial thermal conduction is inhibited, with  $f \lesssim 10\%$ . This is true even in light of the somewhat speculative  $I(r,t)$ .

The self-similar solution is more difficult to implement for thick foil shots; the incident pulse has to be modelled with a top-hat function. Constant density contours are shown in Fig. 5.14 for a number of foil thicknesses and should be compared with the experimental data (Fig. 4.13). The correct qualitative behaviour is displayed by the model.

### 5.7 1D Computational Models of the Expansion

In this section, the experimentally determined burn through time ( $t_{BT} - t_{op}$ ) is compared with the prediction of a computational model. The model, namely the MEDUSA code, is described briefly in 5.7(a). The code is run in three different regimes;

- (i) to model adiabatic expansion i.e. without an incident laser pulse, (5.7(b)),
- (ii) to model power driven expansion by artificially holding  $T_e$  and  $T_i$  constant but otherwise with no laser pulse, (5.7(c)),
- (iii) to model laser driven expansion by incorporating a number of deposition and transport processes, (5.7(d)).

In 5.7(d), the effect of varying the thermal conductivity and the flux limit is discussed and compared with the results of Ref. M3. Fast electron transport is also modelled. A conclusion is included in 5.7(e).

Fig 5.16 MEDUSA constant temperature model of foil expansion; scaling with foil thickness

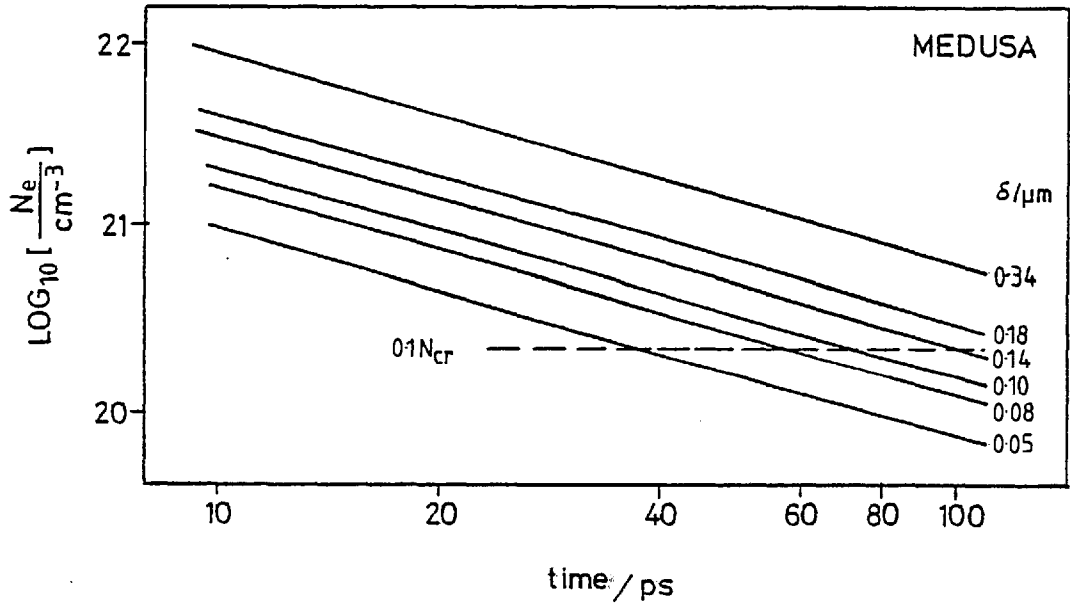
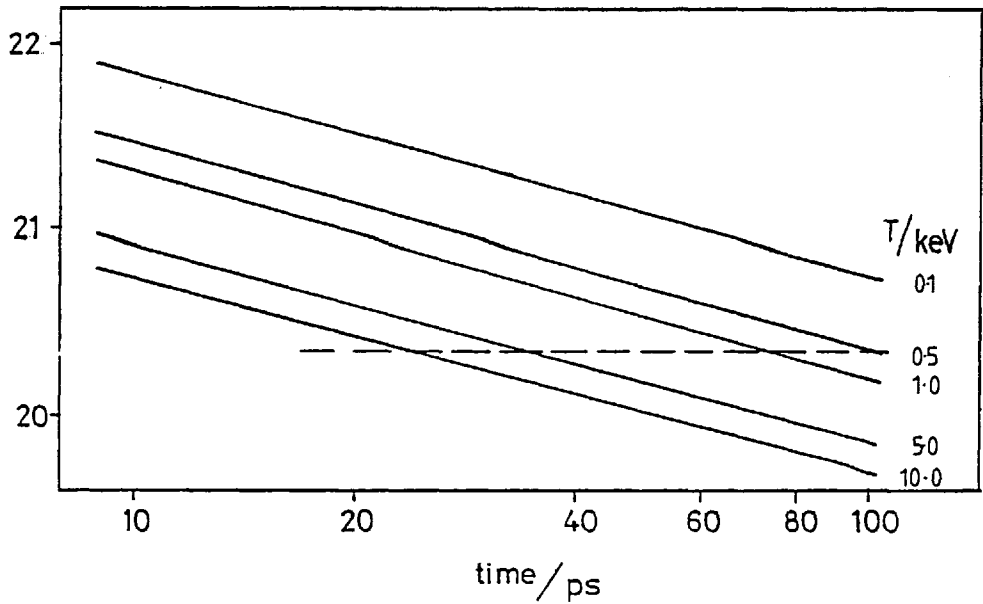


Fig 5.17 MEDUSA constant temperature model of foil expansion; scaling with temperature



(a) MEDUSA

The MEDUSA code is a one-dimensional, Lagrangian fluid code which attempts to model the hydrodynamic and thermodynamic behaviour of a plasma irradiated by an intense laser beam. Originally developed at Culham Laboratory (C2), it is principally designed to model pellet implosion. However, planar geometry experiments can also be simulated. More recently, the code has been developed at the Rutherford Laboratory with the addition of a number of processes including fast electron production and transport, ponderomotive force and ionization physics. These developments are described in Refs. R4 and R6.

Absorption of laser light is by inverse bremsstrahlung in the underdense plasma and by resonance absorption near the critical surface. The fraction of the incident energy which is dumped at  $n_{cr}$  can be chosen; usually this taken as 10%. Of that energy which is resonantly absorbed, a fraction (generally taken to be 90%) is dumped into fast electrons. Of that energy passed to fast electrons a certain fraction (usually 50%) is deposited into the plasma.

The thermal conductivity can be varied as some fraction of the classical conductivity and the flux limit parameter,  $f$ , can be adjusted independently.

Ionization is modelled assuming coronal equilibrium.

(b) Adiabatic expansion model

The foil material is assigned an initial temperature, a fixed state of ionization ( $Z = 3.5$ ) and is allowed to expand freely into vacuum. The temperature falls as a result of the  $pdV$  work required to sustain the isentropic expansion and the peak density falls because of the fixed amount of mass present. Fig. 5.15 shows the MEDUSA prediction for the peak density as a function of time for polystyrene foils of initial temperature 1 keV. The equation of the line for a  $0.10 \mu m$  foil is

$$\left\{ \frac{n_e}{\text{cm}^{-3}} \right\} = 3.4 \cdot 10^{22} \left( \frac{t}{\text{ps}} \right)^{-1.02}$$

This may be compared with the self-similar solution for adiabatic expansion given in 5.6.

For a 0.10  $\mu\text{m}$  foil at the same initial temperature, the self-similar solution reduces to

$$\left\{ \frac{n_e}{\text{cm}^{-3}} \right\} = 3.7 \cdot 10^{22} \left( \frac{t}{\text{ps}} \right)^{-1.0}$$

in good agreement with the MEDUSA result.

(c) Constant temperature model

This model is the same as (b) except that the temperature is artificially held constant throughout the expansion. The assumption is that the  $p dV$  work expended is balanced by the deposited laser power.

The decay of the maximum in the density distribution, as predicted by MEDUSA, is shown in Fig. 5.16 for various foil thicknesses held at a temperature of 1 keV. Scaling with temperature is displayed in Fig. 5.17 for a 0.10  $\mu\text{m}$  foil.

These curves have equations

$$\left\{ \frac{n_{e,m}}{\text{cm}^{-3}} \right\} = \left( \frac{t}{\text{ps}} \right)^{-1.1} \left( \frac{T}{\text{keV}} \right)^{-0.55} \left( \frac{\delta}{\mu\text{m}} \right)^{1.14} \cdot 3.65 \cdot 10^{23}$$

The time taken for the maximum density to fall to  $n_{e,m}$  is given by

$$\left( \frac{t}{\text{ps}} \right)^{1.1} = \left\{ \frac{n_{cr}}{n_{e,m}} \right\} \left( \frac{T}{\text{keV}} \right)^{-0.55} \left( \frac{\delta}{\mu\text{m}} \right)^{1.14} \cdot 157.80$$

This opacity time is plotted in Fig. 5.18 for various values of  $(n_{e,m}/n_{cr})$  and with the experimental values derived from the S20 streak measurements. A constant temperature of 1 keV is assumed. Values of  $(n_{e,m}/n_{cr}) \approx 0.1$  fit the data best. In Fig. 5.19, the variation of opacity time with temperature is shown for a 0.10  $\mu\text{m}$  foil. Again

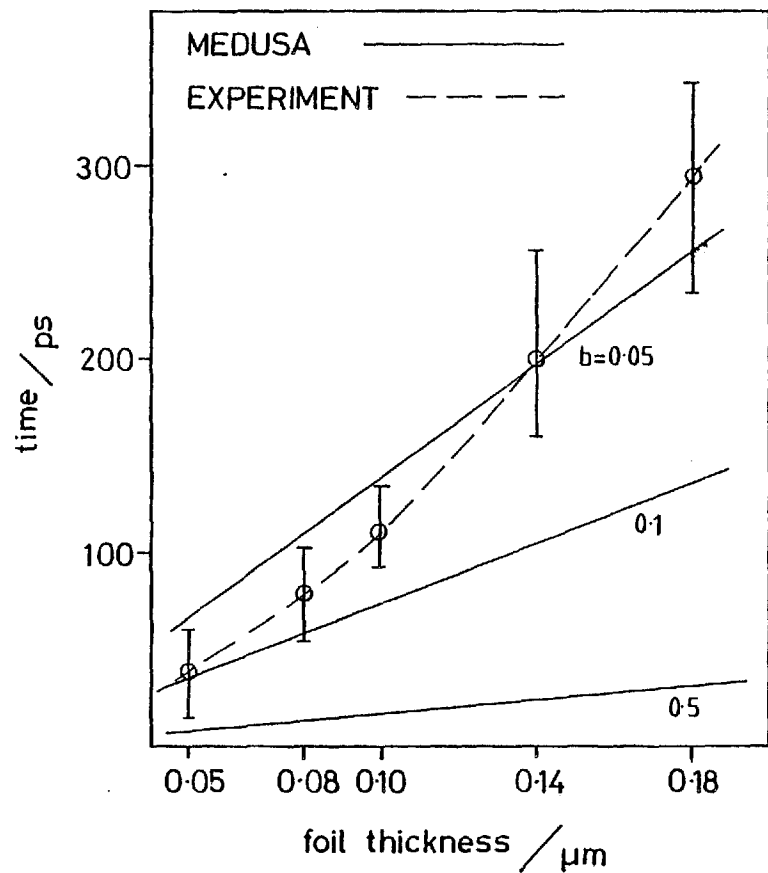


Fig 5.18 MEDUSA constant temperature model; predicted duration of opacity as a function of foil thickness

$$b = n_e/n_{cr}$$

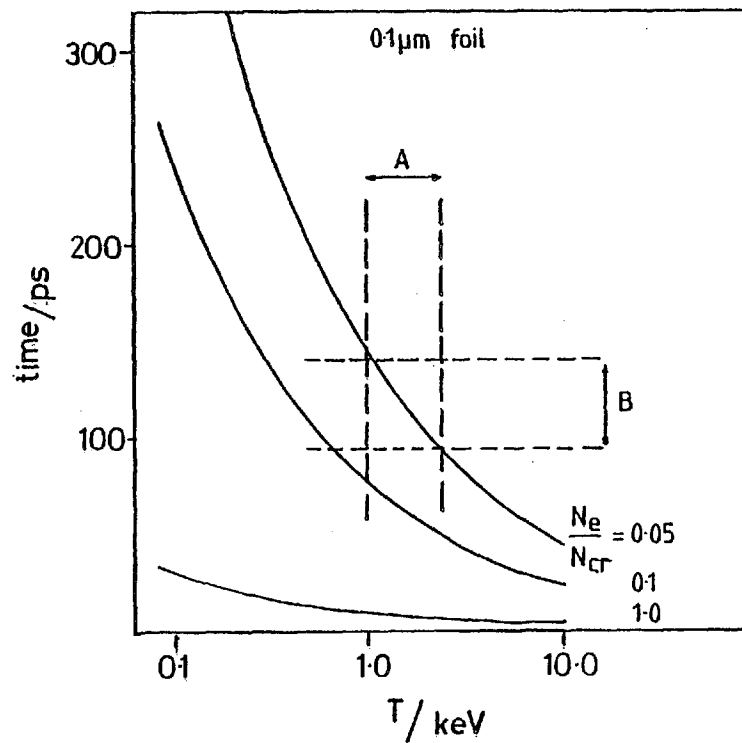


Fig 5.19 MEDUSA constant temperature model; predicted duration of opacity as a function of temperature

- A: X ray diode measurements
- B: S20 measurements of  $t_{op}$

$(n_{e,m}/n_{cr}) \lesssim 0.1$  is implied by the data. Certainly, on the basis of this model, the experimental observations cannot be reproduced if the plasma becomes transparent as soon as the density drops below  $n_{cr}$ . Rather, the threshold for transmission must be  $\sim 0.1 n_{cr}$  in order to explain the long opacity time.

(d) Laser driven expansion

Results are now presented from the complete model available in MEDUSA. The foil is assigned a low initial temperature (100 K) with average  $Z = 1.0$ . The incident pulse is modelled by a Gaussian of peak power  $5 \cdot 10^{15} \text{ W cm}^{-2}$  and duration 100 ps FWHM. The simulation is started when the incident irradiance is  $\sim 0.1\%$  of the peak value. Absorption of laser light is by the processes outlined in 5.7(a) and the resulting state of ionization of the foil plasma is calculated on the basis of a coronal equilibrium model, IONBAL.

The maximum electron density is plotted as a function of time in Fig. 5.20 for a number of foil thicknesses. For these simulations, classical thermal conduction is assumed, with the maximum flux limited to 1% of the free streaming value,  $Q_{FS}$ . Fast electrons are modelled as indicated in 5.7(a) and the ponderomotive force is included. The maximum density drops below  $0.1 n_{cr}$  at times -39, -10 and +49 ps for foils of thickness 0.08, 0.10 and 0.14  $\mu\text{m}$  respectively, where times are measured from the pulse peak. These values are plotted on Fig. 4.16 with the experimental data. It is seen that the scaling of the burn through time with foil thickness is in good agreement with experimental observations, but that the predicted burn through times are less than the observed values by  $\sim 30$  ps. This discrepancy may be due to the crude modelling of the early stages of plasma formation. Starting the simulation at  $1\% P_{max}$  instead of  $0.1\% P_{max}$  reduces the 30 ps discrepancy by nearly one half. This brings the code prediction almost

Fig 5.20 MEDUSA results with absorption and transport processes included

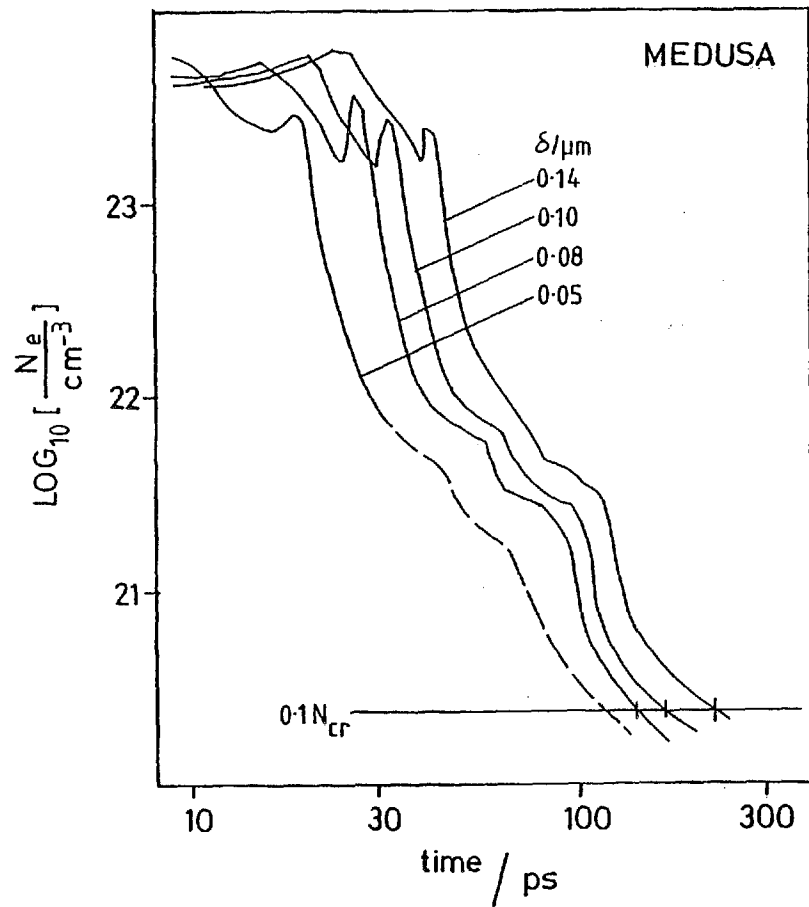
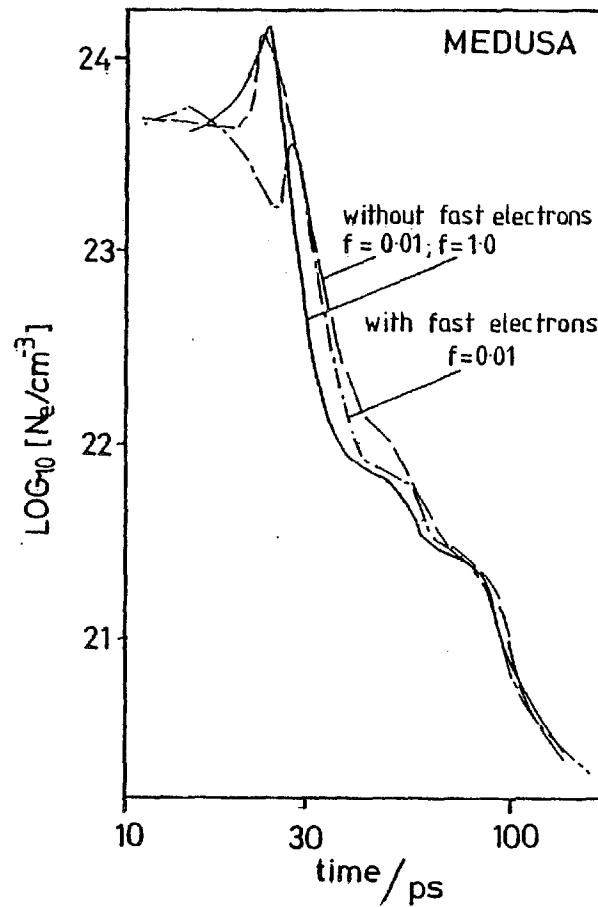


Fig 5.21 MEDUSA results; effect of varying the flux limit parameter f





inside the error bar on the S20 data ( $\pm 10$  ps). If the foils become transparent at  $2.3 \cdot 10^{21} \text{ cm}^{-3}$  (the critical density for ruby light) the code prediction for the burnthrough time is not only very early; it also scales incorrectly with foil thickness.

Therefore, a comparison between MEDUSA and the experimental results indicates that the thin foils are opaque even after the electron density has become sub-critical. An onset of transmission as the density falls below  $0.1 n_{\text{cr}}$  fits the data best.

The above conclusion is based on simulations with classical conductivity,  $f = 0.01$  and including fast electron transport. A discussion of the effects of varying the conductivity and flux limit in the code forms the remainder of this section.

Fig. 5.21 shows the evolution of the maximum density for  $0.08 \mu\text{m}$  foils with  $f = 1.0$  and  $0.01$ . The effect of switching off the fast electrons is also shown. It is seen that, although the foil behaviour is different in the three runs at  $t \sim 30$  ps (after the start of the simulation), by the time the density has dropped to  $n_{\text{cr}}$ , the runs are very similar. The observation that the burnthrough time is independent of the flux limit parameter  $f$  is unexpected and appears to contradict the results of Malone et al. (M4). In order to make a comparison with the simulations of Ref. M4, MEDUSA was run with a 25 ps FWHM Gaussian laser pulse, without fast electrons and ponderomotive force and without IONBAL. A constant state of ionization was assumed ( $Z = 3.5$ ). The simulation was started with the incident power equal to 1% of the peak value, as was done by Malone et al. The results are shown in Fig. 5.22 where the maximum of the density profile is plotted as a function of time for different values of the flux limit. Classical thermal conductivity holds below the maximum flux. It is clear that varying  $f$  in the range  $1.0 < f < 0.01$  makes little difference to the foil behaviour. However, in the range  $0.01 < f < 0.001$ , the expansion is considerably

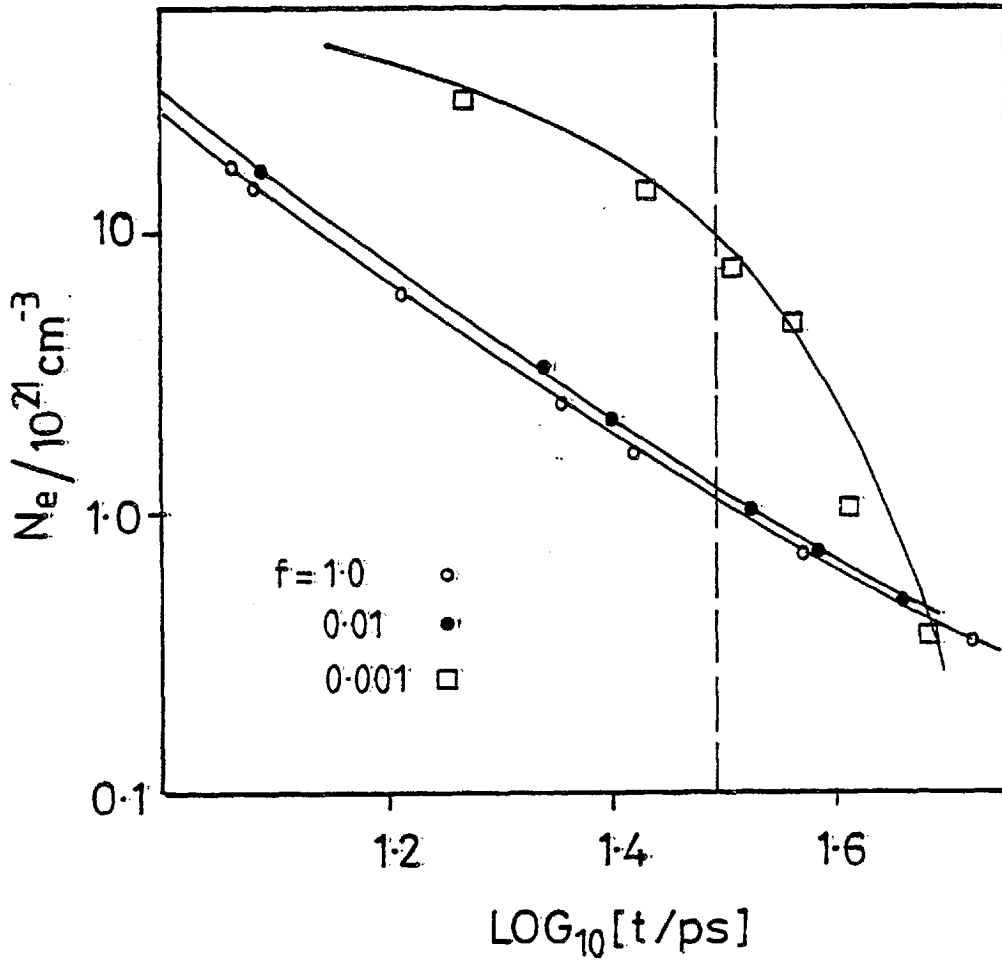


Fig 5.22 MEDUSA model with a 25ps FWHM incident pulse

The dashed line indicates the position of the peak of the incident pulse

delayed. The same behaviour is observed for 100 ps laser pulses.

The reason for this result is that the axial flux is in the range  $10^{-2} - 10^{-3} Q_{FS}$  during most of the expansion. Fig. 5.23 shows the density, temperature and thermal flux as a function of position at one instant during the expansion of a 0.10  $\mu\text{m}$  foil. The foil is initially situated at  $x = 100 \mu\text{m}$  and is irradiated with a 100 ps FWHM pulse. The simulation is in all other respects identical to those of Fig. 5.22. The heat flux is maximum just behind the critical surface and is equal to 20%  $Q_{FS}$  at this point. However, generally, the flux is a few percent of  $Q_{FS}$ . The variation with time of the maximum flux is shown in Fig. 5.24, and is seen to be below 10%  $Q_{FS}$  for the majority of the expansion. Therefore it is plausible that the flux is predominantly in the range  $10^{-2} - 10^{-3} Q_{FS}$  throughout most of the foil volume.

It is not clear where the discrepancy with the results of Ref. M4 lies. However, we note that in Ref. M4, the simulation has been fitted (by varying  $f$ ) to experimental data which is also inconsistent with our data; the results of Fig. 4.3 imply a much lower transmission for 25 ps pulses.

Variation in the thermal conductivity below the flux limit does affect the MEDUSA burnthrough times. Holding  $f$  at 1%, the maximum density falls below  $n_{cr}(Nd)$  at times;

t/ps after start of simulation	K/K <sub>cl</sub>
76	1.0
81	0.5
105	0.1
≥ 110	0.01

Restricting the conductivity to a fraction  $\sim 0.5$  of the classical value can bring the code prediction for  $t_{BT}$  into better agreement with experiment.

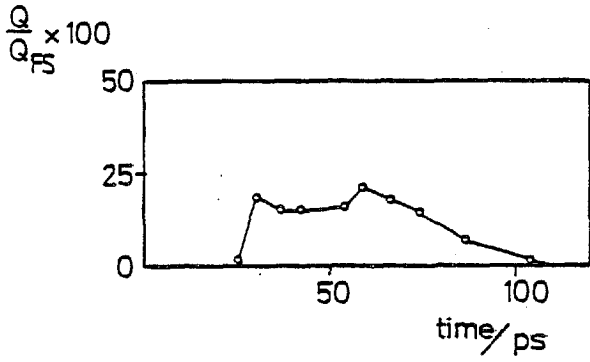
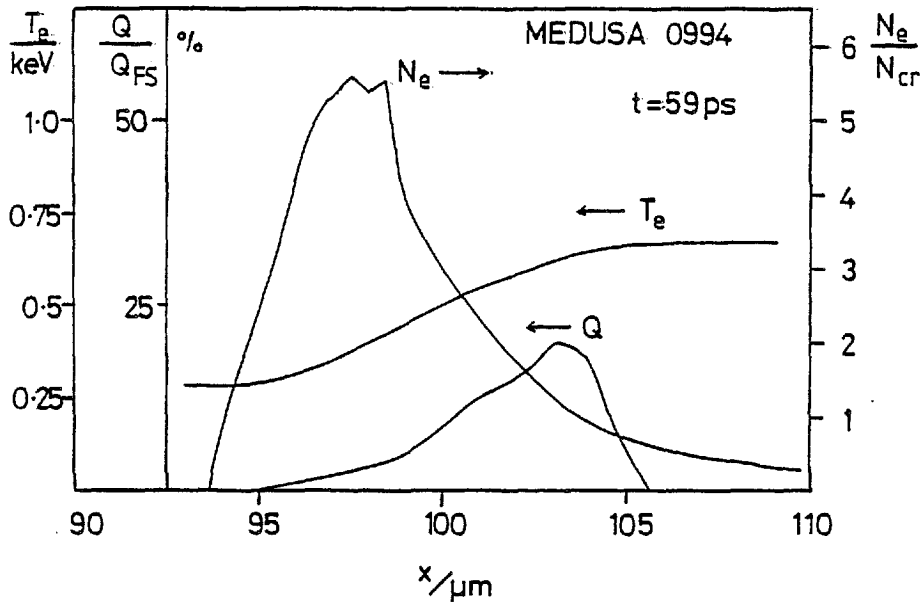


Fig 5.24 MEDUSA prediction of the maximum thermal flux as a function of time

Fig 5.23 MEDUSA prediction of the density, temperature and heat flux as a function of position



Fast electrons allow rapid transport of energy into the volume of the foil. However, the MEDUSA simulations show that, in the absence of fast electrons, the plasma rapidly becomes isothermal, even with the modest heat fluxes discussed above. Therefore the presence of fast electrons cannot modify the burnthrough time (except indirectly by diverting some of the incident energy into fast ions). As far as the burnthrough time is concerned, fast electrons may or may not be present. But if they are present, their motion must be restricted to the axial direction because radial flux inhibition is implied by the burnthrough hole diameter measurements (5.8).

(e) Conclusion

The expansion of thin foil targets has been modelled with the 1D code MEDUSA.

(i) Adiabatic expansion is obtained by switching off the laser pulse in the simulation. The resulting expansion is identical with the adiabatic self-similar solution, as indeed it should be.

(ii) The electron and ion temperatures may be artificially held constant in the code and the resulting expansion is faster than (i). The time for which foils are predicted to be opaque to backlighting has been compared with experiment. The S20 observations can be reproduced only if the target remains opaque down to densities  $\sim 0.1 n_{cr}$ .

(iii) The MEDUSA code has been run with a number of absorption and transport processes. Although the early stages of plasma formation are inadequately modelled, some features of the experimental data can be reproduced. In particular, the scaling of burnthrough time with foil thickness agrees with the data, provided that it is assumed that the foil becomes transparent at  $0.1 n_{cr}$ .

It is found that, in the code, modest axial thermal fluxes are present and are sufficient to rapidly remove the temperature gradients.

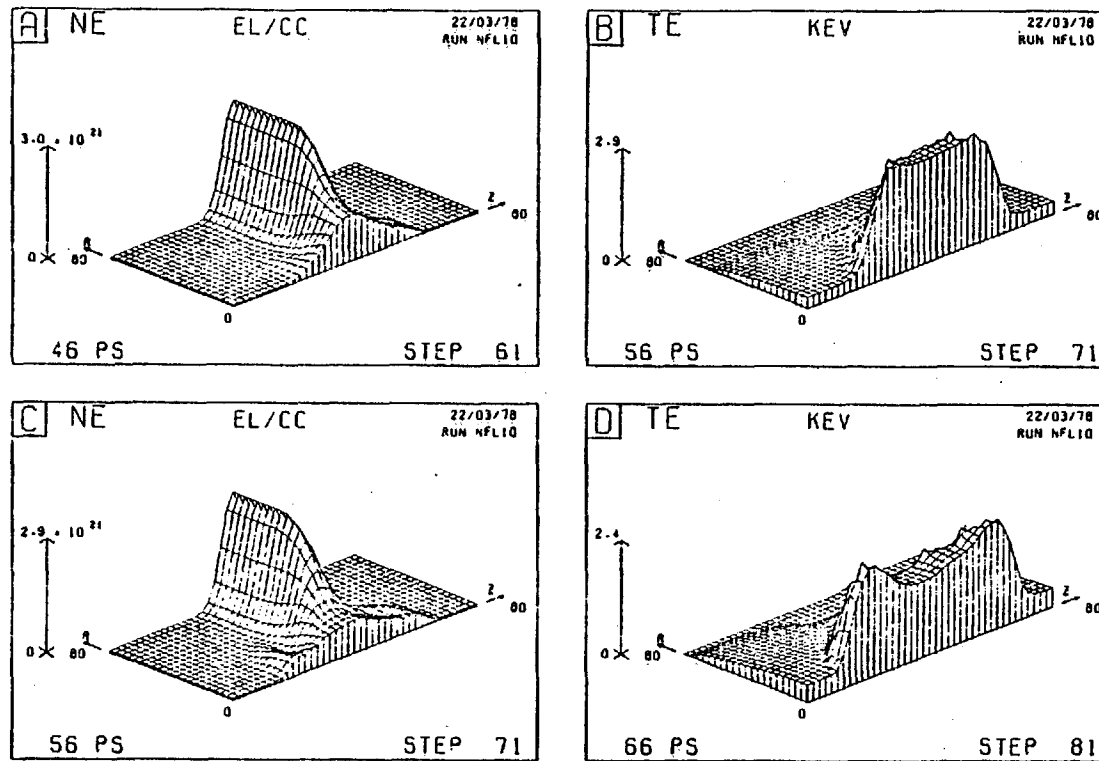


Fig 5.25 LASERB prediction of the density and temperature of a 0.15 $\mu$ m foil

This results in the predicted burnthrough time being insensitive to  $f$  in the range  $10^0 - 10^{-2}$  and also insensitive to the presence of fast electrons. However, the burnthrough time is dependent on the conductivity coefficient  $K/K_{c1}$  and there is some suggestion that the conductivity is slightly reduced from  $K_{c1}$ .

### 5.8 Two-Dimensional Computer Model

A simple model assuming one-dimensional expansion and incorporating a self-similar solution (5.6) indicated that the spreading of the transmission region was consistent with very little thermal conduction in the plane of the target. A number of assumptions were made including that of volume deposition of the incident energy. In this section the experimental results are compared with a 2D computational model, LASERB, with a view to checking the conclusions drawn in 5.6.

LASERB (C3) is a 2D Eulerian fluid code originally designed to study the spontaneous generation of magnetic fields (C4). No atomic physics is included and ponderomotive force effects are not modelled. Resonance and inverse bremsstrahlung absorption are included as well as  $\omega\tau$  inhibition of the heat flux (1.2(f)). The heat flux may be reduced further if required to fit the experimental data.

Typical results for the electron density and temperature are shown in Fig. 5.25. (The laser target geometry is shown in Fig. 5.26.) In this run,  $\omega\tau$  inhibition results in the radial heat flux distribution of Fig. 5.27. The predicted burn through hole diameter is weakly dependent on the thermal conductivity. The two curves of Fig. 5.28 have a factor of 100 difference between the conductivities; the lower curve is a better fit to the experimental data (Fig. 4.13).

A number of points are discussed arising from the LASERB simulation:

- (i) Initially the temperature is approximately constant in the axial

Fig 5.26 Laser-target geometry of LASERB pictures

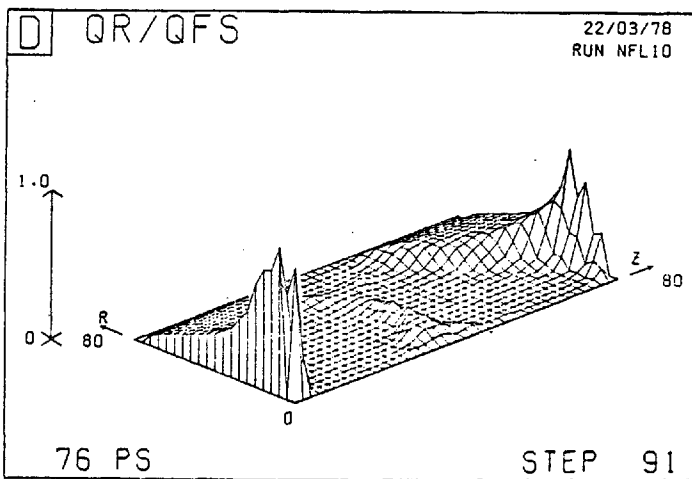
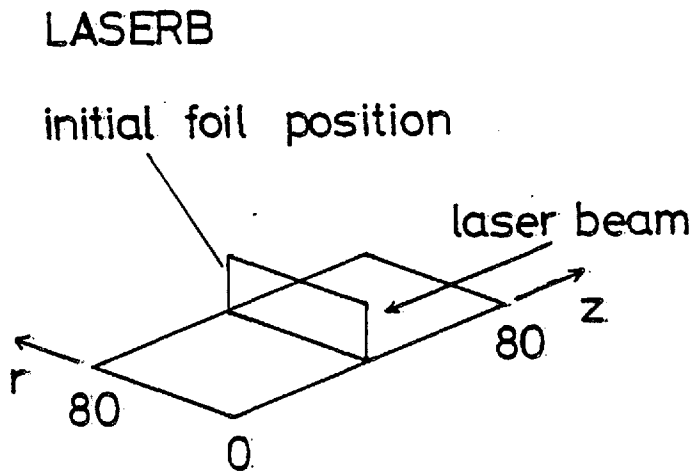


Fig 5.27 LASERB prediction of the radial heat flux distribution



direction in agreement with MEDUSA (Fig. 5.25,  $t = 56$  ps). At later times, as the plasma moves away from the original target plane, the temperature falls in the centre with respect to the outer regions (Fig. 5.25,  $t = 66$  ps). Fast electron transport is not included in LASERB. The conclusion that may be drawn is that, if fast electrons do not dominate the heat transport, then the thermal conductivity is inhibited by the large magnetic fields (Fig. 5.29). This results in a non-isothermal expansion and the self-similar model (5.5) is not realistic.

(ii) The radial heat flux (Fig. 5.27) is large in the plane of the foil, even in the presence of magnetic fields. This can be understood with reference to Fig. 5.29 which shows the LASERB prediction of the azimuthal magnetic field at  $r = 16 \mu\text{m}$  as a function of  $Z$ . The foil is initially at  $Z = 40 \mu\text{m}$  and here the field is zero. This is because the azimuthal fields (1.2(f)) are in opposite directions either side of the foil (Fig. 5.30) and cancel at the centre. Therefore, large ( $\Delta\text{MG}$ ) fields, which have been observed in plane target experiments (R8) do not severely attenuate the heat flux in the original target plane.

(iii) The burn through hole size is predicted to be larger than is observed even with  $\omega\tau$  reduction of the heat flux. Reducing the thermal conductivity further, brings the code into better, although not perfect, agreement with experiment. A mechanism other than spontaneously generated magnetic fields must therefore be acting to reduce the radial heat flux.

LASERB has also been used to predict the transmission of the incident  $1.06 \mu\text{m}$  beam. As soon as the density drops below  $0.9 n_{\text{cr}}$  (neodymium) approximately 100% transmission is predicted. This is clearly in disagreement with experiment. It is proposed that short wavelength ion turbulence (1.2(d)) is responsible for both the radial heat flux

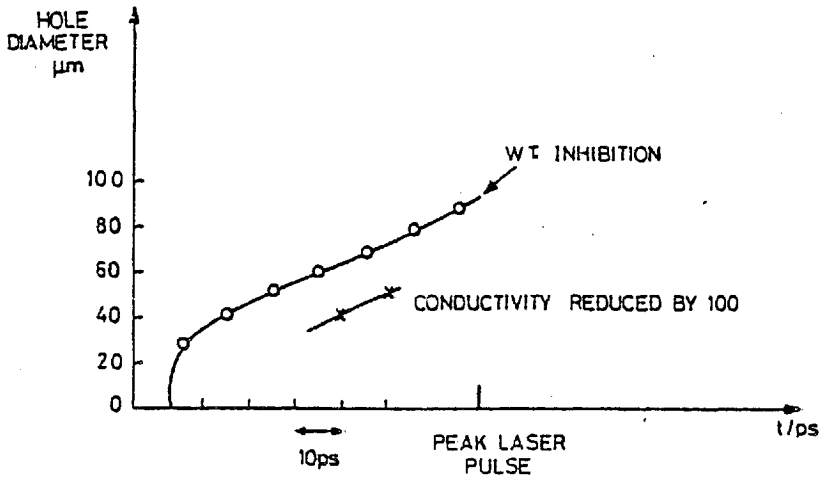


Fig 5.28 Diameter of transmission region as predicted by LASERB

Fig 5.29 Azimuthal magnetic fields as predicted by LASERB

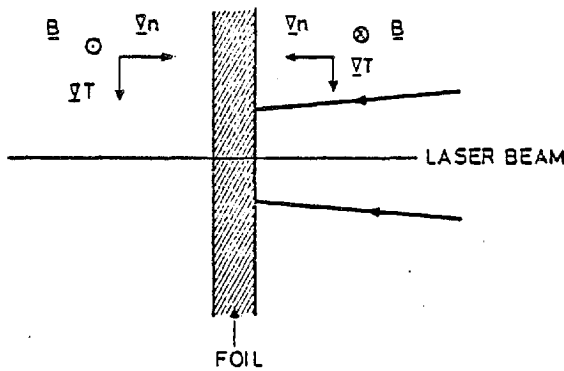
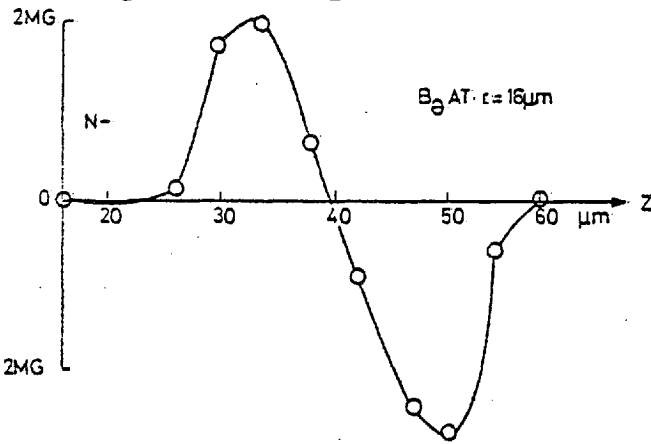


Fig 5.30 Reversal of  $B$  either side of the foil

inhibition and the anomalous absorption of laser light.

(iv) The time with respect to the incident pulse peak at which LASERB predicts burn through is earlier than observed. However, the simulation starts with a pre-formed plasma and ionization effects are not modelled. Good agreement with experiment is not therefore expected.

In conclusion, LASERB supports the inference that thermal transport in the target plane must be low to explain the experimental data. However, because of the symmetry of the plasma expansion, magnetic fields cannot be solely responsible for the reduced radial conductivity. Ion turbulence may be responsible for the flux inhibition as well as for the low transmission after burn through which is not predicted by LASERB. Axial heat flow is inhibited by the magnetic fields leading to thermal gradients (in the absence of fast electrons).

### 5.9 Ion Turbulence

A number of experimental observations suggest that ion turbulence may be present in the underdense plasma;

- (i) the time for which the plasma is opaque to ruby backlighting compared with simulations,
- (ii) the presence of Brillouin backscatter indicated by finite reflection after burn through and by the azimuthal dependence of scattered light. Brillouin scattering in the strong coupling limit (6.1) drives a range of wavenumber of ion waves, thereby generating turbulence.
- (iii) the high integrated absorption implying that the laser light cannot be freely transmitted after burn through,
- (iv) the low ( $\sim 20\%$ ) transmission of the  $1.06 \mu\text{m}$  beam after transmission, derived from the S1 streak data,
- (v) inhibited radial conduction that cannot be explained entirely by magnetic fields (because of symmetry).

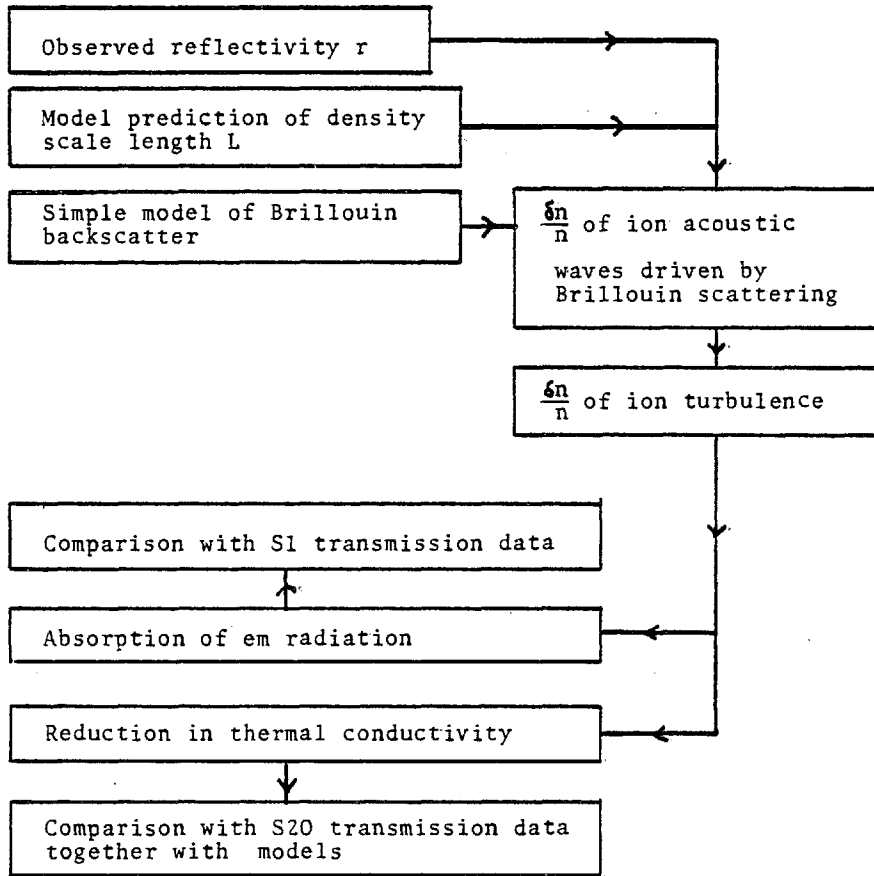


Fig 5.31 Summary of the logic of 5.9

In this section, order of magnitude calculations are performed to check if ion turbulence can explain these features of the data.

The observed Brillouin backscatter of  $r \sim 20\%$  from the underdense plasma (4.3(b)) implies that ion waves are pumped by the incident laser light. The wavelength of the ion waves is (6.1)

$$\lambda_s \approx \frac{1}{2} \lambda_o = 0.53 \mu\text{m}$$

but a spectrum of wavenumbers can be pumped in the strong coupling limit (F1). Short wavelength ion turbulence has wavelengths of the order of  $10 \lambda_D$  (F6) where

$$10\lambda_D = 5.257 \cdot 10^3 \text{ cm} \left( \left[ \frac{T_e}{\text{eV}} \right] \left[ \frac{\text{cm}^{-3}}{n_e} \right] \right)^{\frac{1}{2}}$$

With  $T_e = 1 \text{ keV}$  and  $n_e = 0.1 n_{cr}$  (Nd) we have,

$$10\lambda_D \approx 0.2 \mu\text{m}$$

which is of the same order as the Brillouin pumped waves. The Brillouin backscattering may therefore be regarded as pumping ion turbulence and the  $\delta n/n$  of the Brillouin pumped waves may be equated with the  $\delta n/n$  of the ion turbulence.

Simple models of Brillouin backscatter (6.1(f)) relate the reflection coefficient  $r$  with  $\delta n/n$  and the plasma density scale length. The fluctuation level  $\delta n/n$  may therefore be chosen to be consistent with the observed reflectivity and with the density scale length predicted by the expansion models. Then the implied absorption of light (1.2(d)) and the reduction in thermal conductivity (1.2(g)) are calculated and the results compared with the observations. The logic of this section is summarised in Fig. 5.31.

The density scale length is given by the self-similar solution for power expansion (5.6). For the shot considered in 5.6 (0.05  $\mu\text{m}$  foil)

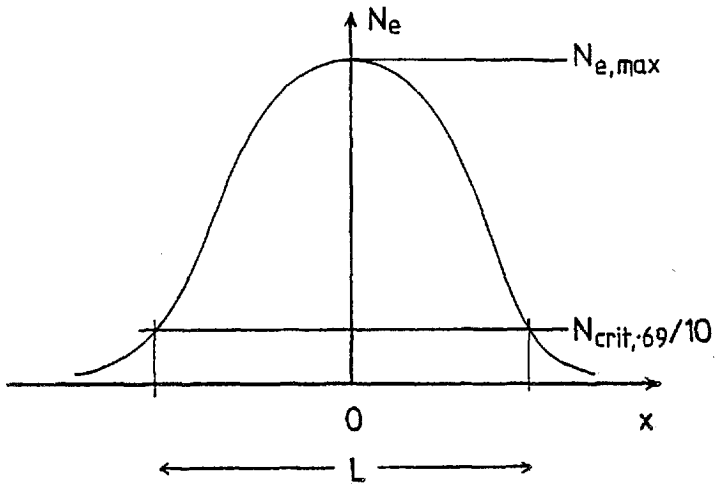


Fig 5.32 Definition of  $L$ , the scalelength for Brillouin backscatter

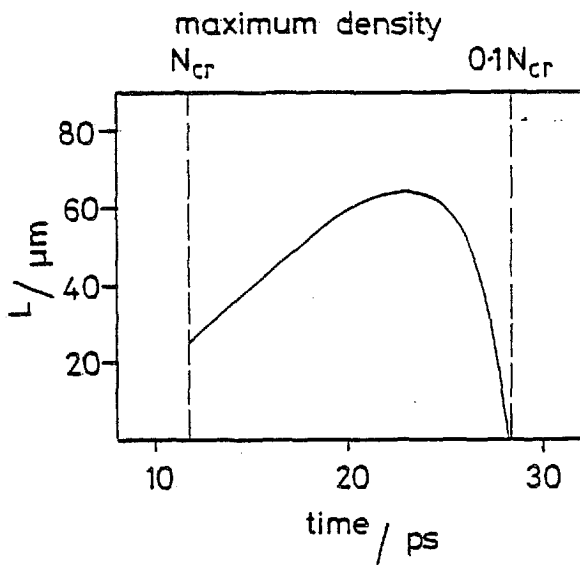


Fig 5.33 Variation of  $L$  with time, according to the self similar solution

the density profile at time t is given by,

$$\frac{n_e}{\text{cm}^{-3}} = 9.395 \left(\frac{t}{\text{ps}}\right)^{-2.493} 10^{23} \exp\left\{-\left(\frac{x}{\mu\text{m}}\right)^2 2.914 \cdot 10^3 \left(\frac{t}{\text{ps}}\right)^{-4.985}\right\}$$

The maximum density drops below  $n_{\text{cr}}$  (ruby) at 11 ps and below 0.1  $n_{\text{cr}}$  at 28 ps. The distance L between 0.1  $n_{\text{cr}}$  points is defined in Fig. 5.32 and given as a function of time in Fig. 5.33. The scale length for Brillouin backscatter is given approximately by  $L = 50 \mu\text{m}$ .

Knowledge of the scale length L and the reflectivity r allows a calculation of the fluctuation level  $\delta n/n$  of the ion waves. Kruer (K2) gives r as a function of  $\theta$  where

$$\theta = \alpha \left(\frac{\delta n}{n}\right) L$$

$$\alpha = \frac{\pi}{2} \frac{n}{n_{\text{cr}}} \frac{1}{\lambda_0} \left(1 - \frac{n}{n_{\text{cr}}}\right)^{-\frac{1}{2}}$$

This result is based on a simple model which neglects ion heating. Ions are heated via ion trapping and ion Landau damping and are cooled by the pdV work associated with the fluid expansion. It is assumed that the cooling dominates the heating processes (E1).

Taking  $n/n_{\text{cr}} = 0.1$  and  $L = 50 \mu\text{m}$ , we have

$$\frac{\delta n}{n} = 0.13 \theta$$

Kruer's model (Fig. 6.1) gives  $\theta = 0.5$  for  $r = 20\%$ . Then  $\delta n/n \sim 7\%$ .

This calculation can be performed in reverse, starting from a turbulence level fixed by the ion-trapping limit (F6) and deriving a scale length for Brillouin scattering. For  $T_i/T_e = 0.1$ , Fig. 1.8 shows that  $\delta n/n \sim 12\%$ . Then, taking  $n/n_{\text{cr}} = 0.1$ , Fig. 6.13 gives the scale length as a function of reflectivity. With  $r = 20\%$ , we have  $L \sim 26 \mu\text{m}$ .

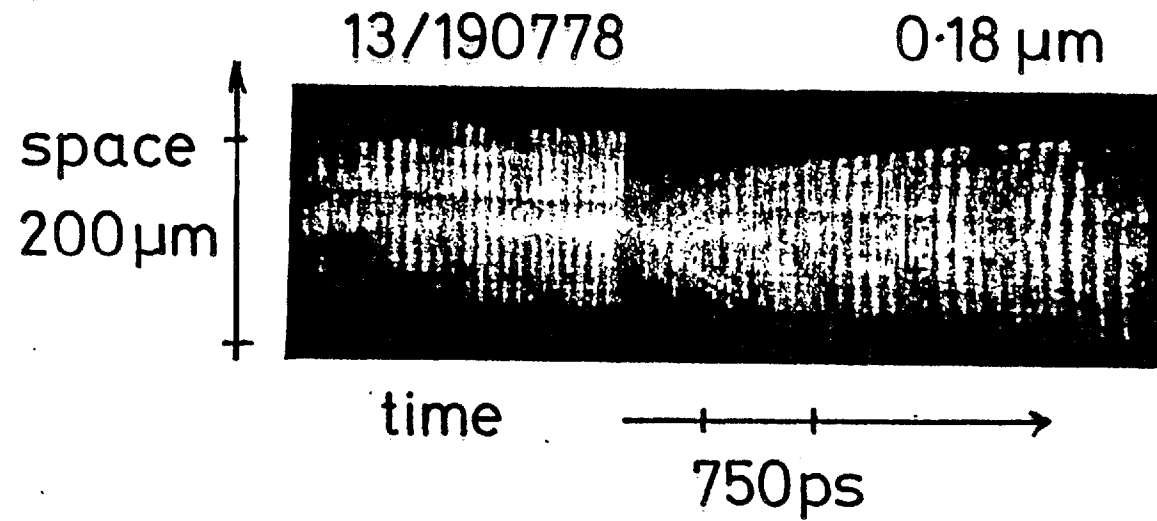


Fig 5.34 S20 streak picture illustrating modulation in the transmitted light after burnthrough



Equating the  $\delta n/n$  derived from the Brillouin scattering with a turbulence level in the ion density, the maximum thermal conductivity is found to be reduced from the free streaming limit by a factor (1.2(g));

$$f = \frac{2\sqrt{2}\pi}{\pi k} \left(\frac{\delta n}{n}\right)^{-2} \frac{1}{L_T}$$

where  $k$  is the wave number of the ion turbulence and  $L_T$  the temperature gradient scale length. Taking

$$\begin{aligned} k &= \frac{1}{2\lambda_D} = 9.51 \cdot 10^{-4} \text{ cm}^{-1} \left[ \left( \frac{T_e}{\text{keV}} \right) \left( \frac{\text{cm}^{-3}}{n_e} \right) \right]^{-\frac{1}{2}} \\ &= 95 \mu\text{m}^{-1} \end{aligned}$$

and  $L_T = 50 \mu\text{m}$ , we have

$$\begin{aligned} f &= 3.36 \cdot 10^{-4} \left(\frac{\delta n}{n}\right)^{-2} = && 0.07 \quad \text{for } \frac{\delta n}{n} = 7\% \\ & && 0.02 \quad \text{for } \frac{\delta n}{n} = 12\% \end{aligned}$$

In 5.5 it was found that such a reduction in the maximum flux was sufficient to account for the small burn through hole diameter.

Absorption of laser light in ion turbulence is discussed in 1.2(d) and Fig. 1.5 gives the absorption length as a function of density. For  $\delta n/n = 10\%$ , the absorption length is  $75 \mu\text{m}$  at half critical density. Therefore an incident laser beam is attenuated by approximately a factor of  $e$  in traversing the underdense plasma for the  $0.05 \mu\text{m}$  foil shot discussed above. This represents a transmission of  $\sim 40\%$  which, when combined with a reflection of  $20\%$ , gives an overall transmission for the laser beam of  $\sim 30\%$ . This is close to the figure of  $20\%$  derived from the S1 data.

In conclusion, a simple model due to Kruer gives an amplitude  $\delta n/n \sim 10\%$  for the ion waves, given an observed Brillouin reflection coefficient of  $\sim 20\%$ . It is assumed that the ion waves are part of a

spectrum of ion turbulence with the same fluctuation level. The presence of ion turbulence leads to a reduced flux limit for the thermal conductivity and to anomalous absorption of laser light. Rough calculations indicate that the calculated level of ion turbulence may be responsible for the experimental observations.

#### 5.10 Features After Burn Through

A large number of the S20 streak pictures display small scale structure after burn through. This structure is usually of the form of V-shaped modulations in the backlighting level; Fig. 5.34 shown an example. The patterns are probably due to lensing effects associated with density modulations in the underdense plasma. The density variations are generated by hot spots in the laser focus.

#### 5.11 Conclusion

Results have been presented from an experiment involving the irradiation of thin foils by high power laser pulses. Experimental observations have been compared with a variety of models and a number of conclusions drawn:

(i) The target plasma absorbs incident laser light significantly even when underdense. Inverse bremsstrahlung alone is not sufficient to explain the absorption.

(ii) Thermal conduction in the plane of the target is inhibited. Magnetic fields, although present in the outer regions of the plasma, are small in the mid-plane of the expansion because of symmetry.

(iii) Finite reflection from the plasma after burnthrough is attributed to Brillouin scattering. Reflection from the edges of the transmission hole is ruled out because the hole is large at late times.

(iv) It is proposed that short wavelength ion turbulence, partially driven by Brillouin scattering, is present in the underdense plasma. Calculations indicate that it is plausible that both the anomalous absorption and the inhibited radial conduction are partly due to ion turbulence.

(v) A one-dimensional simulation indicates that the burnthrough time is insensitive to variations in the flux limit down to a few percent and unaffected by the presence of fast electrons. Both these results are due to the fact that axial temperature gradients are rapidly removed during the early stages of the expansion.

CHAPTER 6

BRILLOUIN BACKSCATTER EXPERIMENT

Results are presented from the observation of light backscattered from spherical targets at around the laser frequency. Long (1.6 ns FWHM) neodymium pulses were used with a range of target size and material. The results show the presence of stimulated Brillouin scattering and other mechanisms. Calorimeter data shows reduced backscatter from high Z targets.

6.1 Review of Theory

The notation used in this chapter is defined as follows. Let the incident beam be denoted by subscript zero ( $\lambda_0, \omega_0, E_0$  etc.) where  $E_0$  is the electric field. The electron quiver velocity is denoted by  $v_0$ ; it is given in 1.3 as a function of  $I_0$ , the incident irradiance.

Let the ion-acoustic waves driven by the backscatter instability be denoted by subscript s ( $\omega_s, k_s, E_s$ ). The speed,  $c_s$ , of these waves is given approximately by

$$c_s = \left( \frac{Z T_e}{m_i} \right)^{\frac{1}{2}}$$

where  $m_e$  ( $m_i$ ) and  $T_e$  ( $T_i$ ) are the electron (ion) mass and temperature respectively. Putting  $m_i = M m_p$ , we have

$$c_s = \left( \frac{Z}{M} \right)^{\frac{1}{2}} \left( \frac{T_e}{eV} \right)^{\frac{1}{2}} 9.782 \cdot 10^5 \text{ cm/s}$$

The electron (ion) thermal velocity is denoted by  $v_e$  ( $v_i$ );

$$v_e = 4.194 \cdot 10^7 \left( \frac{T_e}{eV} \right)^{\frac{1}{2}} \text{ cm/s}$$

$$v_i = 9.789 \cdot 10^5 \left( \frac{T_i}{\text{eV}} \frac{1}{M} \right)^{\frac{1}{2}} \text{ cm/s}$$

The electron and ion plasma frequencies are labelled  $\omega_{pe}$  and  $\omega_{pi}$  respectively;

$$\omega_{pe} = \left( \frac{4\pi n_e e^2}{m_e} \right)^{\frac{1}{2}}, \quad \omega_{pi} = \left( \frac{4\pi n_i Z e^2}{m_i} \right)^{\frac{1}{2}}$$

so

$$\omega_{pe} = 5.642 \cdot 10^4 \left( \frac{n_e}{\text{cm}^{-3}} \right)^{\frac{1}{2}} \text{ rad/s}$$

$$\omega_{pi} = 1.317 \cdot 10^3 \left( \frac{Z}{M} \right)^{\frac{1}{2}} \left( \frac{n_i}{\text{cm}^{-3}} \right)^{\frac{1}{2}} \text{ rad/s.}$$

Finally, the Debye length,  $\lambda_D$ , is given in 5.9.

(a) Threshold for the Brillouin instability

Liu et al. (L1) give for the threshold in an expanding, inhomogeneous plasma;

$$\frac{v_o^2}{v_e^2} \left( \frac{\omega_{pe}}{\omega_o} \right)^2 k_o L_u > 1 \quad (1)$$

where  $L_u$  is the scale length of the expansion velocity gradient. This reduces to,

$$\left( \frac{\lambda_o}{\mu\text{m}} \right)^3 \left( \frac{I_o}{\text{W cm}^{-2}} \right) > 4.764 \cdot 10^{32} \left( \frac{\mu\text{m}}{L_u} \right) \left( \frac{T_e}{\text{eV}} \right) \left( \frac{\text{cm}^{-3}}{n_e} \right).$$

For typical values ( $\lambda_o = 1.06 \mu\text{m}$ ,  $T_e = 1 \text{ keV}$ ,  $n_e = 10^{20} \text{ cm}^{-3}$ ,  $L_u = 5 \mu\text{m}$ ) we have

$$I_o > 8 \cdot 10^{14} \text{ W cm}^{-2}.$$

From the same paper, if the pump wave  $I_o$  is sufficiently intense, Brillouin quasi-mode scattering results. This regime is reached when

$$\left(\frac{v_o}{c}\right)^2 > \left(\frac{\omega_{pi}}{\omega_o}\right) (k_s \lambda_D)^3 \quad (2)$$

or, numerically

$$\left(\frac{\lambda_o}{\mu\text{m}}\right)^4 \left(\frac{I_o}{\text{W cm}^{-2}}\right) > 2.764 \cdot 10^{29} \left(\frac{Z}{M}\right)^{\frac{1}{2}} \left(\frac{T_e}{\text{eV}}\right)^{\frac{3}{2}} \left(\frac{\text{cm}^{-3}}{n_e}\right)$$

With the same values as above we have

$$I_o > 7 \cdot 10^{13} \text{ W cm}^{-2} .$$

This régime corresponds to the strong coupling limit discussed by Forslund et al. (F1, F2). The threshold for Brillouin (quasi-mode) scattering is then

$$\left(\frac{v_o}{v_e}\right)^2 (k_o L_n) > 1 \quad (3)$$

where  $L_n$  is the scale length of the density gradient. This reduces to

$$\left(\frac{\lambda_o}{\mu\text{m}}\right) \left(\frac{I_o}{\text{W cm}^{-2}}\right) > 4.268 \cdot 10^{11} \left(\frac{T_e}{\text{eV}}\right) \left(\frac{\mu\text{m}}{L_n}\right)$$

$$\text{or } I_o > 8 \cdot 10^{13} \text{ W cm}^{-2} .$$

In the experiments to be described below, we expect to be in the strong coupling régime and above threshold for a large part of the incident pulse. We also note that thresholds are lower for longer scale length plasmas.

(b) Growth rate

The growth rate for quasi-mode scattering (that is, for Brillouin scattering in the strong coupling limit) is (F1)

$$\Gamma = \frac{\sqrt{3}}{2} \left( \frac{\omega_{pi}^2 k_s^2 v_o}{\omega_o} \right)^{\frac{1}{3}}$$

$$= 17.3 \left( \frac{Z}{M} \frac{n_i}{\text{cm}^{-3}} \frac{\lambda_o}{\mu\text{m}} \frac{I_o}{W \text{ cm}^{-2}} \right)^{\frac{1}{3}} \text{ Hz}$$

$\sim 10^{13}$  Hz for typical parameters. A similar result is obtained by Drake et al. (D1).

(c) Saturation

The linear theory of Brillouin backscattering discussed in Ref. L1 and part of F1 yields thresholds and growth rates as summarised in (a) and (b). However, in reality, the pumped ion waves do not grow indefinitely but are damped by such mechanisms as wave-breaking (F1) and particle trapping. Particle trapping has been discussed in 1.2(g).

A non-linear theory is required to describe these saturation mechanisms as given in F1 (sec. IV) and F2. Here the density fluctuation in the ion waves is given for the strong coupling régime;

$$\frac{\delta n}{n} \sim \left( \frac{v_o}{v_e} \right)^2 \left( \frac{\omega_s}{\Gamma} \right)^2$$

$\sim 10\%$  for typical values.

(d) Damping of ion-acoustic waves

Energy coupled to the ion-acoustic waves is eventually thermalised as the waves are damped. The thermal collisional damping rate is (T1)

$$\gamma_{\text{coll}} = \omega_{pe} \left( \frac{m_e}{m_i} \right)^{\frac{1}{2}} \sqrt{\pi/2} \frac{v_e}{c}$$

The Landau damping rate is (F3)

$$\gamma_L = \omega_s \sqrt{\pi/2} \left[ \left( \frac{T_e}{T_i} \right)^{\frac{3}{2}} \exp \left( -\frac{1}{2} \left( \frac{T_e}{T_i} + 3 \right) \right) + \left( \frac{m_e}{m_i} \right)^{\frac{1}{2}} \right]$$

(e) Electric field, potential and density fluctuation in an ion wave

A simple fluid model (G1) gives

$$\frac{\delta n}{n} = \frac{eE_s}{m_e k_s v_e^2} = \frac{eE_s}{2k_o T_e}$$

If  $\phi_s$  is the electric potential associated with the ion wave, then

$$\frac{\delta n}{n} \equiv \frac{e\phi_s}{T_e}$$

(f) Reflection coefficient

The linear theory of Brillouin scattering predicts that a large fraction of the incident laser energy is backscattered. However, the amount of backscattered light is limited in practice by the non-linear saturation mechanisms, by self-consistent ion heating and by density profile steepening. Profile steepening, caused by the ponderomotive pressure, increases the threshold for scattering because of the reduced density scale length (a). A number of models have been proposed to calculate the effective reflection coefficient in the presence of non-linear processes.

We begin by deciding whether or not profile steepening limits the backscatter. This depends on the relative magnitudes of the light pressure,  $p_o$ , and the plasma pressure,  $p_e$ ,

$$p_e = n_e T_e$$

$$= 1.6 \cdot 10^{12} \left( \frac{T_e}{\text{keV}} \right) \frac{\text{dyn}}{\text{cm}^2} \quad \text{if } n_e = 10^{21} \text{ cm}^{-3}$$

The light pressure is given by (1.3(a));

$$p_o = 3.33 \cdot 10^{-4} \left( \frac{I_o}{\text{W cm}^{-2}} \right) \frac{\text{dyn}}{\text{cm}^2}$$



where the  $\left(1 - \frac{n_e}{n_{cr}}\right)^{-\frac{1}{2}}$  factor in the ponderomotive force is neglected. Brillouin backscatter will be limited by profile steepening if

$$\frac{I_o}{W \text{ cm}^{-2}} \gtrsim 5 \cdot 10^{15} \left(\frac{T_e}{\text{keV}}\right)$$

Under these circumstances, Kruer et al. (K1) estimate that the backscattered pulse will last for a time

$$\tau \sim L_n \left(\frac{m_i}{m_e}\right)^{\frac{1}{2}} \frac{1}{v_o}$$

where  $L_n$  is the density scale length. This is the time taken for the reflection front to propagate through the underdense region. Numerically,

$$\tau \sim 5.3 \left(\frac{L_n}{\lambda_o}\right) \left(\frac{10^{15} \text{ W cm}^{-2}}{I_o}\right) M^{\frac{1}{2}} \text{ ps}$$

~15 ps for typical parameters.

If the irradiance is lower than  $5 \cdot 10^{15} \text{ W cm}^{-2}$ , Brillouin backscatter is limited by mechanisms other than profile steepening.

Kruer (K2) has described a simple, non-linear model in which the ion waves are limited by trapping. He obtains for the reflection coefficient;

$$r = \frac{1 - B^2}{1 + B^2}$$

where

$$B = e^{-\theta}$$

$$\theta = \alpha L_n \frac{\delta n}{n_e}$$

$$\alpha = \frac{\pi}{2} \frac{n_e}{n_{cr}} \frac{1}{\lambda_o} \left(1 - \frac{n_e}{n_{cr}}\right)^{-\frac{1}{2}}$$

In Fig.6.1,  $r$  is plotted as a function of  $\theta$ . Ion trapping (1.2(g)) limits  $\delta n/n$  to

$$\frac{\delta n}{n_e} = \frac{1}{2} \left[ \left( 1 + \frac{T_i}{T_e} \right)^{\frac{1}{2}} - \left( \frac{3T_i}{T_e} \right)^{\frac{1}{2}} \right]^2$$

This model may overestimate the amount of backscattered light because ion heating is neglected. As ions are trapped and heated, the ratio  $T_i/T_e$  increases and limits the backscatter because ion waves become heavily Landau damped.

Phillion et al. (P1) give the induced reflectivity in the presence of heavily damped ion waves caused by ion heating. Fig. 6.2 shows the predicted reflectivity as a function of  $L_n$  for the following parameters;  $I_0 = 3 \cdot 10^{15} \text{ W cm}^{-2}$ ,  $n_e/n_{cr} = 0.2$ ,  $T_e = 6 \text{ keV}$ . The reflectivity rises more slowly with increasing  $L_n$  than in the absence of ion-heating.

According to Kruer (K2), ion heating may be neglected for times shorter than the ion heating time

$$t_h = L_n \left( 3c_s \frac{n_{cr}}{n_e} \cdot r \frac{v^2}{v_e^2} \right)^{-1}$$

giving 100 ps with the above parameters and with  $L_n = 100 \mu\text{m}$ . However, ions are cooled by the  $p dV$  work required for the hydrodynamic expansion of the plasma. For neodymium laser experiments, the ions are probably never heated enough for the Phillion et al. model to apply (E1). We shall use the simpler model which assumes  $T_i < ZT_e$ .

(g) Effect on second harmonic emission

There are two ways Brillouin backscatter can modify second harmonic emission.

Firstly, backscattering occurs in the density range  $0.1 < n_e < n_{cr}$  and so can reduce the amount of laser light that penetrates to the critical surface.

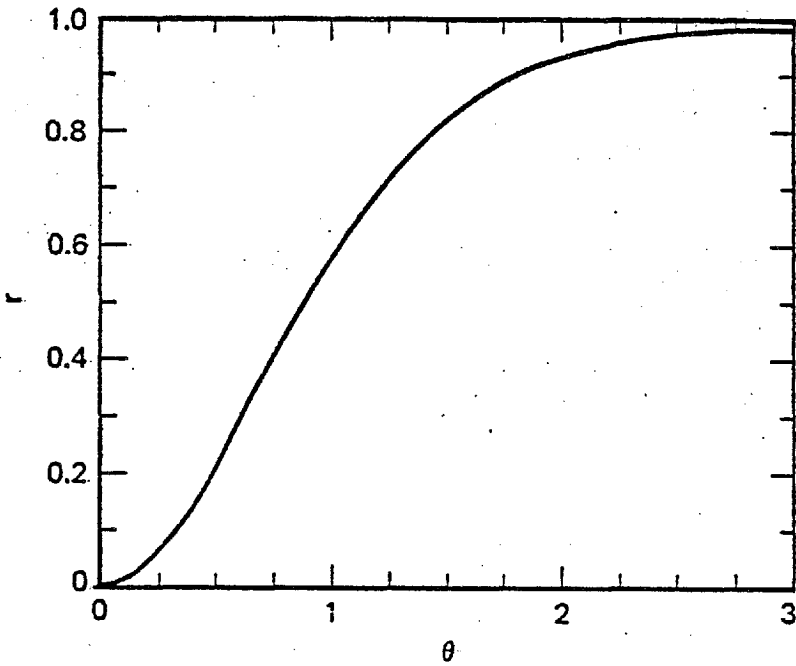
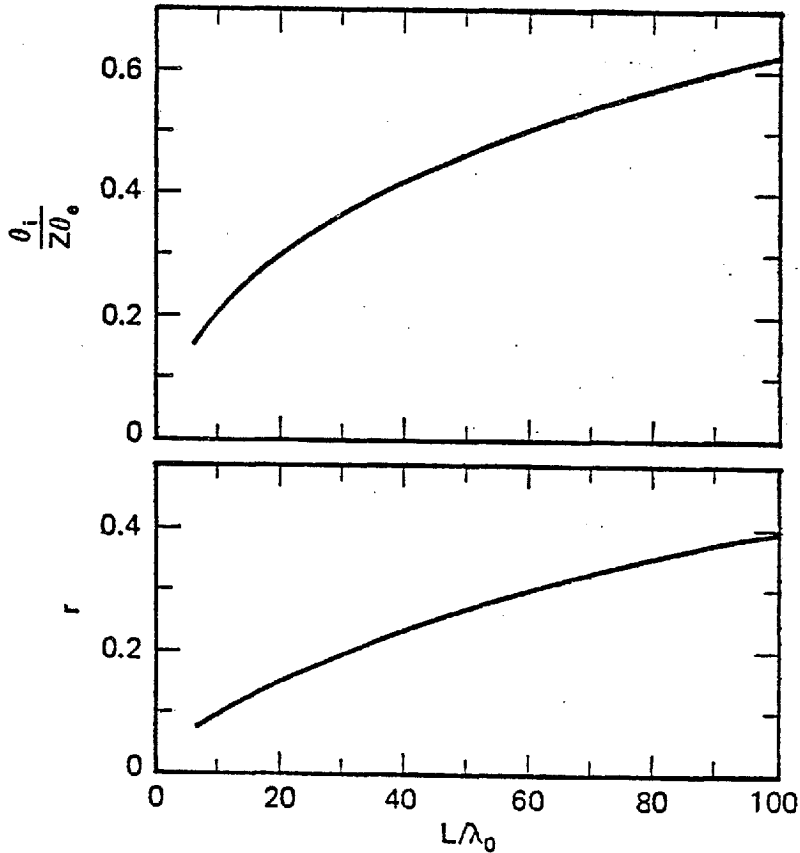


Fig 6.1 Reflectivity due to Brillouin scattering as a function of density fluctuation level (see Ref K2 and text)

Fig 6.2 Reflectivity as a function of the density scalelength (see Ref P1)



Secondly, second harmonic light can couple with ion-acoustic waves

$$\omega_{SH} - \omega_s \longrightarrow \omega_{SH}^1 .$$

This gives the second harmonic emission a broadened spectral line. If the  $\omega_o$  backscattered line has a broad red wing, indicating the presence of ion waves, the  $2\omega_o$  line should also have a red wing.

(h) Spectral shifts

Laser light which has suffered Brillouin backscattering is shifted from the original frequency  $\omega_o$ , by an amount

$$\Delta\omega_B = 2k_o c_s = 2k_o \left( \frac{ZT_e}{Mm_p} \right)^{\frac{1}{2}}$$

or

$$\Delta\lambda_B = 2\lambda_o \frac{c_s}{c}$$

If the plasma is homogeneous and stationary, then the backscattered light has one well-defined frequency, namely  $\omega_o - \Delta\omega_B$ . Fig. 6.3 shows  $\Delta\lambda_B$  as a function of  $T_e$ . Inhomogeneities in the plasma result in a range of matchable wave numbers and the backscattered light is spectrally broadened. Similarly, broadening occurs at high irradiance in the strong coupling limit, because a range of wave numbers may then be pumped.

If the plasma is moving with respect to the detector, a Doppler shift is superimposed on the backscattered light;

$$\Delta\omega_D = \frac{2v_f}{c} \omega_o = 2k_o m c_s$$

or

$$\Delta\lambda_D = 2\lambda_o \frac{v_f}{c_s}$$

where  $v_f$  is the fluid velocity and  $m$  is the corresponding Mach number. Fig. 6.4 shows  $\Delta\lambda_D$  as a function of  $v_f$ . The factor two appears in the

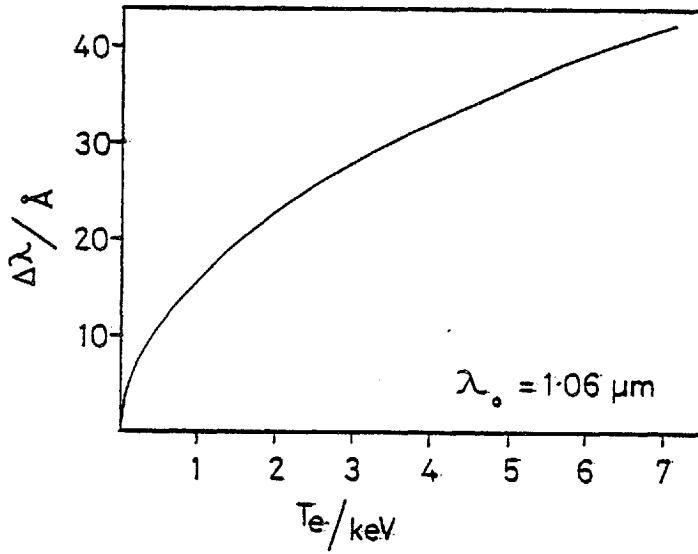


Fig 6.3 Spectral shift due to Brillouin scattering as a function of electron temperature

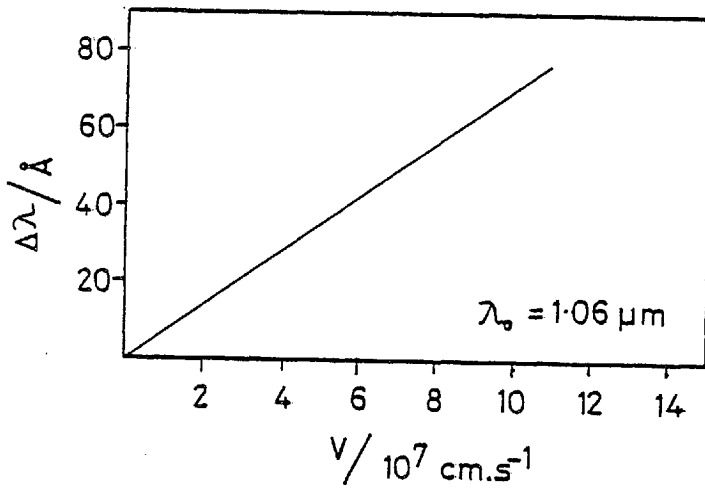


Fig 6.4 Spectral shift due to a moving scattering volume as a function of velocity

expression for  $\Delta\omega_D$  because two Doppler shifts are involved, one in the scattering and one in the observation (Fig. 6.5).

The discussion is now restricted to scattering off an approaching plasma. The two shifts  $\Delta\omega_B$  and  $\Delta\omega_D$  then have opposite signs so the blue shift  $\Delta\omega$  is

$$\begin{aligned}\Delta\omega &= \Delta\omega_D - \Delta\omega_B \\ &= 2k_o c_s m - 2k_o c_s \\ &= 2k_o c_s (m - 1)\end{aligned}$$

or

$$\frac{\Delta\lambda}{\lambda_o} = \frac{2c_s}{c} (m - 1)$$

A subsonic ( $m < 1$ ) flow results in a net red shift and a supersonic ( $m > 1$ ) flow in a blue shift. The fact that the expansion velocity is approximately equal to the sound speed means that  $\Delta\lambda$  is usually small.

If  $m$  is known, then a measurement of  $\Delta\lambda$  gives an estimate of the coronal electron temperature;

$$c_s = \frac{\Delta\lambda}{\lambda_o} \frac{c}{2} \frac{1}{m - 1}$$

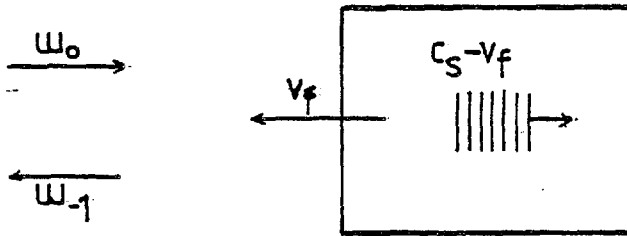
so

$$T_e = \left( \frac{\Delta\lambda}{\lambda_o} \frac{c}{2(m - 1)} \right)^2 \frac{M}{Z} m_p .$$

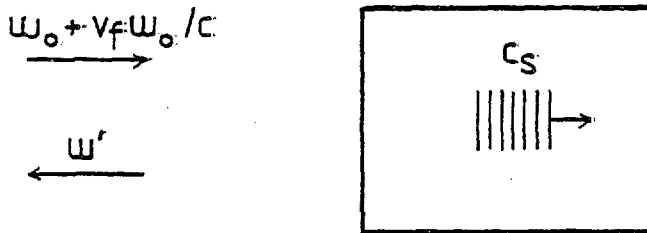
One way of determining  $m$  is to tilt plane targets and compare the resulting shift with the normal incidence result (R1). The flow velocity may be calculated under two assumptions; (i) that the Brillouin shift is independent of angle of incidence and (ii) that the flow is normal to the target surface (Fig. 6.6). The Doppler shift will then vary with the cosine of  $\theta$ , the angle of incidence. Then

$$\Delta\lambda = \Delta\lambda_D - \Delta\lambda_B \quad \text{at} \quad \theta = 0$$

LAB frame



FLUID frame



$$\omega' + \omega' \frac{v_f}{c} = \omega_{-1}$$

$$\omega_0 + \omega_0 \frac{v_f}{c} = k_s c_s + \omega'$$

$$\Rightarrow \underline{\Delta\omega \approx 2k_0(v_f - c_s)}$$

Fig 6.5 Explanation of the two Doppler shifts suffered by backscattered light

and  $\Delta\lambda_{\theta} = \Delta\lambda_D \cos\theta - \Delta\lambda_B$  at  $\theta$

so

$$\Delta\lambda_D = \frac{\Delta\lambda - \Delta\lambda_{\theta}}{1 - \cos\theta}$$

and  $\Delta\lambda_B = \Delta\lambda - \Delta\lambda_D$ .

The Mach number of the flow is then

$$m = \frac{v_f}{c_s} = \frac{\Delta\lambda_D}{\Delta\lambda_B}$$

typical values of  $m$  at  $I_{INC} \sim 10^{15} \text{ W cm}^{-2}$  are 0.8 - 0.85.

Laser light which is not Brillouin backscattered, but is retro-reflected from the critical surface, will suffer only a Doppler shift.

## 6.2 Review of Experimental Work

The fraction of incident laser energy backscattered into the main focussing lens has been studied at NRL by Ripin et al. (R2) with particular attention to the effect of prepulses. With prepulse energy  $> 10^{-4} E_{INC}$ , they observed enhanced backscatter (up to a factor of 3) and reduced absorption, (from 50% with prepulse  $< 10^{-7}$  to 20% with prepulse  $\sim 10^{-2}$ ). They employed solid, planar polystyrene targets with 75 ps FWHM, 9J neodymium pulses focussed to a 30  $\mu\text{m}$  diameter focal spot.

They also tilted the target in order to verify that the back-reflected light was due to Brillouin scattering and, if so, to estimate the density at which the scattering was taking place. The sensitivity to the angle of incidence in the low prepulse measurements was reduced when a preformed plasma was present. This is due to the different scale-lengths in the underdense region.

Results from the Argus and Janus lasers at Livermore are compared by Phillion et al. (P1). When long pulses (400 ps FWHM) and large focal spots (200  $\mu\text{m}$  diam) are used, the absorption is reduced compared with 30 ps,



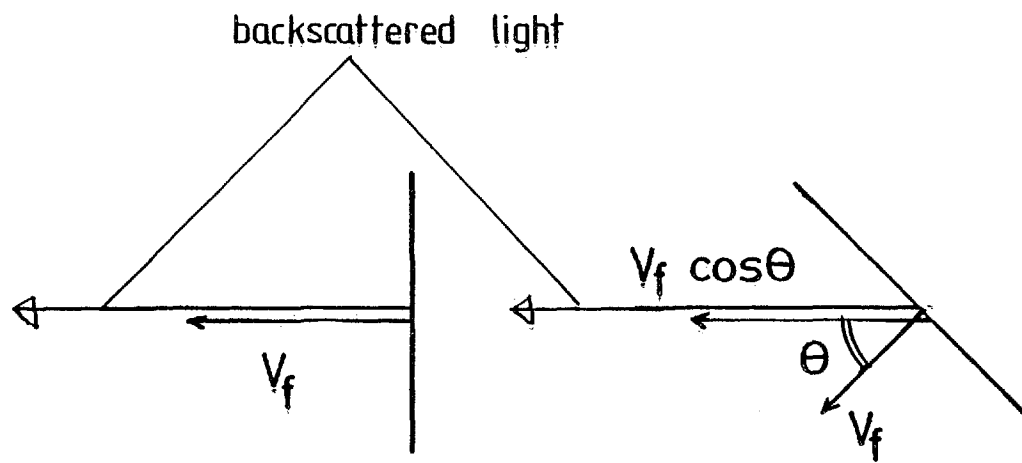


Fig 6.6 Reduction of the Doppler component by tilting plane targets

50  $\mu\text{m}$  diam. irradiation. Around 30-50% of the incident energy is backscattered with large foci. Approximately twice the energy is scattered out of than into the plane of polarisation of the incident pulse. For these experiments 22  $\mu\text{m}$  thick Parylene discs were irradiated at  $10^{15} - 10^{16} \text{ W cm}^{-2}$ . Prepulse level was  $< 10^{-7} E_{\text{INC}}$ :

These results are generally consistent with the enhancement of Brillouin scattering by a larger volume of underdense plasma.

In addition, backreflected light was spectrally resolved: With a 140  $\mu\text{m}$  diameter microballoon target, irradiated with a 220 J, 220 ps pulse, the backscattered line was shifted to the red by  $\sim 10 \text{ \AA}$  and was 10  $\text{\AA}$  wide, typical of Brillouin scattering. The Parylene disc experiments gave shifts to the blue as below;

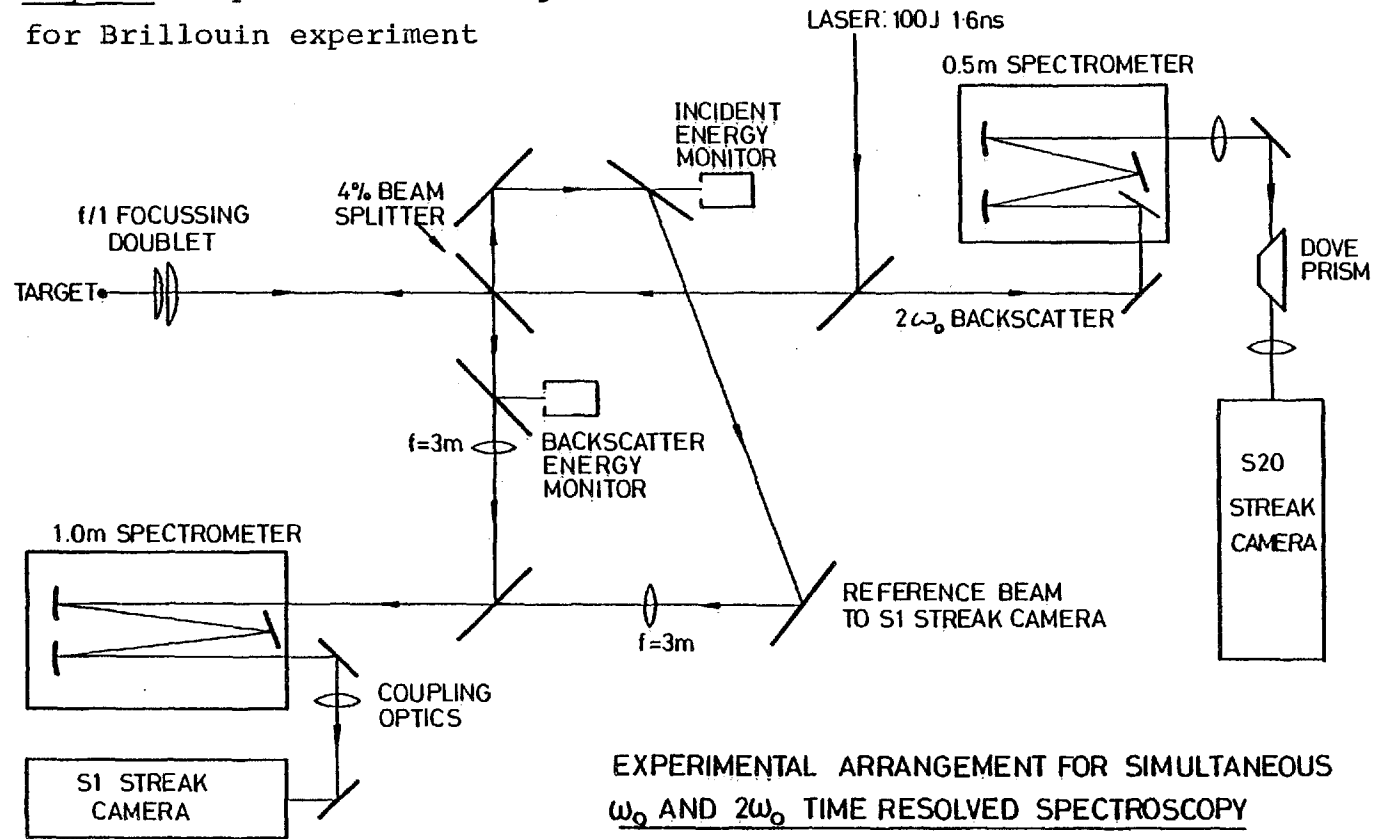
$E_{\text{INC}}$	FWHM	Focal diam	Shift	Width
14 J	200 ps	100 $\mu\text{m}$	10 $\text{\AA}$	20 $\text{\AA}$
	28	50	23	11

This was understood as implying a reduction in Brillouin scattering because of the smaller scattering volume.

The backscattered light was temporally resolved in a series of experiments on Janus reported by Mead et al. (M1) and Haas et al. (H1). Parylene discs 10  $\mu\text{m}$  thick were irradiated by 6 - 12 J Nd laser pulses with a focus of 10 - 90  $\mu\text{m}$  diameter. At  $10^{15} \text{ W cm}^{-2}$ , the backscattered light followed the incident pulse shape in time. However, at  $I \geq 2 \cdot 10^{16} \text{ W cm}^{-2}$ , the reflected pulse switched off before the end of the incident pulse and was  $\sim 20$  ps long. This is consistent with the results of Kruer et al. (K1). The absorption was lower than reported for the NRL work;  $27 \pm 9\%$  at  $2 \cdot 10^{15} \text{ W cm}^{-2}$  and  $41 \pm 8\%$  at  $4 \cdot 10^{16} \text{ W cm}^{-2}$ .

Simultaneous time and wavelength resolution was achieved in earlier NRL experiments (R3) by employing a spectrograph and EPL streak camera

Fig 6.7 Experimental arrangement  
for Brillouin experiment



in series. Slab targets with  $I \lesssim 5 \cdot 10^{15} \text{ W cm}^{-2}$  were used. A pre-pulse ( $.05 E_{\text{INC}}$ ) was applied to the target 700 ps before the main pulse (50 - 900 ps FWHM). An initial red shift of 2 - 10 Å was observed followed by a gradual shift to the blue. This was understood to be due to Doppler effects associated with the accelerating plasma. In addition, they observed the backscattered light switching on with an instrument limited rise time before the peak of the incident pulse.

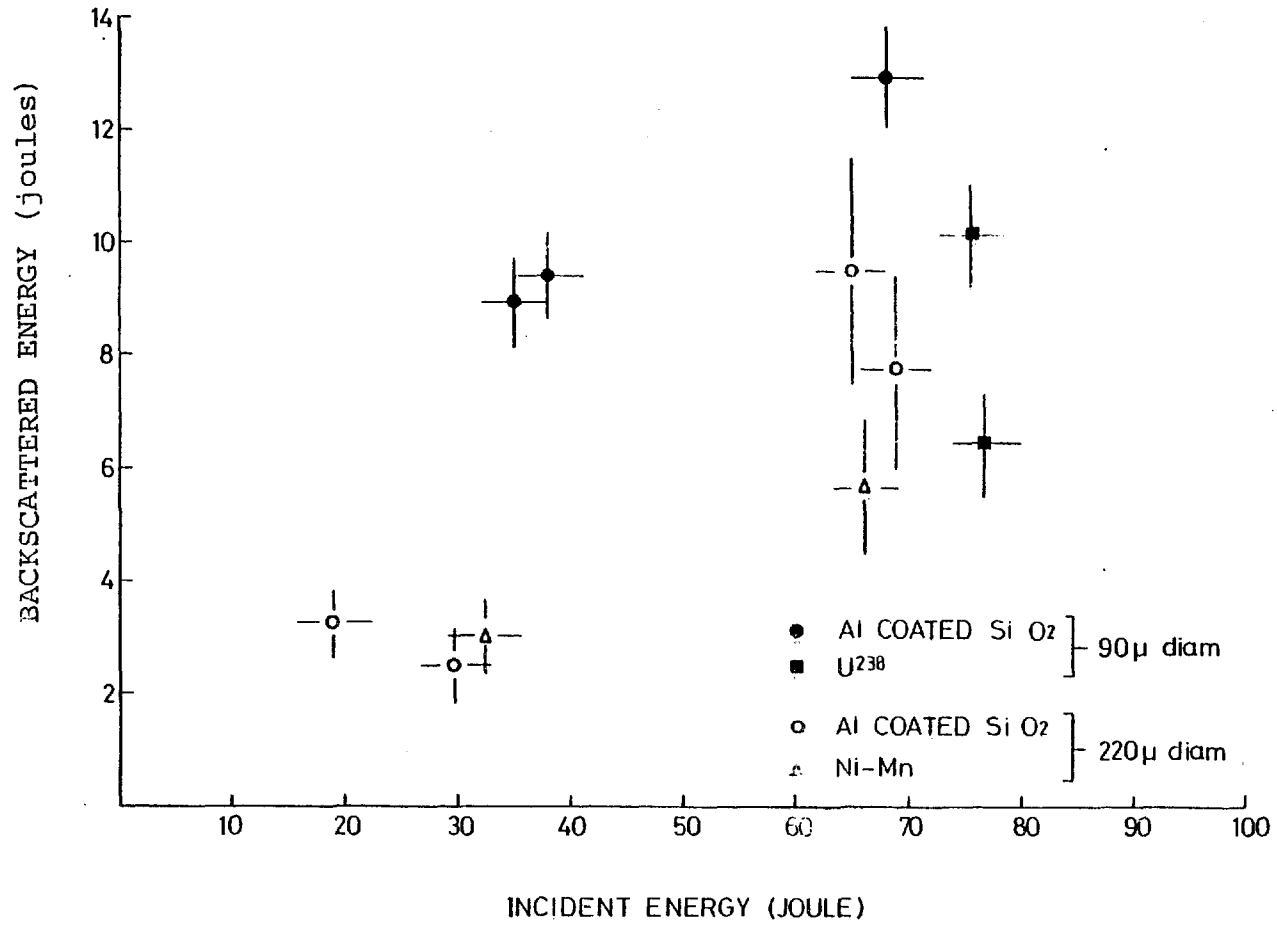
By tilting the target, they found that 5 - 10% of  $E_{\text{INC}}$  was specularly reflected and that the time-integrated spectrum of the backscattered light shifts to the red with increased angle of incidence. At normal incidence, the line is 10 - 50 Å broad and shifted to the blue by up to 10 Å. This data could be explained by postulating a Doppler component ( $\Delta\lambda = 14 \text{ Å}$ ) due to a normal flow velocity of  $4 \cdot 10^7 \text{ cm/s}$  and a red shift of  $\Delta f = 7 \cdot 10^{11} \text{ Hz}$  (27 Å) due to Brillouin scattering (Fig. 6.6).

By varying the incident pulse energy, and focal spot size, it was found that the backscattered energy increases exponentially with  $E_{\text{INC}}$ . An f/1.9 lens was used for these measurements. A smaller lens (f/14) gave a saturation type behaviour with varying  $E_{\text{INC}}$ .

Time-integrated spectra from tilted plane targets have been obtained more recently in a series of Argus experiments at Livermore (R1). Gold discs were irradiated at two angles of incidence,  $0^\circ$  and  $45^\circ$  and the resulting red shifts were observed;

$I_{\text{INC}}$	$\theta_{\text{INC}}$	$\Delta\lambda$	Z	$T_e$
$3 \cdot 10^{14}$	$0^\circ$	$4 \text{ Å}$	51	$5 \pm 3 \text{ keV}$
$\text{W cm}^{-2}$	45	9		
$3 \cdot 10^{15}$	0	4	58	$20 \pm 10$
	45	11		

Fig 6.8 Backscatter energy measurements



Under the two assumptions of Sec. 6.1(h) and Z values based on LASNEX calculations, they deduced coronal electron temperatures as shown. The total amount of energy backscattered ( $\theta < 30^\circ$ ) and sidescattered ( $\theta > 30^\circ$ ) was estimated to be;

$I_{\text{INC}}$	Backscatter	Sidescatter	Total
$3 \cdot 10^{14} \text{ W cm}^{-2}$	$13 \pm 5\%$	$16 \pm 5\%$	$29 \pm 10\%$
$3 \cdot 10^{15}$	$20 \pm 6$	$20 \pm 6$	$40 \pm 12$

Time-resolved data have been obtained at Osaka (A1). Long (1ns) laser pulses of  $\sim 10^{14} \text{ W cm}^{-2}$  were focussed onto glass microballoon targets. For long pulses of power exceeding  $10^{14} \text{ W cm}^{-2}$ , the back-scattered light was observed to cut off half way through the incident pulse. This behaviour was not observed for shorter ( $< 500 \text{ ps FWHM}$ ) or lower energy pulses. They suggested that enhanced damping of ion waves and/or ponderomotive scale length shortening may be responsible for the observations.

Irradiation of plane polyethylene and aluminium targets by Nd pulses up to  $6 \cdot 10^{14} \text{ W cm}^{-2}$  has been reported by the Lebedev group (G2). Temporally and spectrally resolved backscattered light showed increased broadening to the red, with increase in power up to  $\sim 10^{13} \text{ W cm}^{-2}$ . At higher irradiance, a blue wing developed which was delayed in time with respect to the red part. This delay decreased with further increase in irradiance and was zero at  $3 - 5 \cdot 10^{14} \text{ W cm}^{-2}$ . Small scale structure in time and wavelength was also observed.

Workers at Rochester (G3) have studied Brillouin scattering from cylindrical targets. They observed high initial reflectivities ( $\sim 80\%$ ) followed by a falling off to  $\sim 10\%$ .

Brillouin backscatter studies of  $\text{CO}_2$  laser plasmas have been conducted by the Alberta group (O1) and the saturation of the backscattering

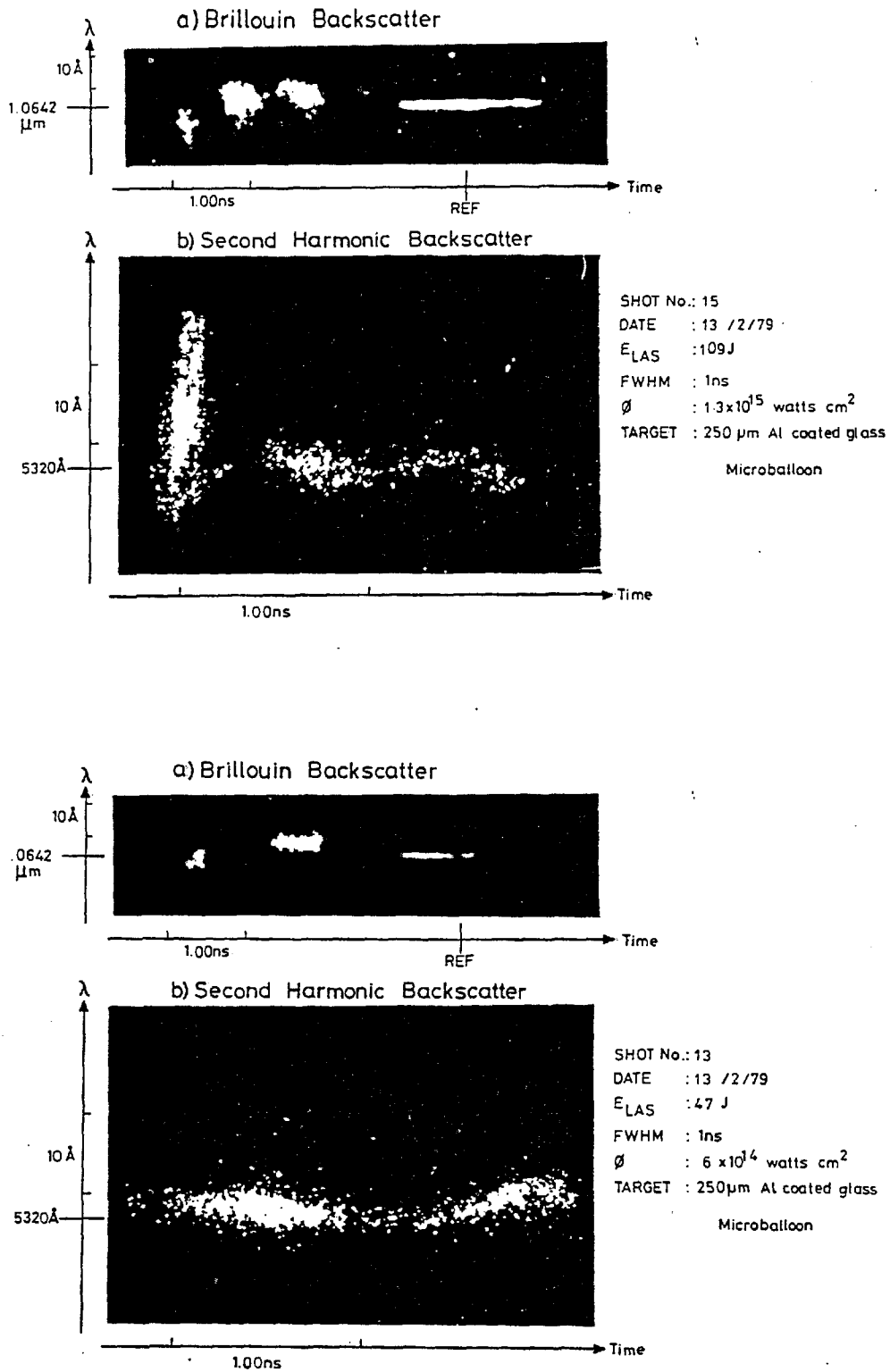


Fig 6.9 examples of backscattered spectra

has been observed at  $10^{13}$  W cm<sup>-2</sup> (N1). Brillouin scattering from pinches (A2) and from a laser heated plasma column (M2) have also been reported.

### 6.3 Experimental Arrangement

The present work provides temporally and spectrally resolved measurements of backscattered light from spherical targets. The observations differ from the NRL data (R3) in two respects; no prepulse preceded the main 1.6 ns FWHM pulse and, in addition, variation with target Z was investigated. A higher irradiance was used than in the Lebedev work (G2).

The experimental arrangement is shown in Fig. 6.7. The main Nd laser beam contained up to 110 J in 1.6 ns and was focussed onto microsphere and microballoon targets by an aspheric doublet f/1 lens. The backscattered  $\omega_0$  radiation was directed onto a 1 m MONOSPEC grating spectrograph and the dispersed output was optically coupled onto an Electro-Photonics S1 streak camera.

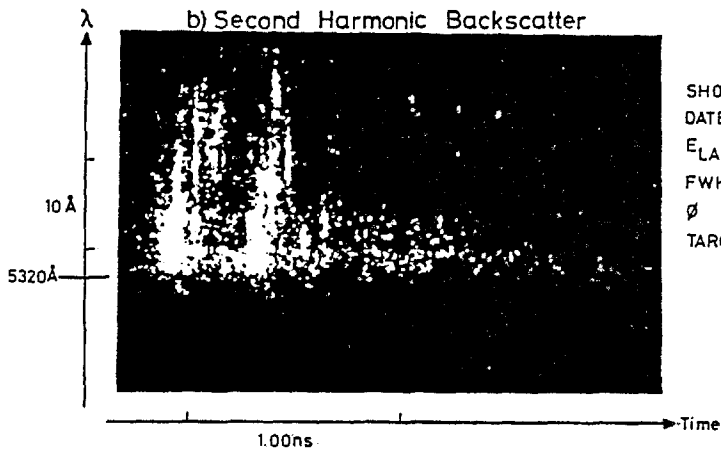
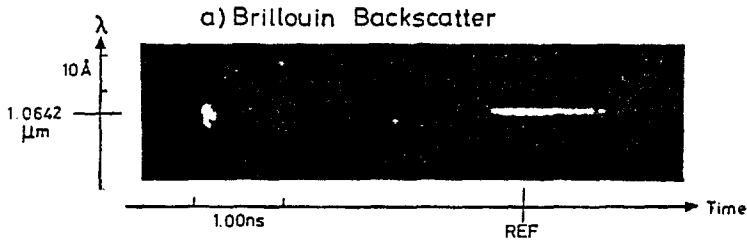
The streak camera was operated at a streak rate of 2 ns cm<sup>-1</sup> with  $\sim 100$   $\mu$ m slit, giving a best temporal resolution of 20 ps. The spectrograph was operated with 250  $\mu$ m slit and had dispersion 4  $\text{\AA}$  mm<sup>-1</sup> in the film plane. The spectral resolution was then  $\sim 1$   $\text{\AA}$ . This implies a temporal resolution (3.10) of

$$\Delta t = \frac{\lambda^2}{c\Delta\lambda} = 37 \text{ ps}$$

The streak camera can resolve 100 - 400  $\mu$ m at its entrance slit when in the streak mode. With x2 magnification from the spectrograph to the streak slit, (2  $\text{\AA}/\text{mm}^{-1}$ ), no further loss of spectral resolution was caused by the streak camera.

The net spectral and temporal resolutions were therefore 1  $\text{\AA}$  and

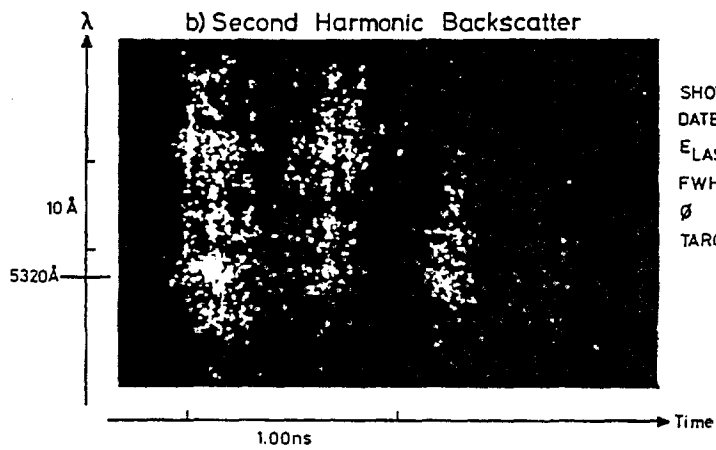
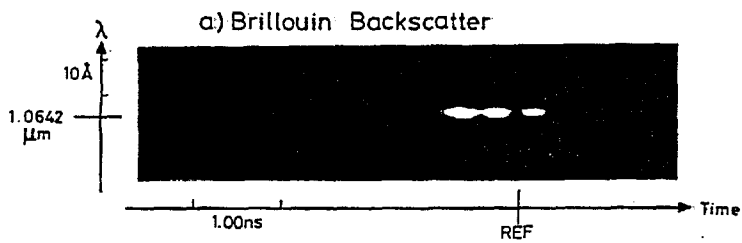




SHOT No.: 9  
DATE : 15 /2/79  
E<sub>LAS</sub> : 50 J  
FWHM : 1ns  
∅ :  $2.5 \times 10^{15}$  watts cm<sup>2</sup>  
TARGET : 90 μm U<sup>238</sup>

Microsphere

Fundamental and Second Harmonic Time Resolved Spectra



SHOT No.: 7  
DATE : 15 /2/79  
E<sub>LAS</sub> : 100J  
FWHM : 1ns  
∅ :  $5 \times 10^{15}$  watts cm<sup>2</sup>  
TARGET : 85 μm Al coated glass

Microballoon

40 ps respectively.

A portion of the incident beam was delayed and guided to the streak camera via the spectrograph. This provided both wavelength and time origins as well as giving the profile of the incident pulse.

Simultaneously with the  $\omega_0$  spectroscopy, backscattered light at  $2\omega_0$  was taken via a dichroic mirror to a 0.5 m SPEX grating spectrograph and an Imacon S-20 streak camera. The wavelength and time resolutions at  $2\omega_0$  were about 1 Å and 15 ps respectively. Results for the  $2\omega_0$  spectroscopy are included in the figures below for completeness and with the kind permission of S. Sim. Further discussion of the  $2\omega_0$  data may be found in Ref. R4.

The incident and reflected energies at 1.06  $\mu\text{m}$  were monitored by two calorimeters as shown in Fig. 6.7.

The targets were microspheres and microballoons in essentially two different sizes; 'small' of 70 - 90  $\mu\text{m}$  diameter and 'large' of 210 - 240  $\mu\text{m}$  diameter. A range of Z was used from plastic polymer to  $\text{U}^{238}$  in the small targets and from plastic to manganese-nickel alloy in the larger size.

The duration and shape of the laser pulses was kept unchanged throughout the measurements except for one or two multi-peaked pulses caused by mode beating in the laser cavity. The focussing of the laser beam by the f/1 lens was onto the centre of the spherical targets so that all rays were close to normal incidence. On the small targets, the irradiance for a beam energy of 100 J was  $4 \cdot 10^{15} \text{ W cm}^{-2}$  and on the larger targets, the corresponding irradiance was  $5.2 \cdot 10^{14} \text{ W cm}^{-2}$ .

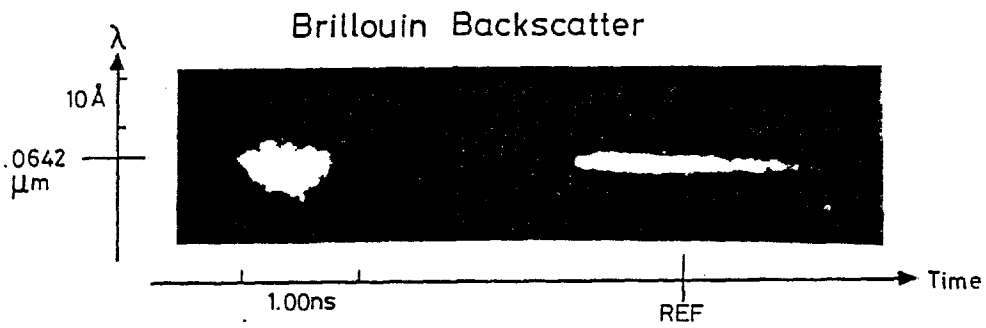


Fig 6.10

Time resolved backscatter spectrum from plane brass target, laser energy 10 J in 1.6 ns pulse.

#### 6.4 Results

The backscattered energy measurements at 1.06  $\mu\text{m}$  are summarized in Fig. 6.8. For a fixed target type, the fraction of laser energy which is backscattered into the focussing lens remains fairly constant over the limited range of irradiance that was studied. We therefore do not see evidence for saturation of the Brillouin backscatter at this irradiance (N1).

For low Z targets, small microballoons generated more backscattered light (20 - 25%) than large microballoons (10 - 15%). This result appears to contradict the association of increased backscatter from larger plasmas. However, the lower irradiance on large targets may reduce the coronal temperatures sufficiently to inhibit the generation of a long scale length underdense region. This will be discussed further in the next section.

Both small and large targets of high Z material exhibit less backscatter (30 - 40% less) compared with the aluminium coated microballoons. This is to be contrasted with the results of Ref. R5 in which short pulses were used and no Z dependence observed.

Some typical time-resolved spectra of the backscattered  $\omega_0$  radiation are shown in Fig. 6.9. The characteristic development of the spectra is as follows. A short burst of blue shifted ( $\approx 5 \text{ \AA}$ ) light occurs early in the incident pulse, followed by a long, red-shifted component. The red component is spectrally broader than the blue and generally lasts throughout the incident pulse. Frequently, the two components appear separate in time on the streak photographs.

The centroid of the long red part of the spectrum, although remaining red-shifted throughout the incident pulse, is generally moving towards the blue at late times.

Results from low irradiance (alignment) shots on plane, brass targets are of the form shown in Fig. 6.10. Here, the early blue-shifted com-

Table 6.1 List of data shots for the Brillouin experiment

SHOT	Target material, diameter	$E_{las} / J$	$E_{bs} / J$	Comments
8/130279	Plane, brass	7.4	1.01	
9	.. ..	7.6	0.54	
10	.. ..	7.6	small	
12	Al coated glass 250 $\mu$ m	18.5	3.2	
13	.. ..	29.4	2.5	
14	.. ..	64.9	9.5	
15	.. ..	68.7	7.8	Mode beating in inc pulse
16	Ni - Mn 240	66.8	5.1	
17	.. ..	32.3	3.0	
2/150279	.. 250	27.9	0	
4	.. ..	55.3	14.6	
5	Al coated glass 90	38.5		
7	.. ..	67.7	12.9	Mode beating in inc pulse
8	.. 84	38.2	9.4	
9	$U^{238}$ 90	34		
10	.. ..	76.5	6.35	
11	.. ..	75.8	10.1	
12	Plastic 80	70		
6	Al coated glass 90	34.5	8.9	No S1 streak available

ponent is the only part of the spectrum that remains. The backscattered light therefore appears to cut off during the incident pulse.

In addition to the broad features, time-resolved spectra (especially the well-exposed pictures) exhibit small scale structure in both time and wavelength. Backscattered power varies over time  $\sim 80$  ps and wavelength  $\sim 2 \text{ \AA}$  in this structure.

Any modulation in the incident pulse due to mode beating shows up in the backscattered pulse. Such a shot can provide information on the Brillouin reflection coefficient for different scale length plasmas (6.5(d)).

A list of data shots for this experiment is included (Table 6.1).

## 6.5 Discussion

### (a) Calorimeter data

Less backscattered energy is observed from high Z targets. This may be due to increased inverse bremsstrahlung absorption due to high Z ions. If the scale length for inverse bremsstrahlung absorption is less than that for Brillouin scattering, then the scattering will be partially quenched.

In addition, the high Z material causes increased line and continuum emission, thereby lowering the coronal electron temperature. This must be balanced against the increased inverse bremsstrahlung absorption. If the electron temperature is reduced, the hydrodynamic scale length will also be reduced leading to less backscatter.

Less backscatter is observed from larger diameter targets. A lower irradiance is generated on the larger microspheres and so a lower electron temperature results. The smaller expansion velocity and scale length compensate for the larger irradiated surface.

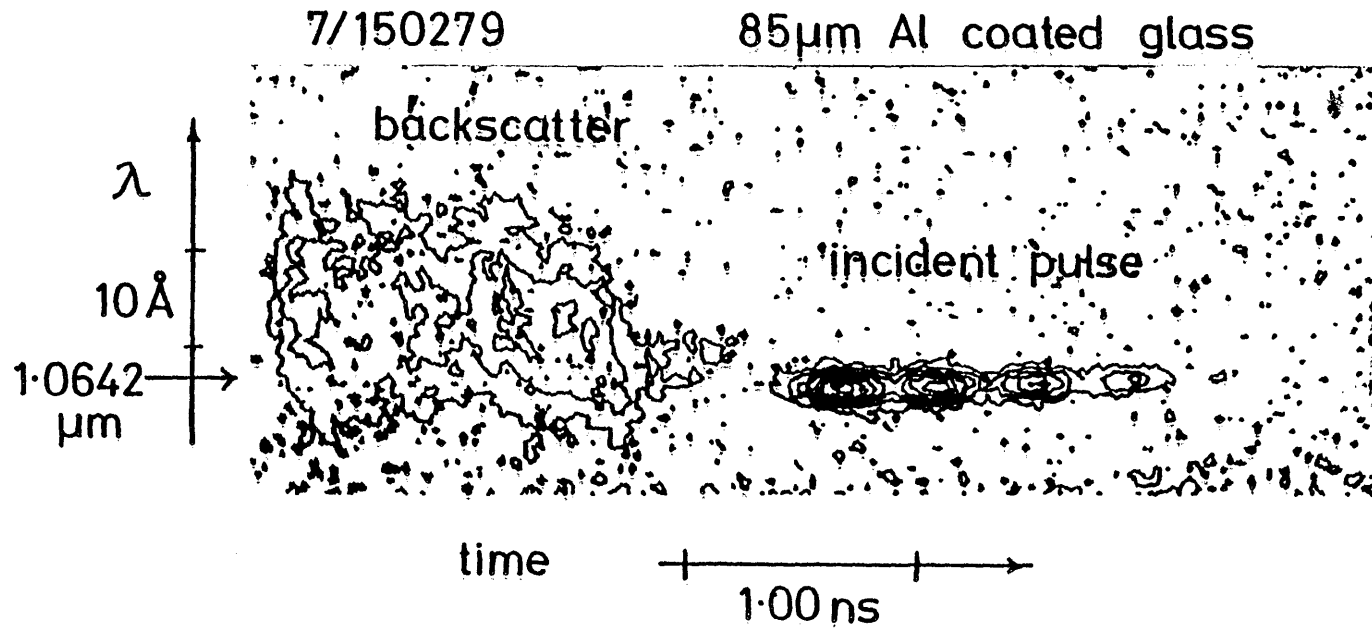


Fig 6.12 Two-dimensional densitometer scan of the streak picture for shot 7/150279

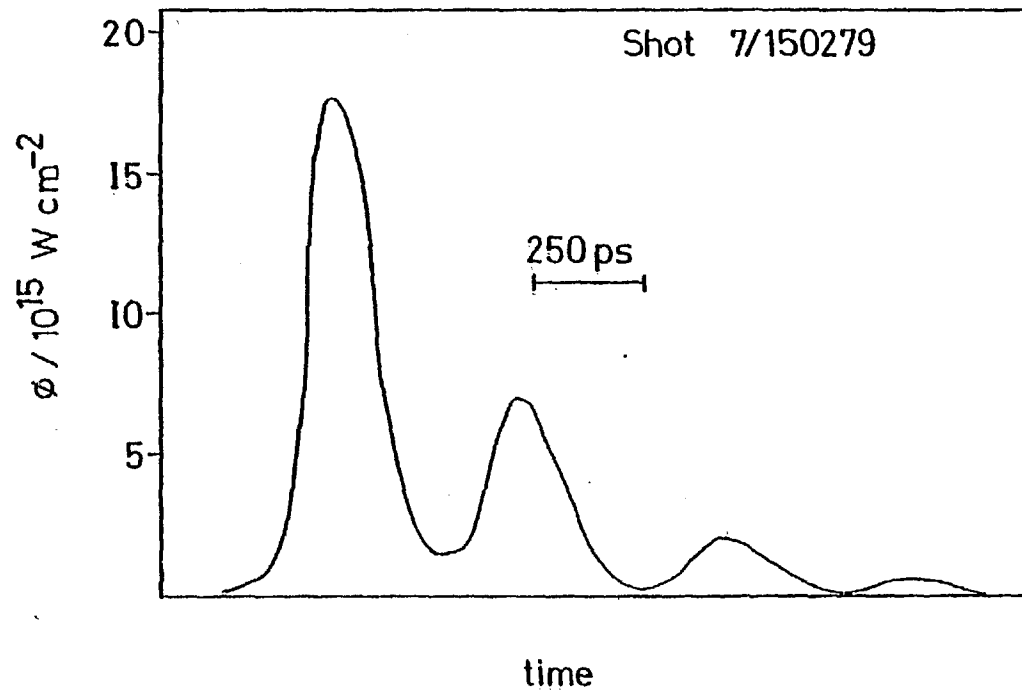


Fig 6.11 Incident pulse with mode beating

Table 6.2

REFLECTIVITY AND IMPLIED SCALELENGTHS FOR SHOT 15/130279

Pulse	1	2	3	4
Reflectivity	6	16	99	100 %
Scalelength	13	23	159	159 $\mu\text{m}$



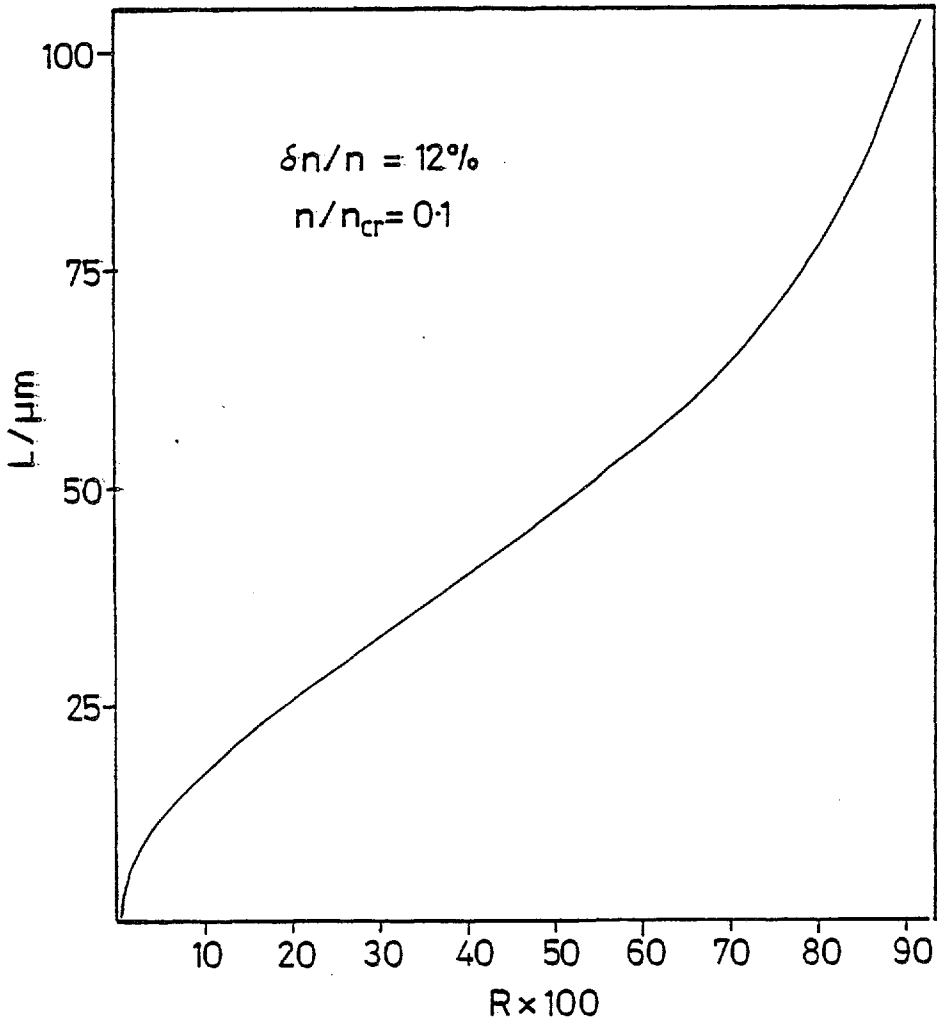


Fig 6.13 Density scalelength as a function of reflectivity with the density fluctuation limited by ion trapping

(b)  $\omega_o$  spectra

The early, blue part of the spectrum is attributed to specular reflection from a steep density jump. At this time, the incident irradiance is below the Brillouin threshold and the density profile is just beginning to evolve. With the generation of an underdense corona and with a sharply rising incident pulse, inverse bremsstrahlung absorption and Brillouin scattering shut off the specular reflection. The back-scattered pulse is then observed with a characteristic net red shift. Towards the end of the pulse, considerable amounts of plasma are in the low density, outer regions of the plasma. At this time, the incident irradiance is lower than at the peak but the flow velocity is maintained (M3). In this way, the gradual decrease in the red shift may be understood, the Doppler component is constant, but the Brillouin component is decreasing. This behaviour is also observed in Refs. G2 and R3.

We now estimate the coronal electron temperature using the results of 6.1(h) and using a Mach number for the flow of 0.82 indicated by the Livermore data (R1).

Taking  $\Delta\lambda = -5 \text{ \AA}$  for the high irradiance shots on aluminium coated microballoons, we have;

$$\begin{aligned} T_e &= \left( \frac{\Delta\lambda}{\lambda_o} \frac{c}{2(m-1)} \right)^2 \frac{M}{Z} m_p \\ &= \left( \frac{5}{10640} \frac{c}{2 \cdot 0.18} \right)^2 \frac{M}{Z} m_p \end{aligned}$$

Taking  $M/Z = 2$ , this gives an electron temperature of 3.2 keV and a sound speed of  $4 \cdot 10^7$  cm/s. The figure for the electron temperature is sensitive to the Mach number used and so should be regarded as an estimate. The electron temperature is estimated in the region where Brillouin scattering predominantly operates, that is around  $0.2 n_{cr}$ .

Rosen et al. (R1) calculate a temperature of  $20 \pm 10$  keV from their

Brillouin shifts. Using the scaling adopted in R1,

$$T_e \sim Z^{2/5}$$

the Rosen et al. data for gold ( $Z = 58$ ) targets imply a temperature for glass microballoons of

$$T_e = \left\{ \frac{4}{58} \right\}^{2/5} 20 \text{ keV} = 6.9 \pm 3.4 \text{ keV}$$

which is in agreement with our data.

(c) Plane target shots

Alignment shots early in the experimental run were onto plane, brass targets. The irradiance on targets was low ( $< 10^{14} \text{ W cm}^{-2}$ ) but is now known exactly. The  $\omega_0$  streak pictures show the early blue part of the spectrum but not the late red component. This is very similar to the data reported in Refs. M1 and A1 although in a lower irradiance régime. In these experiments, (M1, A1) the backscattered light was temporally, but not spectrally, resolved. This behaviour has been explained by profile modification caused by the ponderomotive force (K1) although our data do not support this.

In contrast, spectrally resolved measurements reported by Gorbunov et al. (G2) and the NRL group (R3) do not show a cut off and are more similar to our microballoon data.

The behaviour of backscattered light from the plane targets is not understood, although specular reflection may be dominating Brillouin effects. However, we do not wish to argue too strongly in the light of uncertainties in our experimental data.

(d) Mode beating shot

Shot 7/150279 consisted of a series of 4 or 5 short (200 ps FWHM) pulses separated by 450 ps due to mode beating in the neodymium laser cavity. Fig. 6.11 shows the incident pulse and Fig. 6.12 a 2-D scan of

the backscatter streak picture .

By integrating under the backscatter "surface" and equating the volume to the backscattered energy, we may estimate the reflection coefficient for each pulse. The results are shown in Table 6.2. The reflectivity is low for the first two pulses but jumps to ~100% for the last two.

Scale lengths for Brillouin matching may be derived from the measured reflectivity assuming  $\delta n/n$  of the ion waves limited by ion trapping. We use Kruer's model (K2) with  $T_i \ll ZT_e$  (E1). Putting  $T_e/T_i = 10$ , the maximum value of  $\delta n/n$  is (Fig. 1.) ~12%. Taking  $n/n_{cr} = 0.1$ , we have from 6.1(f);

$$\alpha = \frac{\pi}{2} \frac{n}{n_{cr}} \frac{1}{\lambda_0} \left( 1 - \frac{n}{n_{cr}} \right)^{-\frac{1}{2}} = \frac{0.166}{\lambda_0}$$

and

$$\theta = \alpha L \frac{\delta n}{n} = 0.0199 \left( \frac{L}{\lambda_0} \right)$$

But

$$\sqrt{r} = \frac{1 - B^2}{1 + B^2} \Rightarrow B = \left( \frac{1 - \sqrt{r}}{1 + \sqrt{r}} \right)^{\frac{1}{2}}$$

so

$$\frac{L}{\lambda_0} 0.0199 = \ln \left( \left( \frac{1 + \sqrt{r}}{1 - \sqrt{r}} \right)^{\frac{1}{2}} \right)$$

For a neodymium laser,

$$L = 26.6 \mu\text{m} \ln \left( \frac{1 + \sqrt{r}}{1 - \sqrt{r}} \right)$$

This is plotted in Fig. 6.13.

The implied scale lengths for each of the mode beats are shown in the last column of Table 6.2. The jump in scale length between the second and third pulses may be due to the turning off of the ponderomotive

force. The irradiance drops from  $7.2$  to  $1.9 \times 10^{15} \text{ W cm}^{-2}$  between the two pulses. We have calculated (6.1(f)) the threshold for profile modification to be around this level.

## 6.6 Conclusion

Time-resolved spectra of the backscattered light from spherical targets have been presented. Long (1.6 ns FWHM) laser pulses were used and unlike similar measurements at NRL, no prepulses were generated prior to the main pulse.

The data show features indicative of Brillouin backscattering and are broadly in agreement with data from other laboratories. High spectral and temporal resolutions have allowed the observation of new features in the backscattered spectra. The backscattered light is not observed to switch off before the end of the incident pulse, as reported by some other workers.

Calorimeter data show a decrease in backscatter from high Z targets.

Simple models have been used to derive coronal temperatures and density scale lengths from the measurements. The electron temperature of a low Z target is in agreement with Livermore data for gold discs, assuming  $T_e$  scales like  $Z^{2/5}$ .

A mode beating shot gave very high ( $\sim 100\%$ ) reflectivities for the last few pulses on a low Z target. A jump in the implied scale lengths between the second and third pulses may be due to a turning off of the ponderomotive pressure.

CHAPTER 7

FURTHER EXPERIMENTS WITH SPHERICAL TARGETS

Two techniques are discussed giving measurements of the coronal expansion velocity of laser-irradiated microballoons. Firstly, time-resolved observations of the second harmonic ( $2\omega_0$ ) emission are presented (7.2). Secondly, streak photography of microballoons, backlit with a ruby laser probe beam, is described (7.3).

7.1 Second Harmonic Generation

Emission at twice the laser frequency has been observed in laser-solid target experiments (C1,B7,B8). The main features of the emission are:

- (i) second harmonic (SH) emission occurs predominantly in the critical surface region,
- (ii) it is closely associated with resonance absorption and occurs only for a p-polarised incident beam,
- (iii) SH intensity varies as the square of the incident ( $\omega_0$ ) intensity,
- (iv) SH light is emitted in the direction of specular reflection of the incident light,
- (v) there is an optimum angle of incidence for which SH emission is a maximum,
- (vi) there is no SH emission for a normally incident beam or in homogeneous plasma.

Some of these statements are modified in the presence of a rippled critical density surface.

The propagation of electromagnetic waves in inhomogeneous plasmas is treated by Ginzburg (G5) and his analysis is extended to SH generation in Refs. E2 and D2. Time-resolved measurements of  $2\omega_0$  light, similar

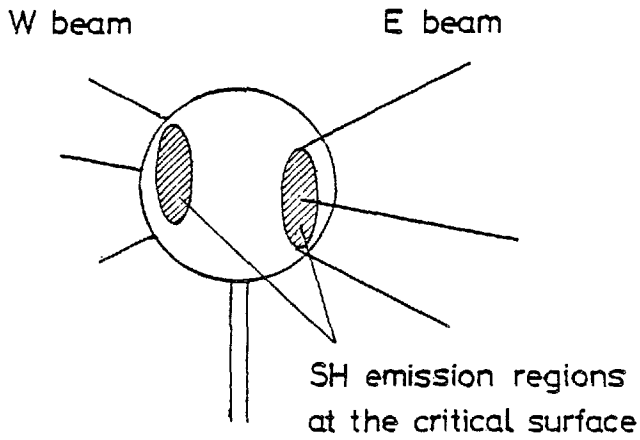


Fig 7.1 Regions that emit second harmonic radiation during the irradiation of microballoons

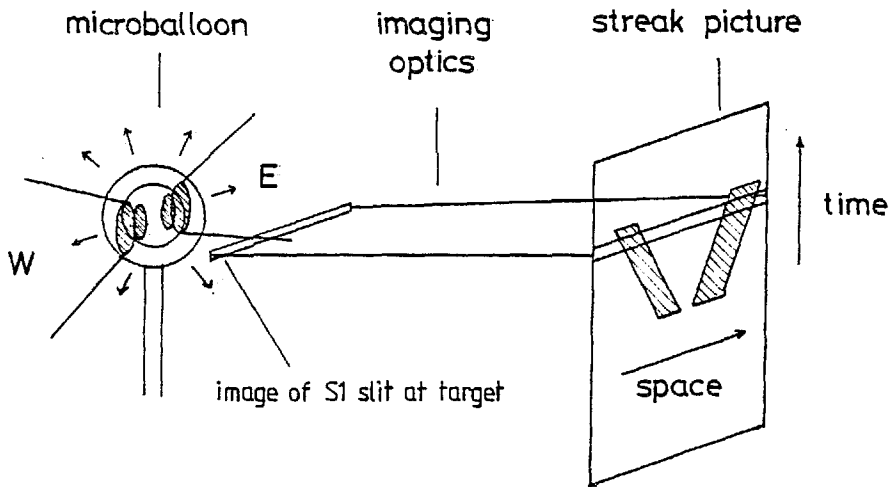


Fig 7.2 Origin of the V-shaped streak pictures

to those presented in 7.2, have been reported in Refs. J2 and J3. Similar results have been obtained by other laboratories.

## 7.2 Second Harmonic Emission From Microballoons

When a spherical target is irradiated by two laser beams,  $2\omega_0$  light is emitted mainly from the critical surface regions within the focal spots (Fig. 7.1). An image of the target is formed at the entrance slit of the S1 streak camera. The streak picture will then show the  $2\omega_0$  emitting regions move during the incident laser pulse. The expanding critical surface will lead to a V-shaped streak picture as shown in Fig. 7.2. The angle  $\theta$  is related to the expansion velocity of the critical surface  $v$ ;

$$v = \frac{\tan \theta}{mr}$$

where  $r$  is the streak rate and  $m$  the target to streak picture magnification.

The experimental arrangement is shown in Fig. 7.3; the lens L is an  $f/2$ , 6 cm focal length lens which images the target T at the streak slit with a magnification of 65. The theoretical best object plane resolution is

$$R = 1.22 \lambda \phi \left(1 + \frac{1}{m}\right)$$

where  $m$  is the magnification and  $\phi$  the f-number of the lens. In the present experiment,  $\lambda = 0.52 \mu\text{m}$  so  $R = 1 \mu\text{m}$ . The streak camera can resolve only 100 - 400  $\mu\text{m}$  at the slit in streak mode. This corresponds to  $\sim 10 \mu\text{m}$  resolution in the target plane.

The target to film plane magnification was checked by backlighting a 30  $\mu\text{m}$  grid positioned at the target. A densitometer scan of the resulting image is shown in Fig. 7.4; the streak camera was on static mode. The overall magnification was  $\times 45$ ; there is  $\sim 2/3$  magnification



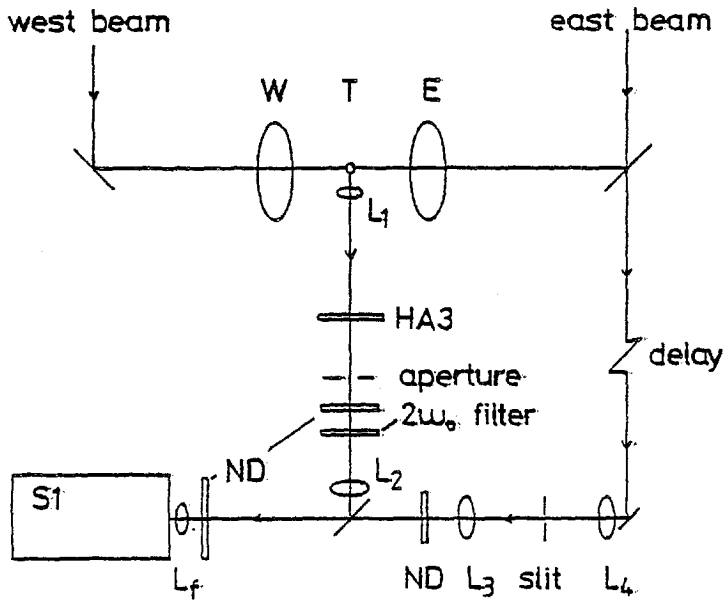


Fig 7.3 Experimental arrangement

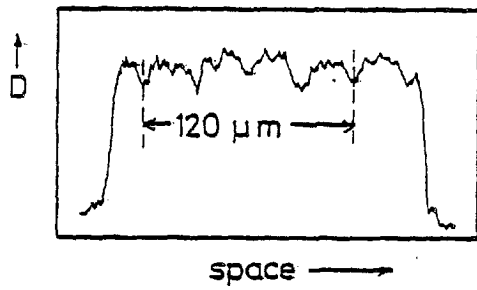


Fig 7.4 Static mode picture of a 30μm grid in the target position

in the streak camera.

The S1 camera was operated at a streak rate of  $500 \text{ ps cm}^{-1}$  with a  $200 \text{ }\mu\text{m}$  slit. This implies a temporal resolution of  $\sim 10 \text{ ps}$ , although overexposure can degrade this.

A fraction of the incident beam was relayed to the camera to provide the incident pulse profile and a time origin.

Examples of the data are shown in Fig. 7.5 and are seen to have the expected shape. They are similar to the results of other laboratories and imply expansion velocities of  $\sim 2 \cdot 10^7 \text{ cm/sec}$  for the critical surface. The emission lasts throughout the incident pulse. Frequently, the expansion velocities each side of the sphere are unequal. Emission at different times indicates poor synchronisation between the two laser pulses (east and west). No emission from one or both faces is due to poor focussing and/or target alignment.

The separation  $d$  (Fig. 7.6) corresponds to the target diameter  $D$ . The measurement  $\Delta$  gives an estimate of the focal spot size. Simple geometry gives

$$\text{focus diameter} = 2\sqrt{\Delta(D-\Delta)}$$

For shot 39/020677,  $D = 72.5 \text{ }\mu\text{m}$  and  $\Delta = 15 \text{ }\mu\text{m}$  which gives a focal spot diameter of  $\sim 60 \text{ }\mu\text{m}$ . For this shot, both laser beams were focussed on the target centre. With thermal lensing, which shifts the focus still further behind the target, the  $60 \text{ }\mu\text{m}$  figure is reasonable.

The 1D fluid code MEDUSA has been used to model the expansion velocity of the critical surface. With fast electrons, the code gives a velocity of  $1.5 - 2 \cdot 10^7 \text{ cm/sec}$  in agreement with experiment. This result is not sensitive to flux inhibition but does require fast electrons. With the fast electrons turned off, expansion is very slow and can become negative. However, the modelling was not very accurate because ponderomotive force effects were not included.

Table 7.1 List of data shots for second harmonic emission from spherical targets

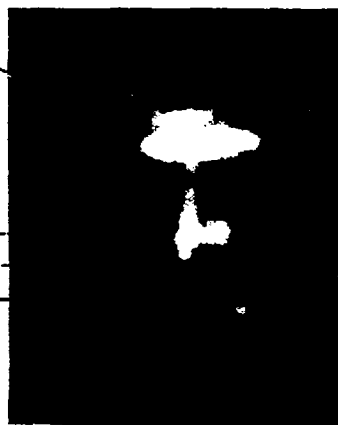
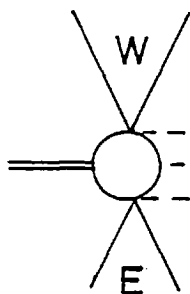
SHOT NUMBER	$E_{las}/J$		TARGET DIAMETER/ $\mu m$ , WALL THICKNESS FOCUS				VELOCITY/ $10^6 cm.sec^{-1}$	
	WEST	EAST			WEST	EAST	WEST	EAST
24/250577	9.8	11.8	75.5	0.91	-2	+1		
25/250577	6.2	9.6	74	1.0	-1	+1	18	4
26/250577	9.9	14.2	66	1.05	-1	+1	10	5
35/010677	5.9	7.9	68	0.8	+1	+1		
36/010677	13.6	17.1	70	0.85	0	0	14	23
39/020677	11.3	13.7	72.5	0.94	+1	+1	17	16
42/020677	11.5	14.2	72	0.98	+2	+2		
43/020677	14.8	18.6	69.5	0.79	0	0		

Target focusing; 0 polar focus (i.e. on balloon surface)  
+1 target moved one balloon diameter towards focusing lens  
-1 .. .. .. away from ..  
etc.

36/010677

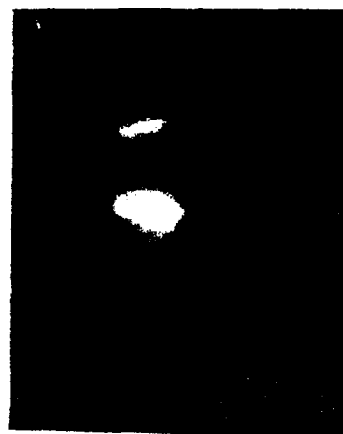
incident pulse

2 $\omega$  emission



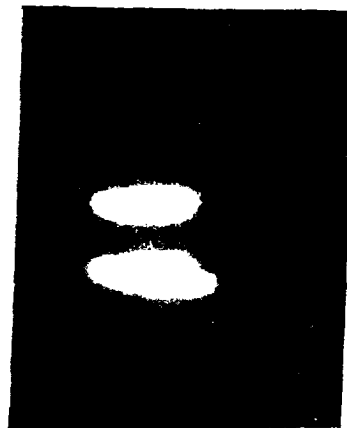
39/020677

100  $\mu$ m  
space



42/020677

200 ps  
time



43/020677



Fig. 7.5 Examples of second harmonic emission from microballoons

A list of data shots for this experiment is given in Table 7.1.

### 7.3 Backlighting of Spherical Targets

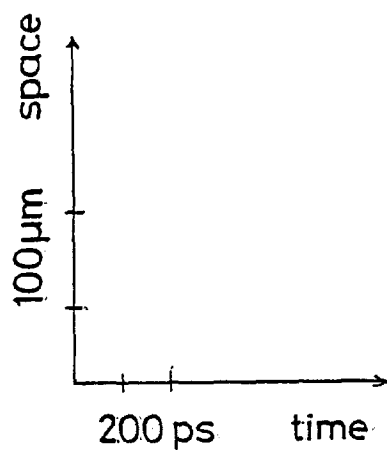
The expansion velocity of the outer regions of the target can be measured by backlighting with a ruby probe beam and imaging at a streak camera. The arrangement is similar to 7.2 and is shown in Fig. 7.7. The expansion velocity of the  $n_e = 2.3 \cdot 10^{21} \text{ cm}^{-3}$  density surface is measured as a function of time.

An example of the data is shown in Fig. 7.8 and the implied velocity is given in Fig. 7.9 as a function of time. The temporal resolution was  $\sim 20$  ps because a slow streak rate was used.

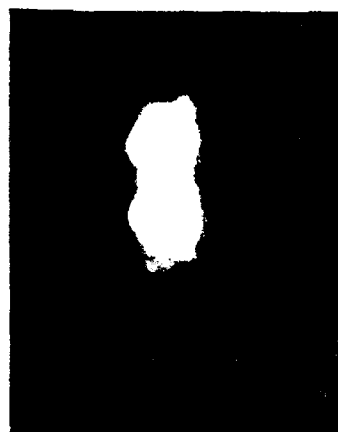
24/250577



25/250577



26/250577



35/010677

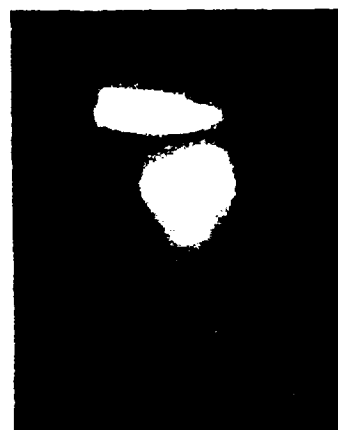
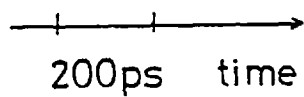


Fig 7.5 continued

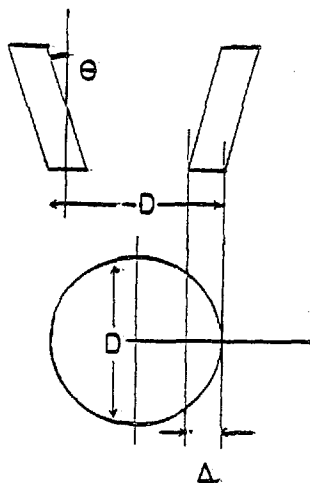
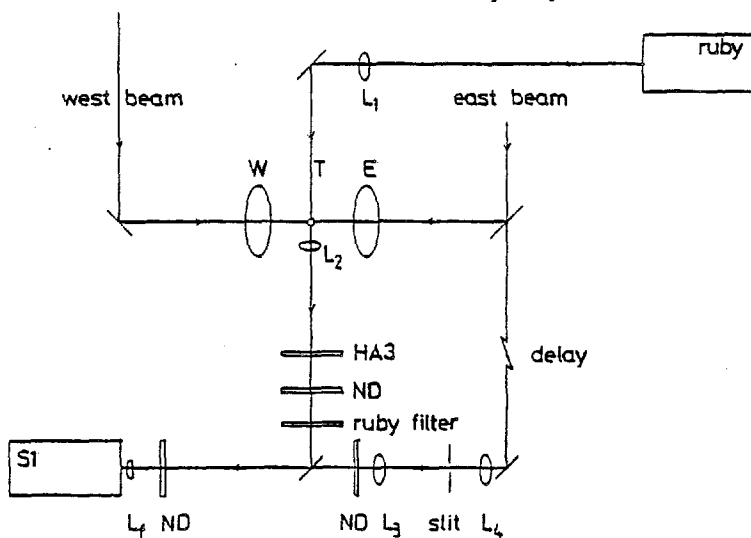


Fig 7.6 Definitions of D and  $\Delta$

Fig 7.7 Experimental arrangement for microballoon backlighting



CHAPTER 8

CONCLUSION

Results have been presented from a number of experiments involving the irradiation of planar and spherical targets by neodymium laser pulses. Observations made during the thin foil experiment have been interpreted as implying the presence of ion turbulence. Anomalous absorption of laser light in the underdense plasma and reduced radial heat conduction can then be understood. In the Brillouin experiment, backscattered light at near the laser frequency has been spectrally and temporally resolved. Spectral shifts have been interpreted in terms of Brillouin and Doppler effects.

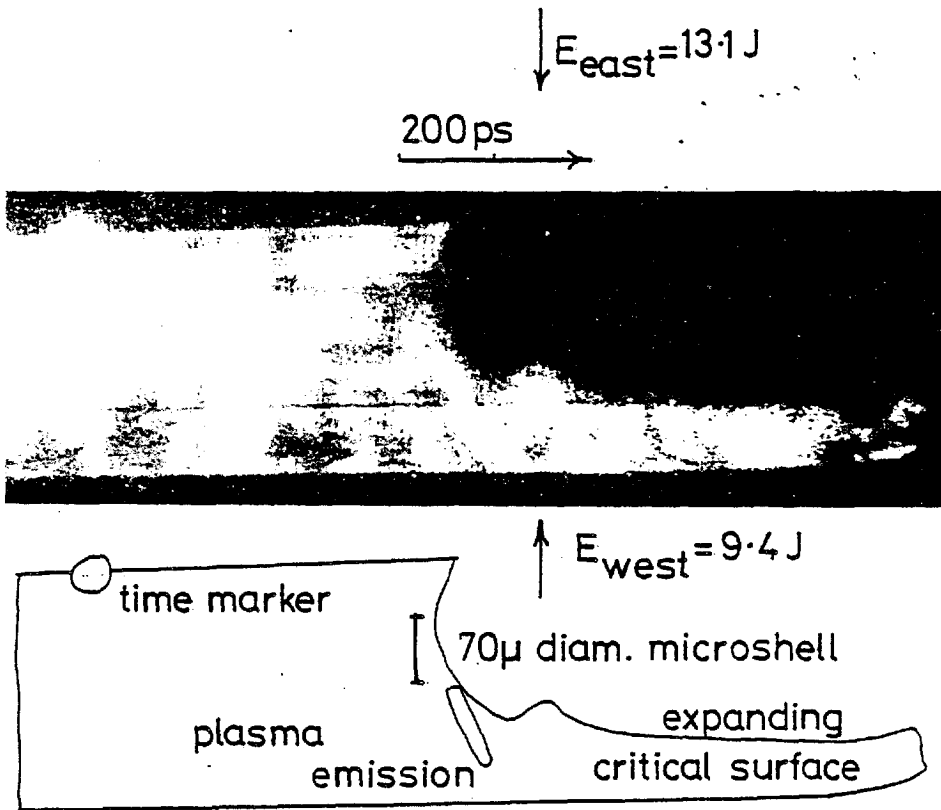
The thin foil work may be extended to include different laser pulse wavelengths and durations. Variation of the target material would give information on the Z scaling of the absorption and thermal conductivity. Work is in progress at the Naval Research Laboratory, Washington D.C. on the ablative acceleration of thin foils. In these experiments, lower irradiances ( $10^{12} - 10^{14} \text{ W cm}^{-2}$ ) and longer pulse lengths ( $\sim 3 \text{ ns}$ ) are used, compared with the parameters of Ch. 4. These correspond more to the conditions envisaged for fusion. In some respects, the diagnostic techniques described in Ch. 3 have been superseded by X-ray methods. Thin layers of fluors, in emitting characteristic radiation under certain density and pressure conditions, give information on the burn depth, burnthrough time and ablation pressure achieved by the incident beam. A considerable amount of work has been done at the Rutherford Laboratory in this direction and further developments will follow.

Investigations of Brillouin scattering have continued at the Rutherford Laboratory since the experiment described in Ch. 6.



Fig 7.8 Example of backlighting data

Ruby side illumination of  
microshell implosion  
SHOT 081277/154



Principally, time-resolved spectra have been obtained with an incident beam wavelength of 0.52  $\mu\text{m}$ . This work may be extended to still shorter laser wavelengths. Further plasma diagnostics may be included, for example interferometry, in order to determine the density scale-length in the outer, scattering region of the target.

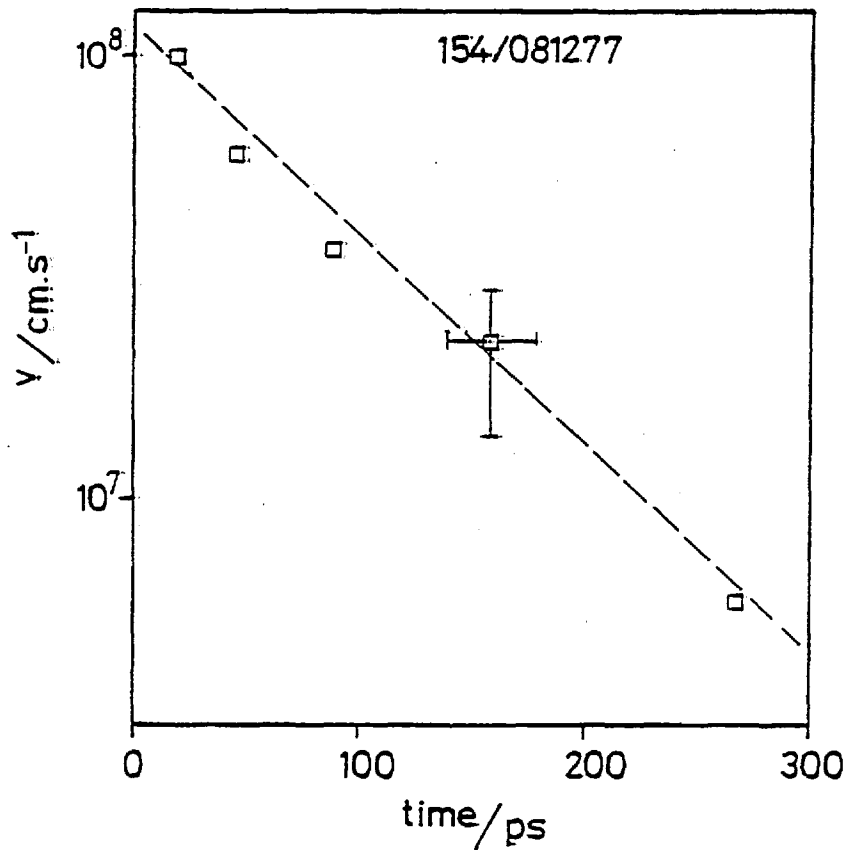


Fig 7.9 Expansion velocity of the ruby critical surface, from the data of Fig 7.8

REFERENCES

- A1 H. Azechi et al, in Proceedings of the Seventh International Conference on Plasma Physics and Controlled Nuclear Fusion Research, Innsbruck, Austria, 1978, paper no. IAEA-CN-37-M-4
- A2 W.T.Armstrong, J.Appl.Phys. 49, 2566 (1978)
- A3 F.Amiranoff et al, in Proceedings of the Seventh Int. Conf. on Plasma Physics and Controlled Nuclear Fusion Research, Innsbruck, Austria, 1978, paper no. IAEA-CN-37-D-4
- A4 F.Amiranoff, R.Fabbro, E.Fabre, C.Garban, J.Virmont and M.Weinfeld, Phys. Rev. Lett. 43, 522 (1979)
- A5 D.E.T.F.Ashby, J.Br.Nucl.Energy Soc. 14, 311 (1975)
- A6 D.T.Attwood, D.W.Sweeney, J.M.Auerbach and P.H.Y.Lee, Phys.Rev.Lett. 40, 184 (1978)
- 
- B1 D.J.Bradley, S.F.Bryant, J.R.Taylor, and W.Sibbett, Rev.Sci.Instrum. 49, 215 (1978)
- B2 N.G.Basov and O.N.Krokhin, Sov.Phys. J.E.T.P. 19, 123 (1964)
- B3 R.J.Bickerton, Nuc.Fus. 13, 457 (1973)
- B4 B.Bezzerides, D.F.DuBois, D.W.Forslund and E.L.Lindman, Phys.Rev.Lett. 38, 495 (1977)
- B5 N.G.Basov et al, Sov.Phys.J.E.T.P. Lett. 8, 14 (1968) Recent experiments have cast doubt on whether, in fact, these neutrons were thermonuclear in origin
- B6 T.J.M.Boyd and J.J.Sanderson, Plasma Dynamics, Nelson, London, 1969
- B7 J.L.Bohin, M.DeCroisette, B.Meyer and Y.Vitel, Phys.Rev.Lett. 30, 594 (1973)
- B8 H.A.Baldis, H.Ripin, T.W.Johnston and K.J.Parbhakar, Phys.Rev.Lett. 35, 37 (1975)
- 
- C1 A.Caruso, A.De Angelio, G.Gratti, R.Gratton and S.Martellucci, Phys.Lett. 33A, 29 (1970)

- C2 J.P.Christiansen, D.E.T.F.Ashby and K.V.Roberts  
Culham Laboratory Report No. CLM-R130, 1973
- C3 R.S.Craxton, PhD Thesis, University of London,  
August 1976
- C4 R.S.Craxton and M.G.Haines, Phys.Rev.Lett. 35,  
1336 (1975)
- C5 F.F.Chen, Introduction to Plasma Physics, Plenum  
New York, 1975
- D1 J.F.Drake, P.K.Kaw, Y.C.Lee, G.Schmidt, C.S.Liu  
and M.N.Rosenbluth, Phys.Fluids 17, 778 (1974)
- D2 N.G.Denisov, Sov.Phys..J.E.T.P. 4, 544 (1957)
- E1 R.G.Evans, Rutherford Laboratory Report No.  
RL-79-061
- E2 N.S.Erokhin, V.E.Zakharov and S.S.Moiseev, Sov.  
Phys. J.E.T.P. 29, 101 (1969)
- E3 K.G.Estabrook, E.Valeo and W.L.Kruer, Phys. Lett.  
49A, 109 (1974)
- E4 K.G.Estabrook, Phys.Fluids 19, 1733 (1976)
- F1 D.W.Forslund, J.M.Kindel and E.L.Lindman, Phys.  
Fluids 18, 1002 (1975)
- F3 D.W.Forslund, J.Geophys.Res. 75, 17 (1970)
- F2 D.W.Forslund, J.M.Kindel and E.L.Lindman, Phys.  
Rev.Lett. 30, 739 (1973)
- F4 D.W.Forslund, J.M.Kindel, K.Lee and E.L.Lindman  
Phys.Rev.Lett. 36, 35 (1976)
- F5 A.V.Farnsworth, M.M.Widner, M.J.Clauser and  
P.J.McDaniel, Phys.Fluids 22, 859 (1979)
- F6 R.J.Faehl and W.L.Kruer, Phys.Fluids 20, 55 (1977)
- F7 J.P.Friedberg, R.W.Mitchel, R.L.Morse and L.I.  
Rudsinski, Phys.Rev.Lett. 28, 795 (1972)
- F8 D.W.Forslund, J.M.Kindel, K.Lee, E.L.Lindman  
and R.L.Morse, Phys.Rev.A, 11, 679 (1975)
- F9 D.W.Forslund, J.M.Kindel and K.Lee, Phys.Rev.Lett  
39, 284 (1977)

- G1 D.R.Gray, PhD thesis, University of London, 1979, p.157
- G2 L.M.Gorbunov, Yu.S.Kos'yanov, V.V.Karobkin, A.N.Polyanichev and A.P.Shevel'ko, Sov.Phys. J.E.T.P.Lett. 27, 226 (1978)
- G3 L.M.Goldman, J.Soures and M.J.Lubin, Phys.Rev Lett. 31, 1184 (1973)
- G4 S.J.Gitomer and D.B.Henderson, Phys.Fluids 22, 364 (1979)
- G5 V.L.Ginzburg, The Propagation of Electromagnetic Waves in Plasmas, Pergamon, 1964
- 
- H1 R.A.Haas, W.C.Mead, W.L.Kruer, D.W.Phillion H.N.Kornblum, J.D.Lindl, D.MacQuigg, V.L.Rupert and K.G.Tirrell, Phys.Fluids 20, 322 (1977)
- 
- J1 T.W.Johnston and J.M.Dawson, Phys.Fluids 16, 722 (1973)
- J2 S.Jackel, J.Albritton and E.Goldman, Phys.Rev. Lett. 35, 514 (1975)
- J3 S.Jackel, B.Perry and M.Lubin, Phys.Rev.Lett. 37, 95 (1976)
- 
- K1 W.L.Kruer, E.J.Valeo and K.G.Estabrook, Phys. Rev.Lett. 35, 1076 (1975)
- K2 W.L.Kruer, Lawrence Livermore Laboratory Report No. UCRL 82701 (1979), submitted to Phys.Fluids
- 
- L1 C.S.Liu, M.N.Rosenbluth and R.B.White, Phys. Fluids 17, 1211 (1974)
- L2 L.D.Landau and E.M.Lifshitz, Fluid Mechanics, Pergamon, Oxford, 1959, Sec.92

- L3 J.M.Ley, C.G.Willey and T.M.Christmas, Proc. IEE 117, 1057 (1970)
- M1 W.C.Mead, R.A.Haas, W.L.Kruer, D.W.Phillion, H.N.Kornblum, J.D.Lindl, D.R.MacQuigg and V.C. Rupert, Phys.Rev.Lett. 37, 489 (1976)
- M2 R.Massey, K.Berggren and Z.A.Pietrzyk, Phys. Rev.Lett. 36, 963 (1976)
- M3 M.K.Matzen and R.L.Morse, Phys.Fluids 22, 654 (1979)
- M4 R.C.Malone, R.L.McCrosy and R.L.Morse, Phys.Rev. Lett. 34, 721 (1975)
- M5 J.Mizui, N.Yamaguchi, T.Yamanaka and C.Yamanaka, Phys.Rev.Lett. 39, 619 (1977)
- M6 W.M.Manheimer, D.Colombant and R.Flynn, Phys. Fluids 19, 1354 (1976)
- M7 W.M.Manheimer, Phys.Fluids 20, 265 (1977)
- M8 C.E.Max, W.M.Manheimer and J.J.Thomson, Phys.Fluids 21, 128 (1978)
- M9 R.J.Mason, Los Alamos Scientific Laboratory Report No. LA-UR-78-2776, 1978, submitted to Phys.Rev.Lett.
- M10 W.M.Manheimer, D.G.Colombant and B.H.Ripin, Phys.Rev.Lett. 38, 1135 (1977)
- M11 W.M.Manheimer and D.G.Colombant, Phys.Fluids 21, 1818 (1978)
- N1 A.Ng, L.Pitt, D.Salzmann and A.A.Offenberger, Phys.Rev.Lett. 42, 307 (1979)
- N2 NRL Memorandum Report 3890, 1978, Laser-plasma Interaction and Ablative Acceleration of Thin Foils at  $10^{12}$  -  $10^{14}$  W cm<sup>-2</sup>
- N3 J.Nuckolls, L.Wood, A.Thiessen and G.Zimmerman, Nature 239, 139 (1972)
- O1 A.A.Offenberger, M.R.Cervenak, A.M.Yam and A.W.Pasternak, J.Appl.Phys. 47, 1451 (1976)

- P1 D.W.Phillion, W.L.Kruer, V.C.Rupert, Phys.Rev. Lett. 39, 1529 (1977)
- P2 J.S.Pearlman and J.P.Anthes, Appl.Phys.Lett. 27, 581 (1975)
- P3 J.S.Pearlman and J.J.Thomson, Appl.Phys.Lett. 32, 703 (1978)
- 
- R1 M.D.Rosen, D.W.Phillion, V.C.Rupert, W.C.Mead, W.L.Kruer, J.J.Thomson, H.N.Kornblum, V.W.Slivinsky G.J.Caporaso, M.J.Boyle and K.G.Tirsell, Lawrence Livermore Report No. UCRL 82146, 1978
- R2 B.H.Ripin, F.C.Young, J.A.Stamper, C.M.Armstrong, R.Decoste, E.A.McLean and S.E.Bodner, Phys.Rev. Lett. 39, 611 (1977)
- R3 B.H.Ripin, J.M.McMahon, E.A.McLean, W.M.Manheimer and J.A.Stamper, Phys.Rev.Lett. 33, 634 (1974)
- R4 Rutherford Laboratory Report No. RL-79-036
- R5 B.H.Ripin and E.A.McLean, Appl. Phys. Lett. 34, 809 (1979)
- R6 Rutherford Laboratory Report No. RL-78-039
- R7 P.D.Rockett, D.G.Steel, J.G.Ackenhusen and D.R.Bach, Phys.Rev.Lett. 41, 554 (1978)
- R8 A.Raven, O.Willi and P.T.Rumsby, Phys.Rev.Lett. 41, 554 (1978)
- R9 RCA Photomultiplier Manual, Technical Series PT-61, 1970
- R10 Science Research Council, Central Laser Facility Rutherford Laboratory, Chilton, Didcot, Oxfordshire
- 
- S1 M.S.Sodha and V.K.Tripathi, Phys.Rev.A 16, 2101 (1977)
- S2 H.D.Shay et al, Phys.Fluids 21, 1634 (1978)
- S3 L.Spitzer, Physics of Fully Ionized Gases, Wiley, New York, 1962

- T1 V.N.Tsyтович, Nonlinear Effects in Plasmas,  
Plenum, New York, 1970
- T2 D.A.Tidman and R.A.Shanny, Phys.Fluids 17, 1207  
(1974)